2004

Experimental determination of stiffness of joints in welded Tuff

Jaak J.K. Daemen
University of Nevada, Reno, daemen@mines.unr.edu

George Danko
University of Nevada, Reno, danko@unr.edu

Amy J. Smiecinski
University of Nevada, Las Vegas, smiecins@unlv.nevada.edu

Final Technical Report – Part 1

Experimental Determination of Stiffness of Joints in Welded Tuff

Long - Term Drift Stability
Task 18
Document ID: TR-03-018
Revision: 0

Prepared for U.S. DOE/UCCSN
Cooperative Agreement DE-FC28-98NV12081

David Nutakor and Jaak Daemen
Department of Mining Engineering
Mail Stop 173
University of Nevada, Reno 89557

Originator: [redacted] 6-1-04

Jaak Daemen — Date

Approvals:

[redacted] 6/1/04

Technical Reviewer, George Danko — Approval Date

[redacted] 6-1-04

Principal Investigator, Jaak Daemen — Approval Date

[redacted] 6-1-04

QA Manager, Amy Smiecinski — Approval Date

ABSTRACT

Fourteen uniaxial joint compression tests were run to determine the normal and shear stiffnesses of type 1 fracture joints (healed joints filled with vapor-phase mineral deposits) obtained from the Yucca Mountain site. The uniaxial joint compression results show that these joints behave linearly up to over 85% of their loading history. They are stiff with strengths very close to the strength of the intact rock. Five direct shear tests were run on open, separated, joints. Results obtained from the direct shear testing show that the normal stiffness increases with increasing normal stress. Shearing through asperities gives high joint shear stiffness values, which reduce gradually as the contact surfaces smooth.

Intact rock Young's moduli obtained from the uniaxial joint compressive tests average 40.6 GPa, and range from 29.42 to 68.68 GPa. The Poisson's ratio averages 0.21, and ranges from 0.12 to 0.5. Joint normal stiffness (average 26 GPa/mm) and joint shear stiffness (average 10.82 GPa/mm) of the healed joints, i.e. joints filled with vapor-altered minerals, range from 7.16 to 64.77 GPa/mm and 3.09 to 28.41 GPa/mm respectively. From the stiffness of the healed joint, we have calculated the Young's modulus of the vapor phase altered joint infilling. The Young's modulus of the vapor-altered joint filling material averages 8.29 GPa and ranges from 2.15 to 19.43 GPa. Given the pervasive presence of such altered rock, usually in the form of sub-spheroidal three-dimensional pockets, this property should be of value for any numerical modeling attempting to describe the mechanical behavior of these tuff formations at the level of detail where inclusions might be a factor.

Recommendations are given for the pursuit of further investigations of the mechanical properties of joints. In order to assure maximum usefulness of the results, it would be desirable to assure that samples can be obtained from those joint systems most likely to affect repository performance.

TABLE OF CONTENTS

LIST OF TABLES

LIST OF FIGURES

1.0 INTRODUCTION

1.1 General overview

Yucca Mountain comprises a thick sequence of variably welded and nonwelded ash-flow tuffs (Rautman and Engstrom, 1996, p.3). The understanding of the fracture properties is useful for characterizing the mechanical stability of the potential repository and for estimating the amount of ground support needed in underground construction (Sweetkind et al, 2000, p. 40). According to Gabrielsen (1990, p.11), knowledge of fractures is important because they represent the weaker parts of the rock body where all types of geological processes (mechanical, thermal, etc.) act together. Rock joint stiffness plays an important role in displacements experienced by a rock block affected by joint deformation (Brady and Brown, 1985, p. 228). Stress, strain, and/or displacement predictions are required for the determination of the spatial extent of the disposal horizon acceptable for waste emplacement with respect to opening stability and liner loading (Tillerson and Nimick, 1984, pp. 5-6). Displacements, and particularly joint movements, are equally important if not more so with respect to rock bolt loading and deformation.

1.2 Joints in Yucca Mountain tuffs

Three types of natural joints are present at Yucca Mountain. They are healed joints with mineralized surfaces, unhealed joints with no infilling and unhealed joints with infilling (Tillerson et al, 1984, p 54). Fractures at Yucca Mountain originated as a result of both initial cooling of the volcanic deposits and tectonic activity. Throckmorton and Verbeek (1995, p.12) studied fractures at outcrops particularly of the Tiva Canyon welded tuff (TCw) unit, and differentiated cooling fractures from those of tectonic origin. According to Sweetkind et al (2000, pp. 22-23), cooling fractures are smooth, gently curved to planar discontinuities that are inferred to have formed early in the history of the volcanic rock mass, in response to localized stresses during the cooling and crystallization of the tuff. They can be identified by tubular structures on the fracture surface if any, or by their low roughness; smooth, continuous traces; great length relative to other fractures; parallelism with proven cooling fractures nearby; presence of demonstrated early age as shown through abutting relations with fractures of other sets; and the presence of vapor-phase rinds composed of minerals that have been formed at high temperatures. Tectonic fractures are the types formed in response to regional tectonic stresses or local stresses. They may also reactivate previously formed cooling joints. These fractures tend to have more scattered orientation distributions. They also tend to be shorter and rougher, and generally lack vapor-phase mineralization on their surfaces. Both cooling and tectonic fractures often terminate abruptly at welding transitions.

Throckmorton and Verbeek (1995, p. 44) identified four sets of fractures of tectonic origin; all dip steeply and are extensional in character. Studies of fractures in the Paintbrush non-welded bedded tuffs (PTn) unit indicate similar fractures to those within welded flow units, however, the overall fracture density of the PTn is low and fractures are poorly connected within and between stratigraphic subunits (Rousseau et al, 1996, p.

74). Rousseau et al (1996, p. 74) further discovered that most fractures in the PTn are strata bound and terminate at welding breaks or lithologic changes. Also, most of the discontinuities within the PTn are minor faults with dips less than 75° and indications of dip-slip tectonic movement. These zones are generally less than 4 cm wide and have thin silica or calcite fillings.

Bodvarsson and Bandurraga (1996, p. 531) reported the fracture density to be:

- Higher near contacts between vitric zones and non-lithophysal units in the Topopah Spring welded devitrified ash flow tuff (TSw).
- Higher in non-lithophysal as compared to lithophysal zones.
- Lower within the Paintbrush non-welded bedded tuffs
- Very low in the Calico hills nonwelded ash flow tuff (CHn) and Crater Flat unit (CFu) hydrogeologic units.

According to Sweetkind et al, 2000, pp 23-24, within the crystallized, densely welded units, fracture intensity varies with the abundance of lithophysal cavities. The middle nonlithophysal zone (Tptpmn) and the lower nonlithophysal zone (Tptpln) of the Topopah Spring tuff are moderately fractured, while throughgoing fractures in the upper lithophysal zone (Tptpul) and the lower lithophysal zone (Tptpll) of the Topopah Spring tuff are rare, but the percentage of lithophysae exceeds 10 percent.

The fracture network acts as a significant pre-existing weakness in the rock mass that can accommodate extensional strain through distributed slip along many reactivated joints. Evidence for reactivation of joints includes the presence of thin breccia zones along cooling joints and observable slip lineations along joint surfaces (Sweetkind, et al, 1996).

1.3 Significance of the research

Yucca Mountain is composed of fracture-bounded blocks over a wide range of size scales. The mechanical stability of excavations in the mountain during and after construction of the underground repository depends in part on the geometry of the fracture networks (Barton et al, 1993, p.3).

Rock mass mechanical properties are required in the design of repository drifts and ramps to assess the impact of thermal loads from the heat-generating wastes on excavation performance and long term structural stability (Lin et al., 1993). According to Hinds and Bodvarsson (2001) "Characterization of fractures is fundamental to assessing the performance of the potential nuclear waste repository at Yucca Mountain". Since a potential repository at Yucca Mountain is located in a highly fractured rock unit (Topopah Spring welded tuff), additional research for the mechanical behaviors as related to the fractured rock mass is necessary (Leem and Kemeny, 2001). If a repository is constructed at Yucca Mountain, the emplaced wastes will emit heat. This heat will influence hydrological, mechanical and chemical conditions in the near-drift environment. For instance, fracture permeability may locally increase or decrease in response to thermal stress because of relative movement on fractures separating

heterogeneous matrix blocks (Hinds and Bodvarsson, 2001). Any such changes will depend on the fracture stiffness.

Hopkins and Cook (1990) state "Normal joint stiffness has been shown to be an important parameter in determining seismic wave propagation across joints and is probably related to their hydraulic properties". Also, the shear stiffness is probably one of the most important required parameters because it controls the shear stress and displacement distribution along the weakness planes (Infanti and Kanji, 1990).

1.4 Objectives and scope of the research

Joint stiffness is a particularly important property for assessing long-term drift stability for a potential repository at Yucca Mountain, because it will have a major impact on stress build up and changes around emplacement drifts. As a result of thermally induced rock expansion, joints will be subjected to changing normal and shear stresses. Joint stiffness will determine to what extent stresses will increase, and to what extent thermal expansion can be accommodated by joint closure and joint slip. Shear stiffness will influence how much shear stress will build up, and hence whether or not increased shear stress might lead to joint slip, and consequent block slips or falls.

The objective of this research is to use laboratory tests to determine the stiffnesses (normal and shear) of joints (i.e. type 1 fractures filled by vapor-phase minerals) in tuff. This study includes the laboratory determination of the joint normal and shear stiffnesses of joints normal and at an angle to the core axis. Normal stiffness can be determined from compression tests on discontinuities (Kulhawy, 1978, p. 224). Lithophysal and non-lithophysal tuff specimens of the Topopah Spring unit have been tested. Strain gages and extensometers have been installed on the specimens for strain and displacement measurements. The instrumentation allows the measurement of the rock elastic properties (i.e. Young's modulus and Poisson's ratio). This study also considers the joint thickness and wall strength.

1.5 Previous studies of joint stiffness

Rock discontinuities have been studied for a large range of rock types and for both natural and induced joints (e.g. see Kulhawy, 1978, Turk and Dearman, 1985, Board et al., 1987, Nimick et al., 1987, Pyrak-Nolte et al., 1987 Goodman, 1989, Bandis, 1990, Amadei and Saeb, 1990, and Infanti and Kanji, 1990). In general, normal stiffness is found to be a rapidly changing curve, but assumed to be linear and constant in many numerical models (Brady and Brown, 1985, p. 125). Figure 1.1 shows a typical normal stress (σ) versus normal displacement (v) curve for a rock joint subject to increasing normal stress. The curve is highly nonlinear, essentially hyperbolic and becomes asymptotic to a vertical line $v = v_{mc}$ corresponding to maximum joint closure (Amadei and Saeb, 1990, p. 582). Shear stiffness is considered to depend more on the joint characteristics than on the lithologies where they occur. Published results (Table 1.1) on

joint normal stiffness range from a low of 0.24 GPa/m in limestone to a high of 67.59 GPa/m in granite while shear stiffness (Table 1.2) ranges from 0.02 GPa/m in limestone to 29.80 GPa/m in sandstone (Kulhawy, 1978, pp. 220 - 223).

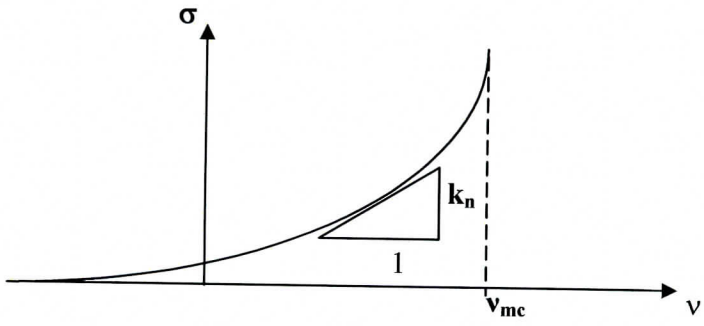

Figure 1.1 Normal stress vs. normal displacement curve for a joint
Source: Goodman (1976, Figure 5-9 b, p. 172)

1.6 Electronic database and original test records

The original test records on which this technical report is based can be found in the electronic database -reference number 018 LM.004, and scientific notebooks UCCSN-UNR-024 volumes 8 and 11.

Table 1.1 Summary of joint normal stiffnesses
Source: Kulhawy (1978, Table 3, p. 220) (Non-Q, for information only)

Specimen description	Joint area m^2	Joint thickness mm	Normal stiffness (GPa/m)
Boise sand with dry, rough sawed joint	0.0005	N/A	35.1
Marly sand filled joint	4.4	1 - 2	1.96
Closely jointed shale zone in limestone	5	2 - 5	0.24
Wet shale interbed	5	2 - 5	0.26
Lyon's sandstone with clay joint	0.0145	2.26	5.59
		1.88	5.40
		0.25	5.40
		0.53	5.43
Sierra White Granite with clay joint		1.47	5.21
		1.37	16.91
		1.22	67.59
		1.07	7.22

Table 1.2 Summary of joint shear stiffnesses
Source: Kulhawy (1978, Table 5, pp. 222 - 223) (Non-Q, for information only)

Specimen Description	Joint area cm^2	Joint thickness cm	Shear stiffness (GPa/m)
Berea sandstone – dry, sawed joint	82	-	29.80
Limestone – dry, sawed joint	82	-	8.73
Boise sandstone – dry, rough saw cut	5	-	1.29
Granite – dry, rough joint from breaking beam	144 – 205	-	1.32
Slate – dry, natural cleavage surface	500	-	0.79
Limestone – oolitic, compact to stylolitic	575	-	2.78
Marl layers in limestone - saturated	605 - 730	0.1 – 0.3	2.13
Marly paintings in limestone - saturated	51 – 63	0.1 – 5.0	2.89
Limestone with marly joints – dry	28 – 47	0.025– 2.0	9.75
Sandstone – marl contact	-	-	0.15
Phyllitic schist fractures	-	-	0.22
Limestone – slightly rough bedding	1,500	-	0.84
Limestone – rough bedding surfaces	1,600	-	3.06
Limestone – rough unfilled fractures	1,600	-	1.98
Foliated gneiss and mylonite	10.6 –24.5	4.0 – 5.0	2.36
Porphyry – dry, natural joint surface	500	-	1.02
Limestone – mylonite along bedding	1,500	-	1.25
Moist marly joint in limestone	980 – 1,243	1.5 – 3.0	1.70
Limestone – thin shale seams along bedding	1,500	-	3.08
Marly joint - saturated	1030 – 1240	1.3 – 3.2	0.78
Limestone – smooth unfilled fractures	1,600	-	0.51
Granitic gneiss fractures	-	-	0.11
Limestone with marly joints – saturated	24 – 40	0.025– 0.2	7.41
Bedding plane in greywacke	2,265	0.5 – 0.8	0.23
	3,510	>0.1	1.21
	3,660	Closed, clean	2.26
Marly sand filled joint	44,000	0.1 – 0.2	2.34
Vertical fault	-	Thick, uneven	0.20
Closely jointed shale zone in limestone	50,000	0.2 – 0.5	0.02
Shale interbed – wet	50,000	0.2 – 0.5	0.02
Schistosity plane in amphibolite	5,000	-	0.59
Unbonded basalt – sandstone contact	307,900	-	0.11
	5 – 307,900	closed-5.0	2.82

2.0 EXPERIMENTAL PROCEDURES

2.1 Specimen preparation procedures for uniaxial joint compression test

Uniaxial joint compression tests were performed on specimens instrumented with strain gages (axial and lateral) and axial extensometers. In order to obtain valid results from tests on a rock specimen, careful and precise specimen preparation is imperative (Hawkes and Mellor, 1970, p. 189). Although neither the American Society for Testing and Materials (ASTM) nor the International Society of Rock Mechanics (IRSM) has published standard procedures for rock joint testing of the type performed in this study, the following preparation procedures were carried out according to ASTM standards and IRSM suggested methods to ensure high quality specimens and tests in order to have uniform normal stress on joints.

2.1.1 Coring

Most specimens tested were prepared from core from the lithophysal and non-lithophysal formations of the Topopah Spring Member of the Paintbrush Tuff obtained from drill holes at Yucca Mountain. Specimens prepared from boulders were cored with a drill press and thin wall diamond bit (Figure 2.1). The drilling feed and its speed were adjusted to achieve smooth and straight side cores. Sufficient clean water was used as a flushing medium and to cool the bit.

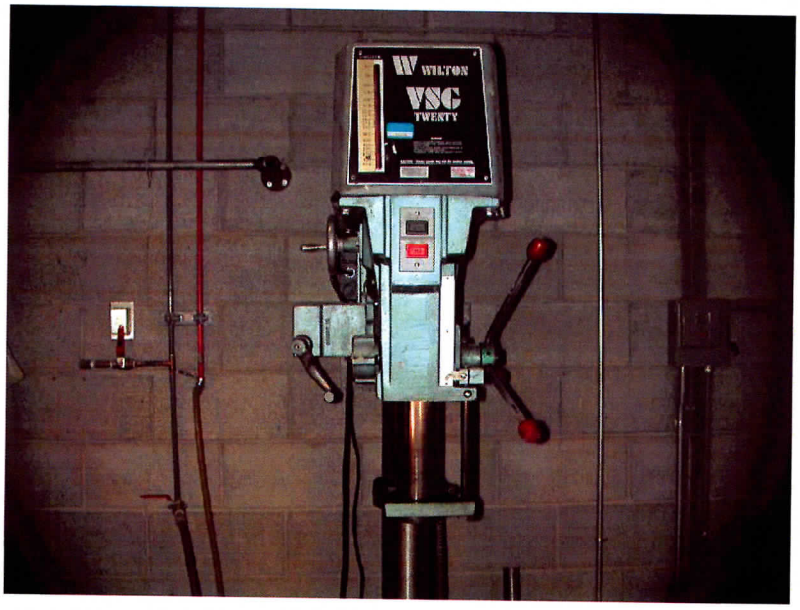

Figure 2.1 W Wilton VSG Twenty Drill Press

2.1.2 Sawing

The automatic diamond blade rock saw shown in Figure 2.2 was used to cut the cores to sizes such that length (L) to diameter (D) ratio of more than two but less than three was achieved for the specimens. Approximate L/D ratio of 2.5 was used for most samples since it meets both ASTM standard D4543 (referenced in ASTM D2664, D2938, D3148, D4341 and D4406) and ISRM suggested methods (Bieniawski et al, 1978; Brown, 1981) for uniaxial compression testing.

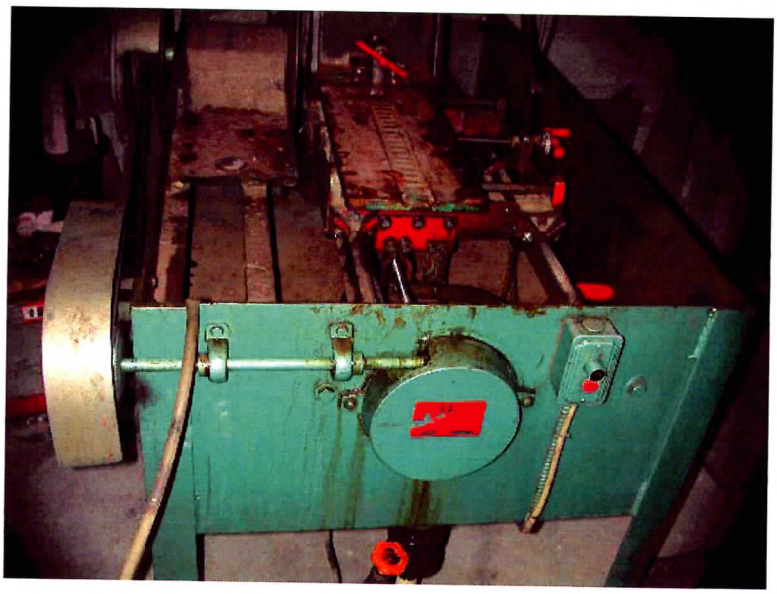

Figure 2.2 Automatic Diamond Blade Rock Saw

2.1.3 End surface grinding

End surfaces of specimens were ground using a Sharp SG-618 grinder (Figure 2.3). In order to obtain flat parallel ends, normal to the specimen axis, the end surfaces were marked with a marker. Approximately 0.002 inch (0.050 mm) or less of the specimen was taken off during each run of the grinding wheel. Grinding is completed when the color is ground off the surface of the specimen.

2.1.4 Dimensional and shape tolerances

The determination of dimensional and shape tolerances has been performed according to ASTM standard D 4543-85 with the equipment shown in Figure 2.4. A displacement dial gage was run across the specimen's ends to determine its end smoothness and along its side to determine its straightness

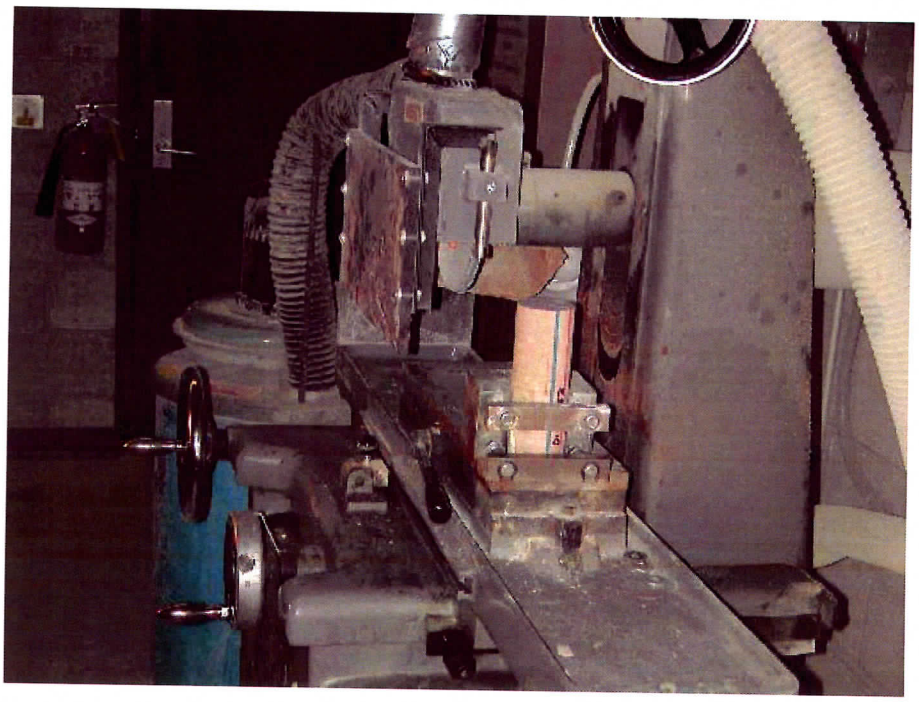

Figure 2.3 Sharp SG-618 Grinder with tuff specimen.

(a) Core straightness

The core straightness was checked by taking the maximum and minimum readings on the dial gage as the specimen was moved from one end to the other along its length. The difference between the maximum and the minimum readings denoted as Δ_0 was recorded. The specimen was rotated 120° twice. Repeating the measurements gave another two differences Δ_{120} andΔ_{240}. The maximum value of these three differences should not exceed 0.020 inch or 0.50 mm (ASTM D 4543-85, reapproved 1991).

(b) Specimen flatness

Smoothness of the end surfaces was determined by taking dial gage readings at every 1/8 inch (3.2 mm) across the diameters of the specimen end surfaces. Readings were plotted on a graph and a smooth curve was drawn through the points to represent the surface profile along a specified diametral plane. The flatness tolerance is met when the smooth curve so determined does not depart from a visual best-fit straight line by more than 0.001 inch or 0.025 mm (ASTM D 4543-85, reapproved 1991). Specimens which did not meet the end surface smoothness after the first grinding were re-ground and re-measured until the requirement was met.

After that, the diameter, length and mass of each specimen were measured using a vernier caliper and an EP-40KA electronic balance respectively. The diameter of the test

specimen was measured by averaging two diameters measured at right angles to each other close to the top, the mid-height and the bottom of specimen as recommended by IRSM SM (1999, p.288). The average diameter was used for calculating the cross-sectional area. The length of the test specimen was determined by averaging three measurements equally distributed at 120°.

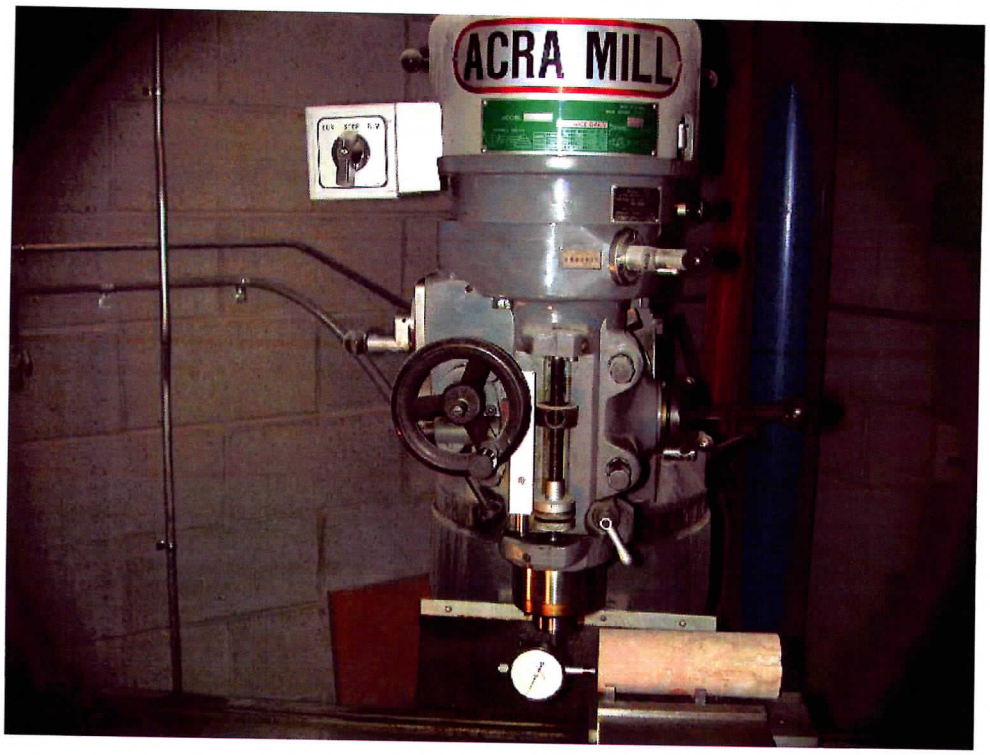

Figure 2.4. Equipment for determination of smoothness. A displacement dial gage is run across specimen ends and along its side.

(c) Perpendicularity

The data sets obtained for checking specimen flatness (i.e. two diameters for each end) were used to determine the perpendicularity. The differences between the maximum and the minimum readings on the dial gage were calculated for diameter 1 and 2 as $\Delta_1$and Δ_2 respectively for one end, $\Delta_1'$and Δ_2' for the other end. Perpendicularity tolerance is met according to ASTM standard D4543-85 when $\frac{\Delta_{max}}{diameter} \leq 0.0043$, where Δ_{max} is the largest of the four differences.

2.1.5 Moisture content determination

Hudson (1993, p. 71) states that all rocks show a change in strength with change in moisture condition due to a combination of the following physical or physicochemical

effects: (i) surface energy changes (Rehbinder effect), (ii) pore pressure changes including negative pore pressures (capillary tension) (iii) friction reduction, and (iv) corrosion. Water and water chemistry are important influences on the deformation and strength of rock. The presence of water alone may reduce the ultimate strength of sandstone by 33 % (Feng et al, 2001). According to Schultz and Li, (1995) "wet specimens have smaller peak strengths than dry ones". Price (1983, p. 10) conducted tests on two saturated and two room dry Calico Hills Tuff specimens. The average strength for the water – saturated specimens was approximately 23% less than for the room – dry specimens. We determined the moisture content for each specimen before or after testing. An EP-40KA electronic balance was used for weighing the samples before and after drying them in a Fisher Scientific oven (model 630F). Oven temperature was maintained within the range of 100 ^{0}C to 125 ^{0}C. Weight measurements were taken at 24-hour intervals according to ASTM standard D 2216-98.

2.1.6 Strain gage installation

Strain gages were installed on each specimen used for the uniaxial joint compression test. The location of the gages was first degreased using Chlorothene SM with cotton swabs. M-Prep Conditioner A was then applied to the surface to remove any loosely bonded adherents and to develop a surface texture suitable for bonding. After that, M-Prep Neutralizer 5A was applied to the cleaned surface to provide optimum alkalinity for strain gage adhesives. M-Bond 200 adhesive and glue were used for bonding the strain gage onto the specimen. M-Bond 200 adhesive was used because of its fast room-temperature cure and ease of application (Student Manual for Strain Gage Technology, Bulletin 309D, 1997, p.17). Figure 2.5 shows a specimen with a strain gage bonded along the 90^0 axis across the joint. After the strain gages were securely attached to the specimen, lead wires were carefully soldered to the strain gage using a soldering iron, solder and flux. A three-wire circuit for single active gage (Quarter Bridge) was used, as shown in Figure 2.6

2.2 Uniaxial joint compressive strength testing

The specimens used in this research are cylindrical specimens with single healed joints (i.e. type 1 fractures filled by vapor-phase minerals) of thickness less than 1 mm (Figures 2.7 and 2.8). The test specimens were from 49.78 to 61.85 mm in diameter and ranged in lengths from 74.60 to 172.31 mm. A multi-step/sustained load/creep test has been performed on five of the fourteen specimens tested while a standard uniaxial joint compressive test was performed on the rest. Strain gages (axial and lateral) and axial extensometers were installed across the joint and on the intact rock specimen to measure the joint and the intact rock properties (Figure 2.9). Figure 2.10 shows a typical test arrangement for the uniaxial joint compressive test before testing. Apart from two specimens intersected by angled joints, and which failed along their pre-existing joints (details in Appendix C), the failure planes are mainly in the direction of loading (tensile splitting) as shown in Figure 2.11.

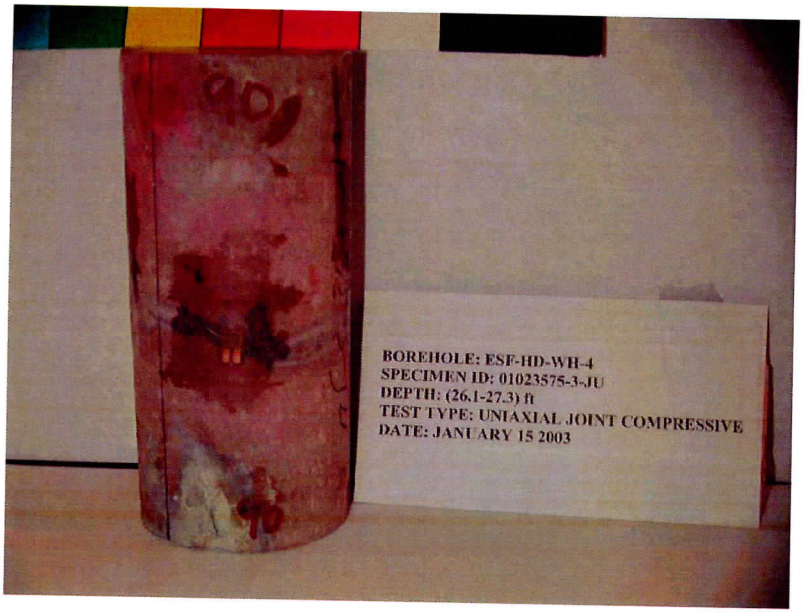

Figure 2.5 Specimen 01023575-3-JU with a strain gage at the 90° axis.
Note that strain gage is installed across a joint.

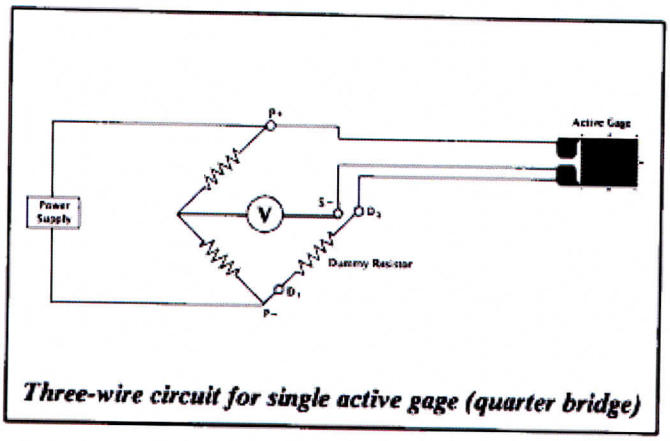

Figure 2.6 Lead wires soldered to a strain gage.
Source: Student Manual for Strain Gage Technology, Bulletin 309D, 1997, p.24.

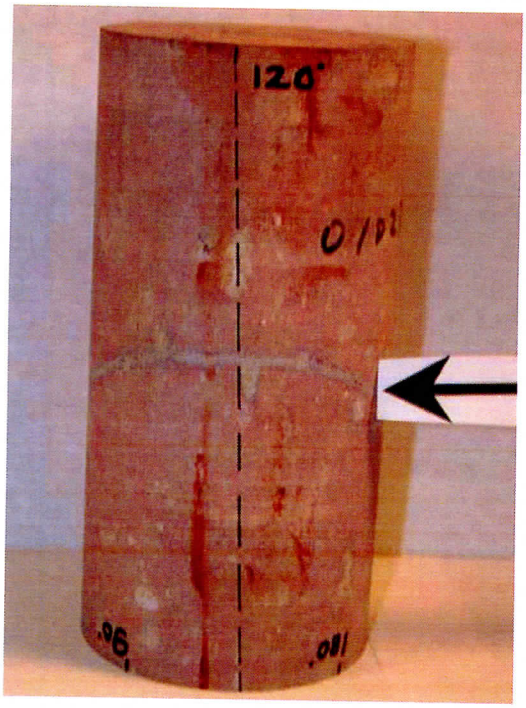

Figure 2.7 Specimen with a typical healed joint (arrowed)
(Diameter D = 61.5 mm, Length L = 124 mm)

Figure 2.8 Some specimens with single joints (Diameters D range from 60.9 mm to 61.01 mm, lengths L range from 74.6 mm to 161.42 mm)

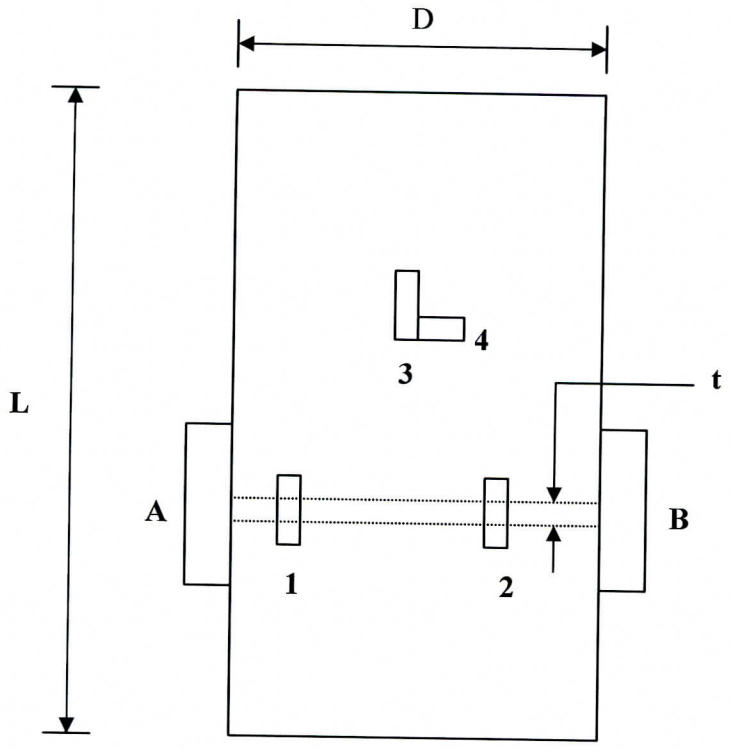

Figure 2.9 Specimen instrumentation for uniaxial joint compressive test

A and B are extensometers installed across the joint
1 and 2 are axial strain gages across the joint
3 and 4 are axial and lateral strain gages on the intact rock
t denotes the thickness of the joint, L is the length of the specimen, D is the diameter.

Data collected during the test include time, strain gage measurements, extensometer data, temperature, load and machine stroke. Axial stresses are calculated by dividing the applied load by the original cross-sectional area of the specimen. Resistance changes in the axial and the diametric strain gages are measured in ohms which are converted to strains. Axial strains for the extensometers are calculated by averaging the measured displacements on two diametrically opposed extensometers mounted on the specimen and dividing by the average value of the original extensometer lengths.

Figure 2.10 A typical specimen with sensors installed.

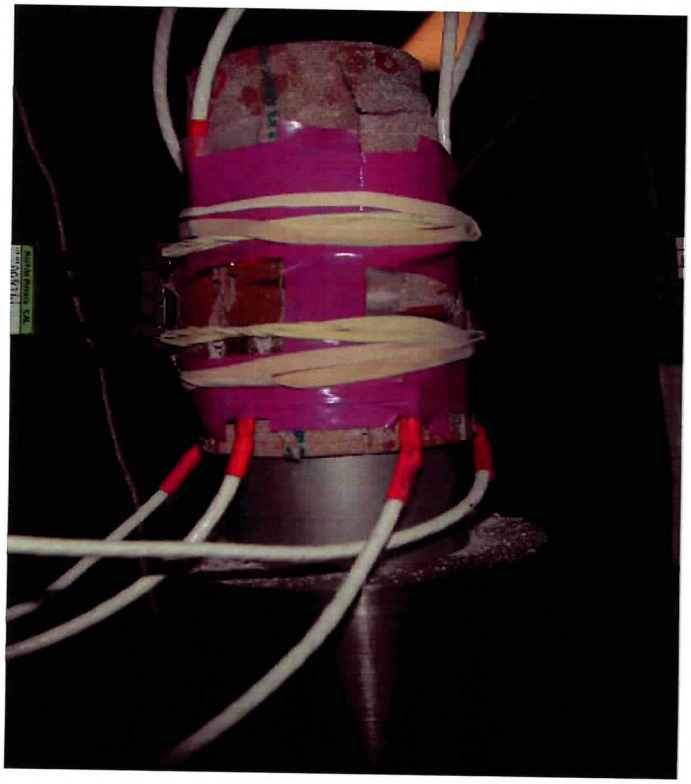

Figure 2.11 A typical specimen in MTS machine after testing.

2.3 Direct shear test

2.3.1 Specimen preparation procedures

Specimens used in the direct shear testing were prepared according to ASTM standard test method (D 5607 - 95). The lower half of the specimen holding ring was placed on a plastic sheet on a suitable level surface. The lower half of the specimen was then centrally positioned in the lower half of the specimen holder ensuring that the shear horizon to be tested was secured in the correct position and orientation. A prepared encapsulating material (fast setting concrete mix) was poured carefully into the annular space between the lower half of specimen and the lower half of the specimen holding ring after which the encapsulating material was allowed to cure (Figure 2.12).

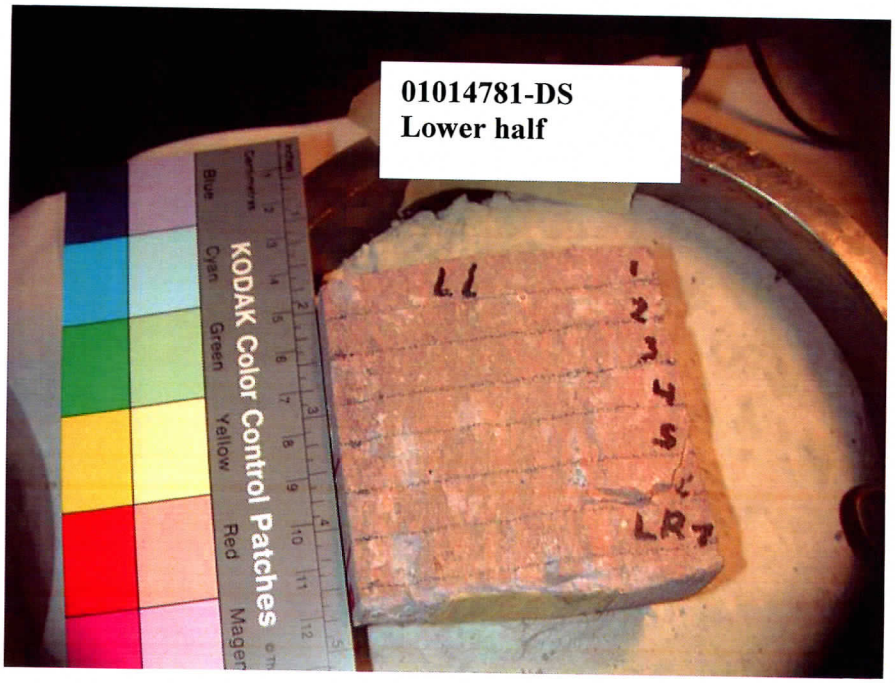

Figure 2.12 Lower half of a direct shear specimen encapsulated in holding ring

After the bottom encapsulated material had sufficiently cured, a split spacer plate was placed on the lower ring and the upper half of the test specimen was placed onto the encapsulated lower half. The upper half of the specimen holder was lowered onto the split spacer plate and the two halves were connected with bolts. The encapsulating material was poured into the annular space between the top half of the specimen holder and the top half of the specimen after which the encapsulating material was allowed to cure. The spacer plates were removed after the encapsulating compound had cured to expose the test horizon for shear testing.

A carpenter contour gage was used to measure joint profiles/roughness of the test specimen before and after testing. Prongs of the gage were lowered to make contact with the shear surface and the tips of the gage trace the shear plane surface along the line of shearing (lines drawn at regular intervals on the surface as shown in Figure 2.13). The tips of the prong were traced onto paper and the tracing compared with standard profile lines (ASTM D 5607 – 95, Fig. 4) to determine the joint roughness coefficient (Barton et al, 1993, p.22, Figure 8B).

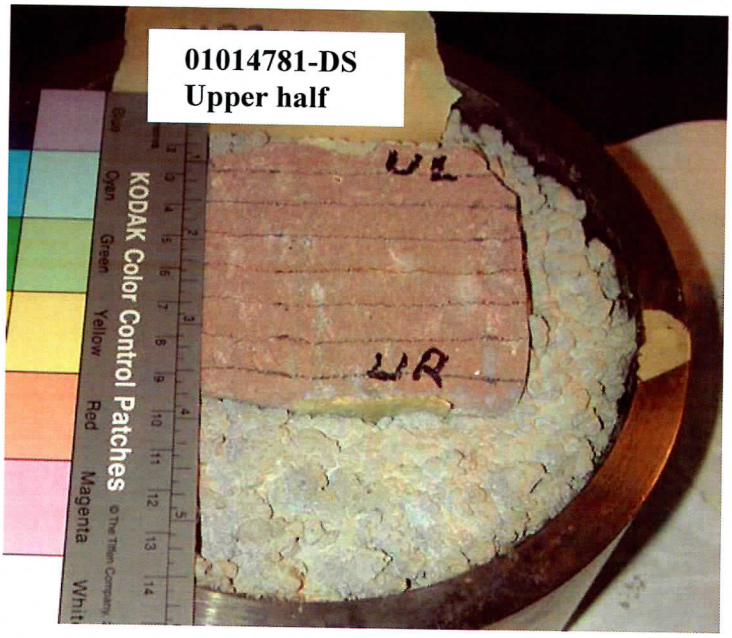

Figure 2.13 Upper half of a direct shear specimen encapsulated in holding ring (joint profile roughness was measured along the lines across the surface)

2.3.2 Testing

The specimens were sheared in a servocontrolled hydraulic direct shear machine. Four displacement - measuring devices – Linear Variable Differential Transformers (LVDTs) were mounted on the machine to measure the normal and the shear displacements. Three of the four LVDTs installed to measure the normal displacement were also used to provide a check on rotation of the specimen during testing. The fourth LVDT measured the shear displacement.

Normal load was applied to attain a stabilized normal displacement after which the shear load was applied. After reaching the peak shear strength, loading continued until residual shear strength was established, or until the shear machine displacement limit (about 12 mm) was reached. The shear load was removed and the specimen repositioned to its initial configuration. We increased the normal load and conducted another shear test. Figures 2.14 and 2.15 show lower and upper halves of specimen 01023540-1-DS after testing. Data collected during the test include normal and shear displacements, normal and shear loads and time.

Figure 2.14 Lower half of a specimen after testing

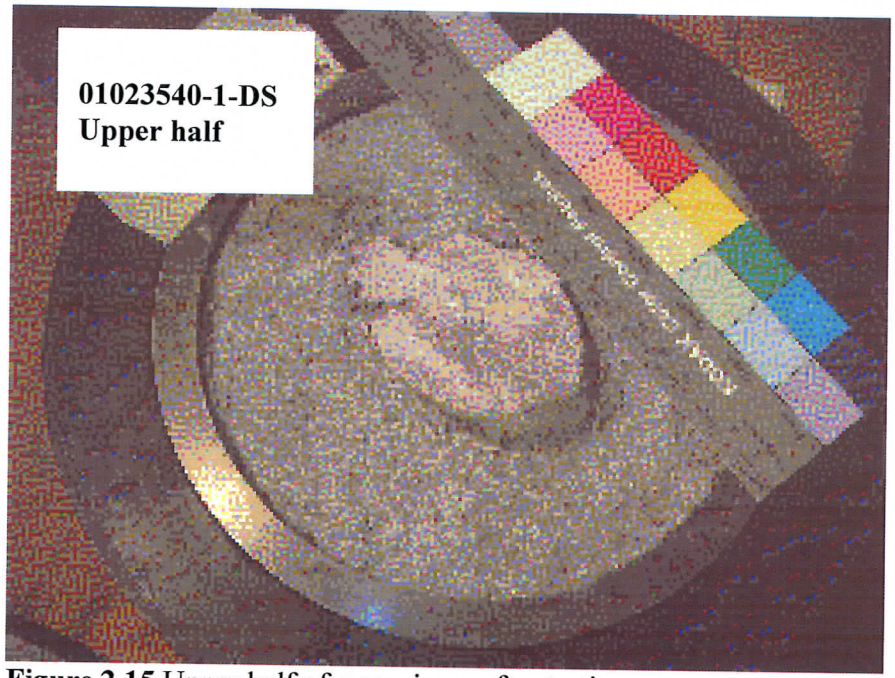

Figure 2.15 Upper half of a specimen after testing

3.0 EXPERIMENTAL RESULTS

3.1 Rock strength and deformability

3.1.1 Compressive strength of rocks

Compressive strength means the compressive stress at which the rock fractures, and it is generally taken as the maximum stress reached before the specimen collapses or separates (Hawkes and Mellor, 1970). The length-to-diameter ratio (L/D) of cylindrical specimens has a significant effect on their crushing strength (Obert and Duvall, 1967, p.332). ASTM standard D4543 specifies that for uniaxial compressive tests the samples should be within the range 2< L/D<2.5. The strengths of tested specimens with L/D values less than 2 were corrected using the following relation:

$$C_o = \frac{C_p}{0.778 + 0.222\frac{D}{L}} \quad \text{.....(3.1)}$$

for 2 > (L/D) > 1.....(Hawkes and Mellor, 1970, p.253)
Where C_o is the corrected uniaxial compressive strength of the specimen
C_p is the measured compressive strength, D is the diameter of the specimen
L is the length of the specimen

Figure 3.1 shows typical loading and unloading curves of one of the specimens tested.

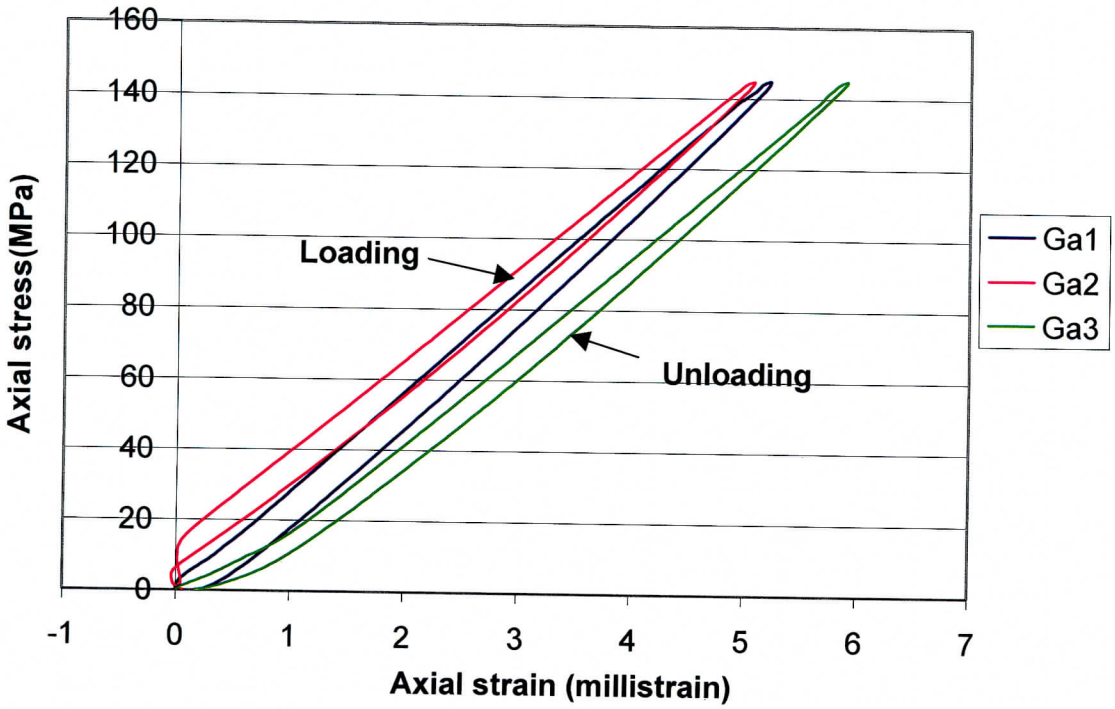

Figure 3.1 Stress-strain curves showing the loading and unloading of axial gages 1, 2 and 3 installed across the joint of specimen 01023575-3-JU from borehole ESF-HD-WH-4. (Refer to Appendix A7 for details).

For most samples tested, any pre-peak damage region is short and the stress-strain curve tends to remain extremely linear until close to the peak. Virtually all the samples tested have shown extremely brittle behavior, i.e. a very steep drop beyond (or at) the peak.

3.1.2 Young's modulus and Poisson's ratio

3.1.2.1 Young's modulus

The Young's modulus of a specimen may vary throughout its loading history and so is not a uniquely determined constant for the material (Brady and Brown, 1985, p. 90; Goodman, 1989, p. 184). It is convenient for practical purposes to regard the slope of the curve, either at a specific point or averaged over a certain section as Young's modulus. However, definitions are necessary to indicate the stress level or stress range for which E is given (Hawkes and Mellor, 1970, p. 205; ASTM D 5407 – 95).

Three methods used to determine the Young's modulus are: (a) tangent Young's modulus, (b) average Young's modulus and (c) secant Young's modulus (ASTM D 5407 – 95; Brady and Brown, p. 90, 1985).

(a) Tangent Young's modulus (E_t) is the slope of the axial stress-axial strain curve at some fixed percentage, generally 50% of the peak strength (Figure 3.2 A).
(b) Average Young's modulus (E_{av}) is the average slope of the linear portion of the axial stress-strain curve (Figure 3.2 B).
(c) Secant Young's modulus (E_s) is the slope of a straight line joining the origin of the axial stress-strain curve to a point on the curve at some fixed percentage of the peak strength (Figure 3.2 C).

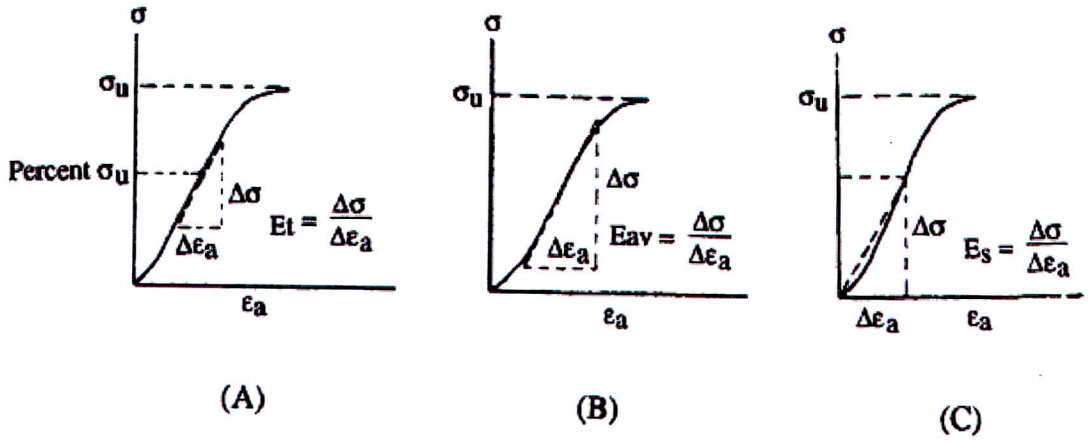

Figure 3.2 Methods for determining the Young's modulus (ASTM D 5407 - 95)

3.1.2.2 Poisson's ratio

The ratio of lateral to axial strain magnitudes determines Poisson's ratio (Goodman, 1989, p.184). At very low loads, Poisson's ratio may be close to zero, whereas at high loads internal cracking and consequent dilation may cause the Poisson's ratio to exceed the theoretical maximum value of 0.5 (Hawkes and Mellor, 1970, p. 206).

3.2. Strain gage measurements and determination of parameters

Strain gage data collected in volts were converted to strain in mm/mm by using the formula:

$$Strain(\varepsilon) = \frac{-4V_r}{G_F(1+2V_r)}\left(1+\frac{R_L}{R_g}\right) \quad \text{.....(3.2)}$$

Hewlett-Packard (1999)

Where $V_r = (V_{out}/V_{in})_{strained} - (V_{out}/V_{in})_{unstrained}$

$(V_{out})_{strained}$ is the gage reading during compression in volts

$(V_{in})_{strained}$ is the excitation voltage during compression in volts

$(V_{out})_{unstrained}$ is the gage reading before compression in volts

$(V_{in})_{unstrained}$ is the initial excitation voltage reading before compression.

R_L is the resistance of the wires soldered onto the strain gage in ohms

R_g is the gage resistance in ohms, G_F is a constant of the gage (gage factor) = 2.1

Values for Young's modulus, normal stiffness and Poisson's ratio were obtained by finding the slopes of the linear portions of the stress-strain, stress-displacement and lateral-axial strain curves respectively. The linear range over which the parameters have been determined for each specimen is listed with respect to the peak stress. Young's modulus and normal stiffness values determined over the 3.2 mm (the length of the axial strain gages installed across the joint) section of the rock with the joint are referred to as equivalent values. For all tests, axial strain gages 1, 2, 3 and 4 where applicable were installed across the joint while axial gages 5 and 7, as well as lateral gages 6 and 8 were installed on the intact rock specimen. Figure 3.3 illustrates the determination of parameters for the 3.2 mm rock section with the joint while Figure 3.4 illustrates the determination of the intact rock parameters. Figures 3.5 and 3.6 show how the Poisson's ratio and the strain rate have been determined.

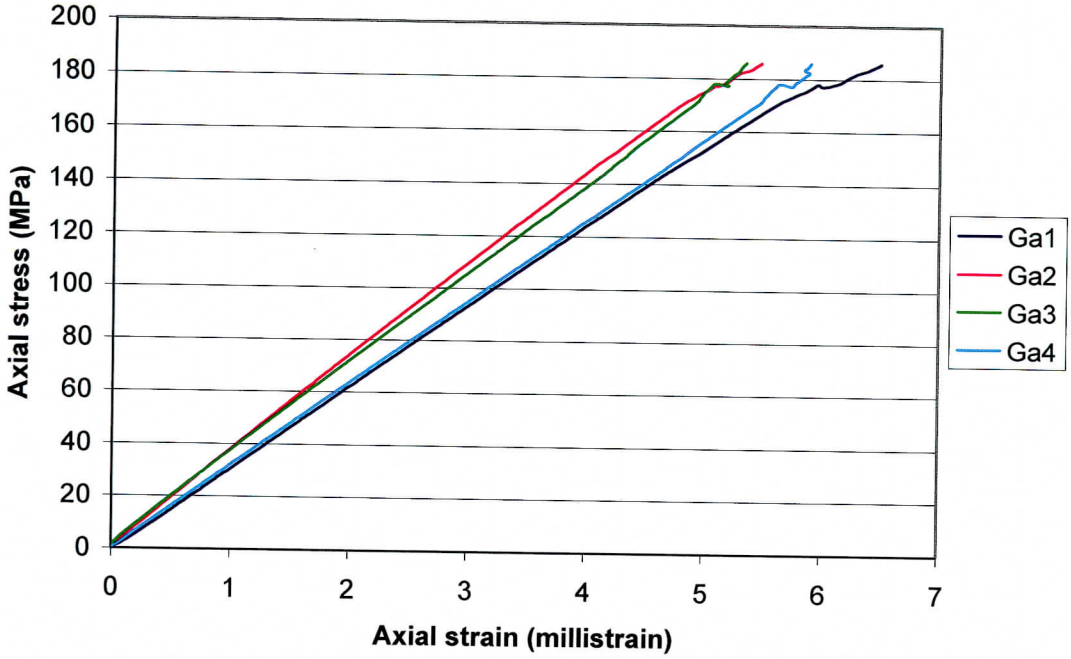

Figure 3.3 A: Typical axial stress-strain curves for four strain gages (Ga1, Ga2, Ga3 and Ga4) installed across a joint.

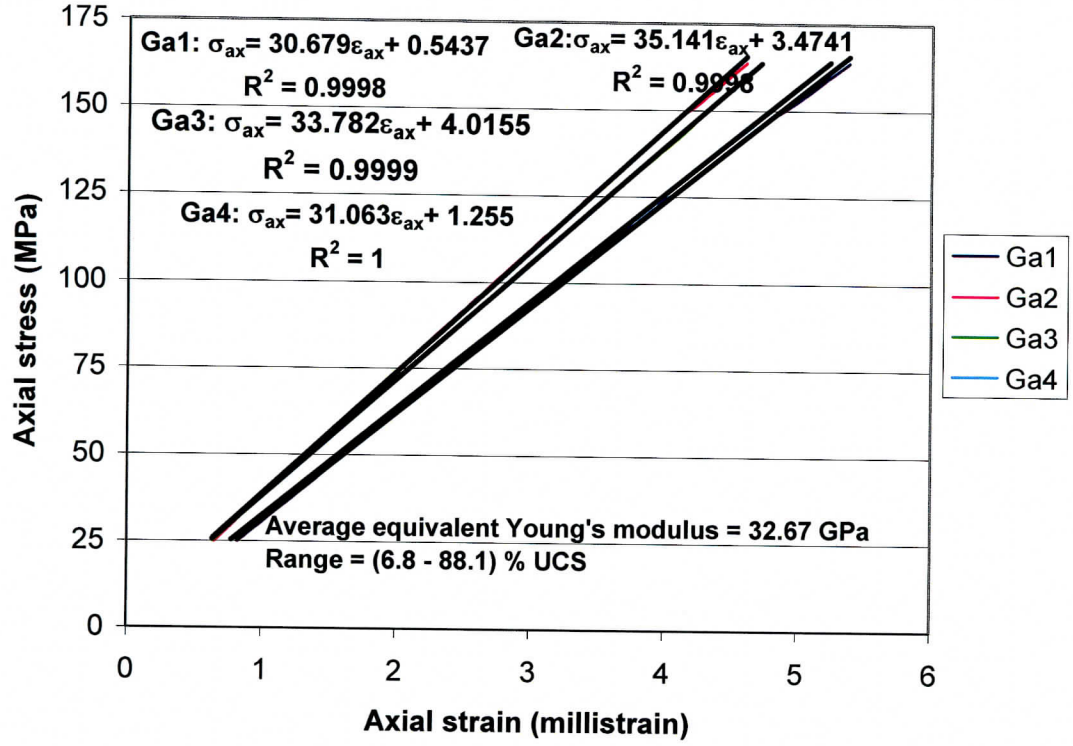

Fig. 3.3 B: Determination of equivalent Young's modulus from the linear best-fit line of the axial stress-strain curves shown in Fig. 3.3 A. (See Appendix A12 for complete analysis).

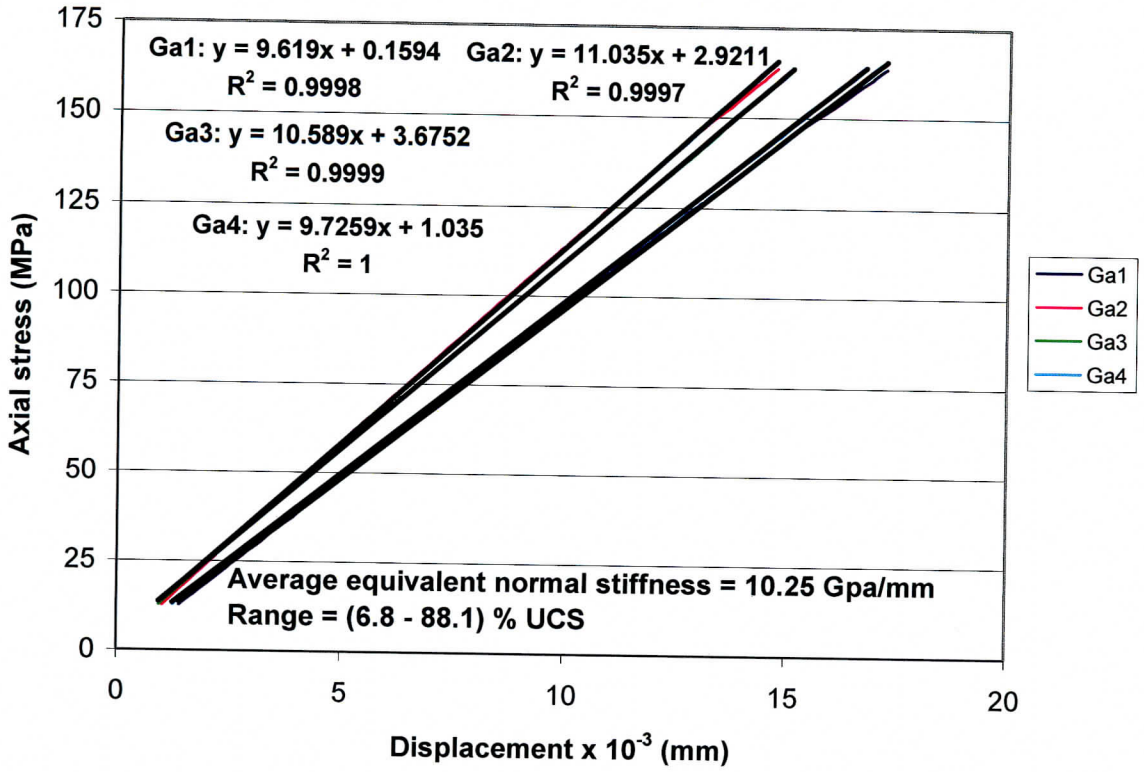

Figure 3.3 C: Determination of equivalent normal stiffness from the linear best-fit line of the axial stress-strain curves shown in Fig. 3.3A. (See Appendix A12 for details).

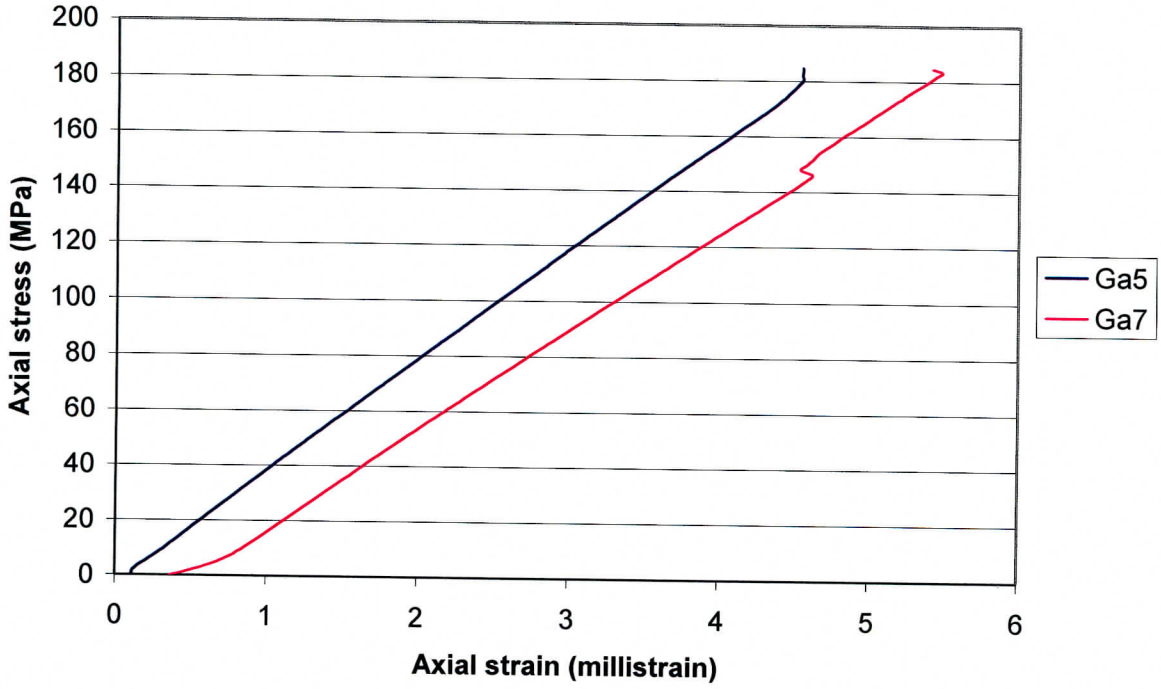

Figure 3.4 A: Typical axial stress-strain curves for two strain gages (Ga5 and Ga7) installed on intact rock

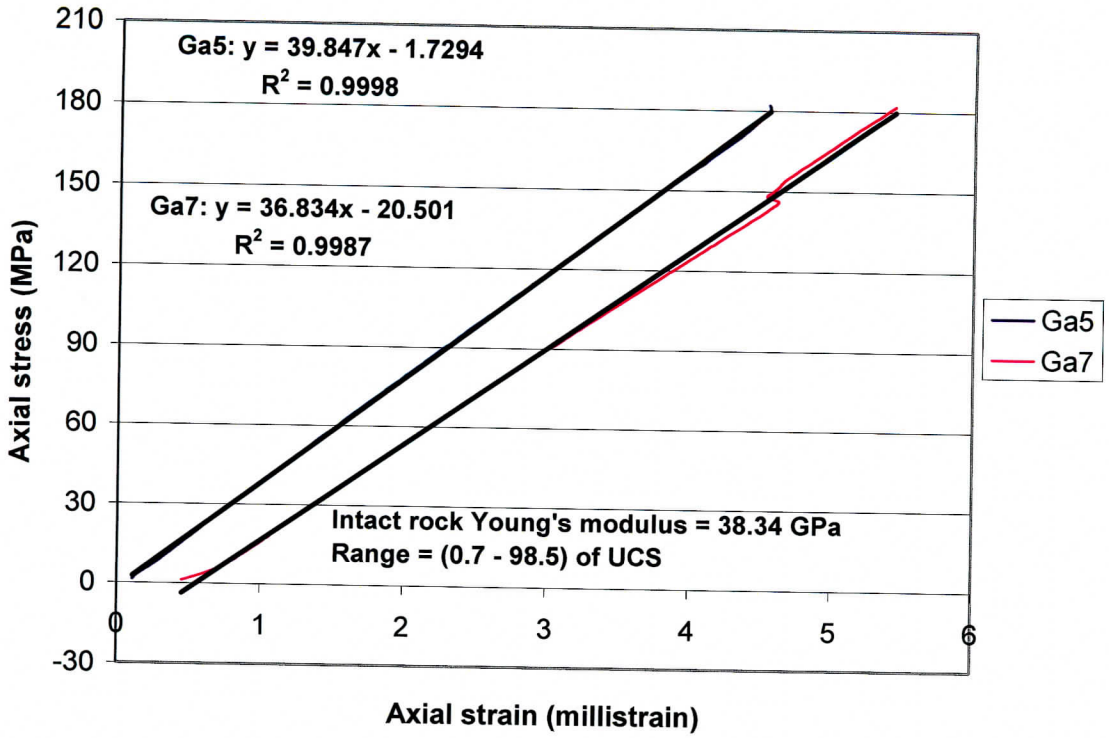

Fig. 3.4 B: Determination of intact rock Young's modulus from the linear best-fit line for the stress-strain curves shown in Fig. 3.4.A. (See Appendix A7 for complete analysis).

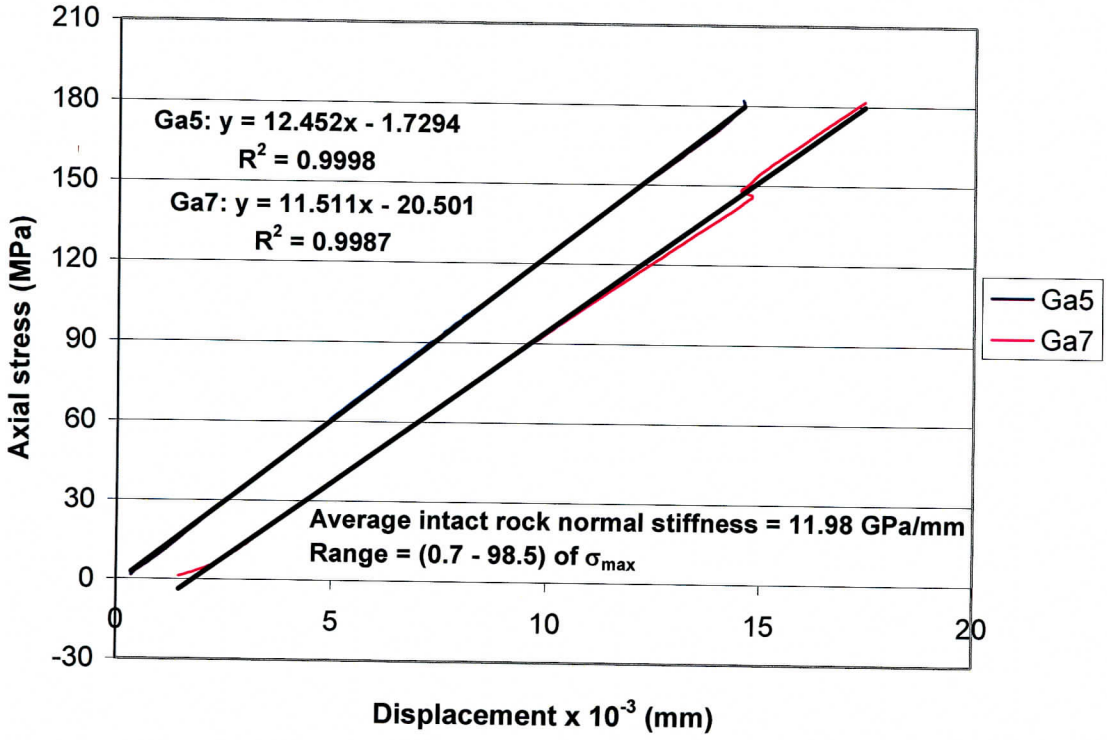

Fig. 3.4 C: Determination of intact rock stiffness from the linear best-fit line for the stress-strain curves shown in Fig. 3.4.A.

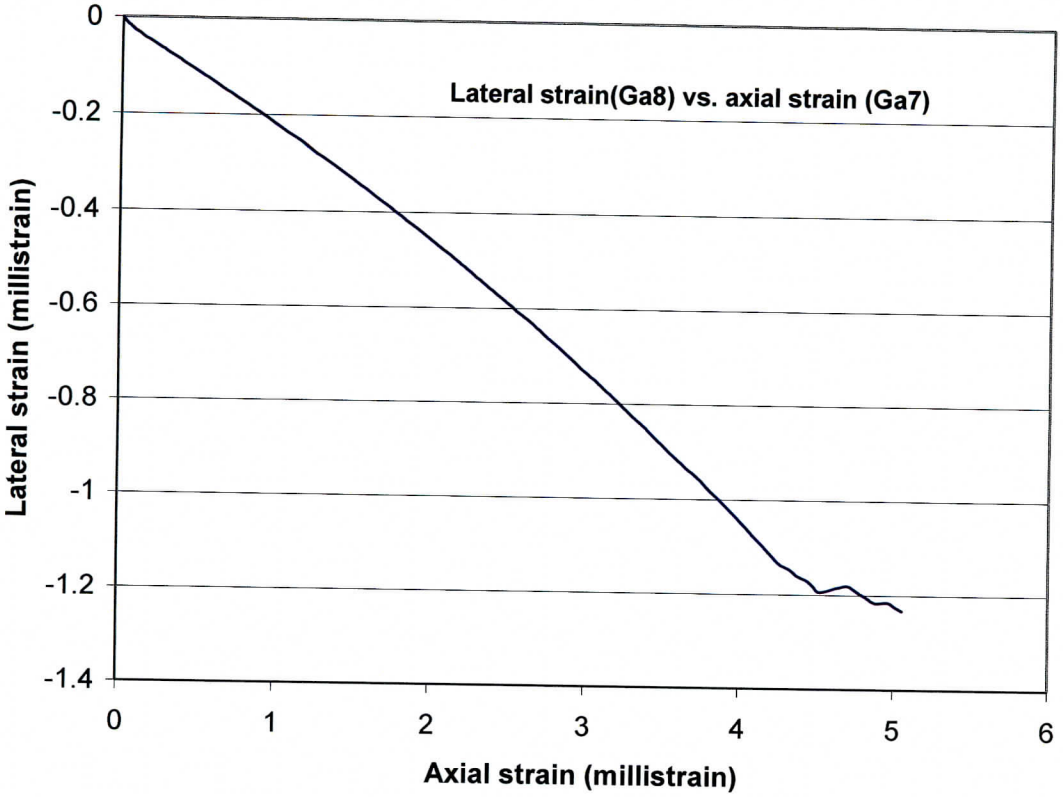

Figure 3.5 A: Typical lateral-axial strain curve for two strain gages (Ga7 and Ga8) installed on intact rock.

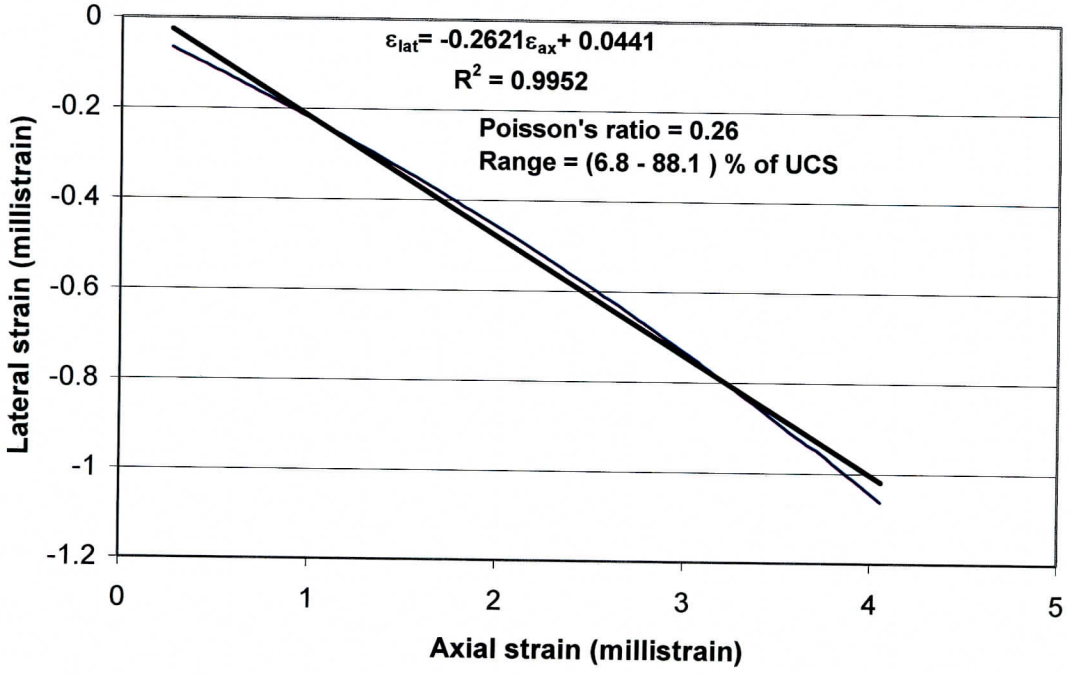

Figure 3.5 B: Determination of Poisson's ratio from the linear best-fit line for the lateral-axial strain curve shown in Fig. 3.5 A. (Refer to Appendix A12 for complete analysis).

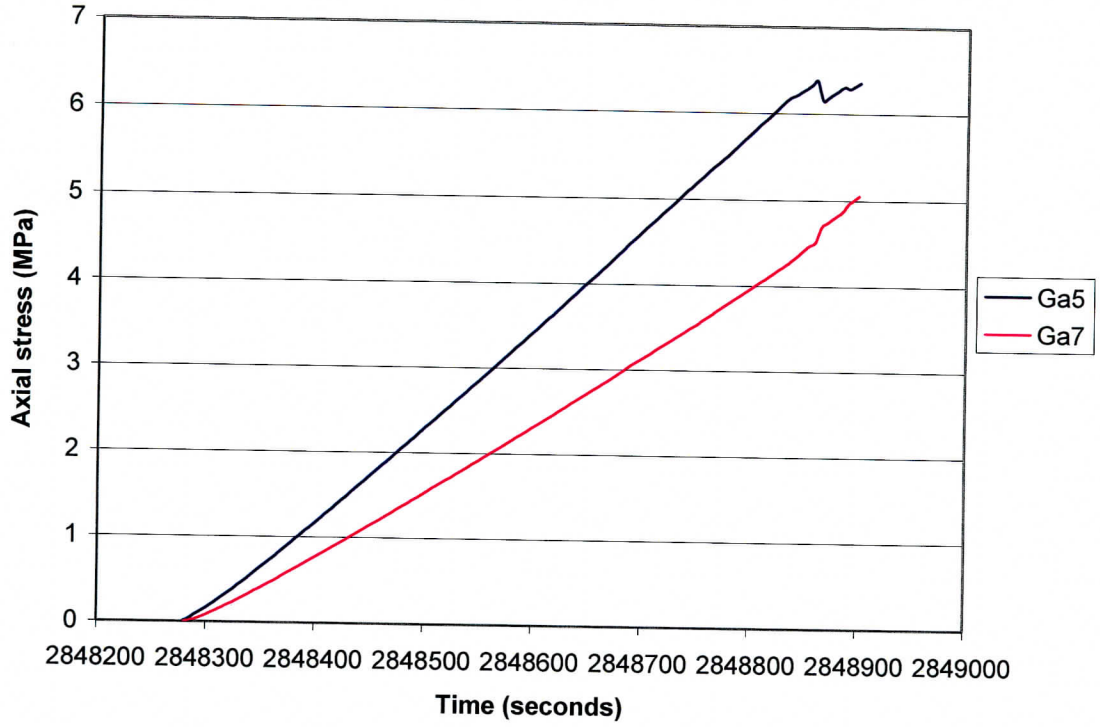

Figure 3.6 A: Typical axial strain-time curves for two strain gages (Ga5 and Ga7) installed on intact rock.

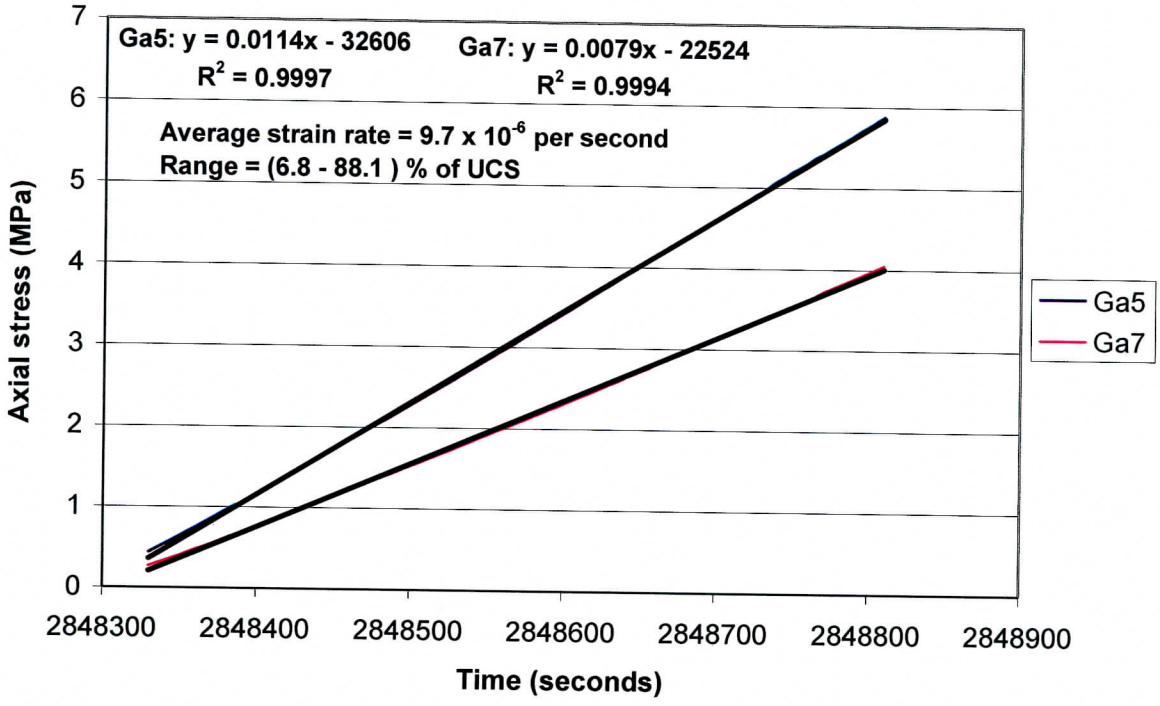

Figure 3.6 B: Determination of strain rate from the linear best-fit line for the axial strain-time curves shown in Fig. 3.6 A.

3.3 Extensometer measurements and determination of parameters

Axial extensometers were installed across the joint in addition to the strain gages in some cases to compare the joint properties as determined by the two measurement methods. The determination of Young's modulus and normal stiffness is the same as described above for the strain gage measurements. Figures 3.7, 3.8 and 3.9 show graphs from extensometer measurements and the determination of the parameters.

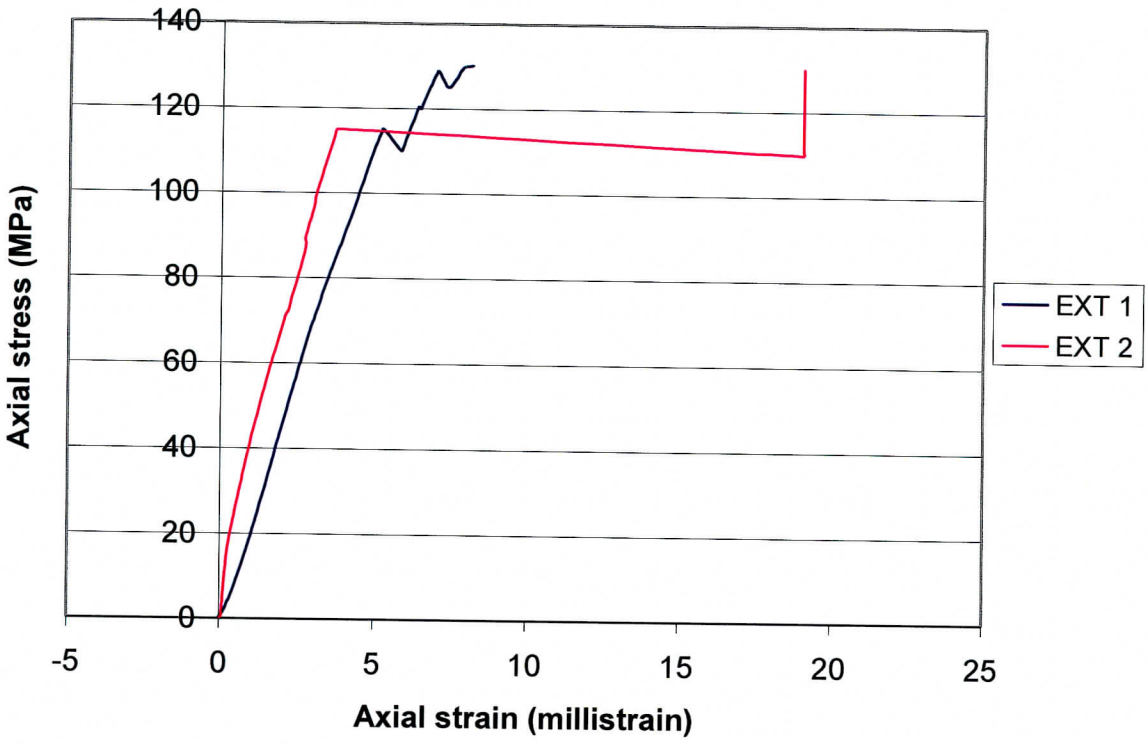

Figure 3.7 Typical axial stress-axial strain curves for two extensometers (EXT 1 and 2) installed across a joint.

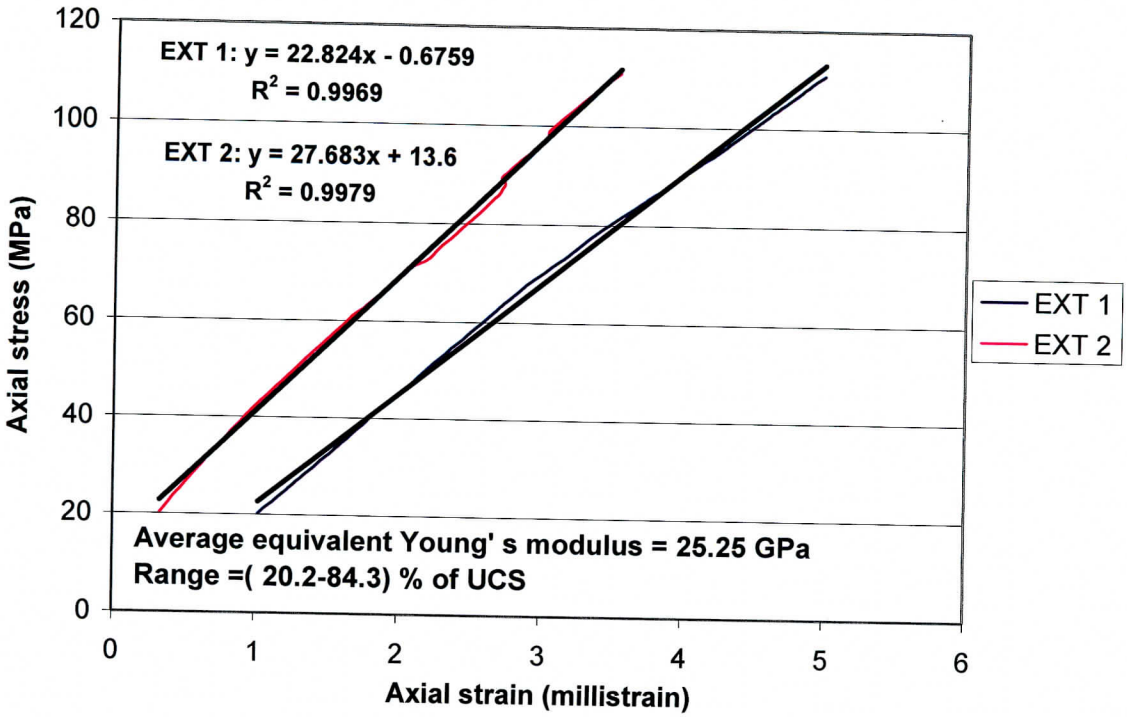

Figure 3.8 Determination of equivalent Young's modulus from the linear best - fit line of the axial stress-axial strain curves shown in Fig. 3.7. (See Appendix A6 for complete analysis).

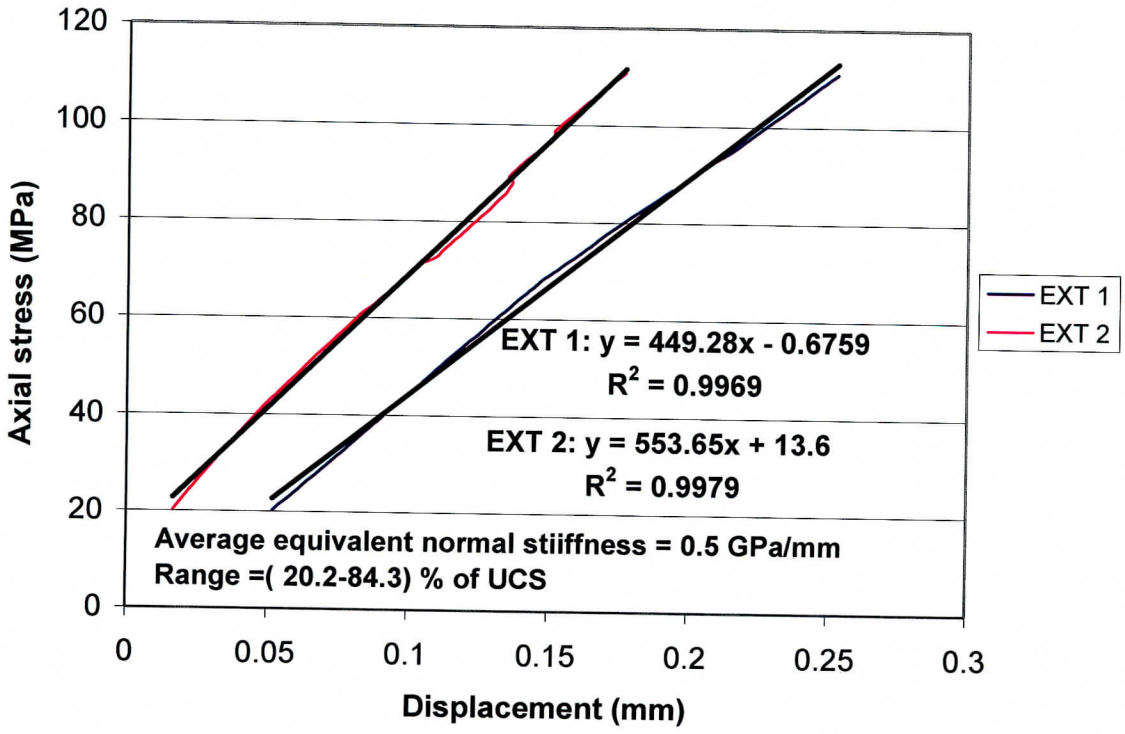

Figure 3.9 Determination of equivalent normal stiffness from the linear best – fit line of the axial stress-axial strain curves shown in Fig 3.7.

3.4 Test results from the uniaxial joint compression tests

Experimental results for twelve of the fourteen specimens with joints normal to the direction of loading are listed in Appendices A.1 through A.12. Test description and results for the two specimens with angled joints are shown in Appendix C. Summary charts of all results are shown in Tables 4.1 and 4.2. The ranges of Young's moduli, Poisson's ratios, bulk densities, moisture contents and unconfined compressive strengths at failure are 29.42 to 68.68 GPa, 0.12 to 0.5, 2.20 to 2.32 g/cm^3, 0 to 1.14 % and 46.3 to 220.6 MPa respectively. The joint normal stiffness determined from the strain gage measurements ranges from a low of 7.16 to a high of 64.77 GPa/mm. Tables 3.1 and 3.2 give examples of (Refer to Appendices A6, A7 and A12 for full details).

Table 3.1: Example of strain gage results
(a) Young's modulus and normal stiffness (Tables A 12.1, A 7.6)

Section of rock	Sensor	Young's modulus (GPa)	Normal stiffness (GPa/mm)	Range (% of UCS)
3.2 mm rock with a joint	Gage 1	30.68	9.62	
	Gage 2	35.14	11.04	6.8 – 88.1
	Gage 3	33.78	10.59	
	Gage 4	31.06	9.73	
	Mean	**32.67**	**10.25**	
	Std. Deviation	**1.86**	**0.59**	
3.2 mm intact rock	Gage 5	39.85	12.45	0.7 – 98.5
	Gage 7	36.83	11.51	
	Mean	**38.34**	**11.98**	
	Std. Deviation	**1.51**	**0.47**	

(b) Poisson's ratio (Table A 12.2)

Sensor	ν	Range (% of UCS)
Lateral Gage 8 vs. axial gage 7	0.26	6.8 – 88.1

(c) Strain rate (Table A 12.2)

Sensor	Strain rate/ per second	Range (% of UCS)
Gage 7	7.9×10^{-6}	6.8 – 88.1

Table 3.2: Example of extensometer results

Young's modulus and normal stiffness (Table A 6.4)

Section of rock	Sensor	Young's modulus (GPa)	Normal stiffness (GPa/mm)	Range (% of UCS)
3.2 mm rock with a joint	Extensometer 1	22.82	0.45	20.2 – 84.3
	Extensometer 2	27.68	0.55	
	Mean	**25.25**	**0.50**	
	Std. Deviation	**2.43**	**0.05**	

3.5 Calculation of joint normal stiffness from uniaxial joint compression tests

3.5.1 Joint normal stiffness calculations from strain gage measurements

Joint normal stiffness (k_n) has been calculated using the intact rock stiffness formula, EA/L (Jaeger and Cook, 1976, p. 179). According to Jaeger and Cook (1976, p. 179), intact rock stiffness (k_r) = AE/L, where A = area, E = intact rock Young's modulus and L = length (in this study, L = length of strain gage installed on rock section with the joint minus the joint thickness).

The joint and the specimen have been treated as two springs in series. The equivalent stiffness of two springs connected in series is given as:

$$\frac{1}{k_{eq}} = \frac{1}{k_r} + \frac{1}{k_n} \quad \text{.....(3.3)}$$

(Ingard and Kraushaar, 1960, p.76)

$$\Rightarrow k_n = \frac{k_{eq} \times k_r}{k_r - k_{eq}} \quad \text{.....(3.4)}$$

k_{eq} = equivalent normal stiffness obtained for rock section with the joint

3.5.2 Joint normal stiffness calculation from extensometer measurements

In calculating the intact rock stiffness (k_r) using the stiffness formula (AE/L), the intact rock Young's modulus obtained from the strain gages installed on intact rock was used. The length L used is the length of the extensometer installed across the joint minus the joint thickness, and k_{eq} is the equivalent normal stiffness obtained for the rock section with the joint (i.e. the rock section over which the extensometers have been installed).

3.6 Parameters determined from the direct shear testing

According to Kulhawy (1975, p. 343), the stiffness values can be determined from direct shear tests on rock samples containing discontinuities by applying normal and shear stresses to the discontinuity plane and measuring the corresponding displacements.

Any opening instabilities in a possible nuclear waste repository at Yucca Mountain, Nevada, are likely to be the result of joint shear movements along pre-existing joints in welded tuffs (Blejwas and Hansen, 1990, p. 185). Bandis et al (1983, p.256) studied a range of fresh and weathered joint types. They observed that apart from extremely tight natural joints which showed linear behavior, all types of joints exhibited non – linear behavior. They also deduced that the peak shear stiffness of a joint is strongly dependent on its past loading history. According to Maki (1985, p. 133), shear strength and shear stiffness depend on the temporary fracture aperture, and their values could be very high in cases where the temporary aperture is limited to small values. The most commonly used method for the shear testing of discontinuities in rock is the direct shear test (Brady and Brown, 1985, p. 115). Direct shear tests are good for joint testing because normal and shear displacements during shearing can be measured easily. Also, shearing can proceed for long distances such that wear is developed and the strength falls to its residual value (Goodman, 1989, p. 161). Indraratna and Haque (2000, p. 28) reported that, if the shearing of joint asperities in direct shear testing occurs after a long shear displacement, the peak stress is observed at a larger shear displacement. Also, when the normal stiffness is increased, the shear strength is also found to increase and the peak is attained at a greater shear displacement.

Shear stiffness represents the resistance of the specimen to shear displacements under an applied shear force prior to reaching the peak shear strength (ASTM D 5607 - 95). It is calculated by dividing the applied apparent shear stress by the resulting shear displacement (slope of the curve prior to peak shear strength, Figure 3.10).

In this study, the joint normal and the shear stiffnesses were determined from the slopes of normal stress versus normal displacement and shear stress versus shear displacement. Angle of internal friction and the cohesion of the joint were obtained from the linear best-fit plot of shear stress versus the normal stress.

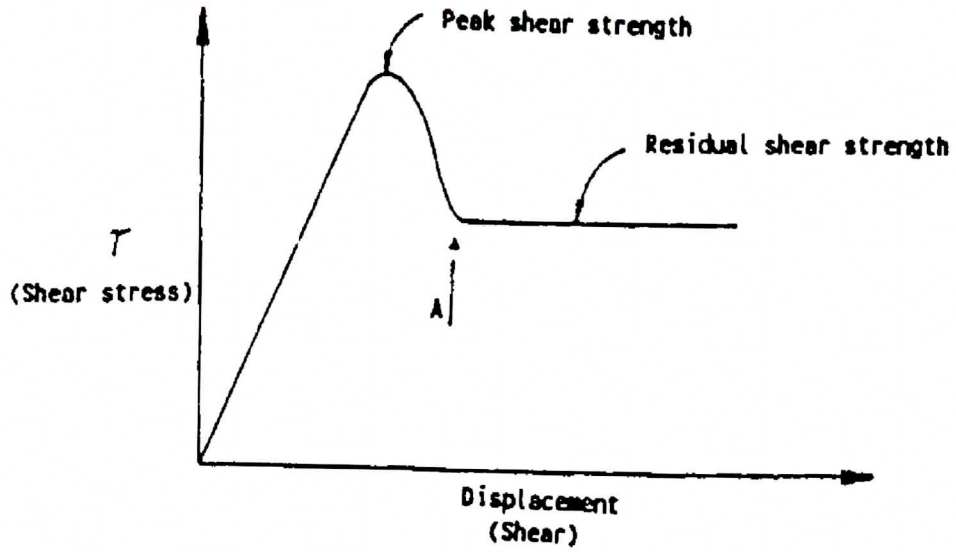

Figure 3.10 Generalized shear stress-shear displacement curve (ASTM D5607-95)

4.0 SUMMARY OF RESULTS AND DISCUSSION

4.1 Stress-strain and stress-displacement curves

The stress-strain (stress-displacement) curves for the axial gages installed across the joints and on the intact rocks exhibited slight initial concave-upward portions, linear regions up to the average of 88% (range from 66.4% to 99.1%) of the peaks and sharp downward breaks for the majority of the tested specimens (Figures 3.3A and 3.4A). These curve characteristics reflect pore collapse and compaction, elastic deformation and material failure respectively (Price et al., 1982, p. 10). Most specimens failed violently. The post-peak region of the stress-strain curves was not well defined. As discussed in chapter 3, the curves for axial gages installed across the joint showed linear elastic behavior instead of the non-linear behavior common with joints (Goodman, 1989 p.196; Bandis, 1990, p.126; Turk and Dearman, 1985, p. 198; Nimick et al., 1987, p. 21; Kulhawy, 1975, p.336; Board et al., 1987, p.43, Blejwas and Hansen, 1990, p. 187). The linear behavior might be due to the initial closed state of joints such that application of normal load is taken up by the joint and by the solid rock above and below the joint. According to Buesch (2003), the more completely a fracture is filled with vapor-phase mineral deposits (tridymite, alkali feldspar or calcite), the closer it will be to just testing a strength similar to that of a well cemented (quartz) sandstone. The stress-strain (load-deformation) curves for the joints are parallel or nearly parallel to the elastic compression curves of the solid rock. This behavior compares quite favorably with the observation by Board et al., (1987, p.43) who state " fracture normal stiffness becomes asymptotic to the intact rock stiffness as the joint closes." Fractures tend to have almost the same strength as the host rock if they have similar mineral composition as the host rock, but with a slightly different crystalline structure. (Buesch, 2003).

Table 4.1 summarizes the results of the stiffnesses of the average intact rock and the 3.2 mm section with the joint. Creep tests were performed on the first five specimens in the Table while conventional (short duration: 10-15 minutes) uniaxial joint compressive tests were performed on the rest (see details of test descriptions in Appendix A).

4.2 Young's modulus and normal stiffness

Apart from specimen 01023752-JU (Figures A10.7 and A10.8) which had four lithophysal cavities contributing to its low strength and low intact rock stiffness, it is evident from the results that the average specimen is stiffer than the 3.2 mm section with the joint. In other words, the Young's modulus and normal stiffness values for the rock section without the joint are higher than those for the rock section with the joint for all the specimens tested.

Table 4.1: Normal stiffness results and elastic properties from strain gage measurements

Specimen	UCS MPa	ν	E_{rock} GPa	$E_{rock/joint}$ GPa	k_{rock} GPa/mm	$k_{rock/joint}$ GPa/mm
01015464-JU	159.8*	0.29	47.98	32.11	15.48	10.03
01015013-2-JU	128.6*	0.16	37.52	14.75	12.94	4.61
01015463-JU	106.0*	0.19	68.68	Joint a: 33.50 Joint b: 31.61	a: 23.93 b: 24.79	a: 10.47 b: 9.88
01014953-1-JU	166.3*,#	0.18	56.81	21.50	24.38	6.72
01014731-JU	61.7*	0.5	37.20	29.12	13.90	9.10
01023570-1-JU	130.1	0.14	30.50	28.99	10.52	9.05
01023575-3-JU	184.7	0.14	38.34	27.34	13.22	8.54
01023682-1-JU	90.8	0.28	33.52	18.83	11.17	5.88
01023663-3-JU	60.7#	0.12	29.42	26.33	10.14	8.23
01023752-JU	46.3	0.17	30.94	35.75	10.67	11.17
01023696-JU	220.6#	0.14	36.41	24.21	12.56	7.57
01023584-3-JU	185.9	0.26	40.09	32.67	13.59	10.25
Average	**128.46**	**0.21**	**40.60**	**27.44**	**15.18**	**8.58**
Std. Deviation	**54.08**	**0.10**	**11.26**	**5.95**	**5.24**	**1.86**

NB: UCS = uniaxial compression strength, ν = Poisson's ratio, E_{rock} = intact rock Young's modulus, $E_{rock/joint}$ = Young's modulus for rock section with the joint, k_{rock} = intact rock normal stiffness and $k_{rock/joint}$ = normal stiffnesss for rock section with the joint. *: Maximum stress reached at the end of extended load application (creep test). #: L/D ≤ 1.7.

4.3 Uniaxial compressive strength and elastic properties

In general, the Young's modulus of a material may be as strong a function of sample variability as its compressive strength. Thus, features such as fractures, lithophysal cavities and test parameters such as sample sizes and strain rates may affect measured moduli (Nimick et al., 1987, p. 21).

Variations in strength, the Young's modulus, Poisson's ratio and other measured properties might be due to variable source of the tested specimens. The specimens tested were obtained from different boreholes (Table 4.2) and therefore expected to exhibit variation in mineralogy, porosity, density, etc. The statistical significance of any given parameter was impossible to determine since individual variations in core lithology could significantly influence material properties (Appendix B). The average intact rock elastic properties for all tests (Young's modulus = 40.62 GPa and Poisson's ratio = 0.21) agree well with the results for most rocks. For most rocks and structural materials E is usually greater than 10^6 psi (6.9 GPa) and the Poisson's ratio is between 0.15 and 0.35 (Obert and Duvall, 1967, p. 49). Our test results also compare well with published test results for rock type formations shown in Tables 1.1 and 1.2 on elastic modulus from 154 uniaxial

compression tests and 107 sets of triaxial compression tests (E = 34.6 ± 17.9), and results on Poisson's ratio (ν = 0.20 ± 0.05) from 129 uniaxial compression and 9 sets of triaxial compression (Kulhawy, 1978, pp. 219 - 221).

4.4. Length-to-Diameter (L/D) ratio and moisture content

Length–to-Diameter ratio of specimens influences test results. Stress distribution in specimens with small L/D ratio tends to be triaxial and they exhibit very high compressive strength. Specimens with large L/D ratio fail due to elastic instability (Vutukuri et al, 1974, p.33). Table 4.2 shows the diameter (D), length (L) and the summary of some physical properties of the tested specimens. Compressive strength results for specimens 01023696-JU (220.6 MPa) and 01023682-1-JU (90.8 MPa) show a very strong effect of L/D ratio on the compressive strength of the specimens. These two specimens from the same borehole (ESF-HD-WH-37) were tested under the same condition (room temperature range of 23-24 degrees centigrade and unconfined). Contrary to the effect described above, the sizes of the first three specimens in Table 4.2, which were obtained from borehole USW SD-12 have variable effect on the compressive strength. The difference may be due to variation in features such as "hidden" fractures, inclusions, etc.

Vutukuri et al., (1974) state "it is best to test specimens under natural environment because the moisture content changes while preparing the specimens." The moisture contents determined in this study might be different from in-situ values since we did not consider how much the samples may have dried. Most of the specimens might have been stored under relatively dry storage room conditions (SMF – Sample Management Facility) for years, without special precautions. Moisture content for the first five specimens in Tables 4.1 and 4.2 were determined after testing while it was determined before testing for the rest. It appears likely that the 0% moisture content of the first five specimens may be due to the fact that the broken samples had been stored in a relatively dry laboratory environment for an extended period of time before testing. Moisture content for most of the tested specimens ranged from 0 to 0.9 % and was less than 1.2 % for all.

4.5 Effects of lithophysae

The effects of lithophysal cavities on strength are important in determining the thickness of the Topopah Spring Member that is acceptable for waste emplacement (Tillerson et al., 1984, p.36). Specimens 01023663-3-JU and 01023752-JU contain lithophysal cavities, the presence of which appears to have caused a decrease in their compressive strengths relative to other tested specimens. Tillerson et al., 1984, p. 36 state "lithophysae are expected to decrease the strength of the tuff in a manner similar to that created by the effects of smaller pore spaces." Presumably the larger the size of the cavities, relative to the size of the specimen, the more significant the strength reduction should be.

Table 4.2 Geometry and some physical properties of the tested specimens

Specimen	Borehole Depth (ft)	Diameter (mm)	Length (mm)	L/D	Water* content (%)	Bulk density (g/cm^3)
01015464-JU**	USW SD-12 1114.9–1115.5	61.01	160.99	2.6	0	2.32
01015013-2-JU**	USW SD-12 781.7–782.5	60.02	113.16	1.9	0	2.29
01015463-JU	USW SD-12 1114.5-1114.9	61.85	134.39	2.2	0	2.20
01014953-1-JU	UE-25 UZ#16 548.0-549.1	60.86	90.09	1.5	0	2.29
01014731-JU	UE-25 UZ#16 803.8-804.2	60.60	123.42	2.0	0	2.28
01023570-1-JU	ESF-HD-WH-3 24.2-25.7	60.73	126.24	2.1	1.03	2.28
01023575-3-JU	ESF-HD-WH-4 26.1-27.3	60.83	131.42	2.2	0.69	2.27
01023682-1-JU	ESF-HD-WH-37 4.5-6.1	60.91	161.42	2.7	1.14	2.27
01023663-3-JU	ESF-HD-WH-36 30.5-31.8	60.99	105.54	1.7	0.85	2.27
01023752-JU	ESF-HD-WH-26 34.0-34.8	60.76	172.31	2.8	0.74	2.26
01023696-JU	ESF-HD-WH-37 37.4-38.0	60.90	74.60	1.2	0.51	2.28
01023584-3-JU	ESF-HD-WH-6 26.9-28.2	61.1	172.3	2.8	0.57	2.29

* Measured after testing for the first five specimens, before testing for the last seven specimens. ** SMF Specimen Custody Receipt, Shipment ID: 01000527, Shipping date: 28-Nov.-2001. Non-Q, for information only.

4.6 Joint normal and shear stiffnesses from uniaxial tests

The stress-strain (load-deformation) curves for axial strain gages installed across the joints as discussed in chapter 3 show that the joints behave as linearly elastic materials. The relationship between the joint normal and shear stiffnesses of a discontinuity (assuming the joint behaves as a linearly elastic isotropic material) is given as:

$$k_s = \frac{k_n}{2(1+\nu)} \quad \cdots\cdots \text{Duncan and Goodman (1968), referenced by Kulhawy (1975)}$$

Where k_s = joint shear stiffness and k_n = joint normal stiffness

The above equation was used to determine the shear stiffness for each of the normal stiffness as shown in Appendices A1 through A12 and summarized in Table 4.3.

Table 4.3 Joint normal and shear stiffnesses of healed joints, and Young's modulus (E_j) of joint fill material (results from extensometer measurements where applicable are in parenthesis).

Specimen	t_j mm	k_n GPa/mm	k_s GPa/mm	* $E_j = k_n \times t_j$ GPa
01015464-JU	0.10	28.49 (25.87)	11.04 (10.03)	2.85
01015013-2-JU	0.30	7.16 (1.82)	3.09 (0.78)	2.15
01015463-JU	0.40	18.61	7.82	7.44
	0.40	16.43	6.90	6.57
01014953-1-JU	0.87	9.28	3.93	8.07
01014731-JU	0.53	26.35	8.78	13.97
01023570-1-JU	0.30	64.77 (2.77)	28.41 (1.21)	19.43
01023575-3-JU	0.30	24.12 (25.48)	10.57 (11.18)	7.24
01023682-1-JU	0.20	12.42 (14.29)	4.85 (5.58)	2.48
01023663-3-JU	0.30	43.69	19.5	13.11
01023752-JU	0.30	N/A	N/A	N/A
01023696-JU	0.30	19.05	8.36	5.72
01023584-3-JU	0.25	41.71	16.55	10.43
Average**	**0.35**	**26.00**	**10.82**	**8.29**
Std. Deviation	**0.18**	**16.04**	**7.04**	**4.97**

NB: t_j = joint thickness, k_n = joint normal stiffness, k_s = joint shear stiffness and E_j = Young's modulus of joint fill material.
*: k_n determined from strain gage measurements was used to calculate E_j.
**: Calculated from strain gage measurements only.

The stiffness results obtained are higher than results from published data (see Tables 1.1 and 1.2). For example, normal stiffness values typically range from 0.24 to 69.59 GPa/m while shear stiffness values range from 0.02 to 29.80 GPa/m (Kulhawy, 1978, pp. 220-223). In general, values for normal and shear stiffnesses for rock joints can range from 10 to 100 MPa/m for joints with soft clay in-filling, to over 100 GPa/m for tight joints in granite and basalt (Itasca, 1997, p. L-12). However, our results are expected since they represent healed (tight) joints whose strengths are supposed to approach or exceed the strength of the intact rock (Tillerson et al., 1984, p. 54). It should be noted that the average intact rock stiffness for specimen 01023752-JU is lower than the 3.2 mm section with the joint due to the presence of four deep lithophysal cavities. It was therefore not possible to calculate its joint normal stiffness, shear stiffness and the Young's modulus of the joint fill material from either strain gage or extensometer measurements (see Appendix A.10).

4.7 Joint normal and shear stiffnesses from the direct shear testing

Direct shear test results show that the joint normal stiffness increases with increasing normal stress. High joint shear stiffness values were obtained when shearing through asperities of the joint and they reduced as the joint surface smoothened out. (Refer to Appendix D for full details).

5.0 SUMMARY OF RESULTS AND RECOMMENDATIONS

5.1 Summary of results

Unconfined compressive strengths and intact rock Young's moduli range from 46.3 to 220.6 MPa and from 29.42 to 68.68 GPa respectively. Joint normal stiffness and joint shear stiffness range from 7.16 to 179.68 GPa/mm and from 3.09 to 78.81 GPa/mm respectively. Bulk densities range from 2.20 to 2.32 g/cm^3 .

5.2 Recommendations

The geological properties of the joint infilling material have not been considered in this study. The mechanical properties of joints are to a great extent dependent upon whether the joints are clean and closed, or open and filled with some infilling material (Indraratna and Haque, 2000, p. 14). The behavior of filled discontinuities depends on a wide range of properties of the filling materials. Some of these properties according to Brady and Brown (1985, p. 58) are mineralogy of the filling material, grading or particle size, and width of filling. Further study is therefore recommended taking into consideration the properties of the infilling material. It is strongly suggested that future uniaxial joint compression tests should be performed on at least 5 to 10 specimens from each borehole so that variations in intact rock and joint properties can be interpreted and the statistical significance and spatial variability of any given parameter determined.

Probably the most important recommendation is that it would be desirable to obtain samples of the joint sets that are most likely to affect the stability of repository excavations. These most likely will be steeply dipping cooling joints that have not been healed by remineralization.

With respect to joint testing, it would be desirable to improve the redundancy in the measurement of joint properties during uniaxial compression testing. This might be accomplished by including machine displacement measurements in the analysis, or by adding additional LVDT's in the circuit. This might help resolve discrepancies between extensometer and strain gage measurements.

Particularly for core with angled joints, triaxial testing probably would be preferable to uniaxial compression testing. This should reduce the severe rotations that tend to dominate the behavior of rough joints with highly localized asperity interactions, at least under high confining pressures. It should allow measurement of normal and shear stiffness, the latter over a range of normal and shear stresses. Triaxial testing has the disadvantage of not allowing direct visual observation during testing, and of greatly complication strain gage and extensometer measurements.

It would be desirable to complement the simple closed form analyses presented in this report with numerical test simulations. Parametric sensitivity analyses might allow a better identification of the variables that affect the results, in particular the influence of

roughness on rotation, and the significance of rotation with respect to stability. A detailed joint roughness characterization prior to testing would be a desirable precursor for such testing and analysis: it has been observed in several of the tests reported on, both uniaxial and direct shear tests, that one or a very small number of asperities may dominate the behavior, by inducing severe rotations.

It would be desirable to have mineralogical characterizations of all specimens tested. This might allow identification of the influence of mineralogical composition on rock properties.

In light of the sensitivity of mechanical properties of tuffs to moisture content (e.g. Martin et al, 1993), it would be desirable to test joints under a range of controlled moisture contents, and over a range of test durations.

From the stiffness of the healed joint, we have calculated the Young's modulus of the vapor phase altered joint infilling. Given the pervasive presence of such altered rock, usually in the form of sub-spheroidal three-dimensional pockets. This property should be of value for any numerical modeling attempting to describe the mechanical behavior of these tuff formations at the level of detail where inclusions might be a factor.

In order to confirm that the mechanical properties (or at least the Young's modulus) of the Type 1 joints are the same or similar to those of other vapor-phased altered inclusions, it would be desirable to perform complementary tests on specimens with such inclusions. Most obvious approaches would be performing uniaxial compression tests on specimens with such inclusions, and instrumenting the specimens with sufficient monitoring instrumentation, e.g. strain gages, extensometers, etc. to provide adequate information to perform a detailed backanalysis of the experimental observations.

References

Amadei, B., and Saeb, S., (1990), " Constitutive Models of Rock Joints," Proceedings of International Symposium on Rock Joints, Loen, Norway, June 4-6, 1990, Nick Barton and Ove Stephansson, ed., Balkema, Rotterdam, pp. 581 – 594.

ASTM, 2000, American Society for Testing and Materials, Annual book of standards Vol., 04.08, Easton, MD, USA.
D 2216 – 98, Laboratory Determination of Water (moisture) Content of Soil and Rock by Mass.
D 2398-95, Standard Test Method for Unconfined Compressive Strength of Intact Rock Core Specimens.
D 5407 - 95, Elastic Moduli of Undrained Intact Rock Core Specimens in triaxial Compression without Pore Pressure Measurement.
D4543 - 85 (1991), Practice for Preparing Rock Core Specimens and Determining Dimensional and Shape Tolerances,
D 5607 – 95, Laboratory Direct Shear Strength Tests of Rock Specimens Under Constant Normal Force.

Bandis, S.C. (1990), " Mechanical Properties of Rock Joints," Proceedings of International Symposium on Rock Joints Loen, Norway, June 4-6, 1990, Nick Barton and Ove Stephansson, ed., Balkema, Rotterda, pp. 125 – 140.

Bandis, S.C., Lumsden, A.C., and Barton, N.R., (1983), "Fundamentals of Rock Joint Deformation" International Journal of Rock Mechanics and Mining Sciences & Geomechanics, Volume 20, No.6, pp. 249 - 268.

Barton, N.R., and Choubey, V., (1977), "The Shear Strength of Rock Joints in Theory and Practice," Rock Mechanics, Volume 10.

Barton, C.C., Larsen, E., Page, W.R., and Howard, T.M., (1993), " Characterizing Fractured Rock for Fluid-Flow, Geomechanical and Paleostress Modelling: Methods and Preliminary Results From Yucca Mountain, Nevada," US Geological Survey, Open-File Report 93-269, Denver, Colorado.

Bieniawski, Z.T., Franklin, J.A., Bernede, M.J., Duffaut, P., Rummel, F., Horibe, T., Broch, E., Rodrigues, E., Van Heerden, W.L., Vogler, U.W., Hansagi, I., Szlavin, J., Brady, B.T., Deere, D.U., Hawkes, I., Milovanovic, D., (1978) " Suggested Methods for Determining the Uniaxial Compressive Strength and Deformability of Rock Materials," International Journal of Rock Mechanics and Mining Sciences & Geomechanics Abstracts, Volume 16, Number 2, pp. 135 – 140.

Blejwas, T.E., and Hansen, F.D., (1990), "Scale Effects in the Shear Behavior of joints in Welded Tuff," Proceedings of the International Symposium on Rock Joints Loen, Norway, June 4-6, 1990, Nick Barton and Ove Stephansson, ed., Balkema, Rotterdam, pp. 185–189.

Board, M.P., Wilson, M.L., and Voegele, M.D., (1987), "Laboratory Determination of the Mechanical, Ultrasonic and Hydrologic Properties of Welded Tuff from the Grouse Canyon Heated Block Site," SAND86-7130, Sandia National Laboratory, Albuquerque, New Mexico.

Bodvarsson, G.S., and Bandurraga, T.M., (1996), " Development and Calibration of the Three Dimensional Site Scale Unsaturated Zone Model of Yucca Mountain,

Nevada," Lawrence Berkeley National Laboratory, Milestone Report MOL 19970211.0176, Berkeley, California.

Brady, B.H.G., and Brown, E.T. (1985), Rock Mechanics for Underground Mining, George Allen and Unwin, London.

Brown, E.T., Editor, 1981. Rock Characterization Testing and Monitoring, ISRM Suggested Methods, International Society for Rock Mechanics, Commission on Testing Methods Pergamon, Press, New York.

Buesch, D.C., (2003), Personal Communication (by e-mail), July 21, 2003.

Duncan, J.M., and Goodman, R.E., (1968), Finite Element Analyses of Slopes in Jointed Rock, U.S. Army Eng. Waterways Exp. Stn., Vicksburg, Miss., Contract Rep. S-68-3.

Feng, X., Chen, S. and Li, S., (2001), Effects of Water Chemistry on Microcracking and Compressive Strength of Granite, International Journal of Rock Mechanics and Mining Sciences, Volume, 38, Number, 4, pp. 557-568.

Gabrielsen, R.H., (1990), "Characteristics of Joints and Faults," Proceedings of International Symposium on Rock Joints, Loen, Norway, June 4-6, 1990, Nick Barton and Ove Stephansson, ed., Balkema, Rotterda, pp. 11 – 17.

Goodman, R.E. (1989), Introduction to Rock Mechanics, 2nd Edition, Wiley and Sons, New York.

Goodman, R.E. (1976), Methods of Geological Engineering in Discontinuous Rocks, West Publishing, New York.

Hawkes, I. and Mellor, M. (1970), "Uniaxial Testing in Rock Mechanics Laboratories." Journal of Engineering Geology, Volume 4, Number 3, pp. 177-285.

Hewlett-Packard (1999), Test and Measurements Catalog, Palo Alto, CA

Hinds, J.J., and Bodvarsson, G.S., (2001), "Role of Fractures in Processes Affecting Potential Repository Performance," High Level Radioactive Waste Management, Proceedings Ninth International Conference, April 29 - May 3, 2001, Las Vegas, Nevada, 4 pp.

Hopkins D.L., and Cook, N.G.W., (1990), " Normal Joint Stiffness as a Function of Spatial Geometry and Surface Roughness," Proceedings International Symposium on Rock Joints, Loen, Norway, June 4-6, 1990, Nick Barton and Ove Stephansson, ed., Balkema, Rotterdam, pp. 203 – 218.

Hudson, J.A., (1993), "Uniaxial Strength Testing" Comprehensive Rock Engineering, Rock Testing and Site Characterization, Volume 3, Chapter 3, Pergamon Press Ltd., Headington Hill Hall, Oxford, England.

Indraratna, B., and Haque, A., (2000), Shear Behavior of Rock Joints, Balkema, Rotterdam.

Infanti Jr, N., and Kanji, M.A., (1990) " Estimating the Shear Stiffness of Rock Joints," Proceedings of International Symposium on Rock Joints, Loen, Norway, June 4-6, 1990, Nick Barton and Ove Stephansson, ed., Balkema, Rotterdam, pp. 799 – 804.

Ingard, U. and Kraushaar, W.L., (1960), Introduction to Mechanics, Matter and Waves, Addison-Wesley, London.

ISRM, (1999), Draft International Society for Rock Mechanics Suggested Method for the Complete Stress-Strain Curve for Intact Rock in Uniaxial Compression,

International Journal of Rock Mechanics and Mining Sciences, Volume, 36, pp. 279-289.

Itasca (1997), Fast Lagrangian Analysis of Continua in 3 Dimensions (FLAC 3^D), User's Manual, Version 2.0, Volumes I, II, III, IV and V, Itasca Consulting Group, Inc., Minneapolis, Minnesota.

Jaeger, J.C., and Cook, N.G.W., (1976), Fundamentals of Rock Mechanics, 2nd Edition, Chapman and Hall, London.

Kulhawy, F.H. (1978), "Geomechanical Model for Rock Foundation Settlement," Journal of Geotechnical Engineering, Volume 104, No.GT 2, pp. 211-227, Proceedings of the American Society of Civil Engineers.

Kulhawy, F.H. (1975), "Stress Deformation Properties of Rock and Rock Discontinuities," Journal of Engineering Geology, Volume 9, No. 4, pp. 327-350.

Leem, J., and Kemeny, J.M., (2001), "Thermal-Hydrologic-Mechanical Fracture Analysis of Yucca Mountain Nuclear Waste Repository," High Level Radioactive Waste Management, Proceedings Ninth International Conference, April 29 – May 3, 2001, American Nuclear Society, University of Nevada, Las Vegas, Nevada, 4 pp.

Lin, M., Brechtel, C.E., and Hardy, M.P., (1993), " Rock Mass Mechanical Property Estimation Strategy for the Yucca Mountain Site Characterization Project," High Level Radioactive Waste Management, Proceedings Fourth Annual International Conference, April 26-30, 1993, Las Vegas, Nevada.

Maki, K. (1985), "Shear Strength and Stiffness of Weakness Planes Created by Controlled Fracturing on Intact Specimens," Fundamentals of Rock Joints, Proceedings of the International Symposium on Fundamentals of Rock Joints, Bjorkliden, September 15 – 20, 1985, Ove Stephansson, ed., Lulea, Sweden, pp.133 – 142.

Martin, R.J. III, Price, R.H., Boyd, P.J., and Noel, J.S., (1993), The Influence of Strain Rate and Sample Inhomogeneity on the Moduli and Strength of Welded Tuff, International Journal of Rock Mechanics, Mining Sciences and Geomechanics. Abstract, Volume 30, No. 7, pp. 1507-10.

Measurements Group Inc., 1997, Student Manual for Strain Gage Technology, Bulletin 309D, Measurements Group, Education Division, Raleigh, North Carolina.

Nimick, F.B., Van Buskirk, R.G., and McFarland, A.F., (1987), "Uniaxial and Triaxial Compression Test Series on the Topopah Spring Member from USW G-2, Yucca Mountain, Nevada," SAND85-0703, Sandia National Laboratory, Albuquerque, New Mexico.

Obert, L. and Duvall, W.I., (1967), Rock Mechanics and the Design of Structures in Rock. John Wiley and Sons, New York.

Price, R.H., (1983), "Analysis of Rock Mechanics Properties of Volcanic Tuff Units from Yucca Mountain, Nevada Test Site," SAND82-1315, Sandia National Laboratory, Albuquerque, New Mexico.

Price, R.H., Nimick, K.G., and Zirzow, J.A. (1982), "Uniaxial and Triaxial Compression Test Series on Topopah Spring Tuff," SAND82-1723, Sandia National Laboratory, Albuquerque, New Mexico

Pyrak-Nolte, L.J., Myer, L.R., Cook, N.G.W., and Witherspoon, P.A., (1987), "Hydraulic and Mechanical Properties of Natural Fractures in low Permeability Rock."

Proceedings of Sixth International Congress of Rock Mechanics, Montreal, pp. 225-231, Rotterdam, Balkema.

Rautman, C.A., and Engstrom, D.A., (1996), " Geology of the USW SD-12 Drill Hole Yucca Mountain, Nevada," SAND96- 1368, Sandia National Laboratory, Albuquerque, New Mexico.

Rousseau, J.P., Kwicklis, E.M., and Gilles, D.C., (1996), "Hydrogeology of the Unsaturated Zone, North Ramp Area of the Exploratory Studies Facility, Yucca Mountain, Nevada," US Geological Survey, Draft Milestone Report 3GUP431M, MOL 19980220.0164, Denver, Colorado.

Schultz, R.A. and Li, Q., (1995), "Uniaxial Strength Testing of Non-Welded Calico Hills Tuff, Yucca Mountain, Nevada," International Journal of Engineering Geology, Volume 40, Number 3-4, pp. 287-299.

Sweetkind, D.S., Beason, S.C., and Buesch, D.C., (2000), " Overview of the Stratigraphic and Structural Setting of Yucca Mountain, Nevada, USA," International Journal of Rock Mechanics (To be published Manuscript; Approved by USGS Director and U.S. Department of Energy).

Sweetkind, D.S., Potter, C.J., and Verbeek, E.R. (1996), "Interaction Between Faults and the Fracture Network at Yucca Mountain, Nevada," EOS, Transactions, American Geophysical Union, TIC 236789, Washington, D.C.

Throckmorton, C.K., and Verbeek, E.R. (1995), "Joint Networks in the Tiva Canyon and Topopah Spring Tuffs of the Paintbrush Group, Southwestern Nevada," US Geological Survey Open-File Report 95 – 2, TIC 235000, Denver, Colorado.

Tillerson, J.R. and Nimick, F.B. (1984), "Geoengineering Properties of Potential Repository Units at Yucca Mountain, Southern Nevada," SAND84-0221, Sandia National Laboratory,Albuquerque, New Mexico.

Turk, N. and Dearman, W.R. (1985), "Investigation of Some Rock Joint Properties: Roughness Angle Determination and Joint Closure," Proceedings of the International Symposium on Fundamentals of Rock Joints, Bjorkliden, September 15-20, 1985, Ove Stephansson, ed., Lulea, Sweden, pp. 197 – 204.

Vutukuri, V.S., Lama, R.D., and Saluja, S.S., (1974), Handbook on Mechanical Properties of Rocks, 1st Edition, Volume 1, Series on Rock and Soil Mechanics Volume 2, No. 1 1974-75, Trans Tech, Bay Village, Ohio.

Appendix A. Description of uniaxial compression tests on joints: specimen instrumentation, data collected, specimen photographs, calculated rock and joint properties.

This Appendix presents information about uniaxial compression tests conducted on rock specimens that contain joints normal to the loading direction. The Appendix is organized by specimen ID, i.e. each section describes in detail one specimen test. The description includes instrumentation used, plots of data collected, photographs of specimen tested, and results calculated: joint stiffness, uniaxial compressive strength, moisture content, rock Young's modulus and Poisson's ratio. Tabulated results and calculated joint stiffnesses were obtained using the procedures and formulas given in chapters 3 and 4.

Creep tests were performed on five of the twelve specimens presented in this Appendix. Their data were reduced by removing the steps corresponding to times the stress was held constant (see Appendices A1 through A5). It must be noted that steps shown in some of the Figures (e.g. Fig. A1.2) are not "creep" strains but signs of data manipulation. In general, strain gages installed gave a better measurement than the extensometers. This is because the extensometers were removed and re-installed in some cases to ensure alignment. In addition to that, the extensometers were removed altogether when there was an indication of failure in order not to damage the extensometers. Joint stiffnesses from extensometer data of three (01015464-JU, 01023575-3-JU and 01023682-1-JU) of the six specimens on which they were installed compare reasonably well with the stiffness results from strain gage measurements. (Refer to Appendices A1, A7 and A8 for details).

A1 – Specimen 01015464 – JU

A2 - Specimen 01015013 - 2 – JU

A3 - Specimen 01015463 – JU

A4 - Specimen 01014953 - 1 – JU

A5 - Specimen 01014731 – JU

A6 - Specimen 01023570 - 1 – JU

A7 - Specimen 01023575 - 3 – JU

A8 - Specimen 01023682 - 1 – JU

A9 - Specimen 01023663-3 – JU

A10 - Specimen 01023752 – JU

A11 - Specimen 01023696 – JU

A12 - Specimen 01023584 - 3 – JU

Appendix A1 – Specimen 01015464-JU

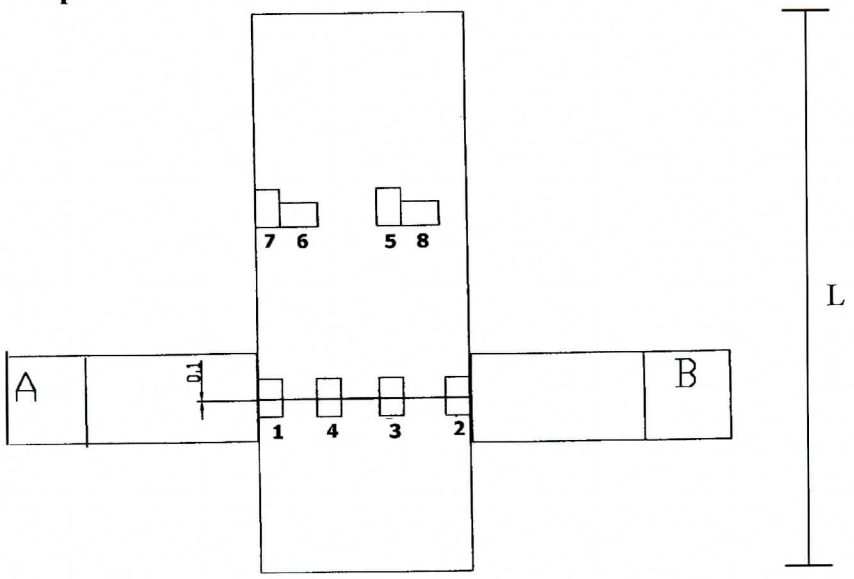

Fig A1.1 Instrumentation in Uniaxial Joint Compression Test (scale 1:0.75)

The figure above shows the position of strain gages (number 1 to 8) each of length 3.2 mm and the extensometers (A and B each of length 25.4 mm) on specimen 01015464-JU (diameter of 61.01 mm and 160.99 mm long). The four axial gages (gages 1, 2, 3 and 4) installed across the joint (thickness of 0.1 mm) were at 90 degrees from each other (i.e. gage 1 along the 0° axis and gage 2 along the 270° axis). Axial gage 5, horizontal gage 8, axial gage 7 and horizontal gage 6 were installed on intact rock at the 180° and 0° axes respectively. The two axial extensometers 2 and 3 were installed across the joint along the 0° and 180° axes respectively.

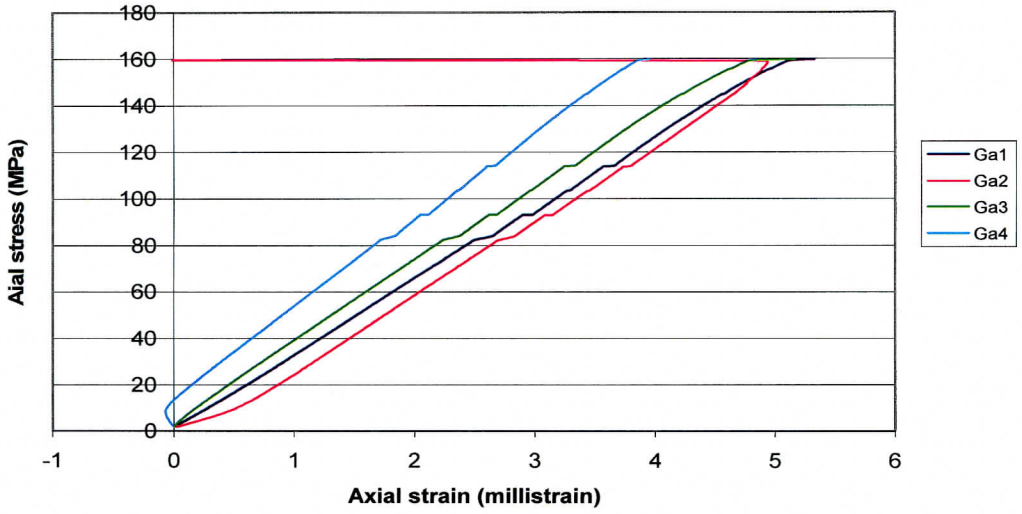

Fig. A1.2 Axial stress vs. axial strain for gages 1, 2, 3 and 4 installed across the joint

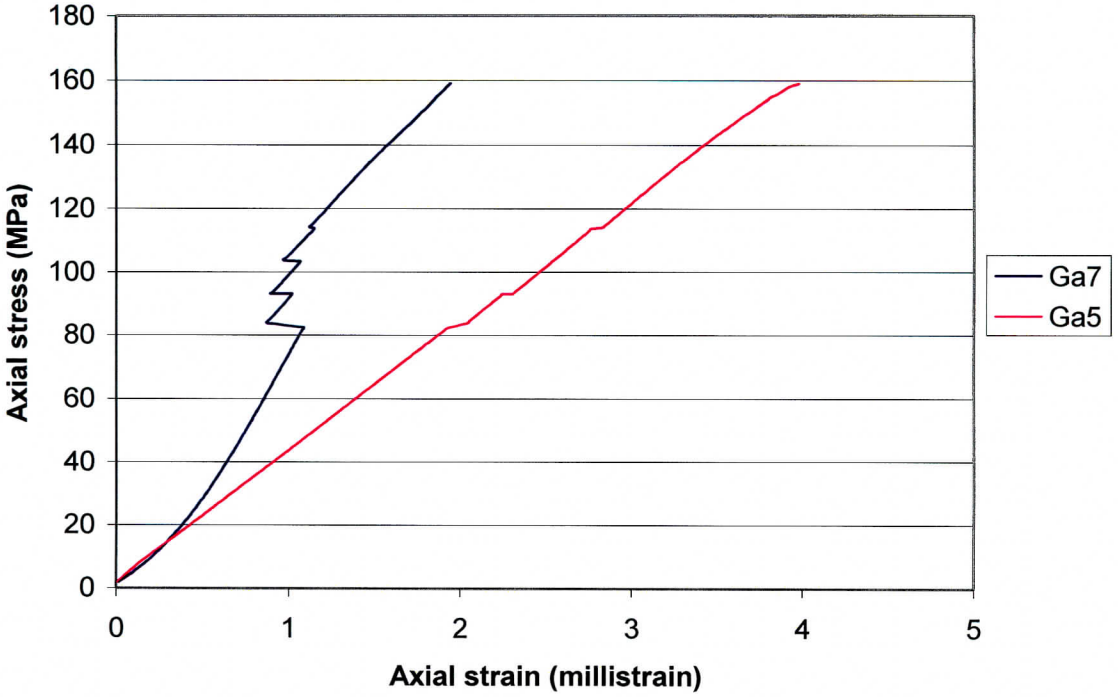

Fig A1.3 Axial stress vs. axial strain for gages 5 and 7 installed on intact rock

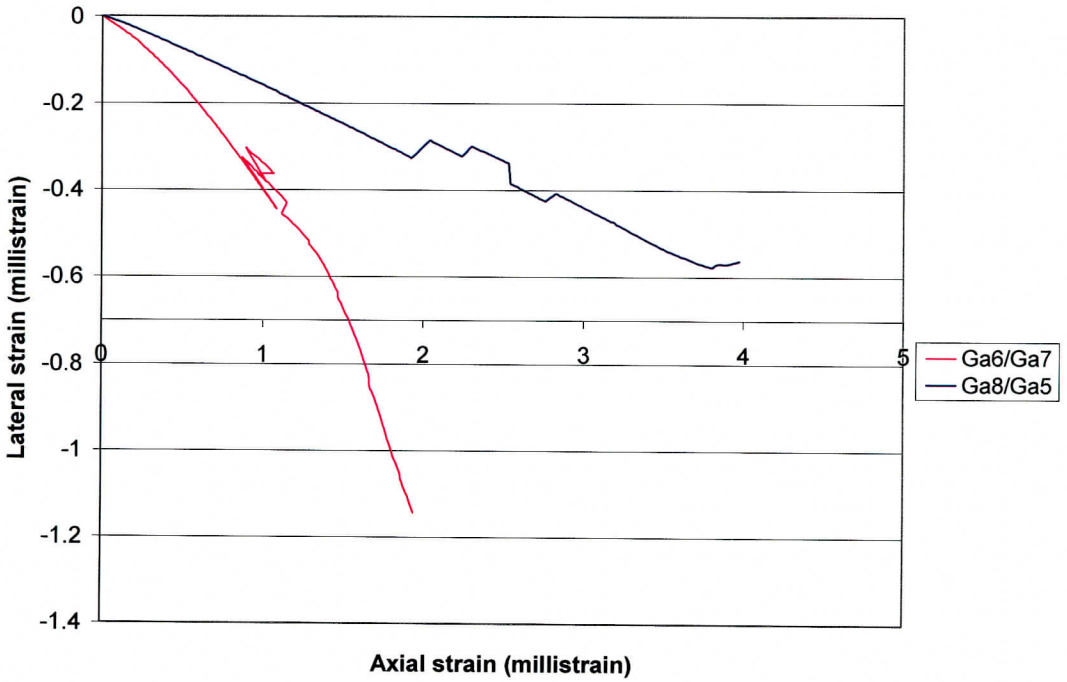

Fig. A1.4 Lateral strain (gage 6) vs. axial strain (gage 7) and lateral strain (gage 8) vs. axial strain (gage 5).

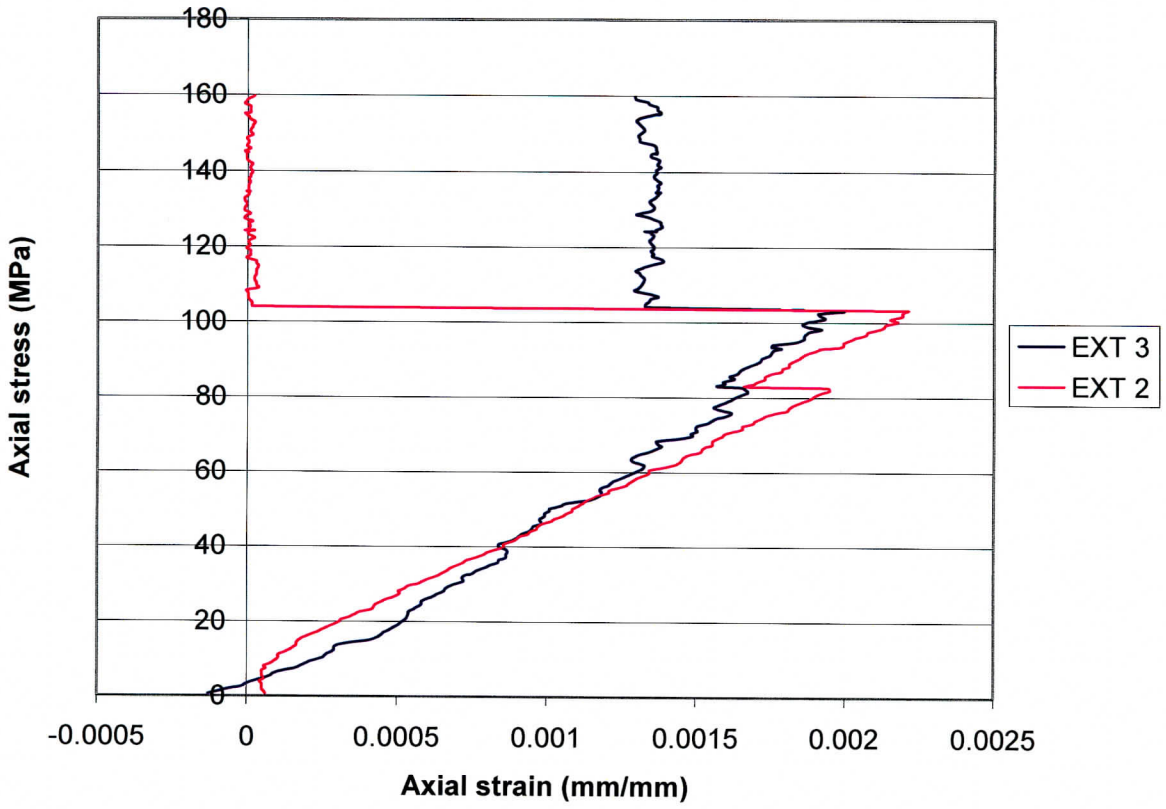

Fig. A1.5 Axial stress vs. axial strain for extensometers 2 and 3

(a) Results from strain gage measurements

Table A1.1 Young's modulus and normal stiffness

Section of rock	Sensor	Young's modulus (GPa)	Normal stiffness (GPa/mm)	Range (% of UCS)
3.2 mm rock/joint	Gage 1	31.15	9.73	8.9 - 86.2
	Gage 2	32.26	10.08	
	Gage 3	32.91	10.29	
	Gage 4*	37.62	11.76	
	Mean	**32.11**	**10.03**	
	Std. Deviation	**0.73**	**0.23**	
3.2 mm intact rock	Gage 5	39.67	12.40	3.7 - 97.1
	Gage 7	56.28	17.59	67.5 - 99.1
	Mean	**47.98**	**15.0**	
	Std. Deviation	**8.31**	**2.60**	

NB: * Values obtained from strain gage 4 are significantly too high after applying the outlier test (i.e. T-statistical test, ASTM E 178 – 94) to the measurements at both the 1% and 5% levels of significance. Therefore, they were not included in the calculation of the mean.

Table A1.2 Poisson's ratio

Sensor	ν	Range (% of UCS)
Lateral Gage 8 vs. axial gage 5	0.17	2.4 - 46.4
Lateral Gage 6 vs. axial gage 7	0.4	8.4 – 31.3
Mean	**0.29**	
Std. Deviation	**0.12**	

UCS = 159.8 MPa,
Moisture content after testing = 0 % (determined approximately 8 months after testing).
Bulk density = 2.32 g/cm^3
Joint normal stiffness is 28.49 GPa/mm and calculated joint shear stiffness is11.04 GPa/mm.

(b) Results from extensometer measurements

Table A1.3 Young's modulus and normal stiffness

Sensor	Young's modulus (GPa)	Normal stiffness (GPa/mm)	Range (% of UCS)
Extensometer 2	38.3	1.51	12.9 - 50.5
Extensometer 3	51.6	2.03	8.6 - 47.0
Mean	**44.95**	**1.77**	
Std. Deviation	**6.65**	**0.26**	

Joint normal stiffness is 25.87 GPa/mm and the calculated joint shear stiffness is 10.03 GPa/mm.

Table A 1.4 Stress History

Applied Load	Stress	Duration
150 kN	51.7 MPa	2 days, 3 hours, 40 minutes, 26 seconds
180 kN	62.1 MPa	2 days, 20 hours, 35 minutes, 26 seconds
210 kN	72.4 MPa	6 days, 6 hours, 23 minutes, 15 seconds
240 kN	82.8 MPa	16 hours, 39 minutes, 25 seconds
270 kN	93.1 MPa	2 days, 23 hours, 46 minutes, 51 seconds
300 kN	103.4 MPa	2 days, 5 hours, 29 minutes, 41 seconds
330 kN	113.4 MPa	1 day, 20 hours, 53 minutes
330 kN to 463 kN (failure)	113.4 MPa to 159.8 MPa	7 minutes, 5 seconds

Fig. A1.6 Pre-failure photograph of specimen 01015464-JU with an axial strain gage along the 90° axis

Appendix A2 – Specimen 01015013-2-JU

Instrumentation

This specimen (60.02 mm diameter and 113.16 mm long) was instrumented with eight gages (each of length 3.2 mm) similar to Figure A1.1. Its axial gages 1, 2, 3 and 4 were installed across the joint (thickness of 0.3 mm) at 0°, 90°, 180° and 270° respectively. Axial gage 5, horizontal gage 8, axial gage 7 and horizontal gage 6 were installed on intact rock at the 270° and 90° axes respectively. The two axial extensometers (each of length 25.4 mm) were installed across the joint along the 90° and 270° axes respectively.

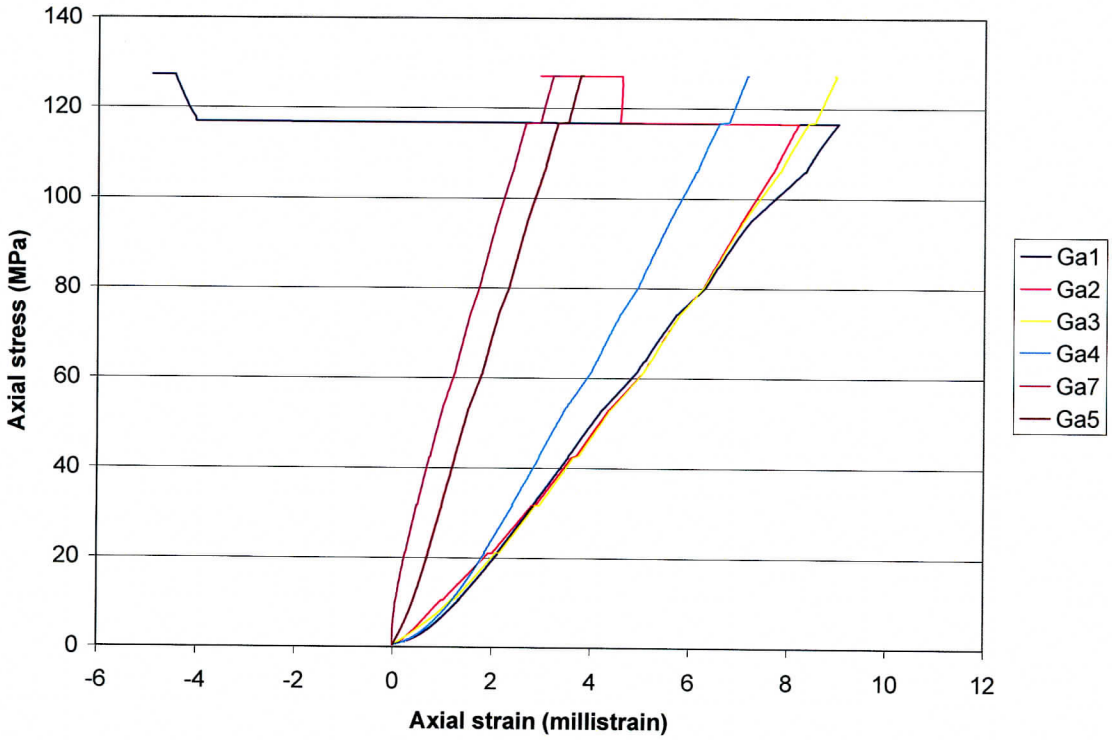

Fig. A2.1 Axial stress vs. axial strain for strain gages 1, 2, 3, 4 installed across the joint and 5 and 7 installed on intact rock.

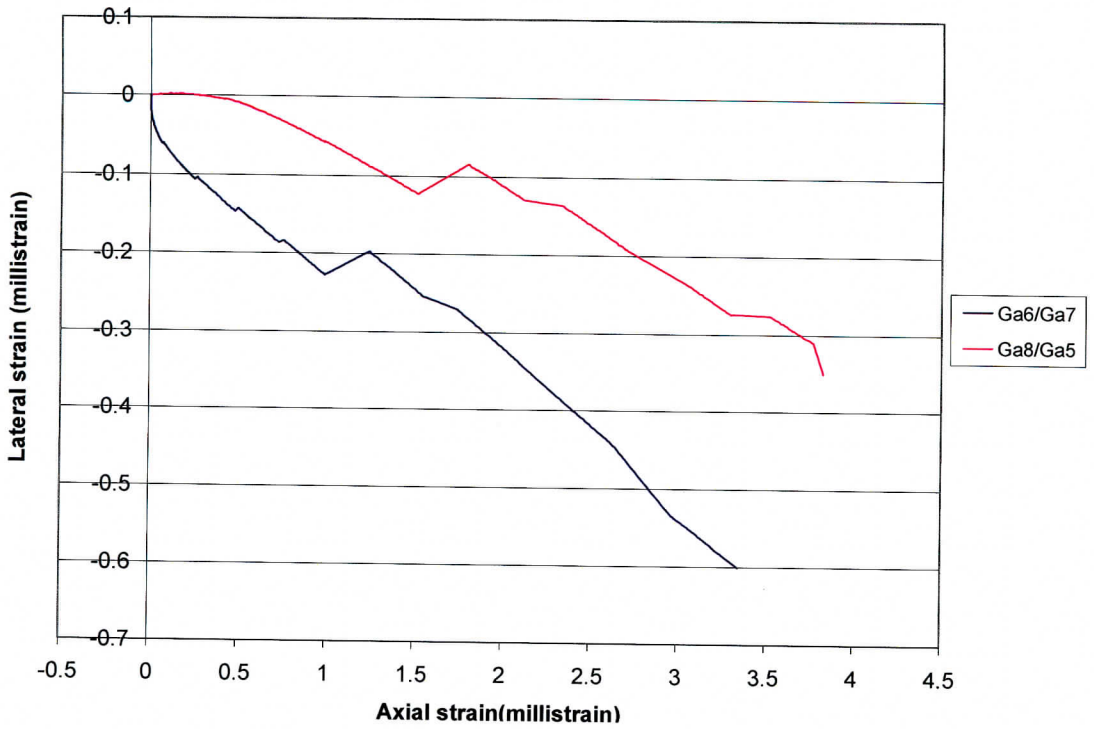

Fig. A2.2 Lateral strain (gage 6) vs. axial strain (gage 7) and lateral strain (gage 8) vs axial strain (gage 5).

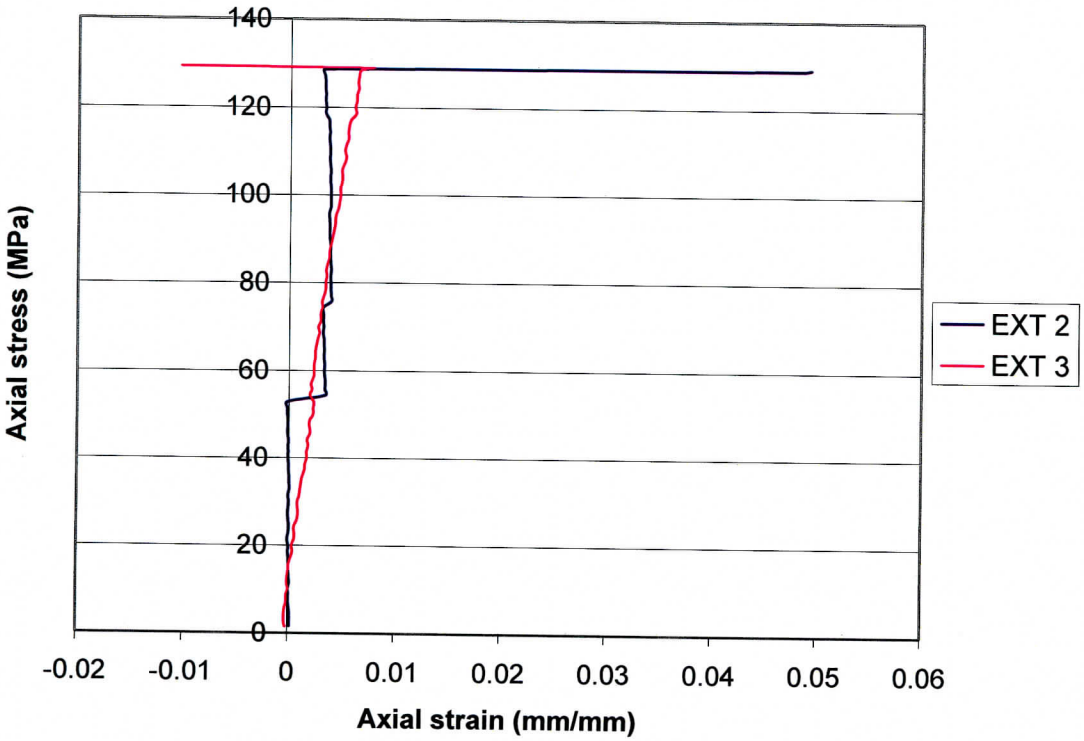

Fig A2.3 Axial stress vs. axial strain for extensometers 2 and 3

(a) Results from strain gage measurements

Table A2.1 Young's modulus and normal stiffness

Section of rock	Sensor	Young's modulus (GPa)	Normal stiffness (GPa/mm)	Range (% of UCS)
3.2 mm rock with the joint	Gage 1	13.77	4.30	22.1-89.7
	Gage 2	15.27	4.77	
	Gage 3	15.22	4.76	
	Gage 4*	19.93	6.23	
	Mean	**14.75**	**4.61**	
	Std. Deviation	**0.70**	**0.22**	
3.2 mm intact rock	Gage 5	36.14	11.29	22.1-89.7
	Gage 7	38.89	12.15	
	Mean	**37.52**	**11.72**	
	Std. Deviation	**1.38**	**0.43**	

NB: * Values obtained from strain gage 4 are significantly too high when applying the outlier test to the measurements at both the 1% and 5% levels of significance (ASTM E 178 - 94). Therefore, they were not included in the mean value calculation.

Table A2.2 Poisson's ratio

Sensor	ν	Range (% of UCS)
Lateral Gage 6 vs. axial gage 7	0.2	50.3-99.8
Lateral Gage 8 vs. axial gage 5	0.12	51.0-91.7
Mean	**0.16**	
Std. Deviation	**0.04**	

UCS = 128.6 MPa,
Moisture content after testing = 0 % (measured some 7 months after performing the test).
Bulk density = 2.29 g/cm^3
Joint normal stiffness is 7.16 GPa/mm and calculated joint shear stiffness is 3.09 GPa/mm.

(b) Results from extensometer measurements

Table A2.3 Young's modulus and normal stiffness

Sensor	Young's modulus (GPa)	Normal stiffness (GPa/mm)	Range (% of UCS)
Extensometer 2	25.37	0.99	45.3 – 94.0
Extensometer 3	16.17	0.64	
Mean	**20.77**	**0.82**	
Std. Deviation	**4.6**	**0.18**	

Joint normal stiffness is 1.82 GPa/mm and the calculated joint shear stiffness is 0.78 GPa/mm.

Table A2.4. Stress History

Applied Load	**Stress**	**Duration**
150 kN	53.1 MPa	22 hours, 45 minutes, 36 seconds
210 kN	75.0 MPa	22 hours, 30 minutes, 12 seconds
270 kN	96.4 MPa	23 hours, 45 minutes, 24 seconds
330kN	117.9 MPa	23 hours, 30 minutes, 29 seconds
360 kN	128.6 MPa	1 hours 6 minutes, 10 seconds

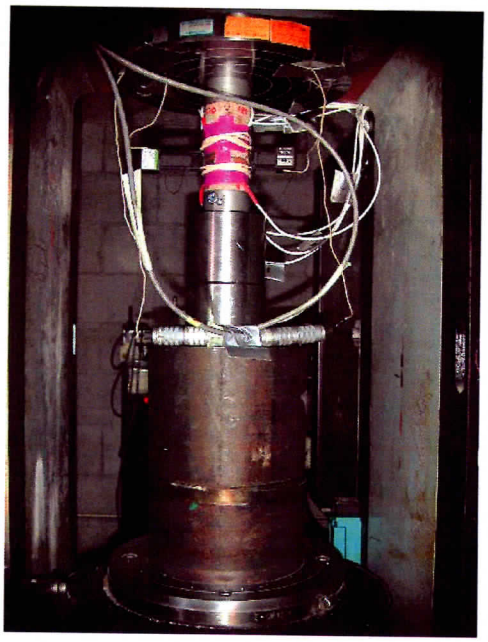

Fig. A2.4 Specimen 01015013-2-JU with sensors Installed in a four post 220 kip MTS machine.

Appendix A3 -Specimen 01015463-JU

Instrumentation

This specimen (diameter of 61.85 mm and 134.39 mm long) with two joints ("a" and "b" each of thickness of 0.4 mm) was instrumented with eight gages (each of length 3.2 mm) similar to Figure A1.1. Axial gages 1 and 2 were installed across joint "a" at 90° and 240° axes respectively while axial gages 3 and 4 were installed across joint "b" at 120° and 270° axes respectively. Axial gage 5, lateral gage 8, axial gage 7 and lateral gage 6 were installed on intact rock along the 180° and 0° axes respectively.

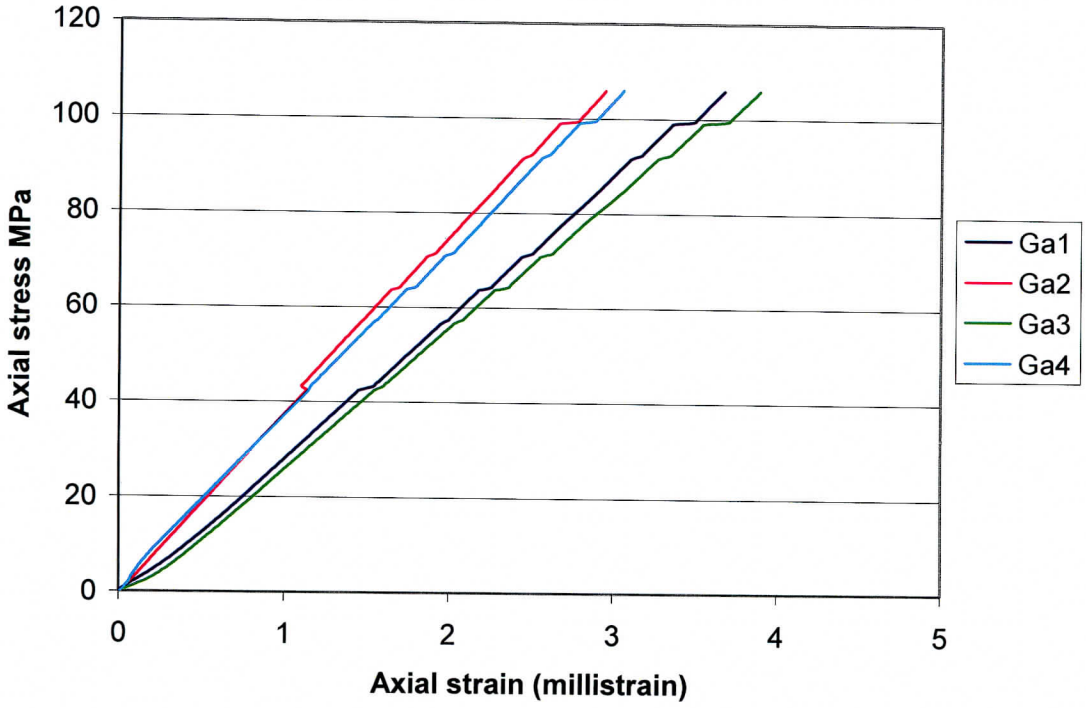

Fig. A3.1 Axial stress vs. axial strain for gages 1, 2,3 and 4 installed across the joints

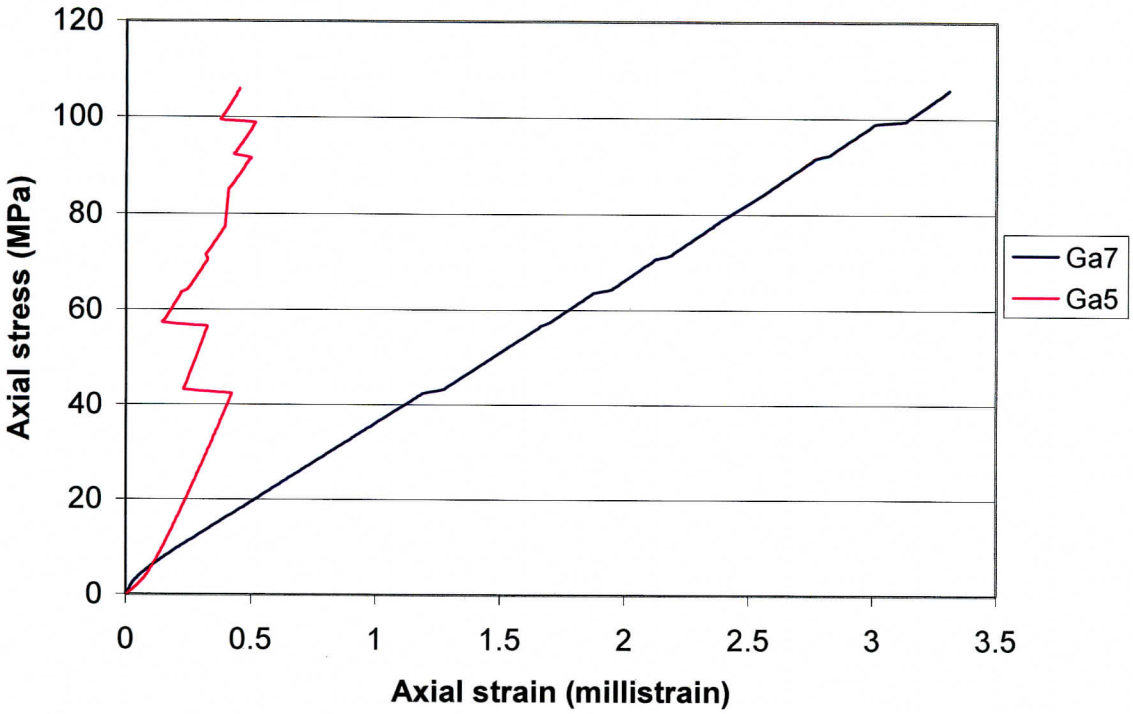

Fig. A3.2 Axial stress vs. axial strain for gages 5 and 7 installed on intact rock

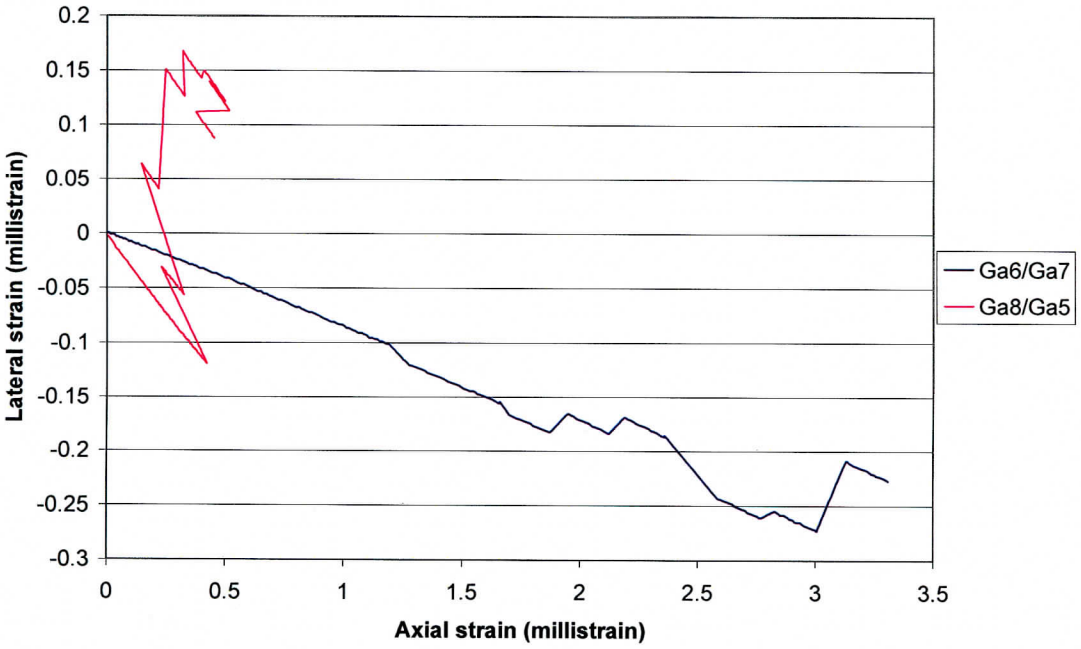

Fig. A3.3 Lateral strain (gage 6) vs. axial strain (gage 7) and lateral strain (gage 8) vs. axial strain (gage 5)

Results from strain gage measurements

Table A3.1 Young's modulus and normal stiffness

Section of rock	Sensor	Young's modulus (GPa)	Normal stiffness (GPa/mm)	Range (% of UCS)
3.2 mm rock with joint	Gage 1	29.83	9.32	17.0 – 93.3
	Gage 2	37.17	11.61	
	Mean	**33.50**	**10.47**	
	Std. Deviation	**3.67**	**1.15**	
	Gage 3	28.60	8.94	
	Gage 4	34.61	10.82	
	Mean	**31.61**	**9.88**	
	Std. Deviation	**3.0**	**0.94**	
3.2 mm intact rock	Gage 5*	106.11	33.16	56.7-86.0
	Gage 7	31.25	9.88	17.0 – 93.3
	Mean	**68.68**	**21.52**	
	Std. Deviation	**37.43**	**11.64**	

NB: *Axial gage 5 installed on intact rock showed highly erratic non-linear behavior. However, its results together with results for gage 7 (i.e. average value) have been used to calculate intact rock Young's modulus and normal stiffness.

Table A3.2 Poisson's ratio

Sensor	ν	Range (% of UCS)
Lateral Gage 6 vs. axial gage 7	0.10	0.7 – 56.7
Lateral Gage 8 vs. axial gage 5	0.28	0.7 – 37.4
Mean	**0.19**	
Std. Deviation	**0.09**	

UCS = 106.0 MPa,
Moisture content after testing = 0 %
Bulk density = 2.20 g/cm^3
Joint normal stiffness for joint "a" is 18.61 GPa/mm and calculated joint shear stiffness is 7.82 GPa/mm.

Joint normal stiffness for joint "b" is 16.43 GPa/mm and calculated joint shear stiffness is 6.90 GPa/mm.

Table A3.3. Stress History

Applied Load (kN)	Stress(MPa)	Duration
120	40.0	2 days, 2 hours, 57 minutes, 50 seconds
140	46.7	1 hour, 25 minutes, 14 seconds
160	53.3	12 hours, 13 minutes, 10 seconds
180	60.0	1 day, 16 hours, 11 minutes, 15 seconds
200	66.7	1 day, 15 hours, 43 minutes, 24 seconds
220	73.3	22 hours, 1 minute, 35 seconds
240	80.0	1 day, 16 hours, 30 seconds
260	86.7	1 day, 18 hours, 44 minutes, 55 seconds
280	93.3	6 days, 13 hrs, 53 minutes, 30 seconds
300	100.0	3 days, 9 hours, 36 minutes, 15 seconds

Fig A3.4 Specimen 01015463-JU with gages along the 270° axis

Fig A3.5 Specimen 01015463-JU in a four-post MTS machine prior to testing

Appendix A4 – Specimen 01014953-1-JU

Instrumentation

This specimen (diameter of 60.86 mm and 90.09 mm long) was instrumented with eight gages (each of length 3.2 mm). Four axial gages 1, 2, 3 and 4 were installed across the joint (thickness of 0.87 mm) similar to Figure A1.1 along the 0°, 90° 180° and 270° axes respectively. Axial gage 5, horizontal gage 6, axial gage 7 and horizontal gage 8 were installed on intact rock along the 90° and 270° axes respectively.

Axial gage 2 and lateral gage 8 debonded prior to testing. Therefore they were not considered in the analysis.

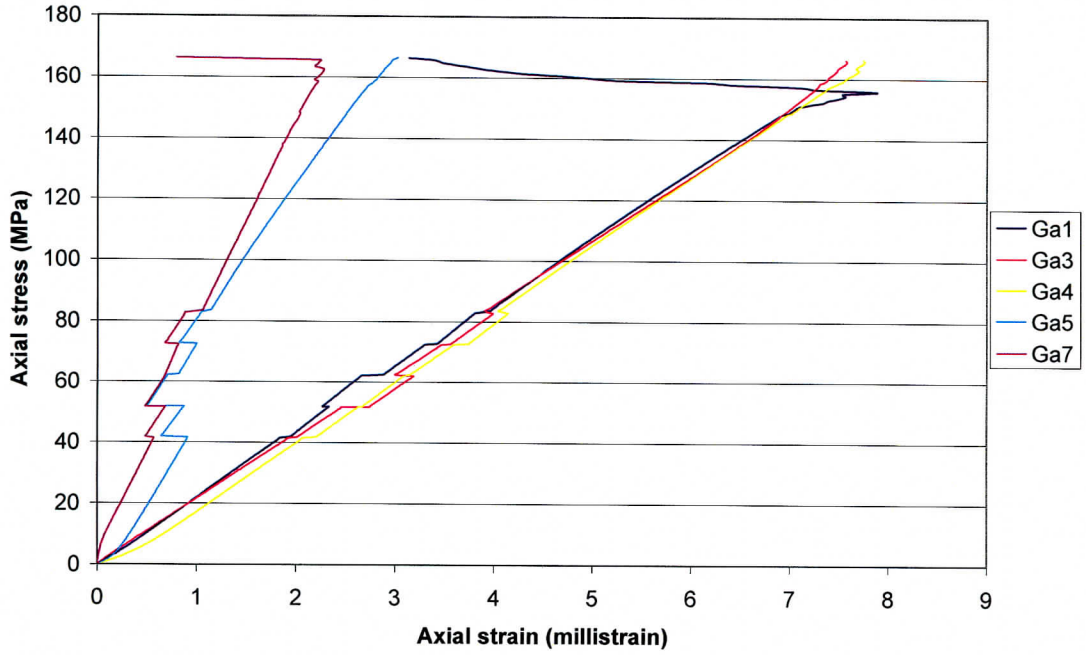

Fig. A4.1 Axial stress vs. axial strain for five strain gages (Ga1, Ga3, Ga4, Ga5 and Ga7) installed on intact rock and across the joint.

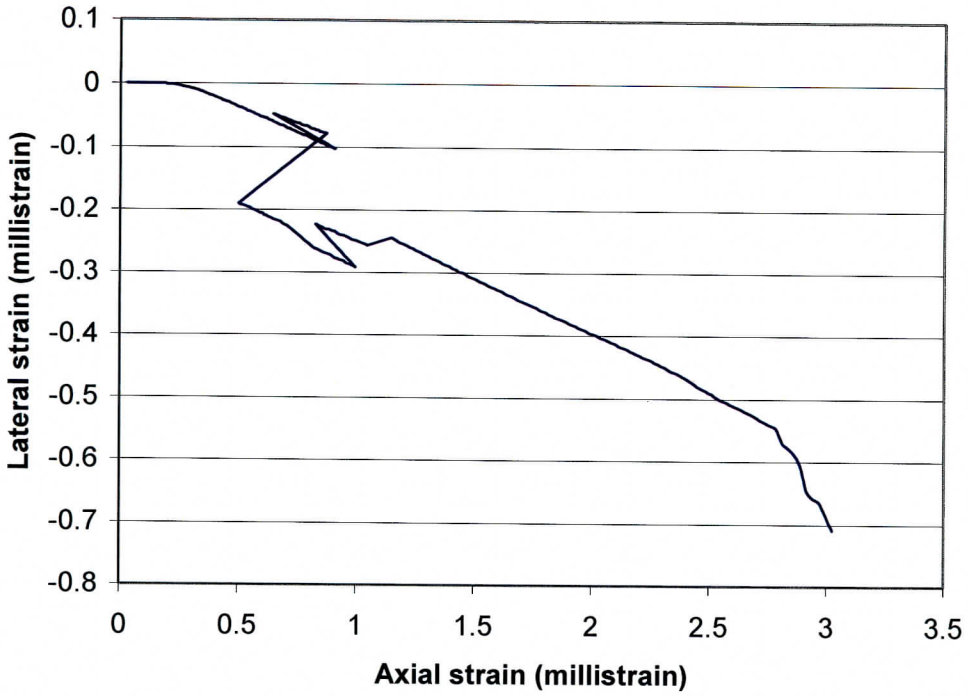

Fig A4.2 Lateral strain (gage 6) vs. axial strain (gage 5).

Results from strain gage measurements

Table A4.1 Young's modulus and normal stiffness

Section of rock	Sensor	Young's modulus (GPa)	Normal stiffness (GPa/mm)	Range (% of UCS)
3.2 mm rock with joint	Gage 1	21.30	6.66	5.4-90.6
	Gage 3	21.28	6.65	
	Gage 4	21.92	6.85	
	Mean	**21.50**	**6.72**	
	Std. Deviation	**0.3**	**0.09**	
3.2 mm intact rock	Gage 5	46.86	14.65	50.2-90.6
	Gage 7	66.76	20.86	
	Mean	**56.81**	**17.76**	
	Std. Deviation	**9.95**	**3.11**	

Table A4.2 Poisson's ratio

Sensor	ν	Range (% of UCS)
Lateral Gage 6 vs. axial gage 5	0.18	50.2-90.6

UCS = 166.3 MPa,
Moisture content after testing = 0 %
Bulk density = 2.29 g/cm^3
Joint normal stiffness is 9.28 GPa/mm and calculated joint shear stiffness is 3.93 GPa/mm.

Table A4.3. Stress History

Applied Load (kN)	Stress(MPa)	Duration
120	41.4	6 days, 17 hours, 10 seconds
150	51.7	4 days , 3 hours, 28 minutes, 40 seconds
180	62.1	1 day, 4 hours, 27 minutes, 30 seconds
210	72.4	6 days, 6 hours, 26 minutes, 10 seconds
240	82.8	8 hours, 39 minutes, 30 seconds
240 to 482.3 (failure)	82.8 to 166.3	10 minute, 30 seconds

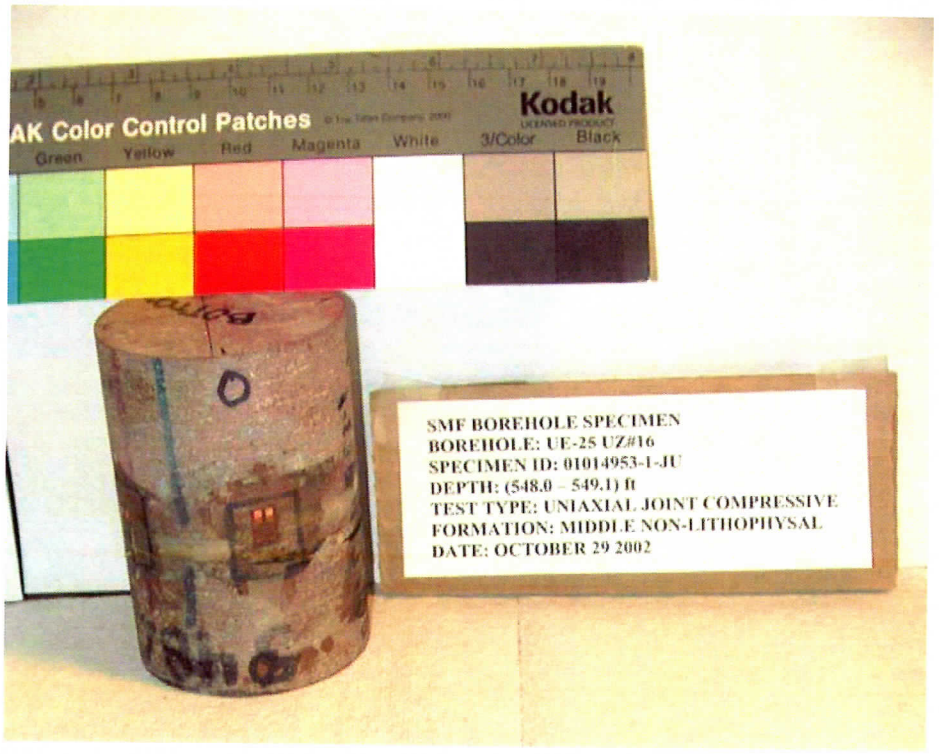

Fig. A4.3 Pre-failure photograph of specimen 01014953-1-JU with an axial gage along the 0° axis.

Fig. A4.4 Post-failure top view of specimen 01014953-1-JU

Appendix A5 – Specimen 01014731-JU

Instrumentation

This specimen (diameter of 60.6 mm and 123.42 mm long) was instrumented with six gages. Gages 1 and 3 were installed across the joint (thickness of 0.53) along the 0° and 180° axes respectively. Installation of four additional gages on intact rock is similar to Figure A1.1.

Axial gage 7 and lateral gage 8 were not considered in the analysis due to installation problems.

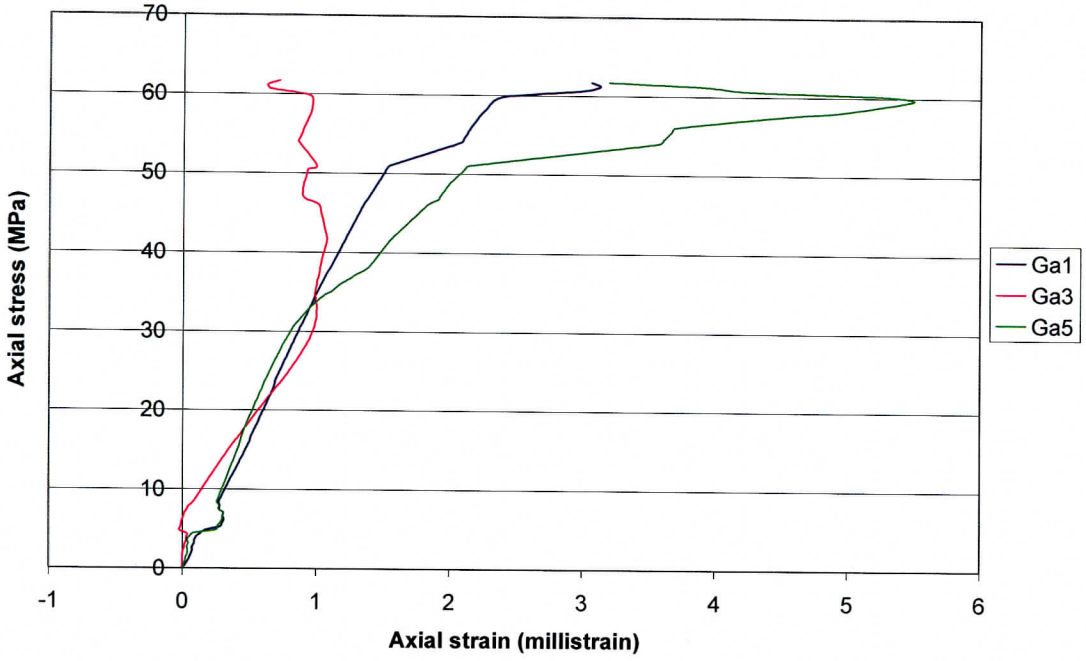

Fig. A5.1 Axial stress vs. axial strain for three strain gages (Ga1, Ga3 and Ga5) installed on intact rock and across the joint.

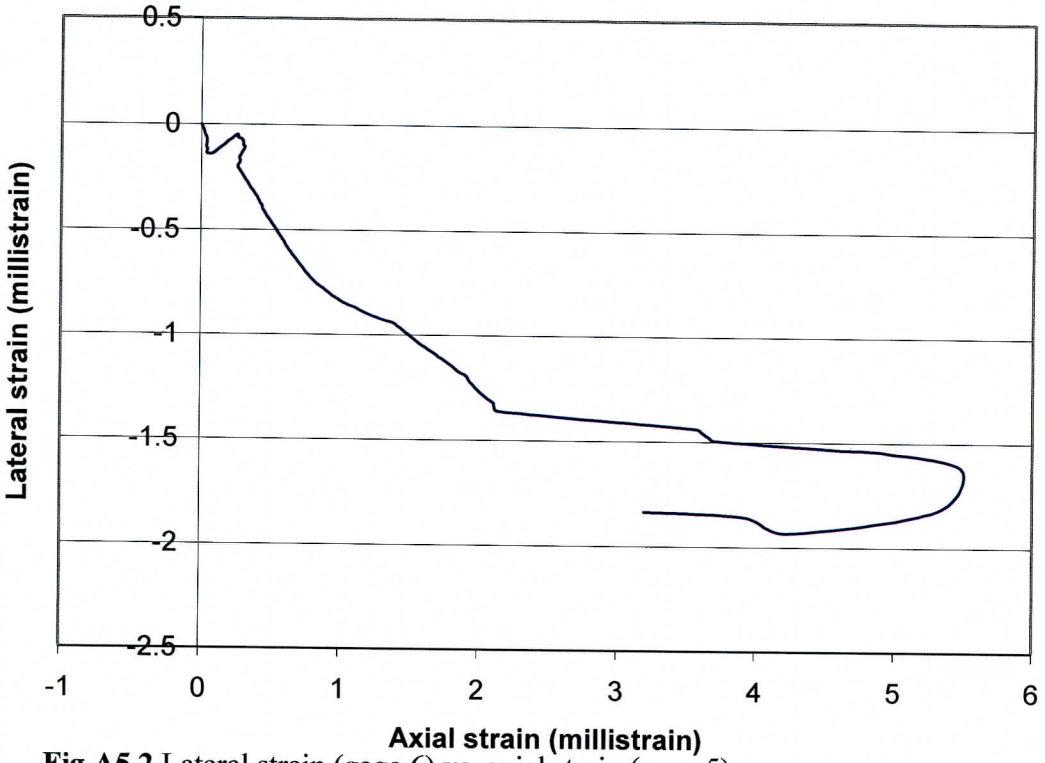

Fig A5.2 Lateral strain (gage 6) vs. axial strain (gage 5)

Results from strain gage measurements

Table A5.1 Young's modulus and normal stiffness

Section of rock	Sensor	Young's modulus (GPa)	Normal stiffness (GPa/mm)	Range (% of UCS)
3.2 mm rock with joint	Gage 1	35.18	10.99	19.7-77.7
	Gage 3	23.06	7.21	13.4-45.6
	Mean	**29.12**	**9.1**	
	Std. Deviation	**6.06**	**1.89**	
3.2 mm intact rock	Gage 5	37.20	11.63	20.4-51.9

Table A5.2 Poisson's ratio

Sensor	ν	Range (% of UCS)
Lateral Gage 6 vs. axial gage 5*	0.5	21.8-78.4

NB: *Short linear range over which the intact rock parameters have been determined shows that this specimen exhibits a non-linear behavior as compared to other tested specimens.

UCS = 61.7 MPa,
Moisture content after testing = 0 %
Bulk density = 2.28 g/cm^3
Joint normal stiffness is 26.35 GPa/mm and calculated joint shear stiffness is 8.78 GPa/mm.

Table A5.3 Stress history

Applied Load (kN)	Stress (MPa)	Duration
150	51.7	3 hours, 30 seconds
150 to 178.9 (failure)	51.7 to 61.7	1 minute, 30 seconds

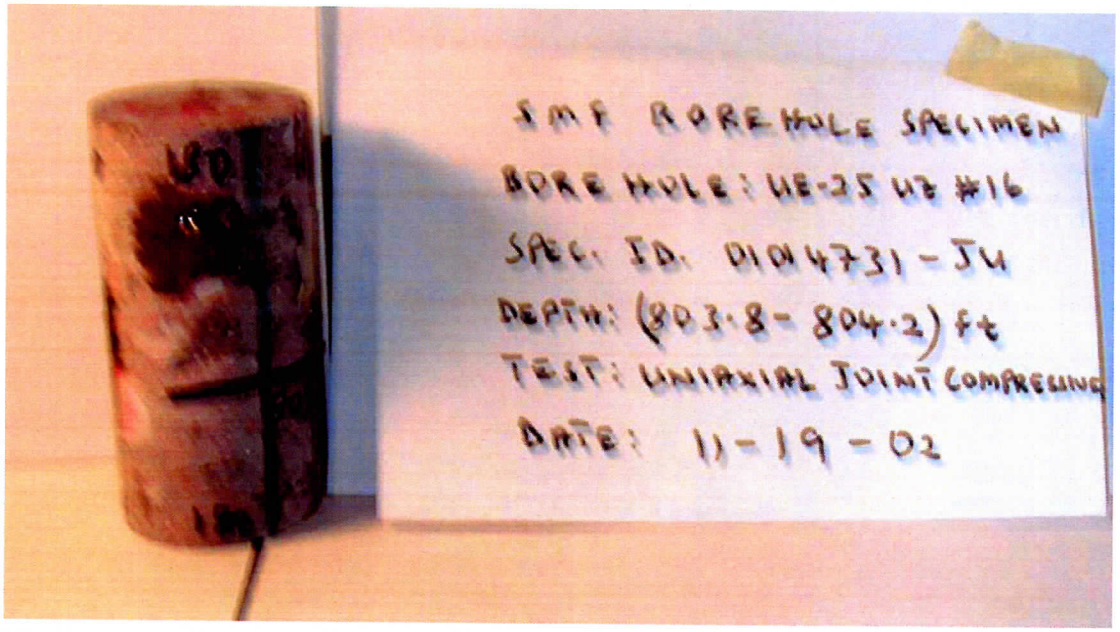

Fig. A5.3 Specimen 01014731-JU with an axial gage installed across the joint along the 180° axis.

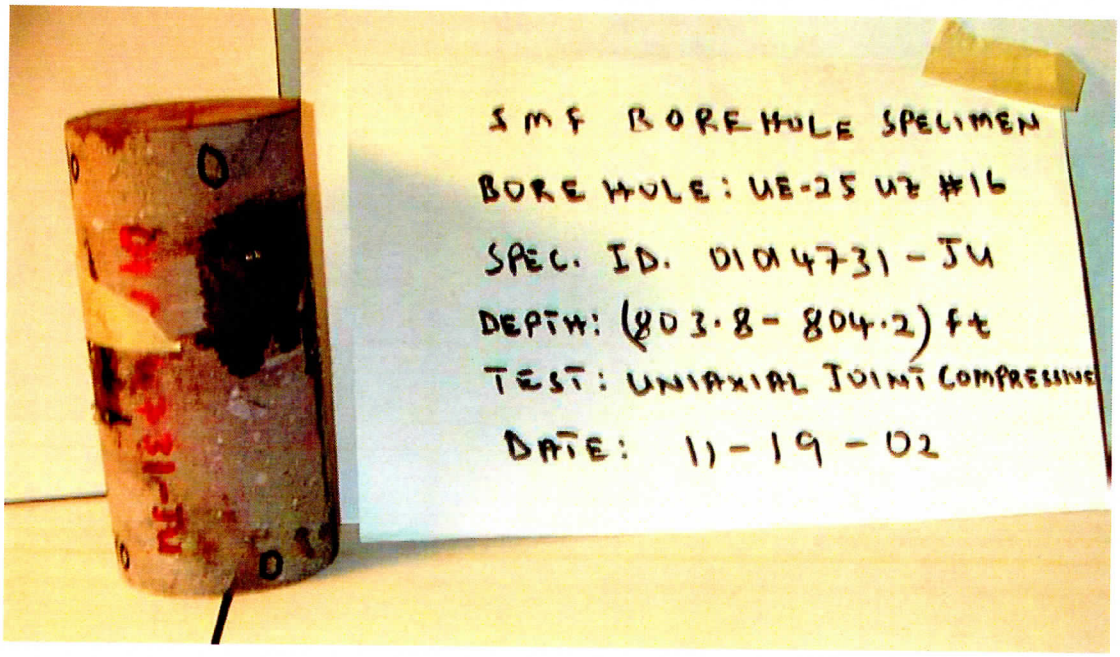

Fig A5.4 Specimen 01014731-JU with an axial gage installed across the joint along the 0° axis.

Appendix A6 – Specimen 01023570-1-JU

Instrumentation

Installation of the strain gages and the extensometers on specimen 01023570-1-JU (diameter of 60.73 mm and 126.24 mm long) is similar to Figure A1.1.Four axial gages (gages 1, 2, 3 and 4) installed across the joint (thickness of 0.3 mm) were at 0°, 90°, 180° and 270° axes respectively. Axial gage 5, horizontal gage 6, axial gage 7 and horizontal gage 8 were installed along the 0° and 180° axes respectively. Two axial extensometers 1 and 2 of lengths 50 mm and 50.8 mm respectively were installed across the joint along the 240° and 60° axes respectively.

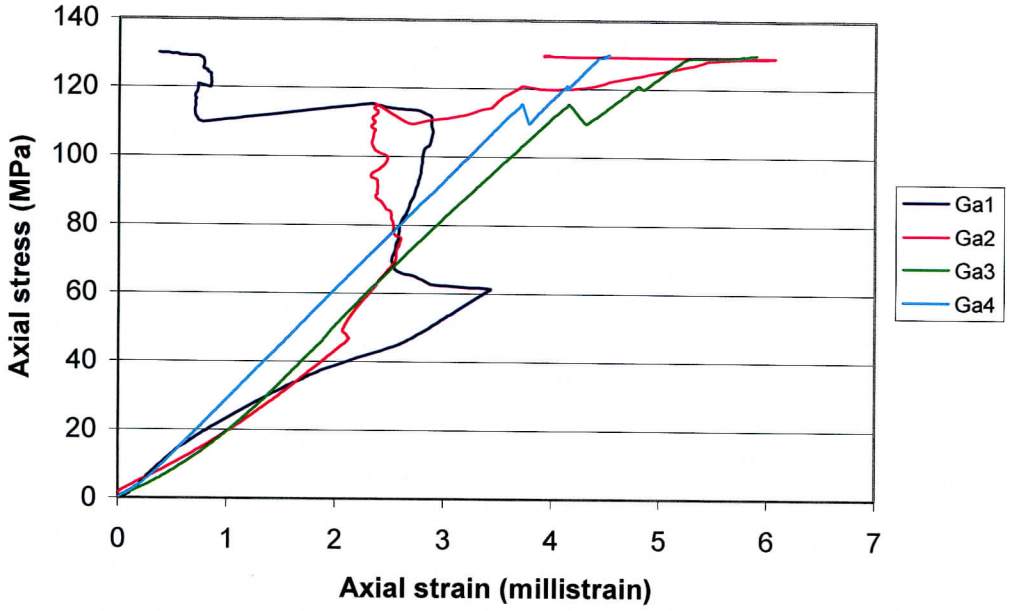

Fig. A6.1 Axial stress vs. axial strain for gages 1, 2, 3 and 4 installed across the joint

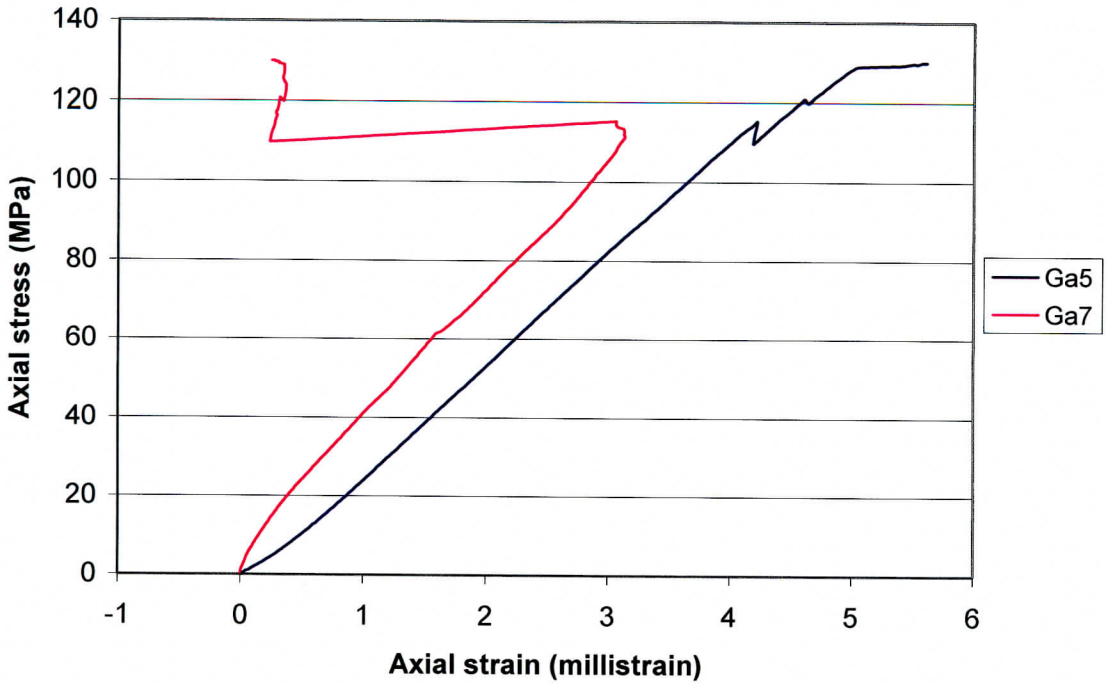

Fig. A6.2 Axial stress vs. axial strain for gages 5 and 7 installed on intact rock

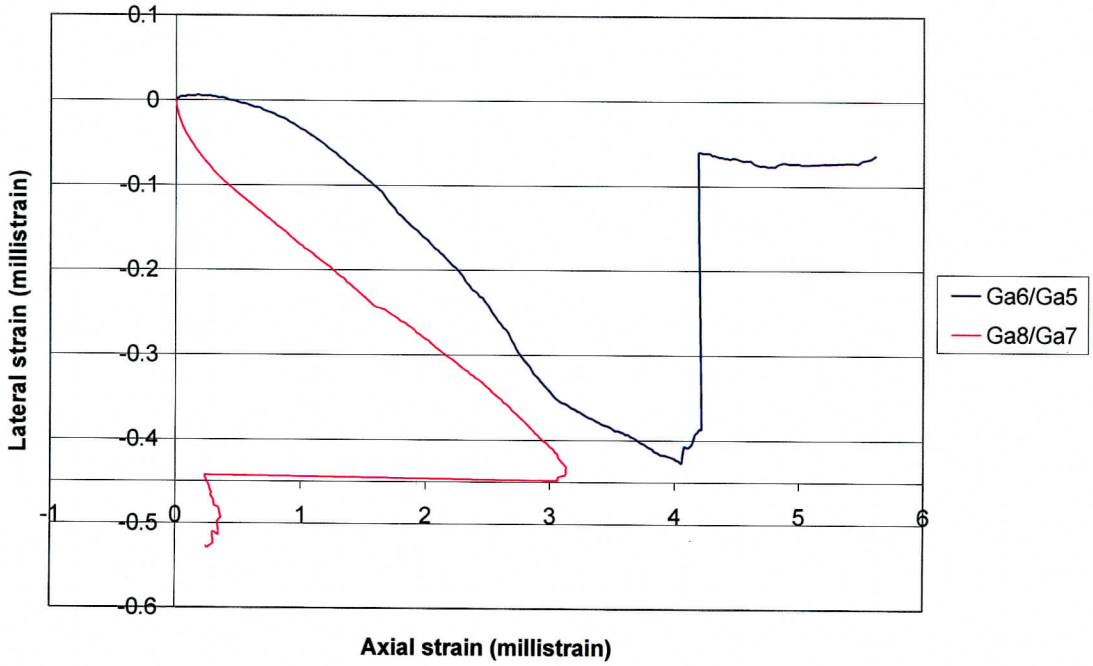

Fig A6.3 Lateral strain (gage 6) vs. axial strain (gage 5) and lateral strain (gage 8) vs. axial strain (gage 7).

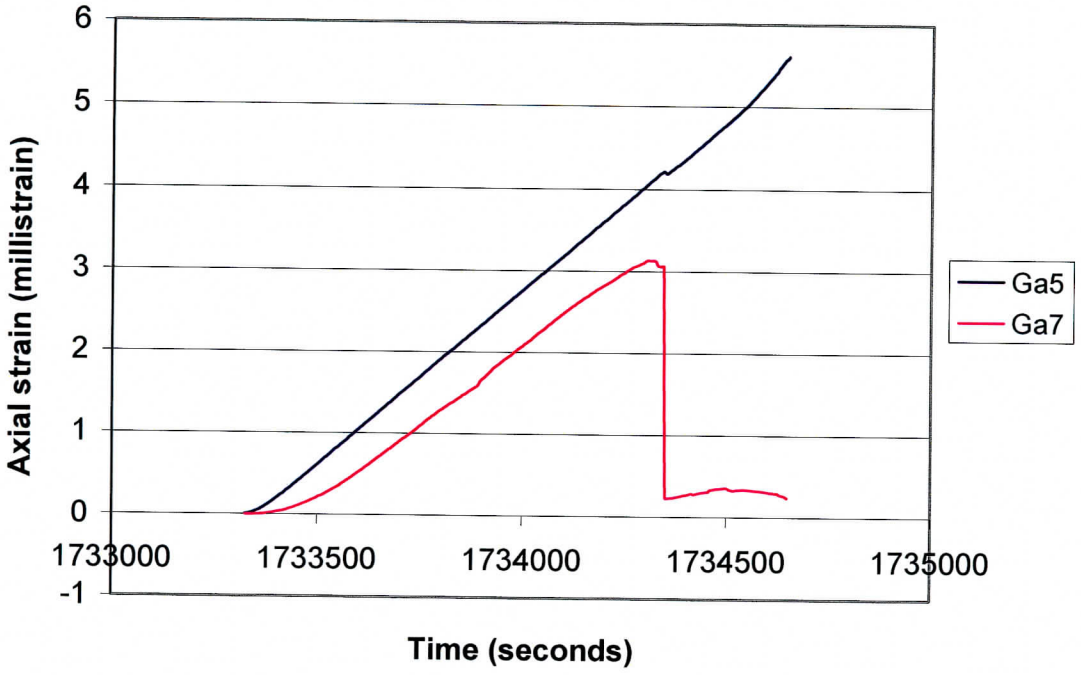

Fig. A6.4 Axial strain vs. time for gages 5 and 7 installed on intact rock

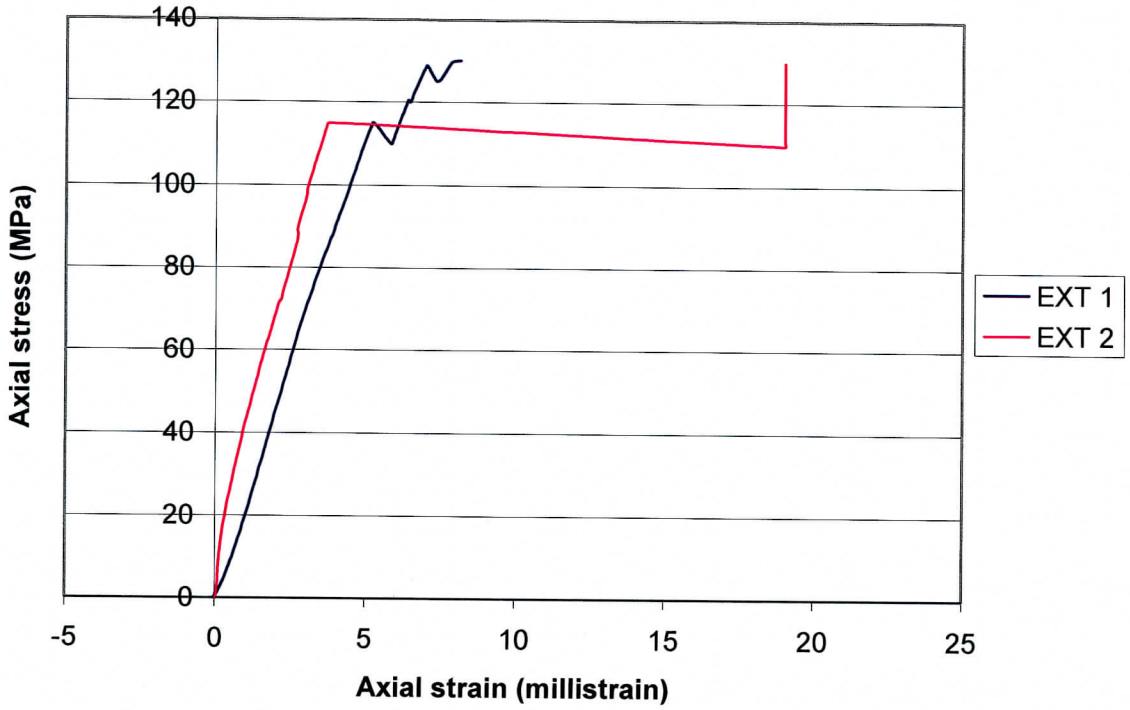

Fig. A6.5 Axial stress vs. axial strain for extensometers 1 and 2

Results from strain gage measurements

Table A6.1 Young's modulus and normal stiffness

Section of rock	Sensor	Young's modulus (GPa)	Normal stiffness (GPa/mm)	Range (% of UCS)
3.2 mm rock with joint	Gage 1*	14.70	4.59	14.6 - 34.3
	Gage 2	24.06	7.52	
	Gage 3	31.07	9.69	14.1 - 87.0
	Gage 4	31.85	9.95	
	Mean	**28.99**	**9.05**	
	Std. Deviation	**3.50**	**1.09**	
3.2 mm intact rock	Gage 5	28.72	8.98	14.1 - 87.0
	Gage 7	32.22	10.07	
	Mean	**30.5**	**9.53**	
	Std. Deviation	**1.75**	**0.55**	

NB: * It has been observed that values obtained from strain gage 1 are significantly too low after applying the outlier test (i.e. T-statistical test ASTM E 174 - 94) to the measurements at both 1% and 5% levels of significance. Therefore, they were not included in the analysis.

Table A6.2 Poisson's ratio

Sensor	ν	Range (% of UCS)
Lateral Gage 6 vs. axial gage 5	0.15	14.1 - 62.8
Lateral Gage 8 vs. axial gage 7	0.12	3.9 - 75.2
Mean	**0.14**	
Std. Deviation	**0.02**	

Table A6.3 Strain rate

Sensor	Strain rate/ per sec.	Range (% of UCS)
Gage 5	4.30×10^{-6}	6.8 - 79.7
Gage 7	3.80×10^{-6}	
Mean	$\mathbf{4.05 \times 10^{-6}}$	
Std. Deviation	$\mathbf{2.5 \times 10^{-5}}$	

UCS = 130.05 MPa,
Moisture content before testing = 1.03 %
Bulk density = 2.28 g/cm^3
Joint normal stiffness is 64.77 GPa/mm and calculated joint shear stiffness is 28.41 GPa/mm.

Table A6.4 Results from extensometer measurements

Sensor	Young's modulus (GPa)	Normal stiffness (GPa/mm)	Range (% of UCS)
Extensometer 1	22.82	0.45	20.2-84.3
Extensometer 2	27.68	0.55	
Mean	**25.25**	**0.5**	
Std. Deviation	**2.43**	**0.05**	

Joint normal stiffness is 2.77 GPa/mm and calculated joint shear stiffness is 1.21 GPa/mm.

Stiffness calculation from extensometer measurements

$$Stiffness\ (k_r) = \frac{EA}{L} = \frac{30.5 \times 0.0029}{0.0501} = 1.765\ MN/mm$$

Where L = 50.4 – 0.3 = 50.1 mm (average length of extensometer used = 50.4 mm)
Converting to GPa/mm gives 0.61 GPa/mm

k_{eq} = 0.5 GPa/mm (i.e. equivalent normal stiffness over 50.4 mm section of rock with the joint).

Joint normal stiffness k_n is given as:

$$k_n = \frac{k_{eq} \times k_r}{k_r - k_{eq}} \quad \text{.....(1)}$$

$$\text{From (1)} \Rightarrow k_n = \frac{0.5 \times 0.61}{0.61 - 0.5} = 2.77\ GPa/mm$$

Assuming the joint behaves as a linearly elastic isotropic material, then shear stiffness (k_s) is given as:

$$k_s = \frac{k_n}{2(1+\nu)} \quad \text{.....(2)}$$

Poisson's ratio (ν) = 0.14 (see Table A6.2)
From (2), shear stiffness = 1.21 GPa/mm

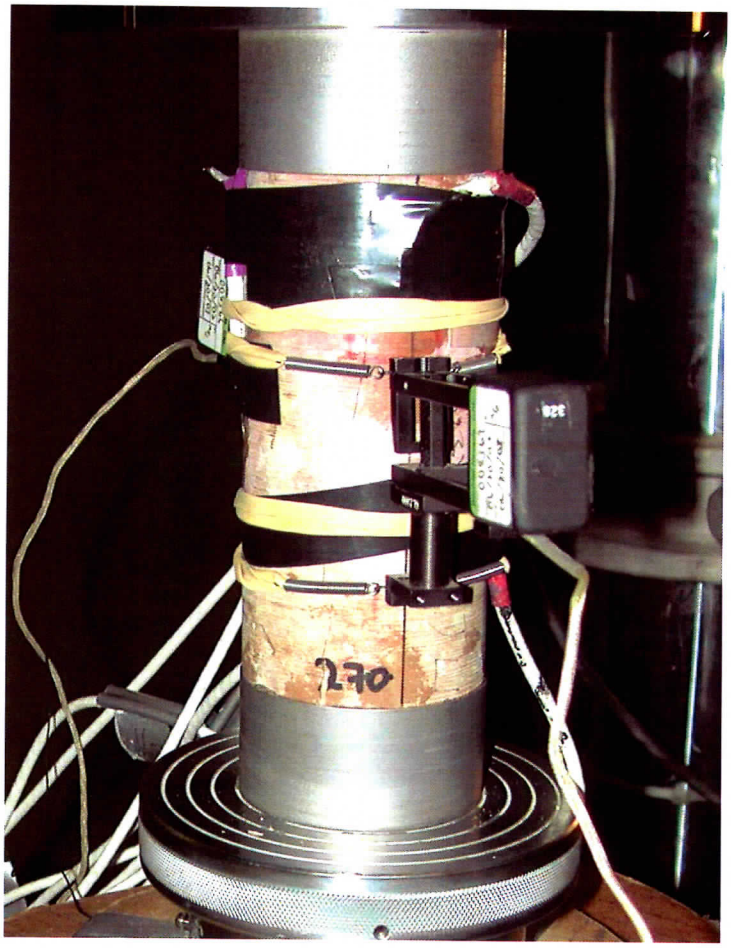

Fig A6.6 Specimen 01023570-1-JU with sensors installed before testing.

Fig. A6.7 Specimen 01023570-1-JU after testing

Appendix A7 – Specimen 01023575-3-JU

Instrumentation

Strain gage and extensometer installation on specimen 01023575-3-JU (diameter of 60.83 mm and 131.42 mm) is similar to Figure A1.1. Four axial gages (gages 1, 2, 3 and 4) installed across the joint (thickness of 0.3 mm) were at 0°, 90°, 180° and 270° axes respectively. Axial gage 5, horizontal gage 6, axial gage 7 and horizontal gage 8 were installed along the 0° and 180° axes respectively. The two axial extensometers 1 and 2 (each of length 25 mm) were installed along the 0° and 180° axes respectively.

Axial gage 4 debonded prior to testing therefore was not included in the analysis. At about 6 minutes into the test and at the stress level of 144.88 MPa, we unloaded for re-installing axial extensometer 1 which was not properly installed at the beginning. Unloading data from stress of 144.88 MPa have been analyzed in addition to the loading data for the strain gages. We were not able to obtain the entire unloading data for the extensometers. Their unloading data were analyzed from the stress of 45.13 MPa in addition to the loading data.

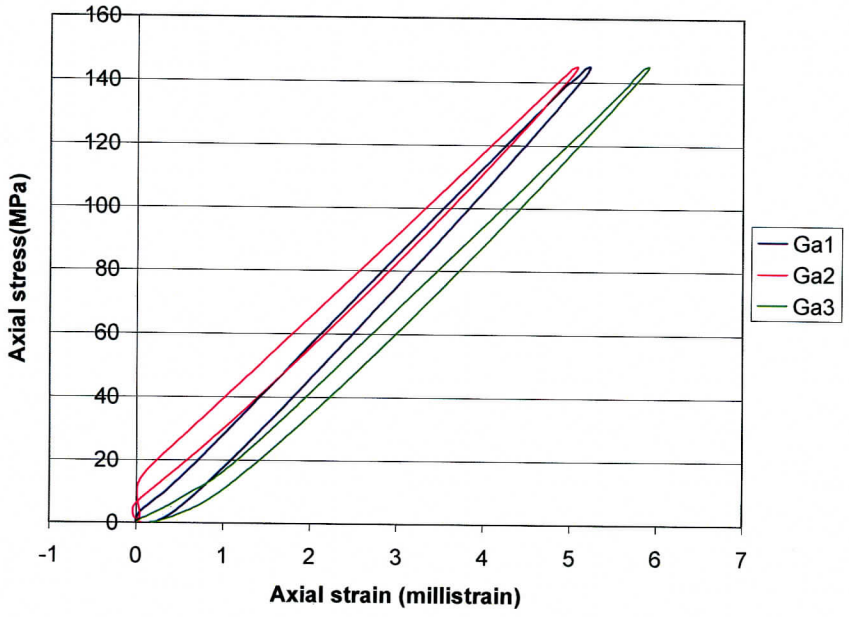

Fig. A7.1 Axial stress vs. axial strain first cycle loading and unloading curves for gages 1, 2 and 3 installed across the joint

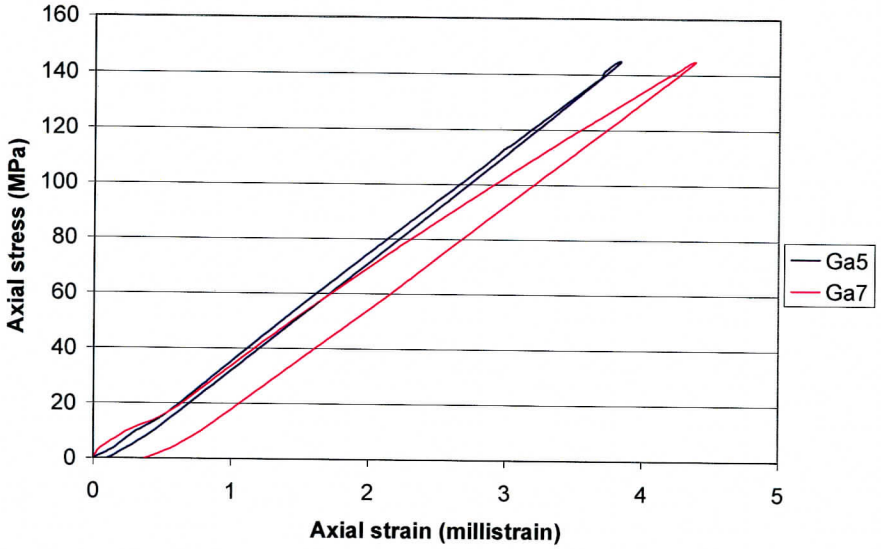

Fig.A7.2 Axial stress vs. axial strain for gages 5 and 7 installed on intact rock (first cycle loading and unloading curves)

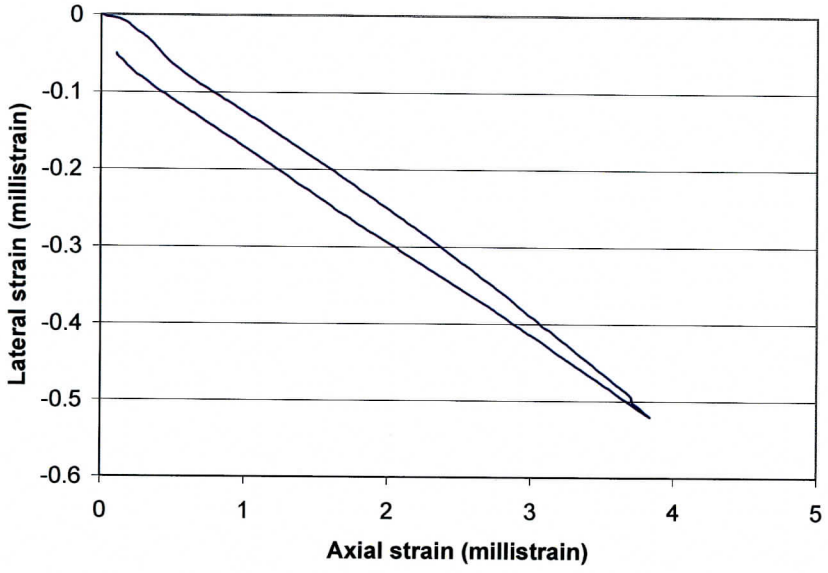

Fig. A7.3 Lateral strain (gage 6) vs. axial strain (gage 5) – first cycle loading and unloading curves.

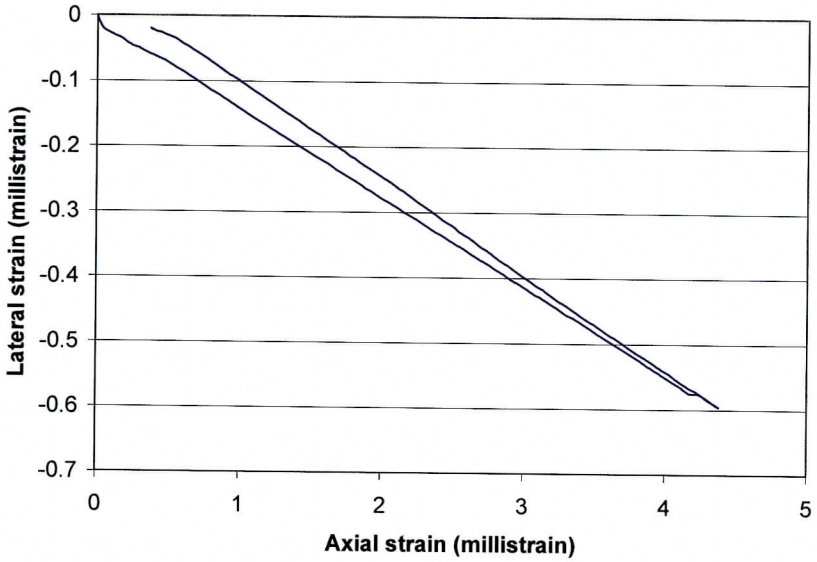

Fig. A7.4 Lateral strain (gage8) vs. axial strain (gage 7) – first cycle loading and unloading curves.

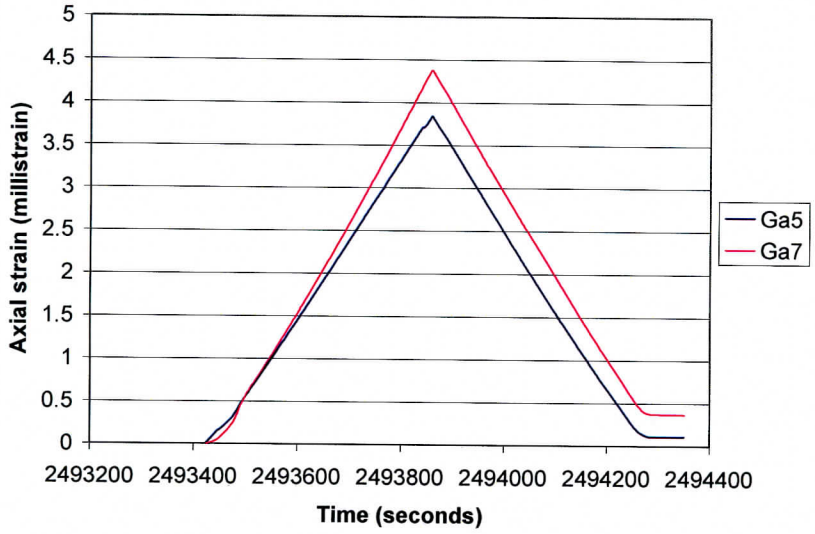

Fig A7.5 Axial strain vs. time for gages 5 and 7 (first cycle loading and unloading curves)

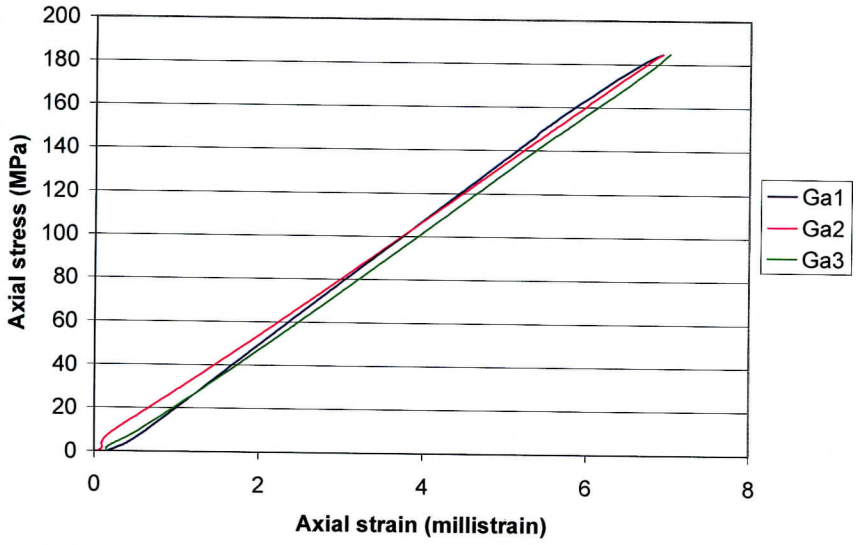

Fig. A7.6 Axial stress vs. axial strain for gages 1, 2, and 3 installed across the joint (second cycle loading curves)

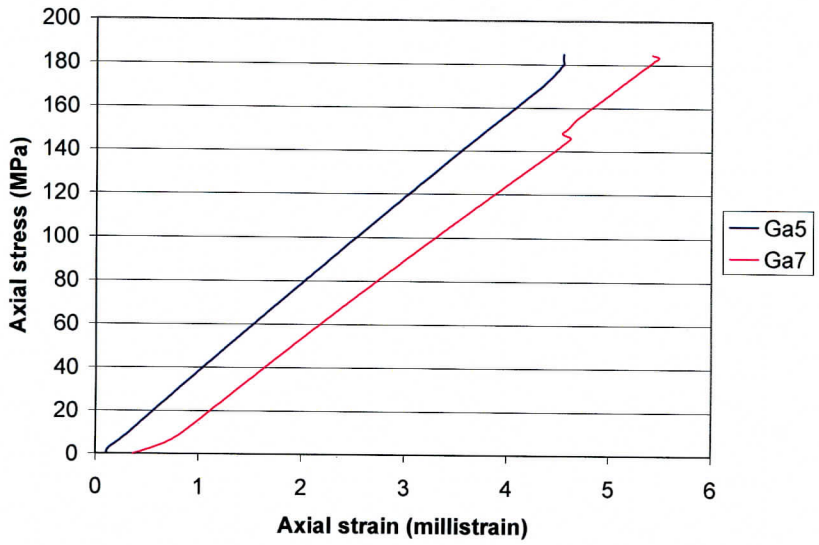

Fig A7.7 Axial stress vs. axial strain for gages 5 and 7 installed on intact rock (second cycle loading curves).

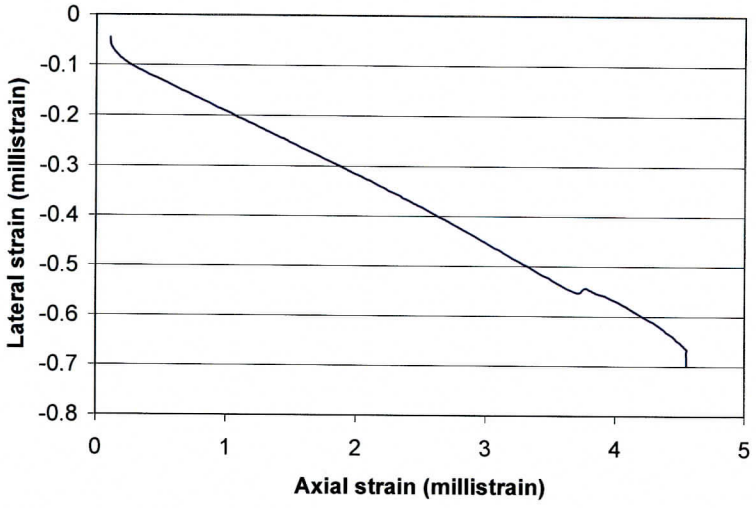

Fig. A7.8 Lateral strain (gage 6) vs. axial strain (gage 5) – second cycle loading curve.

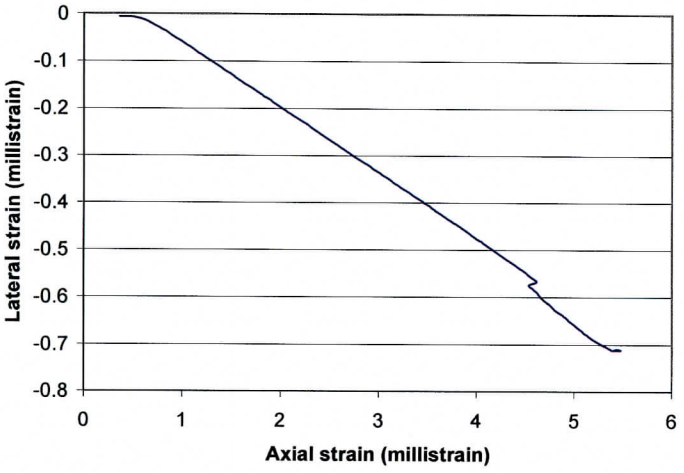

Fig. A7.9 Lateral strain (gage 8) vs. axial strain (gage 7) – second cycle loading curve.

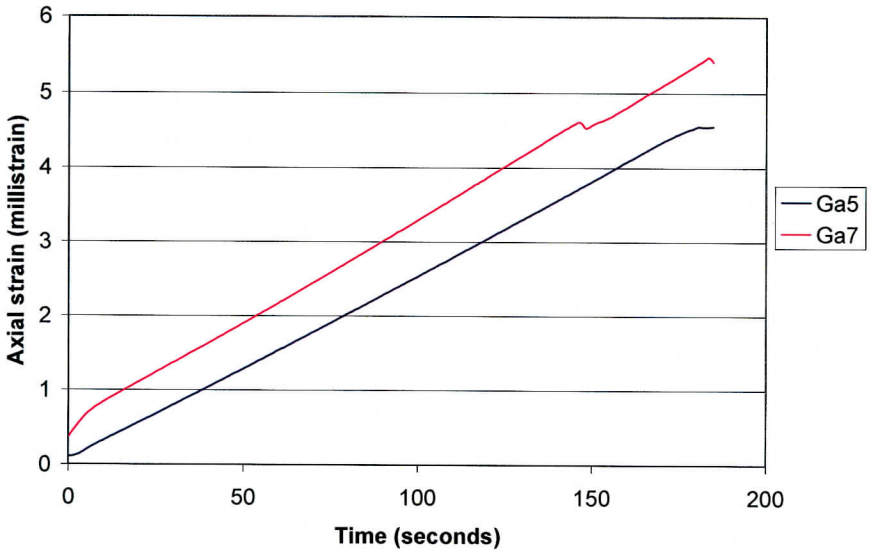

Fig A7.10 Axial strain vs. time for gages 5 and 7 (second cycle loading curves)

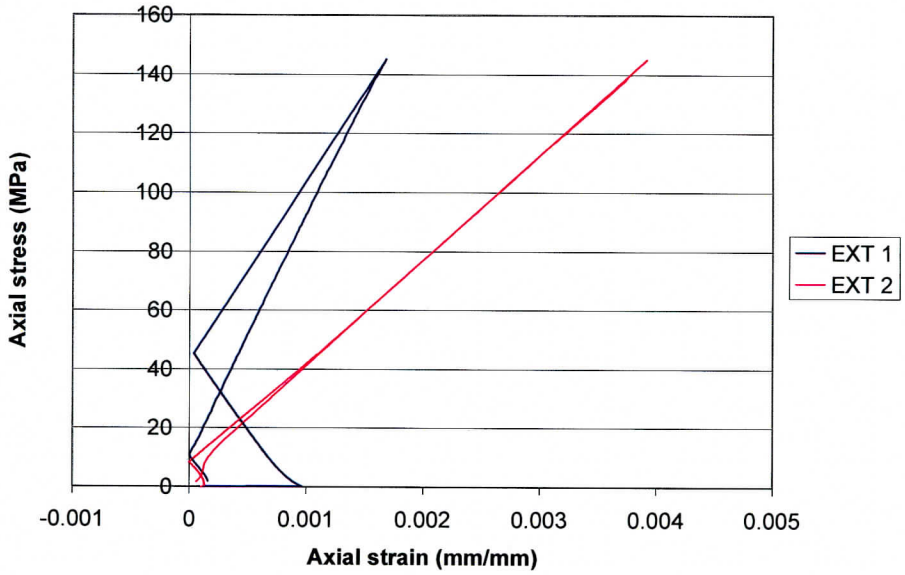

Fig. A7.11 Axial stress vs. axial strain for extensometers 1 and 2 installed across the joint (first cycle loading and unloading curves)

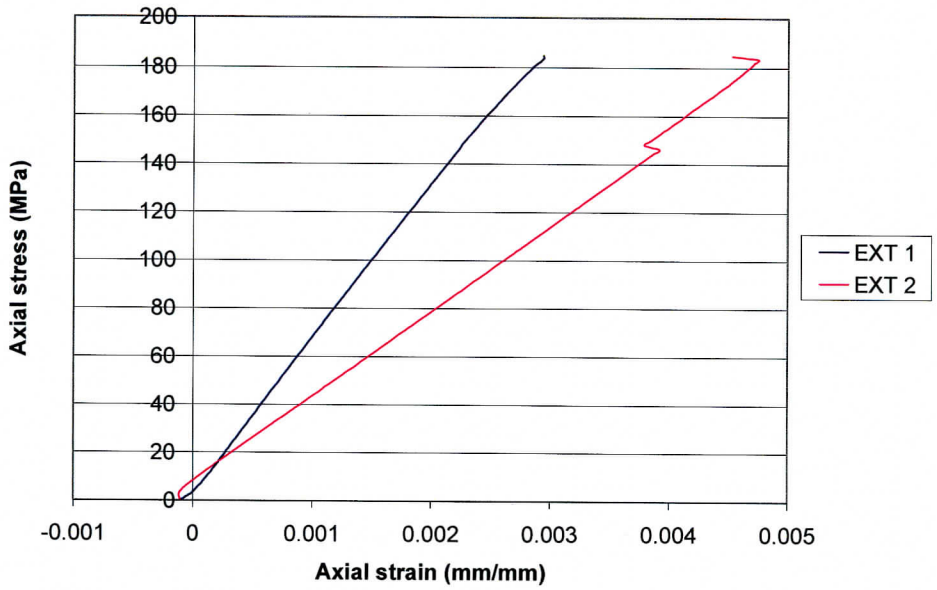

Fig A7.12 Axial stress vs. axial strain for extensometers 1 and 2 (second cycle loading curves)

Results from strain gage measurement (first loading and unloading cycles)

Table A7.1 Young's modulus and normal stiffness of the gages installed across the joint

Strain gages for the 3.2 mm rock section with the joint	Young's modulus (GPa)	Normal stiffness (GPa/mm)	Range (% of σ_{max})
Gage 1*	28.20 (29.88)	8.81 (9.34)	(14.3 - 92.2) for loading.
Gage 2	26.07 (27.55)	8.15 (8.61)	
Gage 3	26.55 (27.73)	8.30 (8.67)	(13.8 – 97.2) for unloading
Mean	**26.31** **(27.64)**	**8.23** **(8.64)**	
Standard deviation	**0.24** **(0.09)**	**0.08** **(0.03)**	

NB: * Loading and unloading values obtained from strain gage 1 are significantly too high when applying the outlier test (i.e. T-statistical test according to ASTM E 178 - 94) to the measurements at both the 1% and 5% levels of significance. Therefore, they were not included in the mean value calculation.

Table A7.2 Young's modulus and normal stiffness of the strain gages installed on intact rock

Strain gages for the 3.2 mm intact rock section	Young's modulus (GPa)	Normal stiffness (GPa/mm)	Range (% of σ_{max})
Gage 5	38.76 (39.61)	12.11 (12.38)	(14.3 - 97.2) for loading.
Gage 7	33.63 (37.63)	10.51 (11.76)	(13.8 – 97.2) for unloading
Mean	**36.20 (38.62)**	**11.31 (12.07)**	
Standard deviation	**2.57 (0.99)**	**0.8 (0.31)**	

Table A7.3 Poisson's ratio

Strain gages installed on intact rock	Loading	Unloading	Range (% of σ_{max})
Lateral gage 6 vs. axial gage 5	0.13	0.12	Entire data for loading and unloading
Lateral gage 8 vs. axial gage 7	0.13	0.15	
Mean	**0.13**	**0.14**	
Standard deviation	**0**	**0.02**	

Table A7.4 Strain rate

Strain gage	Strain rate/ per sec.	Range (% of σ_{max})
Gage 5	9.1×10^{-6} (9.3×10^{-6})	Entire data for loading (10.6 – 100) for unloading
Gage 7	10.4×10^{-6} (9.8×10^{-6})	
Mean	**9.75×10^{-6} (9.55×10^{-6})**	
Std. Deviation	**6.5×10^{-5} (2.5×10^{-5})**	

NB: Unloading results are in parenthesis

σ_{max} is the maximum stress (144.88 MPa) during the first loading cycle

Results from strain gage measurement (second loading cycle)

Table A7.5 Young's modulus and normal stiffness of the gages installed across the joint

Strain gages for the 3.2 mm rock section with the joint	Young's modulus (GPa)	Normal stiffness (GPa/mm)	Range (% of UCS)
Gage 1	28.56	8.92	0.7 – 98.5
Gage 2	26.46	8.27	
Gage 3	27.00	8.44	
Mean	**27.34**	**8.54**	
Standard deviation	**0.89**	**0.28**	

Table A7.6 Young's modulus and normal stiffness of the gages installed on intact rock

Strain gages for the 3.2 mm intact rock section	Young's modulus (GPa)	Normal stiffness (GPa/mm)	Range (% of UCS)
Gage 5	39.85	12.45	0.7 – 98.5
Gage 7	36.83	11.51	
Mean	**38.34**	**11.98**	
Standard deviation	**1.51**	**0.47**	

Table A7.7 Poisson's ratio

Strain gages installed on intact rock	ν	Range (% of UCS)
Lateral gage 6 vs. axial gage 5	0.13	Entire data
Lateral gage 8 vs. axial gage 7	0.14	
Mean	**0.14**	
Standard deviation	**0.005**	

Table A7.8 Strain rate

Strain gage	Strain rate/ per second	Range (% of UCS)
Gage 5	24.9×10^{-6}	Entire data
Gage 7	27.3×10^{-6}	
Mean	$\mathbf{26.1 \times 10^{-6}}$	
Std. Deviation	$\mathbf{1.2 \times 10^{-6}}$	

Results from extensometer measurements (first loading and unloading cycles)

Table A7.9 Young's modulus and normal stiffness

Sensors installed over the 25 mm rock section with the joint	Young's modulus (GPa)	Normal stiffness for (GPa/mm)	Range (% of σ_{max})
Extensometer1*	81.0 (55.57)	3.24 (2.22)	(8.3 – 98.8) for loading (24.2 – 99.8) for unloading
Extensometer 2	35.6 (33.44)	1.42 (1.34)	

NB: Unloading results are in parenthesis

Results from extensometer measurements (second loading cycle)

Table A7.10 Young's modulus and normal stiffness

Sensors installed over the 25 mm rock section with the joint	Young's modulus (GPa)	Normal stiffness for (GPa/mm)	Range (% of UCS)
Extensometer 1*	62.87	2.51	14.9 – 97.7
Extensometer 2	36.83	1.47	

*NB: Due to extensometer installation problems stated earlier, results from extensometer 1 were not used in the calculations.

Summary of joint stiffness results

Table A7.11 Joint stiffness results from strain gage measurements

Cycle	k_n (GPa/mm)	k_s (GPa/mm)
First loading	24.13	10.68
First unloading	24.59	10.79
Second loading to failure	24.12	10.57

Table A7.12 Joint stiffness from extensometer measurements

Cycle	k_n (GPa/mm)	k_s (GPa/mm)
First loading	41.75	18.47
First unloading	9.5	4.17
Second loading to failure	25.48	11.18

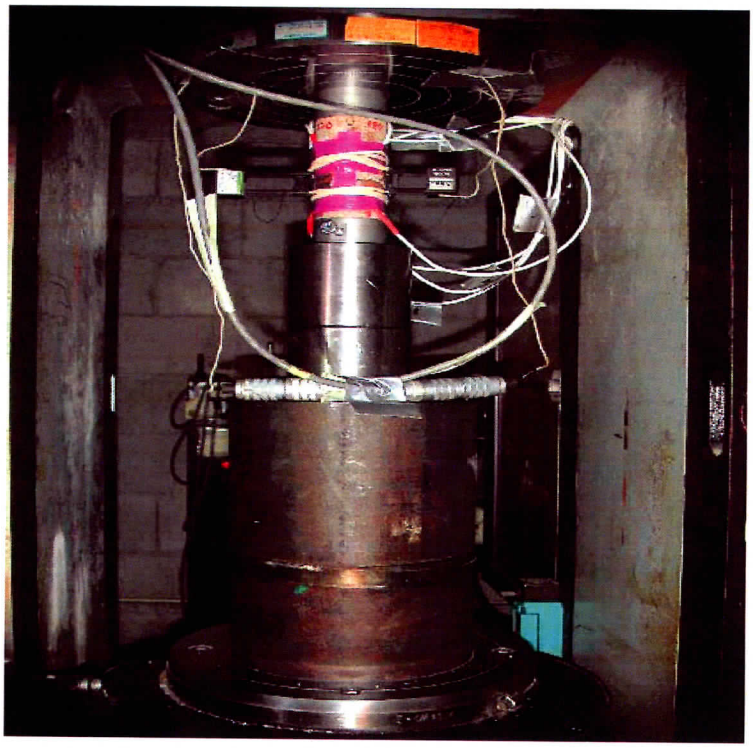

Fig.A7.13 Specimen 01023575-3-JU with sensors installed before testing

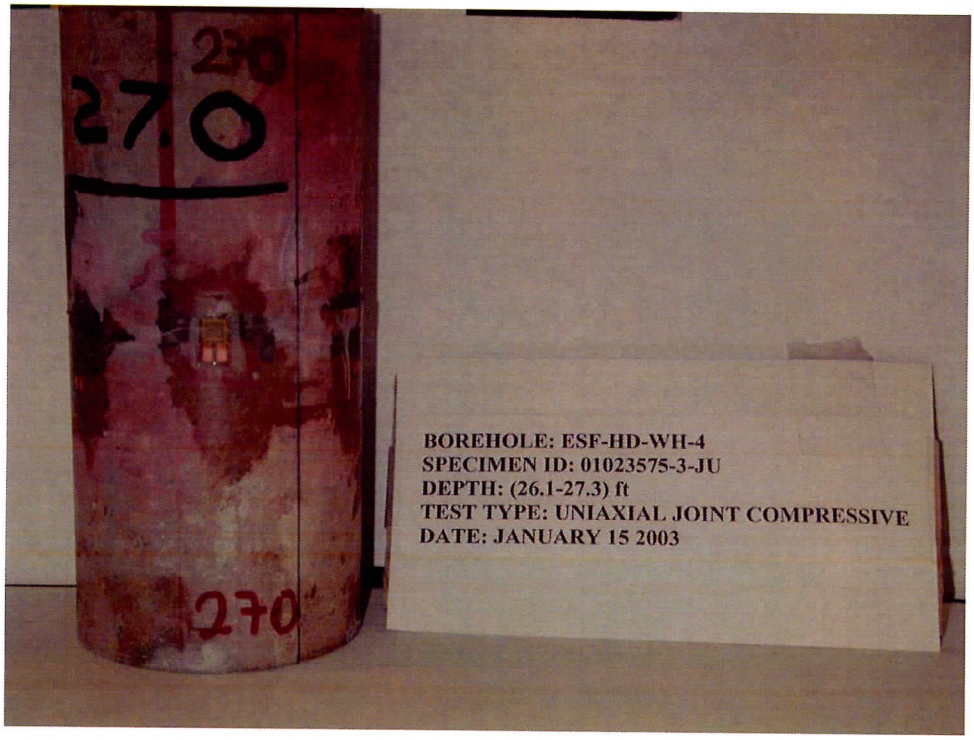

Fig A7.14 Specimen 01023575-3-JU with an axial strain gage along the 270° axis

Appendix A8 - Specimen 01023682-1-JU

Instrumentation

Installation of strain gages and extensometers on specimen 01023682-1-JU (diameter of 60.91 mm and 161.42 mm long) is similar to Figure A1.1. Four axial gages (gages 1, 2, 3 and 4) installed across the joint (thickness of 0.2 mm) were at 0°, 90°, 180° and 270° axes respectively. Axial gage 5, horizontal gage 6, axial gage 7 and horizontal gage 8 were installed along the 0° and 180° axes respectively. The two axial extensometers 1 and 2 of lengths 50 mm and 50.8 mm respectively were installed along the 0° and 180° axes respectively.

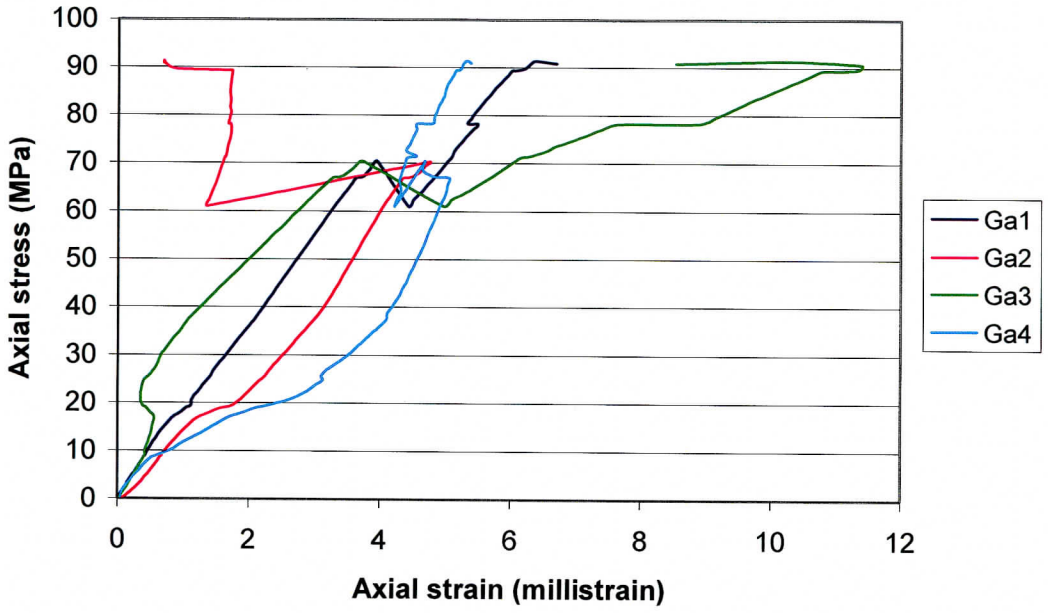

Fig A8.1 Axial stress vs. axial strain for gages 1, 2, 3 and 4 installed across the joint

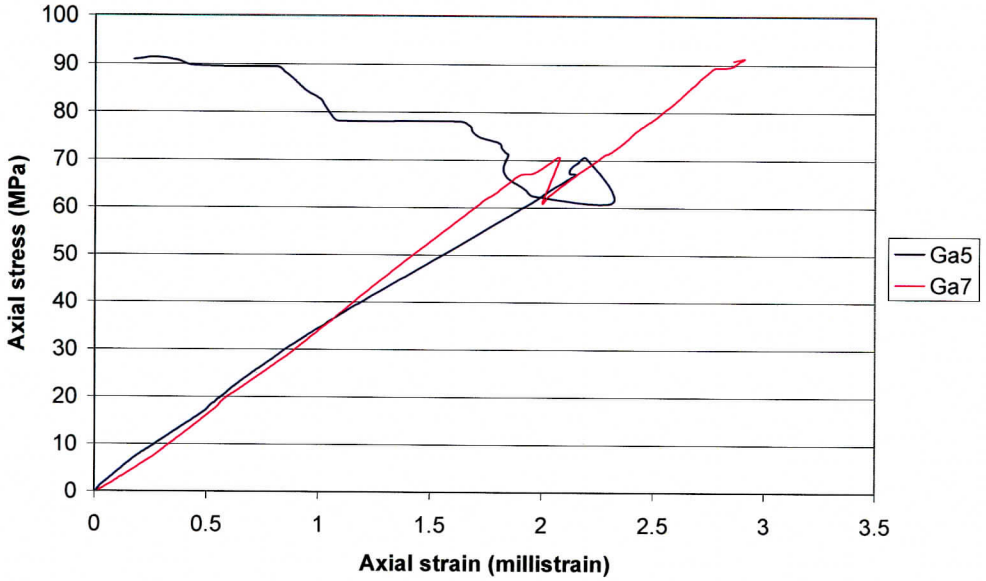

Fig. A8.2 Axial stress vs. axial strain for gages 5 and 7 installed on intact rock

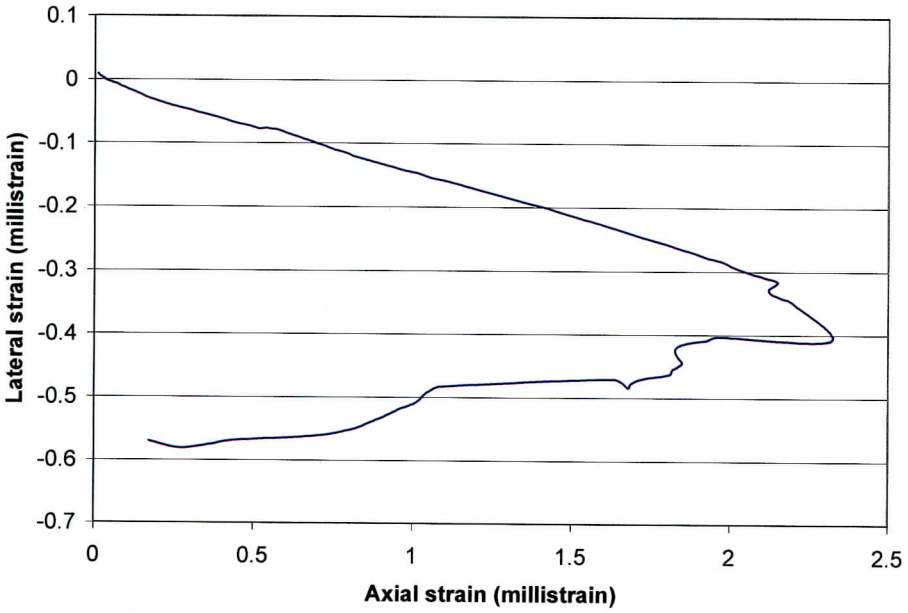

Fig A8.3 Lateral strain (gage 6) vs. axial strain (gage 5)

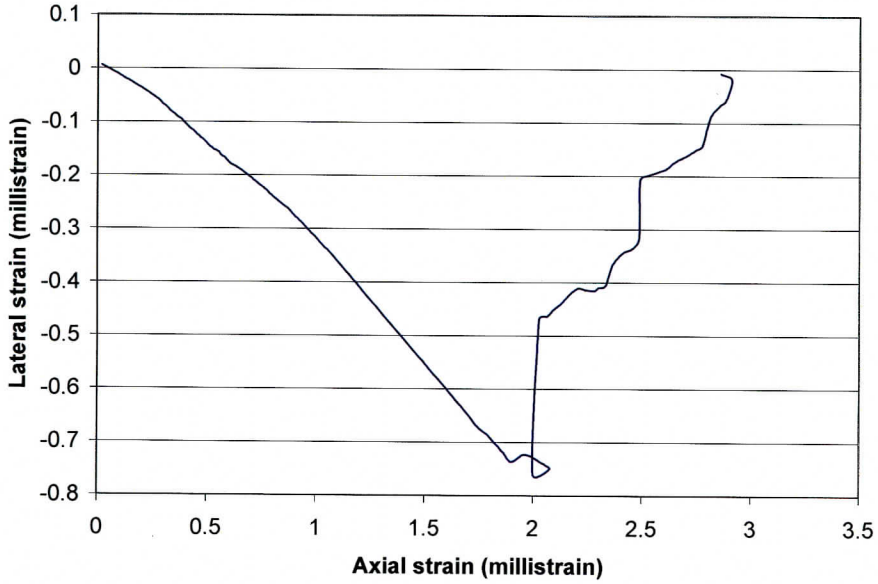

Fig A8.4 Lateral strain (gage 8) vs. axial strain (gage 7)

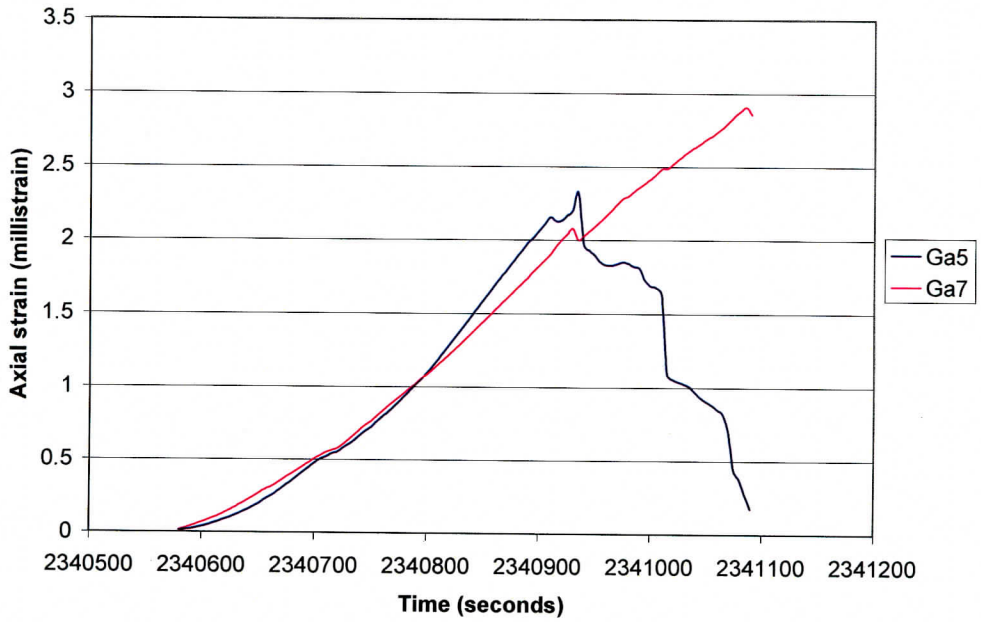

Fig A8.5 Axial strain vs. time for gages 5 and 7

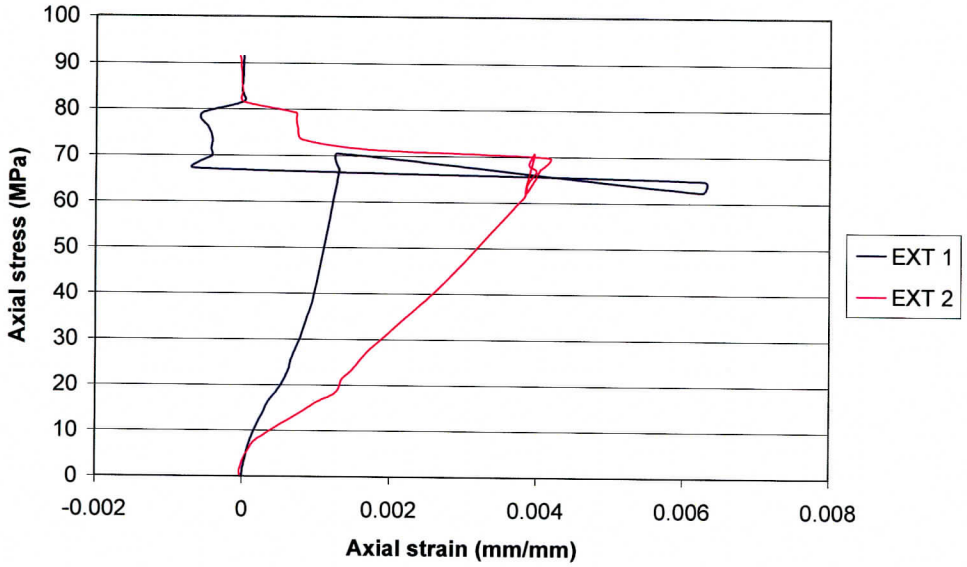

Fig A8.6 Axial stress vs. axial strain for extensometers 1 and 2 installed across the joint

Results from the strain gage measurements

Table A8.1 Young's modulus and normal stiffness

Section of rock	Strain gage	Young's modulus (GPa)	Normal stiffness (GPa/mm)	Range (% of UCS)
3.2 mm rock section with the joint	Gage 1	18.58	5.81	22.5 - 73.7
	Gage 2	19.05	5.95	
	Gage 3*	14.99	4.68	
	Gage 4	18.85	5.89	
	Mean	**18.83**	**5.88**	
	Std. Deviation	**1.67**	**0.52**	
3.2 mm intact rock	Gage 5	30.47	9.52	10.1 - 66.4
	Gage 7	36.56	11.43	
	Mean	**33.52**	**10.48**	
	Std. Deviation	**3.05**	**0.96**	

NB: * Values obtained from strain gage 3 are significantly too low when applying the outlier test (i.e. T-statistical test according to ASTM E 178 - 94) to the measurements at both the 1% and 5% levels of significance. Therefore, they were not included in the mean value calculation.

Table A8.2 Poisson's ratio

Strain gage	ν	Range (% of UCS)
Lateral Gage 6 vs. axial gage 5	0.14	2.2 – 72.2
Lateral Gage 8 vs. axial gage 7	0.42	13.0 - 70.8
Mean	**0.28**	
Std. Deviation	**0.14**	

Table A8.3 Strain rate

Strain gage	Strain rate/per second	Range (% of UCS)
Gage 5	8.2×10^{-6}	13.0 - 70.8
Gage 7	6.7×10^{-6}	
Mean	**7.45×10^{-6}**	
Std. Deviation	**7.5×10^{-5}**	

UCS = 90.83 MPa,
Moisture content before testing = 1.14 %
Bulk density = 2.27 g/cm^3
Joint normal stiffness is 12.42 GPa/mm and calculated joint shear stiffness is 4.85 GPa/mm.

Results from the extensometer measurements

Table A8.4 Young's modulus and normal stiffness

Extensometer	Young's Modulus (GPa)	Normal Stiffness (GPa/mm)	Range (% of UCS)
Extensometer 1	47.91	0.96	13.8-67.4
Extensometer 2	15.65	0.31	
Mean	**31.78**	**0.64**	
Std. Deviation	**16.13**	**0.33**	

Joint normal stiffness is 14.29 GPa/mm and calculated joint shear stiffness is 5.58 GPa/mm.

Fig A8.7 Specimen 01023682-1-JU in a four post 220kip MTS machine in LME 112 before testing.

Fig A8.8 Post-failure bottom view of specimen 01023682-1-JU

Appendix A9 - Specimen 01023663-3-JU

Instrumentation

Installation of strain gages on specimen 01023663-3-JU (diameter of 60.99 mm and 105.54 mm long) is similar to Figure A1.1. Four axial gages (gages 1, 2, 3 and 4) installed across the joint (thickness of 0.3 mm) were at 0°, 90°, 180° and 270° axes respectively. Axial gage 5, horizontal gage 6, axial gage 7 and horizontal gage 8 were installed along the 0° and 180° axes respectively. Axial gage 1 and lateral gage 8 debonded prior to testing and were not included in the analysis.

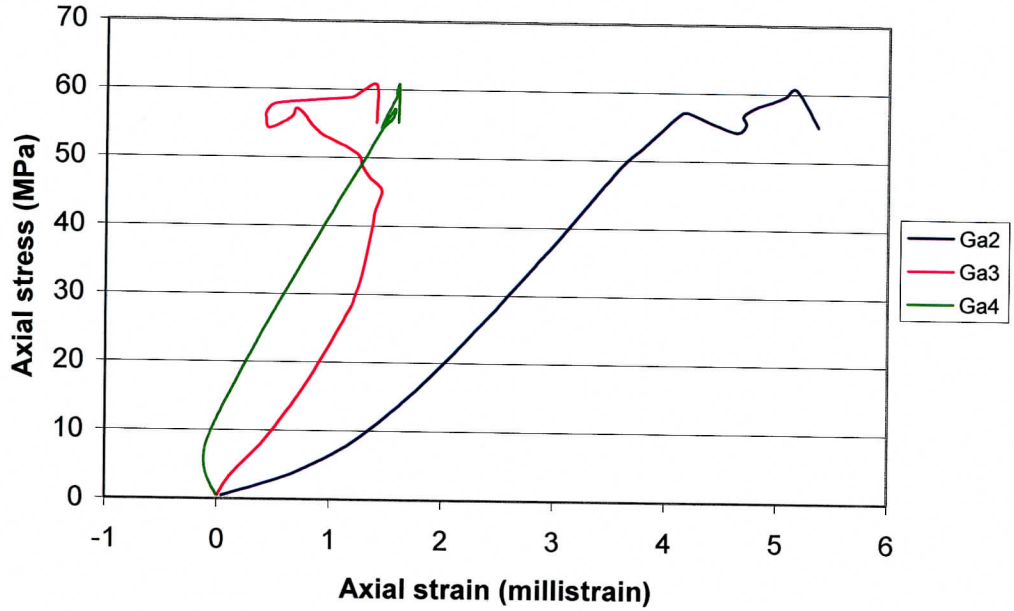

Fig A9.1 Axial stress vs. axial strain for gages 2, 3 and 4 installed across the joint

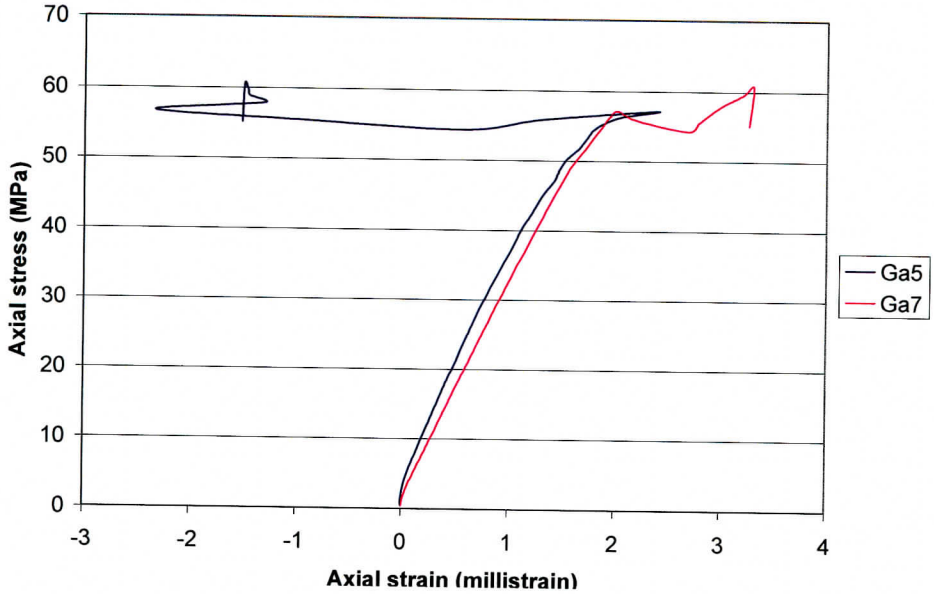

Fig. A9.2 Axial stress vs. axial strain for gages 5 and 7 installed on intact rock

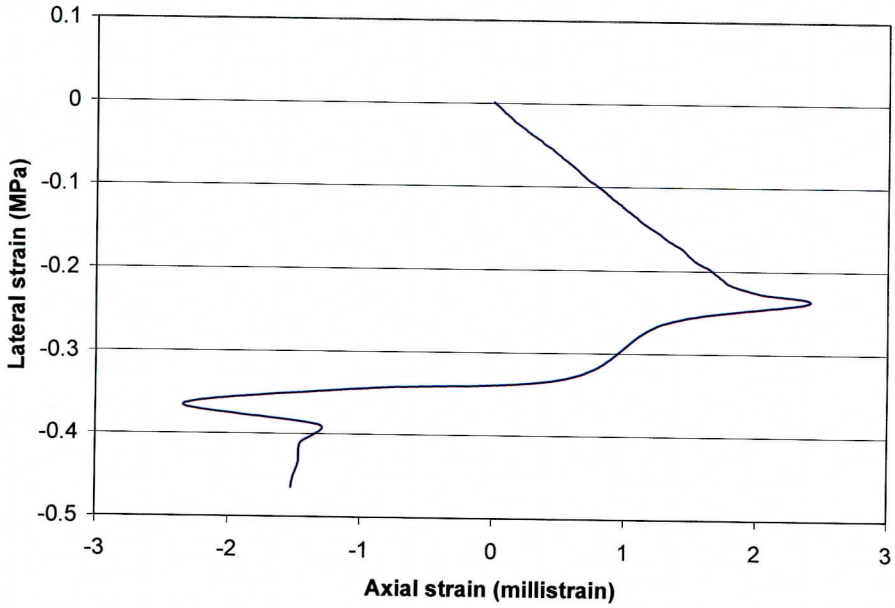

Fig A9.3 Lateral strain (gage 6) vs. axial strain (gage 5)

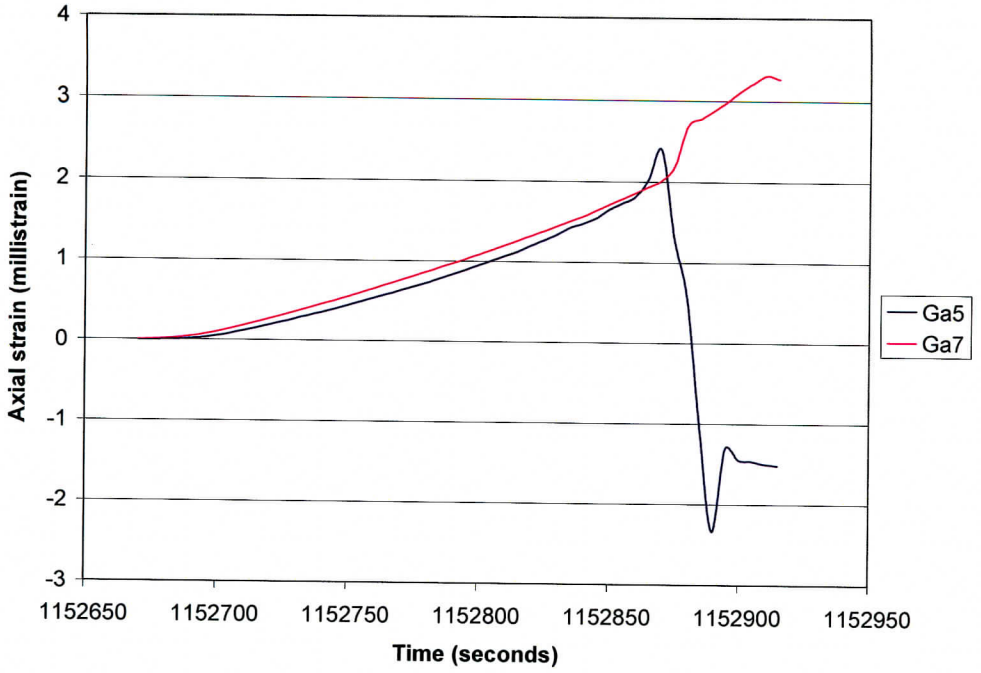

Fig A9.4 Axial strain vs. time for gages 5 and 7

Results from strain gage measurements

Table A9.1 Young's modulus and normal stiffness

Section of rock	Sensor	Young's modulus (GPa)	Normal stiffness (GPa/mm)	Range (% of UCS)
3.2 mm intact rock with the joint	Gage 2*	17.01	5.32	16.4-66.5
	Gage 3	32.10	10.03	
	Gage 4	29.89	9.34	
	Mean	**26.33**	**8.23**	
	Std. Deviation	**6.65**	**2.08**	
3.2 mm intact rock	Gage 5	29.36	9.17	16.4-85.2
	Gage 7	29.48	9.21	
	Mean	**29.42**	**9.19**	
	Std. Deviation	**0.06**	**0.02**	

NB: * Results obtained for gage 2 seem too low. This might be due to improper installation, or to being installed on a locally more strained location.

Table A9.2 Poisson's ratio

Sensor	ν	Range (% of UCS)
Lateral Gage 6 vs. axial gage 5	0.12	4.7 – 82.9

Table A9.3 Strain rate

Sensor	Strain rate	Range (% of UCS)
Gage 5	11.1 x 10^{-6} /sec	12.0 – 90.2
Gage 7	11.1 x 10^{-6} /sec	
Mean	**11.1 x 10^{-6}/sec**	
Std. Deviation	**0**	

UCS = 60.7 MPa,
Moisture content before testing = 0.85 %
Bulk density = 2.27 g/cm^3
Joint normal stiffness is 43.69 GPa/mm and calculated joint shear stiffness is 19.5 GPa/mm.

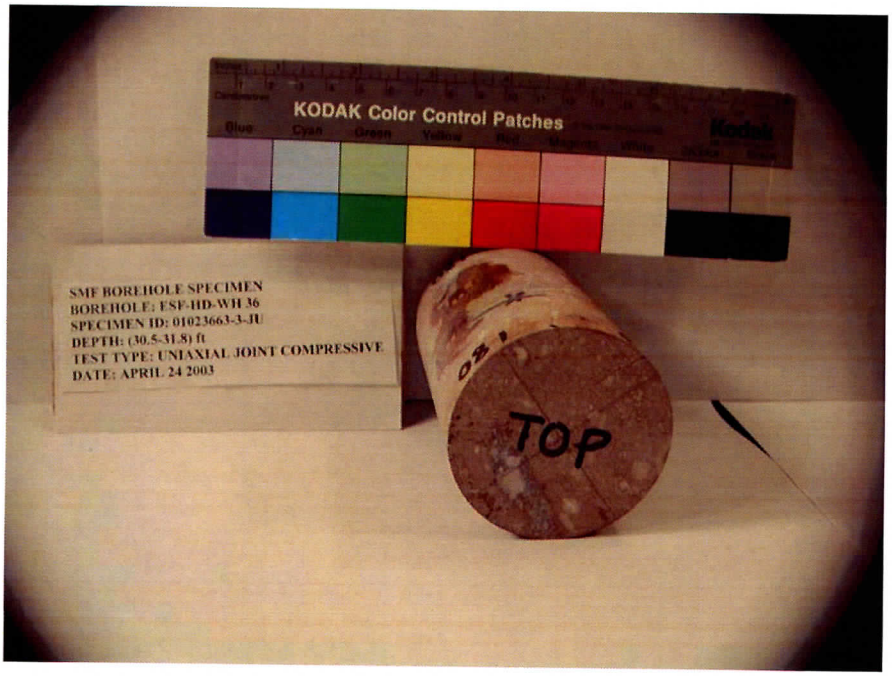

Fig A9.5 Pre-failure top view of specimen 01023663-3-JU

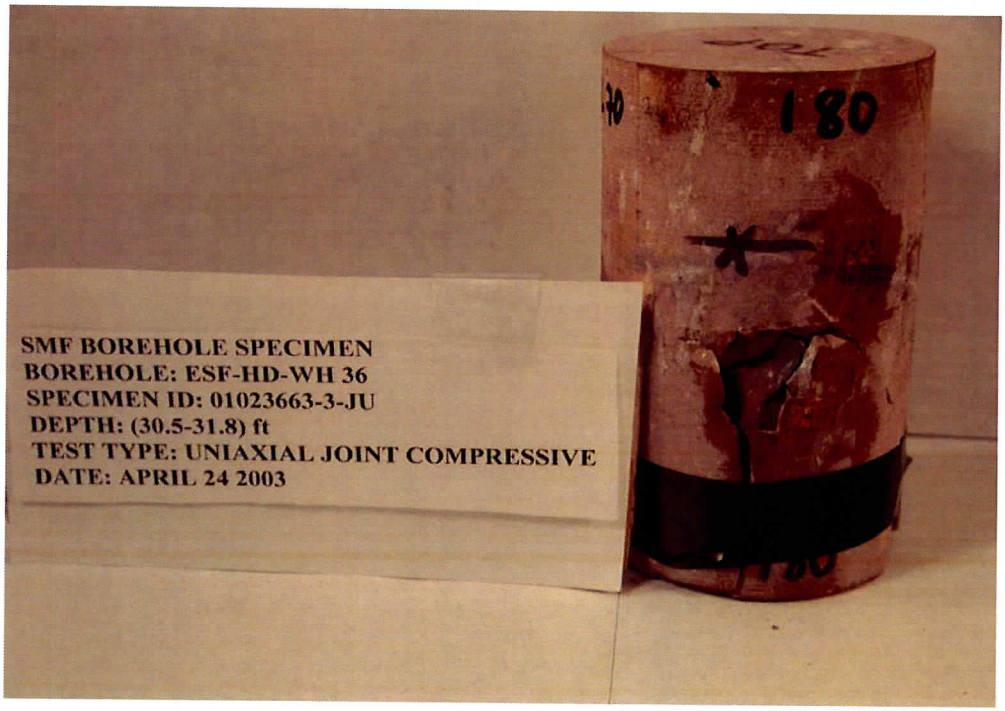

Fig A9.6 Post-failure photograph of specimen 01023663-3-JU

Appendix A10 - Specimen 01023752-JU

Specimen description

This specimen had 4 lithophysal cavities (Figures A10.1 and A10.2), moderately welded and had a horizontal joint of thickness 0.3 mm, diameter of 60.76 mm and length of 172.31 mm.

Instrumentation

Instrumentation of specimen 01023752 – JU is similar to Fig A1.1. Axial gages 1, 2, 3 and 4 were installed across the joint at 0°, 90°, 180° and 270° axes respectively. Axial gages 5, lateral gage 6, axial gage 7 and lateral gage 8 were installed on intact rock at 90° and 270° axes respectively. Extensometers 1 and 2 of lengths 50 mm and 50.8 mm respectively were installed along the 0° and 180° axes respectively.

Fig A10.1 Pre-failure photograph of specimen 01023752-JU showing gages along the 90°axis and the more shallow lithophysal cavities.

Fig A10.2 Pre-failure photograph of specimen 01023752-JU showing deeper lithophysal cavities and the gages installed along the 270° axis

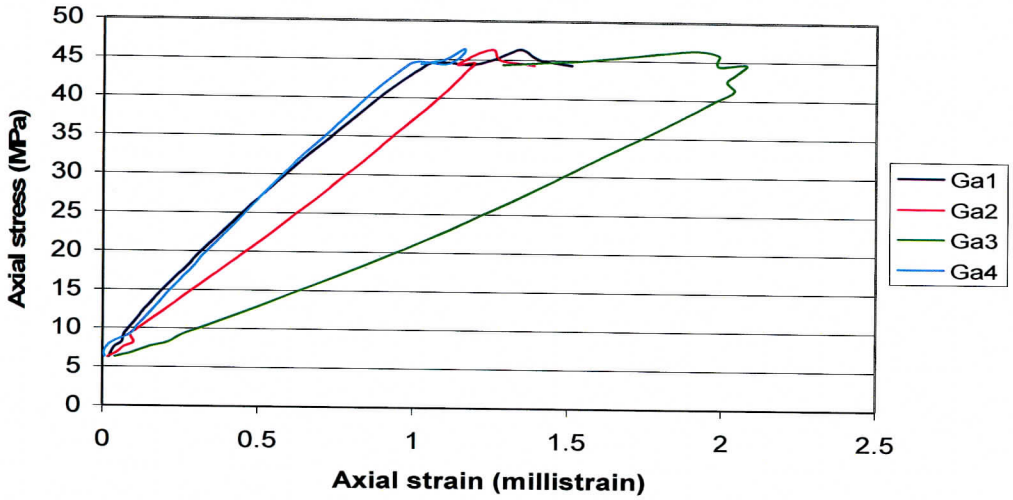

Fig A10.3 Axial stress vs. axial strain for gages 1, 2, 3 and 4 installed across the joint

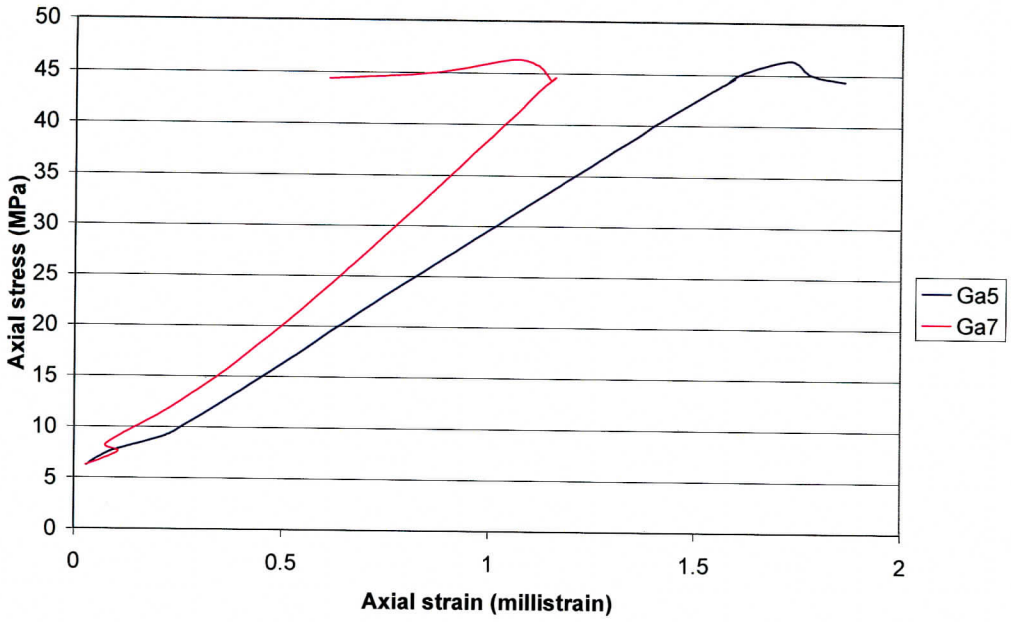

Fig. A10.4 Axial stress vs. axial strain for gages 5 and 7 installed on intact rock

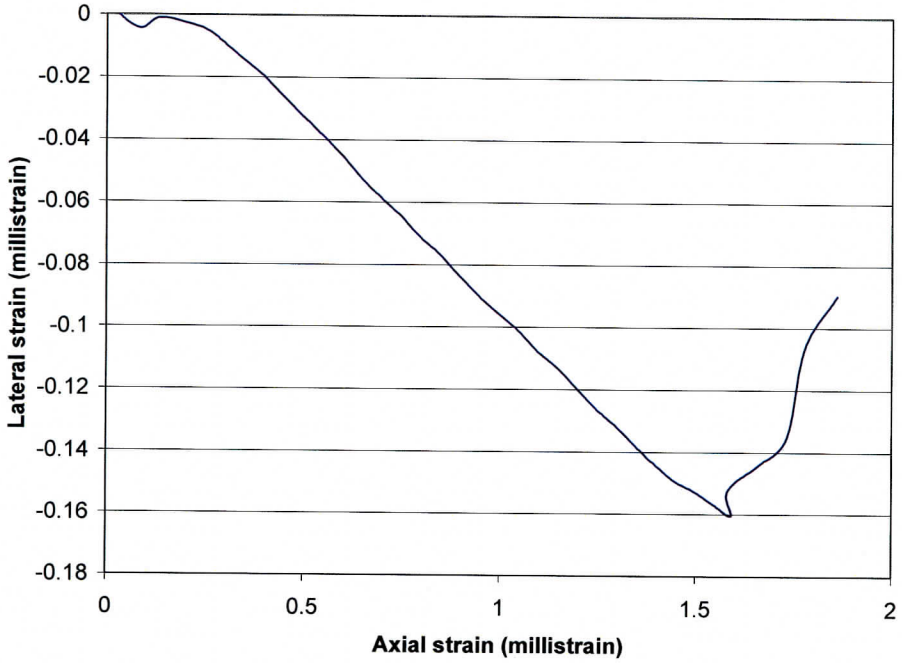

Fig A10.5 Lateral strain (gage 6) vs. axial strain (gage 5)

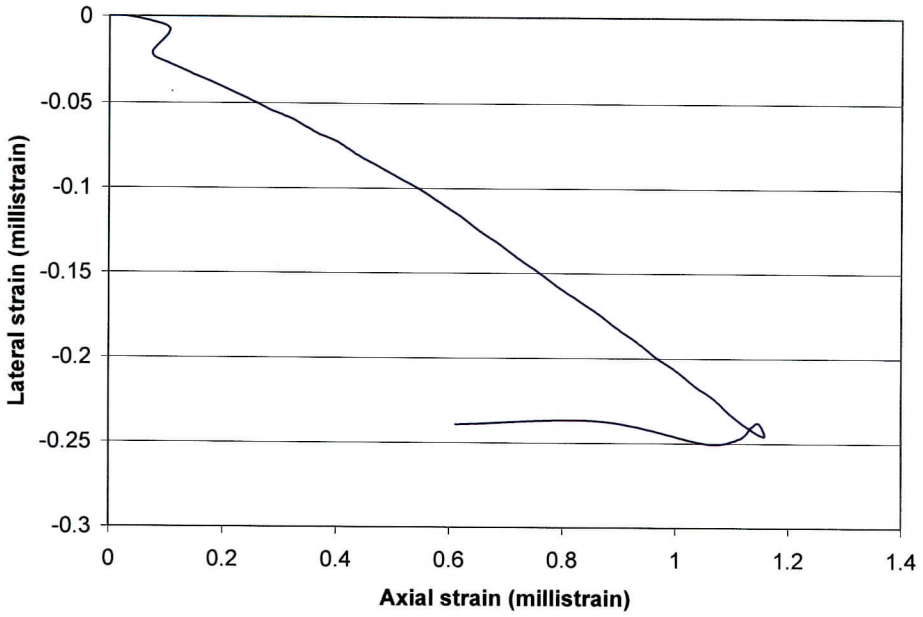

Fig A10.6 Lateral strain (gage 8) vs. axial strain (gage 7)

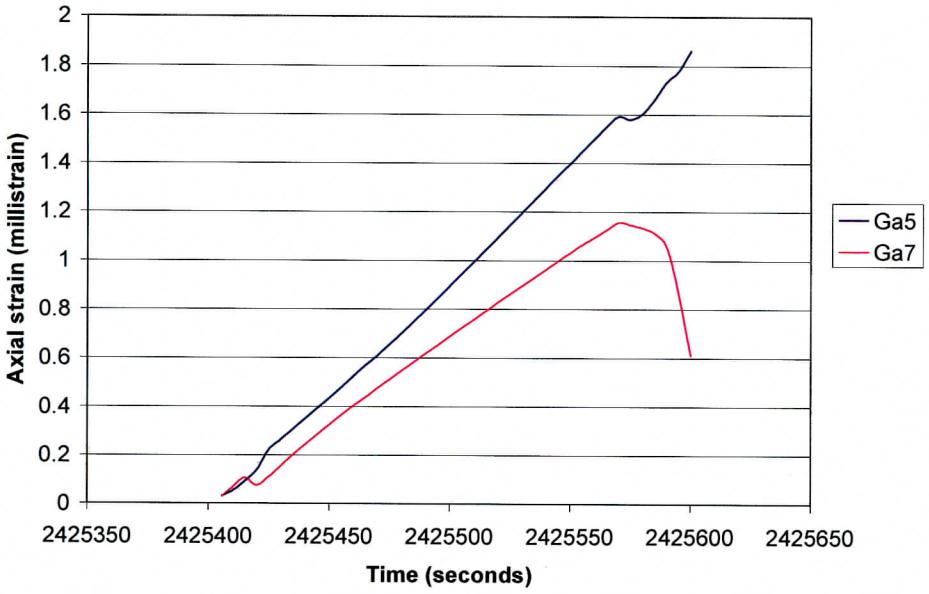

Fig A10.7 Axial strain vs time for gages 5 and 7

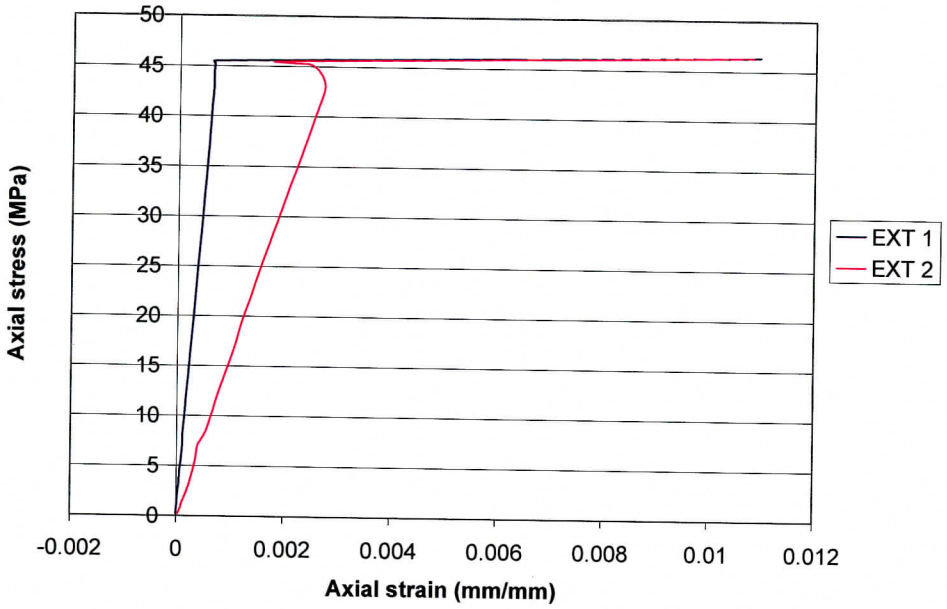

Fig A10.8 Axial stress vs. axial strain for extensometers 1 and 2 installed across the joint

Mode of failure

Two shallower lithophysal cavities along the 90° axis (Fig A10.1) acted as initiators of tensile fractures. The other two deeper lithophysal cavities shown in Fig. A10.2 (on the back side – opposite side of the major splitting fracture and close to the 270°) showed no sign of having acted as initiators of tensile fractures. The difference may very well be that the shallower ones, which extended to the bottom of the sample, are favorably oriented to generate tensile stresses near the ends of their long axes (see completely damaged bottom portion in Fig A10.12).

Results from the strain gage measurements

Table A10.1 Young's modulus and normal stiffness

Section of rock	Strain gage	Young's modulus (GPa)	Normal stiffness (GPa/mm)	Range (% of UCS)
3.2 mm rock with the joint	Gage 1	36.13	11.29	24.2 - 91.6
	Gage 2	31.39	9.81	
	Gage 3 *	18.55	5.80	
	Gage 4	39.74	12.42	
	Mean	**35.75**	**11.17**	
	Std. Deviation	**3.42**	**1.07**	
3.2 mm intact rock	Gage 5	26.34	8.23	24.2 - 91.6
	Gage 7	35.54	11.11	
	Mean	**30.94**	**9.67**	
	Std. Deviation	**4.6**	**1.44**	

* Gage 3 was not included in the analysis. For some unknown reason, its values are comparatively lower. One explanation could be that it was not properly installed. Another explanation might be that it was installed on a soft spot (e.g. above a "hidden" lithophysal cavity).

Table A10.2 Poisson's ratio

Strain gage	ν	Range (% of UCS)
Lateral gage 6 vs. axial gage 5	0.12	17.6 - 89.0
Lateral gage 8 vs. axial gage 7	0.22	24.2 - 91.6
Mean	**0.17**	
Std. Deviation	**0.05**	

Table A10.3 Strain rate

Strain gage	Strain rate/per second	Range (% of UCS)
Gage 5	9.6×10^{-6}	24.2 - 91.6
Gage 7	7.1×10^{-6}	
Mean	**8.35×10^{-6}**	
Std. Deviation	**1.25×10^{-6}**	

UCS = 46.3 MPa
Bulk density = 2.26 g/cm^3
Moisture content = 0.74 %

Calculation of joint normal stiffness from strain gage measurements

k_r = AE/L (Jaeger and Cook 1976, p. 179). Where A = area, L = length and E = Young's modulus (i.e. E value obtained for the intact rock).

Area = 0.0029 m^2, E = 30.94 GPa and L = 3.2 – 0.3 = 2.9 mm

$$k_r = \frac{0.0029 \times 30.94}{0.0029} = 30.94 MN/mm$$

Converting to GPa/mm gives k_r = 10.67 GPa/mm

The equivalent normal stiffness (11.17 GPa/mm) obtained for the 3.2 mm rock section with the joint is higher than the intact rock normal stiffness obtained (10.67 GPa/mm). It was therefore not possible to calculate the joint normal stiffness since the average intact rock specimen seems to be softer than the 3.2 mm portion with the joint therefore giving a negative joint normal stiffness. It is evident that the lithophysal cavities contributed to low uniaxial compressive strength and stiffness of this specimen.

Results from the extensometer measurements

Table A10.4 Young's modulus and normal stiffness

Sensor	Young's modulus (GPa)	Normal stiffness (GPa/mm)	Range (% of UCS)
Extensometer 1	65.52	1.31	22.7-87.0
Extensometer 2	15.62	0.31	
Mean	**40.55**	**0.81**	
Std. Deviation	**24.95**	**0.5**	

NB: Results obtained from the extensometers, although significantly different were used in the analysis since no instrumental problem was detected during testing. The difference in the two measurements might be due to their locations on the specimen.

Stiffness calculation from extensometer measurements

$$k_r = \frac{EA}{L} = \frac{30.94 \times 0.0029}{0.0501} = 1.791 MN/mm$$

Where L = 50.4 – 0.3 = 50.1 mm (average length of extensometer used = 50.4 mm)
Converting to GPa/mm gives 0.62 GPa/mm

Again, the equivalent normal stiffness (0.81 GPa/mm) obtained for the average 50.4 mm rock section with the joint is higher than the intact rock normal stiffness obtained (0.62 GPa/mm). It was therefore not possible to calculate the joint normal stiffness.

Fig A10.9 Post-failure photograph showing non-affected deeper lithophysal cavities

Fig A10.10 Post-failure photograph showing axial splitting through more shallow lithophysal cavities.

Fig A10.11 Pre-failure bottom view of specimen 01023752-JU

Fig A10.12 Post-failure bottom view of specimen 01023752-JU

Appendix A11 - Specimen 01023696-JU

Instrumentation

Installation of strain gages on specimen 01023696-JU (diameter of 60.9 mm and 74.6 mm long) is similar to Fig.A1.1 Four axial gages (gages 1, 2, 3 and 4) installed across the joint (thickness of 0.3 mm) were at 0°, 90°, 180° and 270° axes respectively. Axial gage 5, horizontal gage 6, axial gage 7 and horizontal gage 8 were installed along the 0° and 180° axes respectively. Axial gage 5 debonded prior to the test..

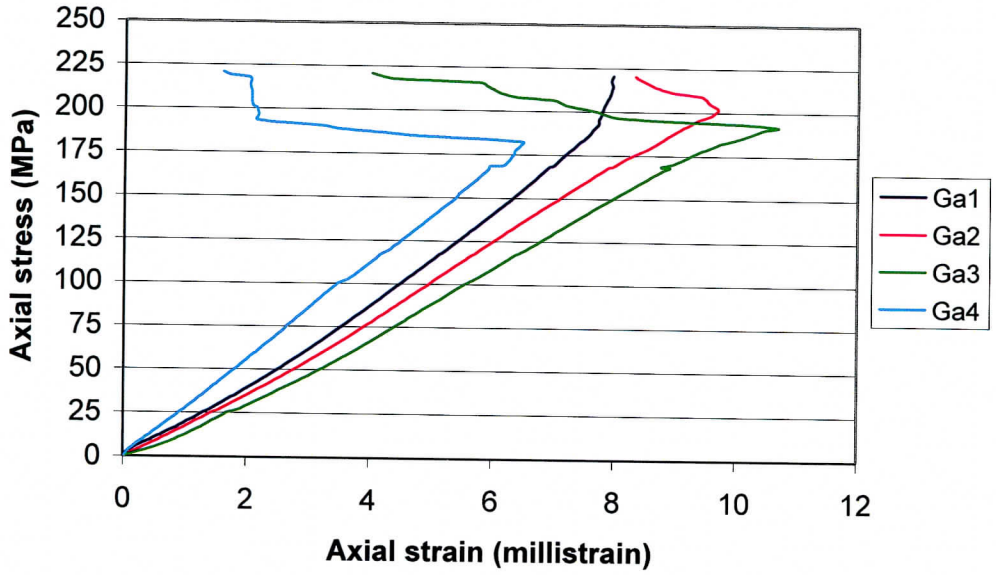

Fig. A11.1 Axial stress vs. axial strain for gages 1, 2, 3 and 4 installed across the joint

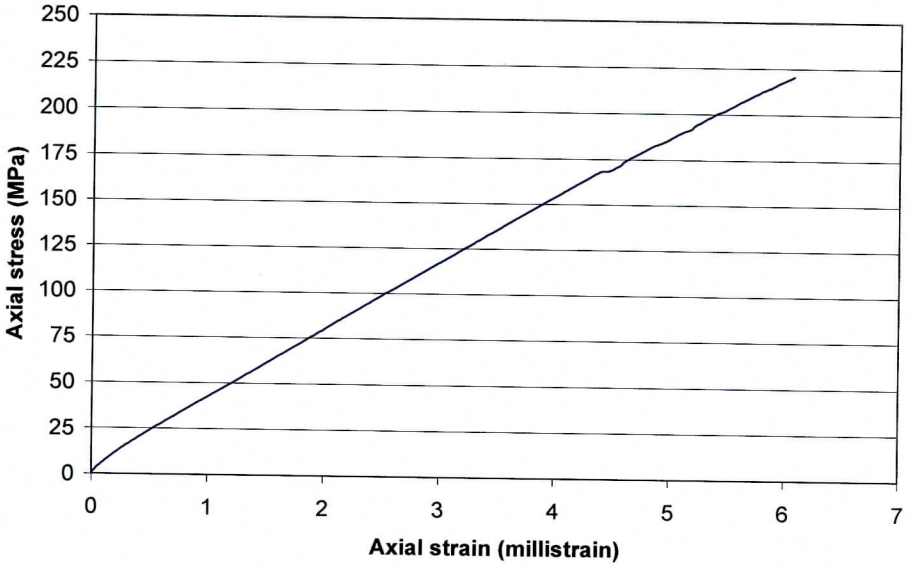

Fig A11.2 Axial stress vs. axial strain for gage 7 installed on intact rock

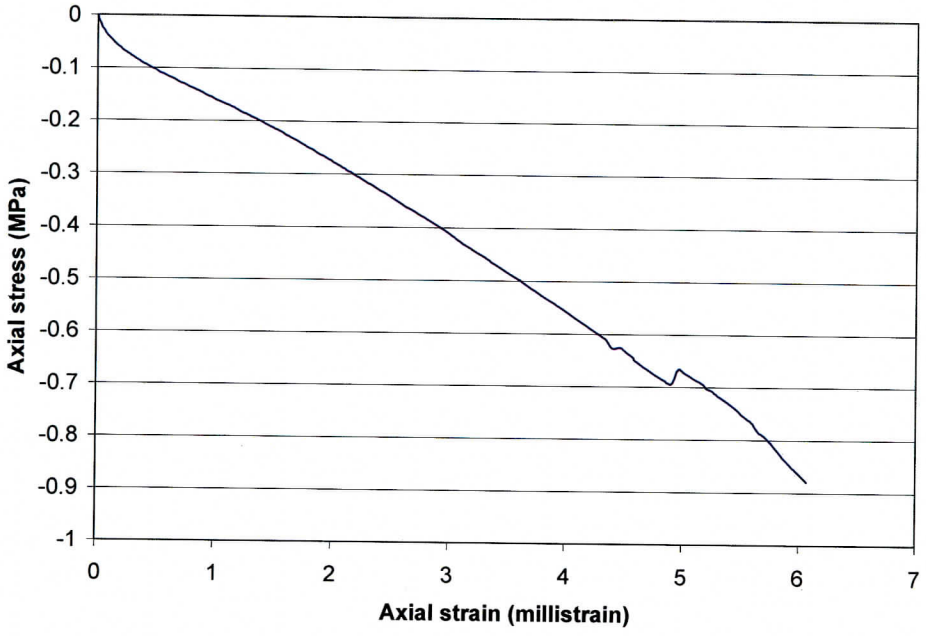

Fig A11.3 Lateral strain (gage 8) vs. axial strain (gage 7)

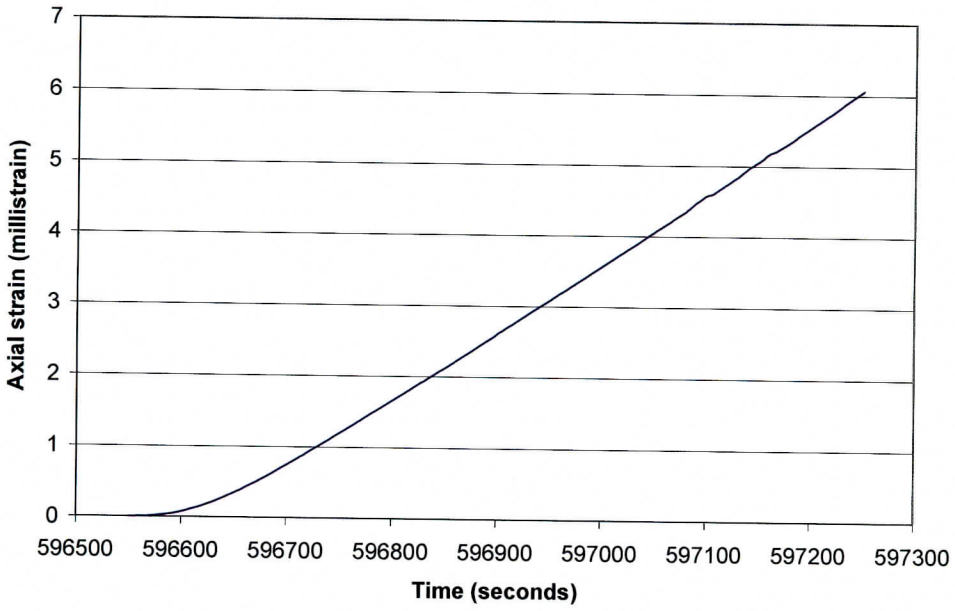

Fig A11.4 Axial strain vs. time for gage 7

Results from the strain gage measurements

Table A11.1 Young's modulus and normal stiffness

Section of rock	Strain gage	Young's modulus (GPa)	Normal stiffness (GPa/mm)	Range (% of UCS)
3.2 mm rock section with the joint	Gage 1	25.93	8.10	12.2 - 80.2
	Gage 2	22.68	7.09	
	Gage 3	20.60	6.44	
	Gage 4	27.64	8.64	
	Mean	**24.21**	**7.57**	
	Std. Deviation	**2.74**	**0.86**	
3.2 mm intact rock	Gage 7	36.41	11.38	Entire data

Table A11.2 Poisson's ratio

Strain gage	ν	Range (% of UCS)
Lateral Gage 8 vs. axial gage 7	0.14	15.1 - 79.4

Table A11.3 Strain rate

Strain gage	Strain rate/sec	Range (% of UCS)
Gage 7	9.2×10^{-6}	Entire data

UCS = 220.56 MPa
Bulk density = 2.28 g/cm^3
Moisture content = 0.51 %

Joint normal stiffness is 19.05 GPa/mm and calculated joint shear stiffness is 8.36 GPa/mm.

Fig. A11. 5 Pre-failure photograph of specimen 01023696-JU with an axial gage along the 90° axis, across a joint.

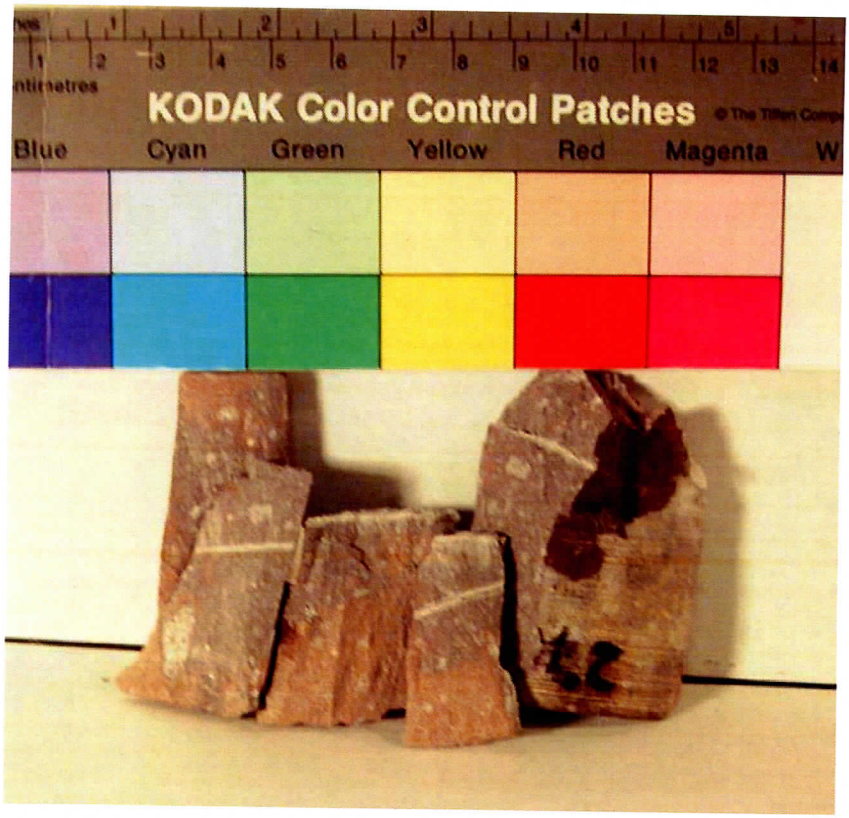

Fig A11. 6: Specimen 01023696-JU after testing. Fractures run through Joints in four pieces, but breakage has occurred along near horizontal Joints (in two central pieces).

Appendix A 12 - Specimen 01023584-3-JU

Instrumentation

Installation of strain gages on specimen 01023584-3-JU (diameter of 61.1 mm and 172.3 mm long) is similar to Fig. A1.1. Axial gages 1, 2, 3 and 4 were installed across the joint (thickness of 0.25 mm) at 0°, 90°, 180° and 270° axes respectively. Axial gages 5, lateral gage 6, axial gage 7 and lateral gage 8 were installed on intact rock at 90° and 270° axes respectively. Axial gage 5 debonded prior to starting the test and has not been included in the analysis.

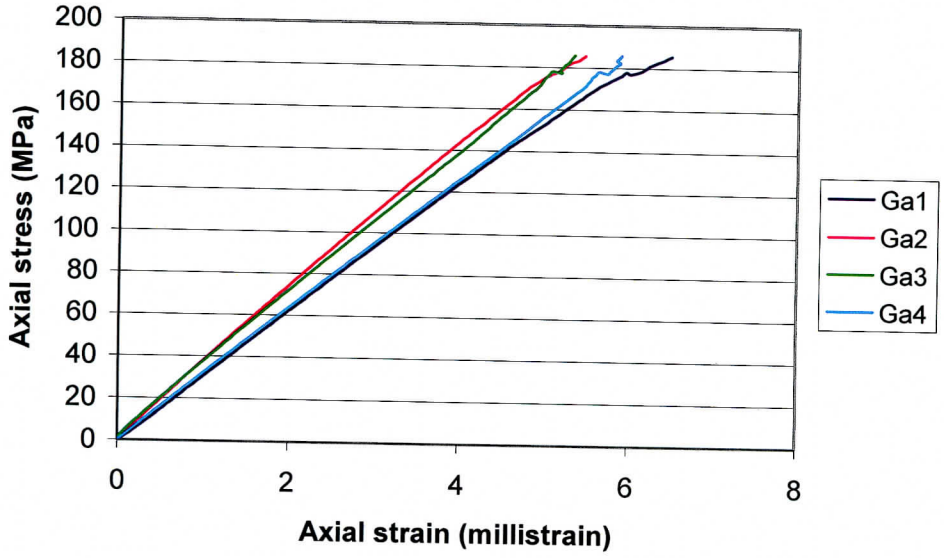

Fig A12.1 Axial stress vs. axial strain for gages 1, 2, 3 and 4 installed across the joint

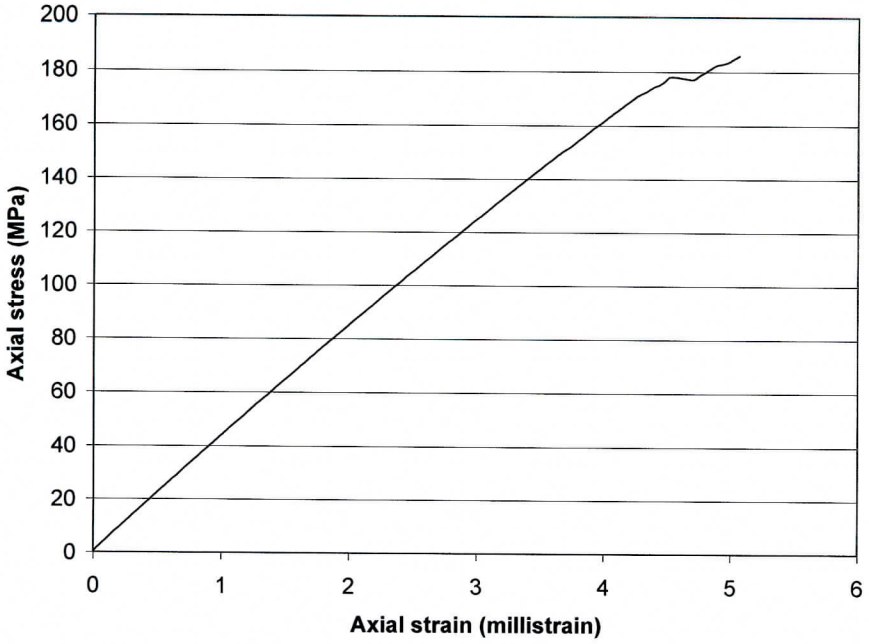

Fig A12.2 Axial stress vs. axial strain for gage 7

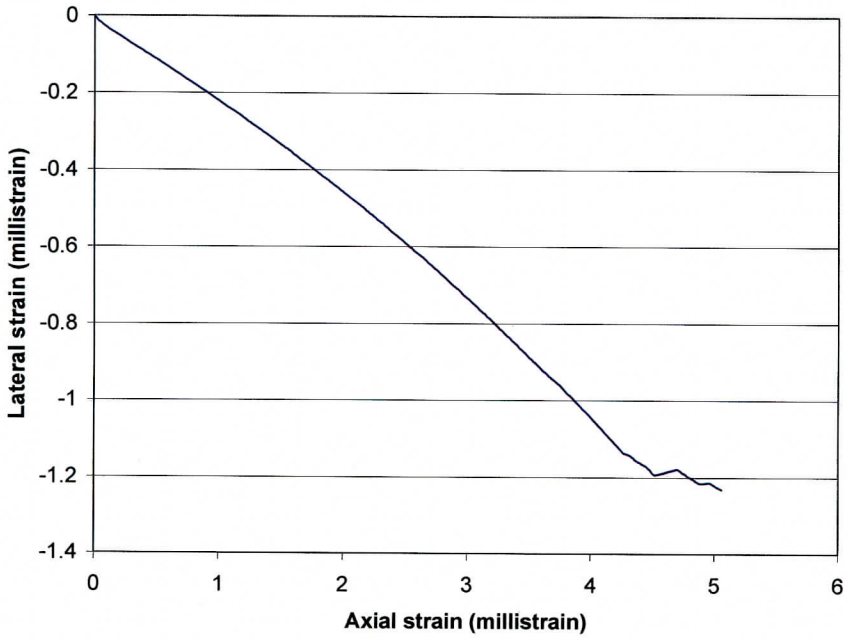

Fig A12.3 Lateral strain (gage 8) vs. axial strain (gage 7)

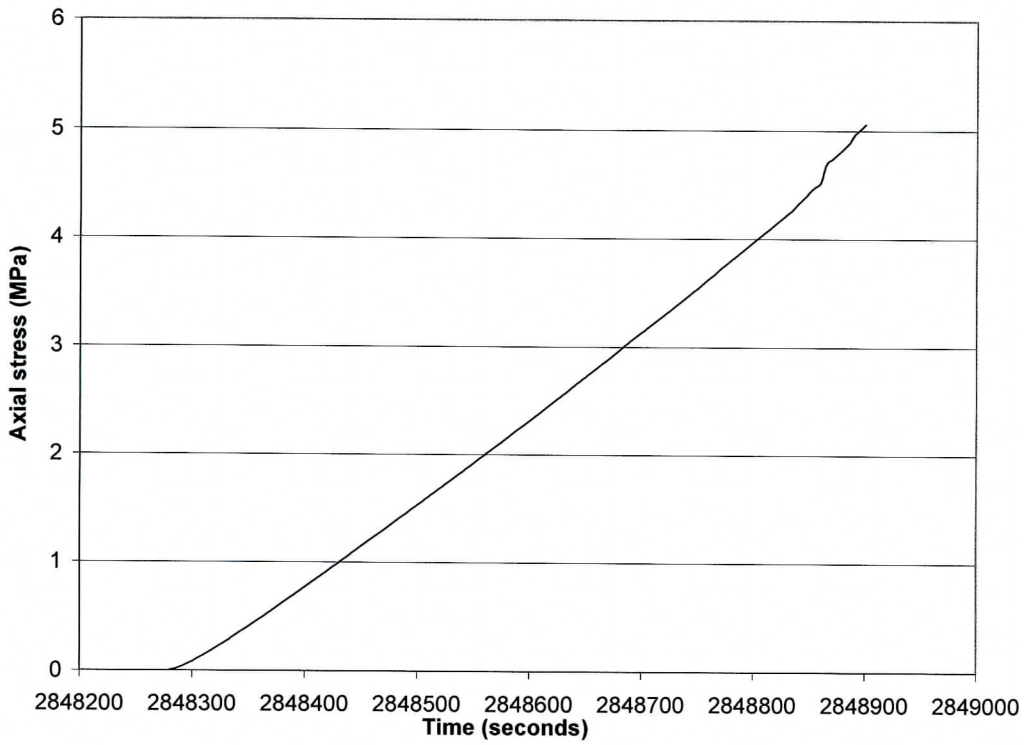

Fig. A12.4 Axial strain vs. time for gage 7

Results from the strain gage measurements

Table A.12.1 Young's modulus and normal stiffness

Section of rock	Strain gage	Young's modulus (GPa)	Normal stiffness (GPa/mm)	Range (% of UCS)
3.2 mm intact rock with the joint	Gage 1	30.68	9.62	
	Gage 2	35.14	11.04	6.8 – 88.1
	Gage 3	33.78	10.59	
	Gage 4	31.06	9.73	
	Mean	**32.67**	**10.25**	
	Std. Deviation	**1.86**	**0.59**	
3.2 mm intact rock	Gage 7	40.09	12.53	6.8 – 88.1

Table A12.2 Poisson's ratio

Strain gage	ν	Range (% of UCS)
Lateral Gage 8 vs. axial gage 7	0.26	6.8 – 88.1

Table A12.3 Strain rate

Strain gage	Strain rate/ per second	Range (% of UCS)
Gage 7	7.9×10^{-6}	6.8 – 88.1

UCS = 185.9 MPa,
Moisture content before testing = 0.57 %
Bulk density = 2.29 g/cm^3
Joint normal stiffness is 41.71 GPa/mm and calculated joint shear stiffness is 16.55 GPa/mm.

Mode of failure: This specimen failed along the loading axis (axial splitting) as shown in Figure A12.7. (A typical failure mode for most of the specimens tested).

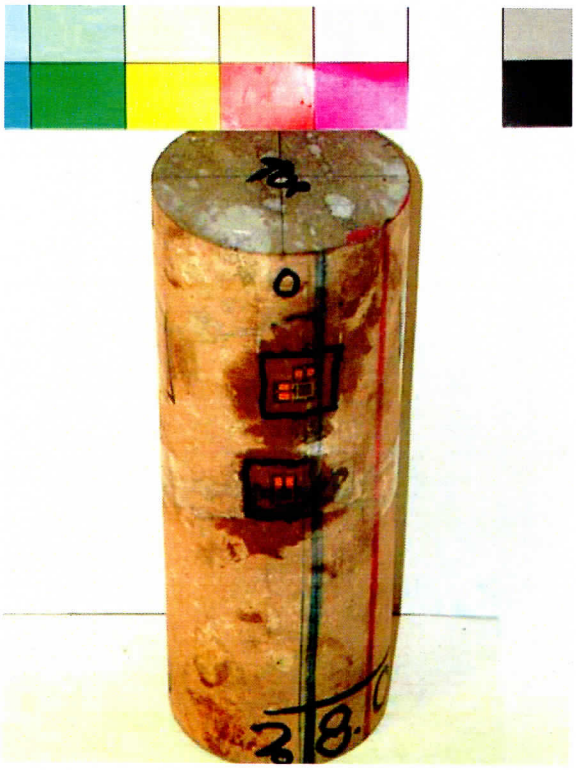

Fig A.12.5 Specimen 010235843-JU with strain gages along the 0^0 axis

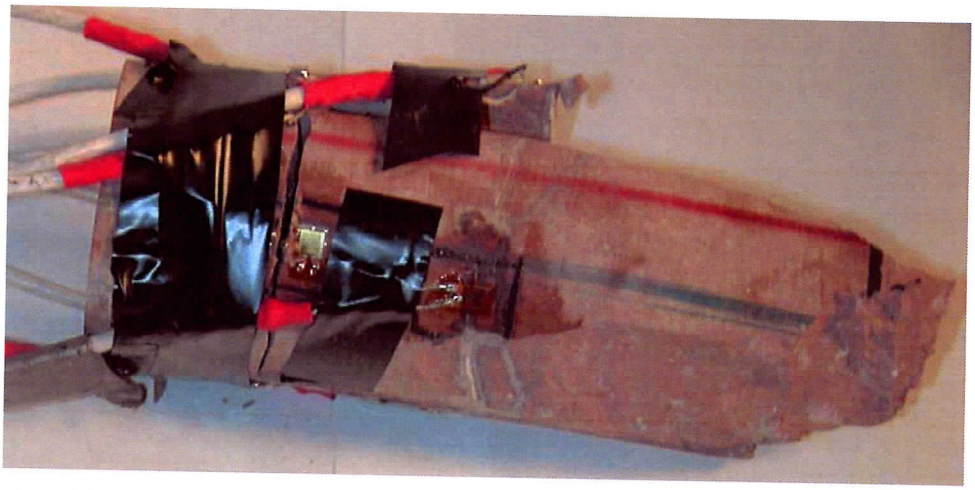

Fig A12.6 Specimen 010235843-JU after testing

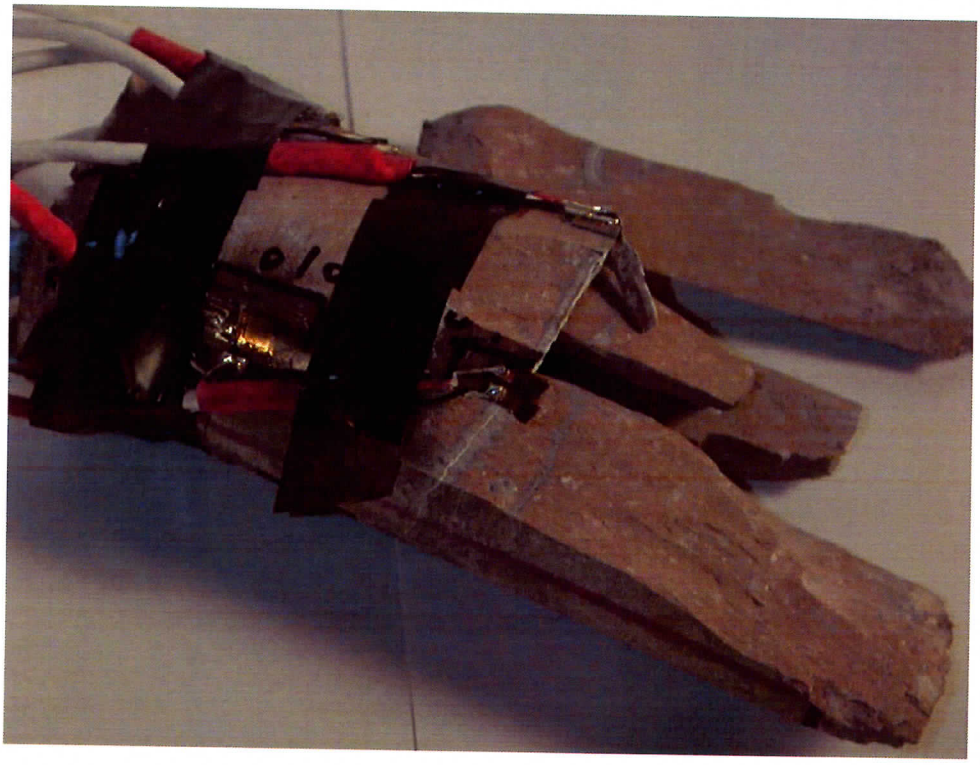

Fig.A12.7 Specimen 01023584-3-JU after testing. Typical characteristic failure pattern.

Appendix B. Plots of specimens' strength and elastic constants versus length to diameter (L/D) ratios.

This Appendix presents the relationship between the strength of the tested specimens (described in Appendix A) and their L/D ratios as well as the relationship between their elastic constants and the L/D ratios. From the "best-fit" linear regression plots of strength versus L/D ratio, Poisson's ratio versus L/D ratio, intact rock Young's modulus versus L/D ratio and Young's modulus versus uniaxial compressive strength, it can be deduced that:

1. The uniaxial compressive strength decreases with increasing L/D ratio (Fig. B2).
2. Intact rock Young's modulus decreases with increasing L/D ratio (Fig. B4).
3. Poisson's ratio increases with increasing L/D ratio as shown in Fig. B6.
4. Intact rock Young's modulus increases with increasing strength (Fig. B8).

Graphs of strengths and elastic parameters vs. L/D ratios were also plotted for the L/D ratios within the standard ranges (i.e. $2<L/D<2.5$ for ASTM and $2.5<L/D<3$ for IRSM). Apart from Young's modulus vs. L/D ratio and Young's modulus vs. the uniaxial compressive strength plots which showed the same trend as when plotted for all the tested specimens (Figures B5 and B9), reverse trends were observed for the other graphs (Figures B3 and B7).

The correlation for all these trends is extremely weak (see R^2 values). The explanation for these trends might be the variability in their intrinsic properties.

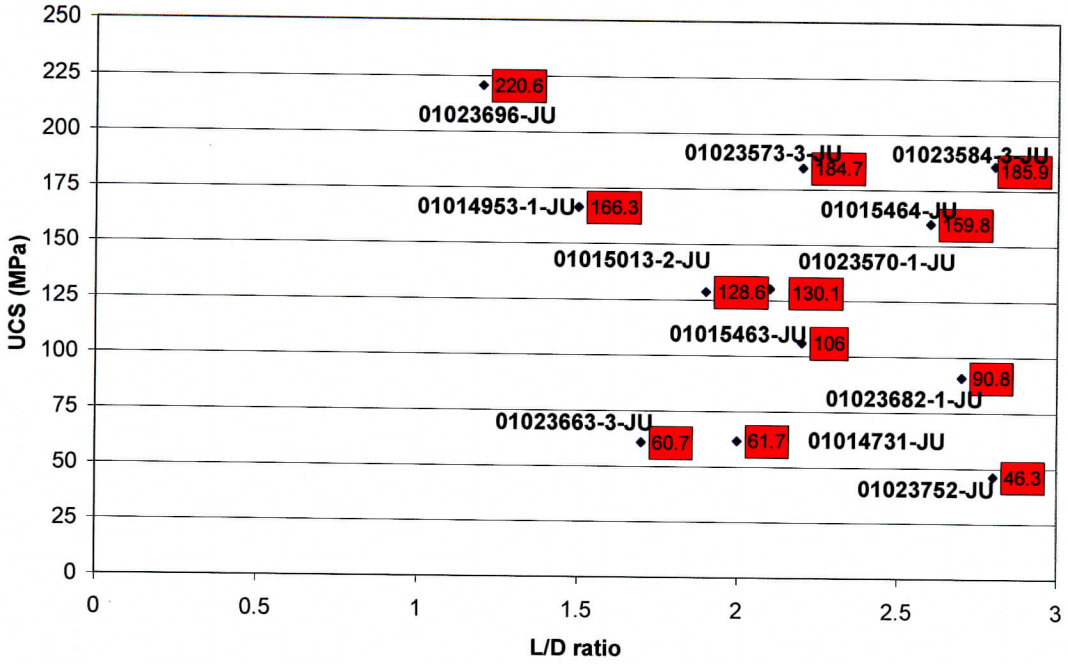

Fig. B1: Uniaxial compressive strength vs. length to diameter ratio with specimen identification.

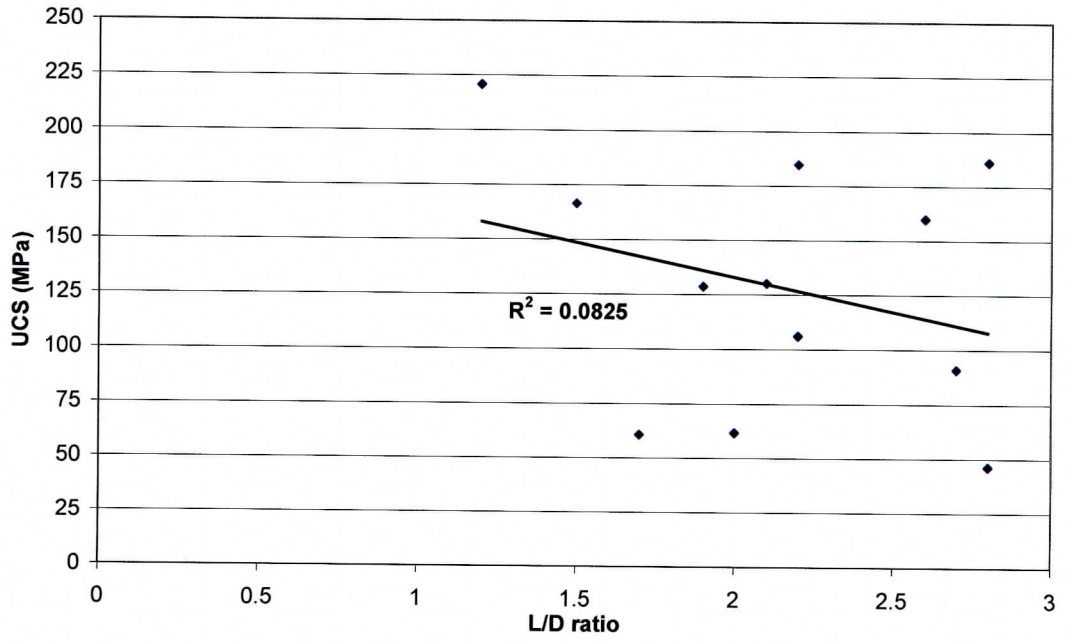

Fig. B2: Best fit linear regression plot of uniaxial compressive strength vs. length to diameter ratio.

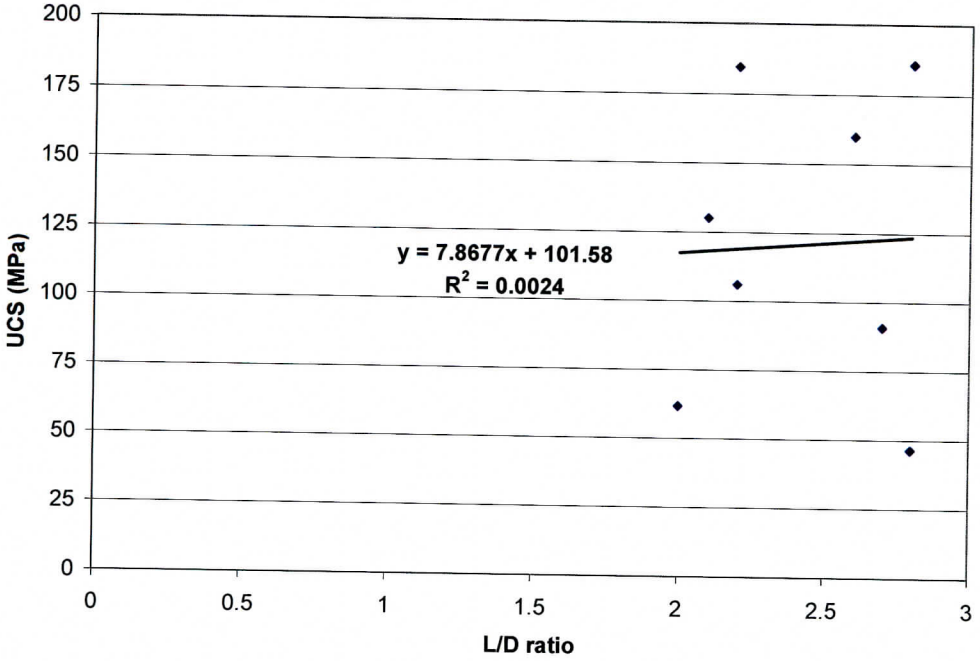

Fig. B3: Best fit linear regression plot of uniaxial compressive strength vs. length to diameter ratio according to ASTM and IRSM L/D ratio standards.

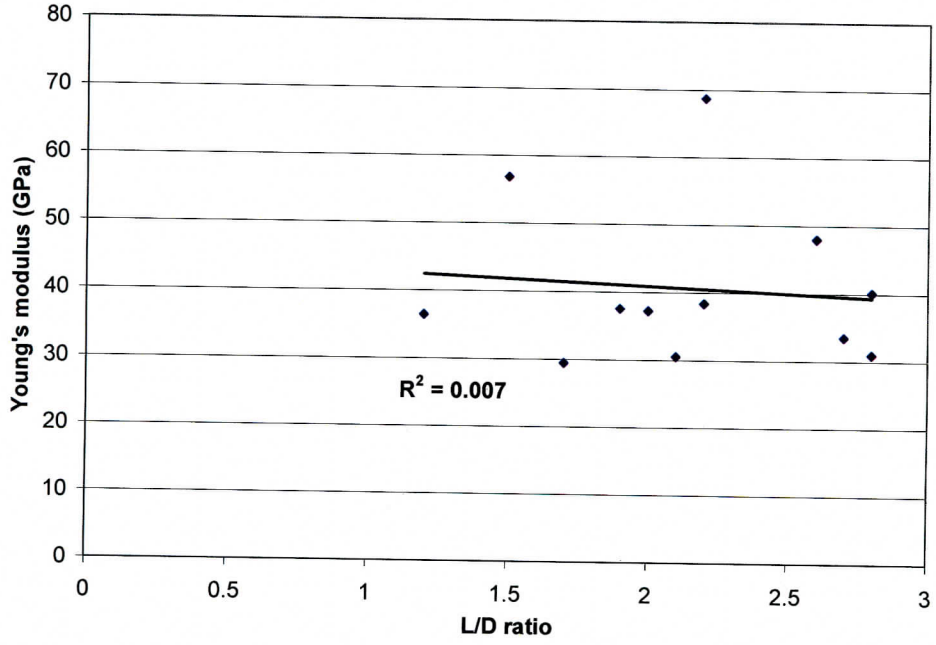

Fig. B4: Best fit linear regression plot of Young's modulus vs. length to diameter ratio.

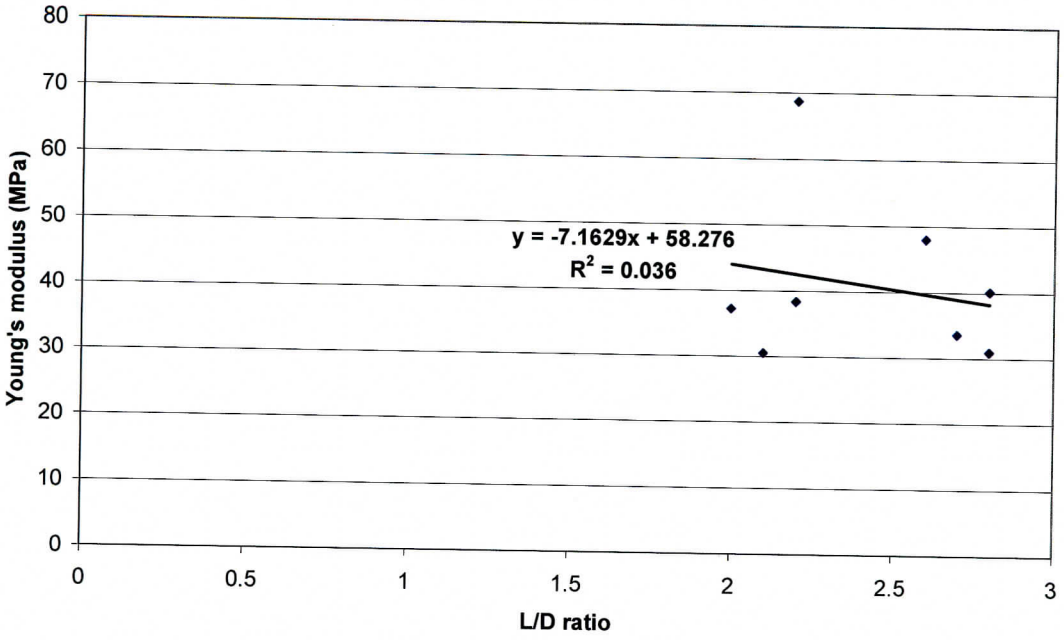

Fig. B5: Best fit linear regression plot of Young's modulus vs. length to diameter ratio according to ASTM and IRSM L/D ratio standards.

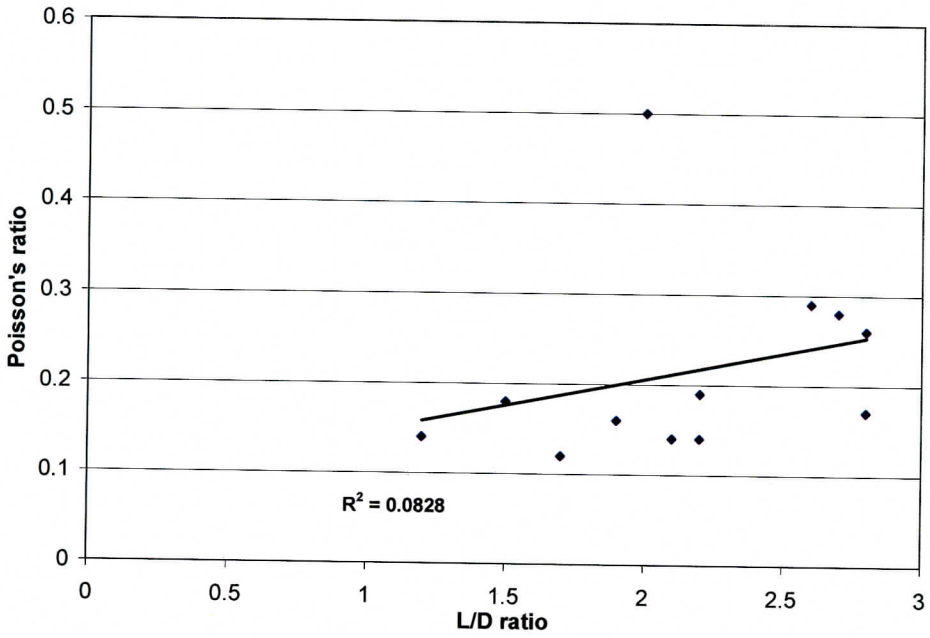

Fig. B6: Best fit linear regression plot of Poisson's ratio vs. length to diameter ratio.

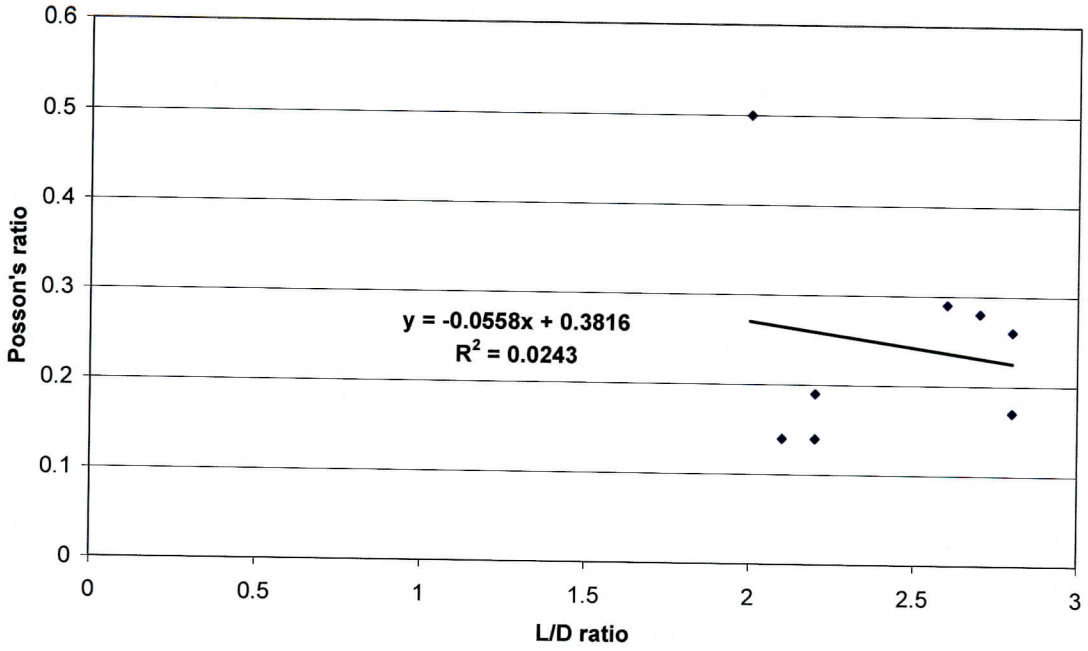

Fig. B7: Best fit linear regression plot of Poisson's ratio vs. length to diameter ratio according to ASTM and IRSM L/D ratio standards.

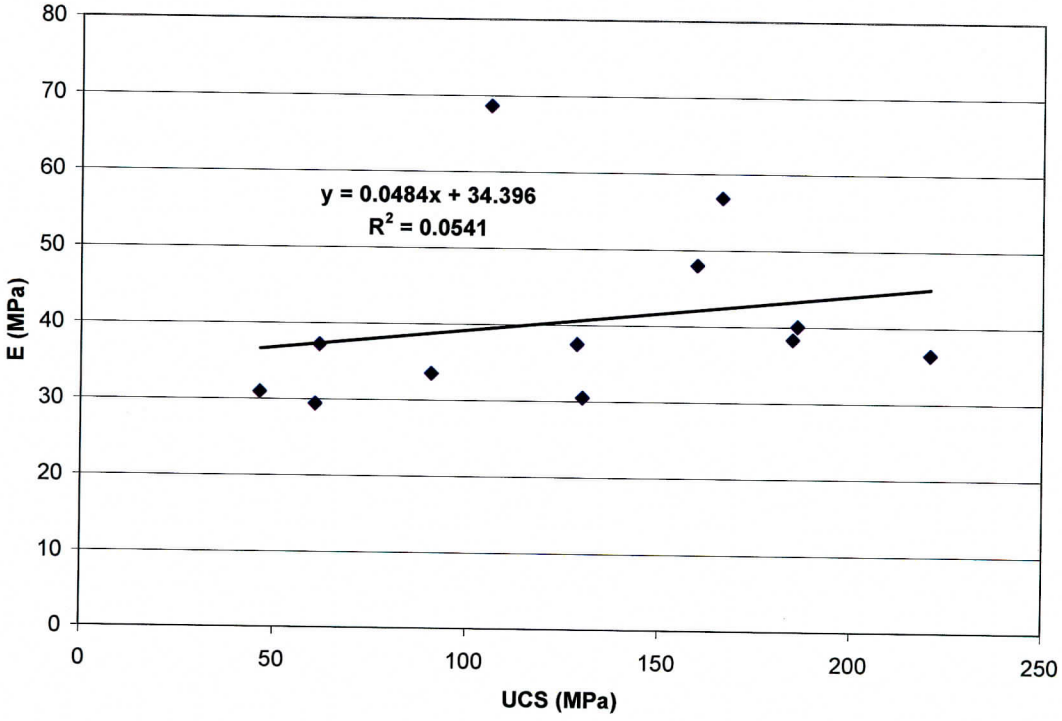

Fig. B8: Best fit linear regression plot of Young's modulus vs. uniaxial compressive strength.

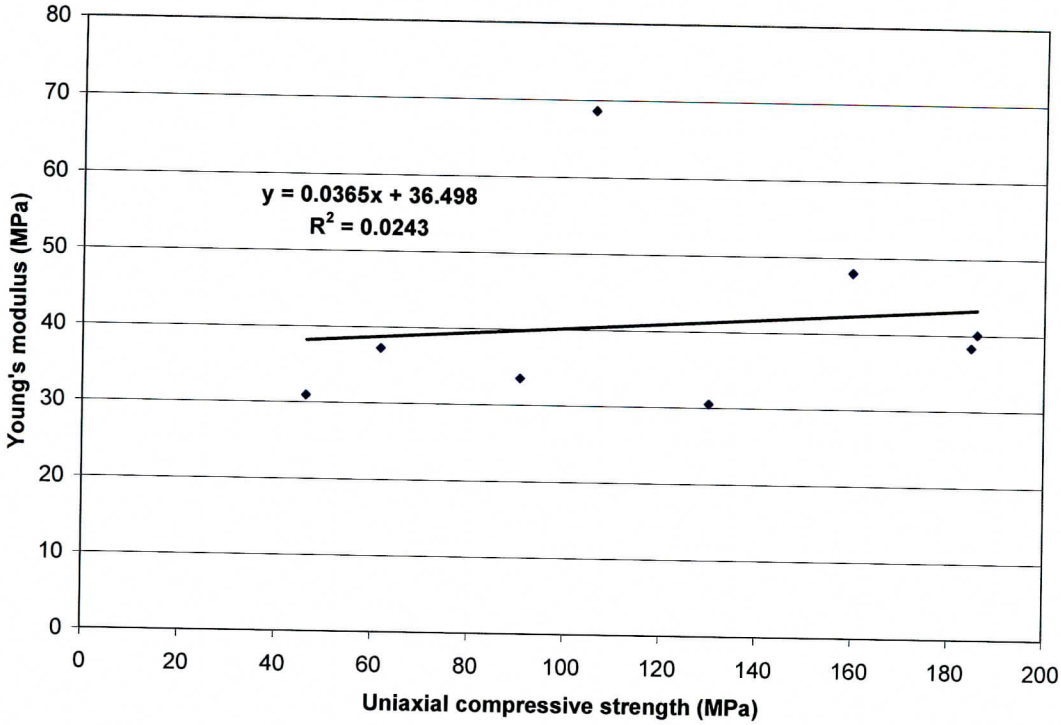

Fig. B9: Best fit linear regression plot of Young's modulus vs. uniaxial compressive strength according to ASTM and IRSM L/D ratio standards.

Appendix C. Description of tests for two specimens with angled joints, which failed along their pre-existing joints.

This Appendix presents information about tests conducted on two specimens with inclined joints (Figures C1.1 and C2.1) which failed along their joints. The Appendix describes in detail the test for each specimen. The description includes instrumentation used, plots of data collected, photographs of specimen tested, and results calculated.

C1 – Specimen 01023540-2 – JU

C2 - Specimen 01023540-5 – JU

Appendix C1 – Specimen 01023540-2-JU

Brief description of test

Uniaxial joint compression test has been performed on a 54.61 mm diameter, 152.45 mm long specimen 01023540-2-JU. The specimen had two healed joints (i.e. type 1 fractures filled by vapor-phase minerals), which were 11 mm apart and have equal thickness of 0.4 mm. They made an equal angle of 45° with respect to the loading axis measured along the 90° axis (Figure C1.1). Unlike the previous tests on specimens with nearly horizontal joints whose failure appeared to be tensile fracturing (axial splitting), this specimen showed an initial failure along one of the joints (joint "b") at the axial stress of 28.7 MPa. We unloaded and reloaded the specimen through four additional cycles until it completely failed along joint "b". Failure for the last 3 loading cycles was mainly due to shearing and rotation.

The test was run in LME 112 on a four-post 220 kip MTS closed servo-controlled hydraulic testing machine. Instrumentation of this specimen is similar to the one described in Appendix A1, Figure A1.1 for specimen 01015464-JU. Eight strain gages were installed on the specimen. Gages 1 and 2 were installed across joint "a" along the 0° and 45° axes respectively. Gages 3 and 4 were installed across joint "b" along the 45° and 270° axes respectively. Axial gage 5, horizontal gage 6, axial gage 7 and horizontal gage 8 were installed along the 120° and 270° axes respectively. One of the two axial gages (gage 4) installed across joint "b" at 270° axis behaved non-linearly during the first loading cycle. Apart from gages 5 and 6 which debonded prior to testing, all the gages worked well during the first and the second cycles. Shearing and rotation dominated the last three cycles therefore making the strain gage measurements meaningless. It was not possible to calculate parameters for the unloading cycles due to sharp drops from the maximum stress levels to values less than zero. The moisture content of the specimen is 1.07 %, measured before testing.

Fig C1.1 Specimen 01023540-2-JU after testing (joint "a" is above "b").

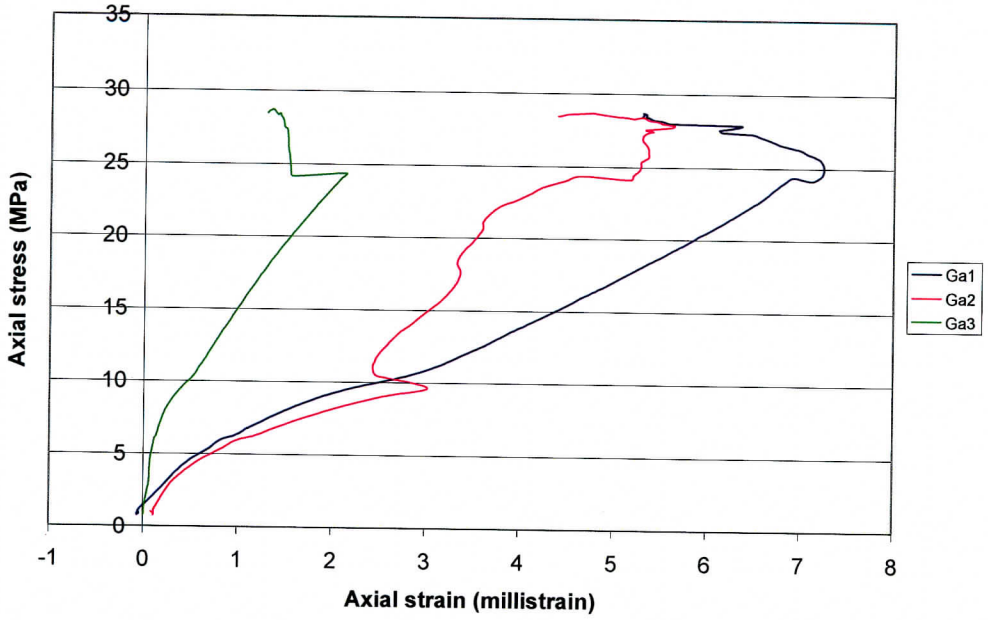

Fig. C1.2: Axial stress-axial strain curves for three axial strain gages (Ga1, Ga2, and Ga3) installed across the joints (first loading cycle).

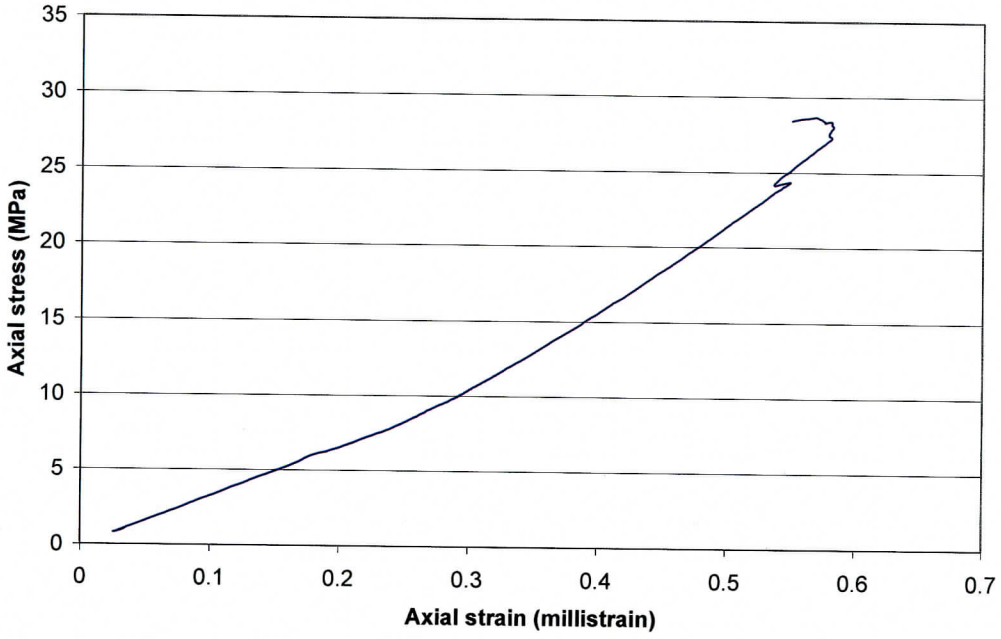

Fig. C1.3: Axial stress vs. axial strain for gage 7 installed on intact rock (first loading cycle).

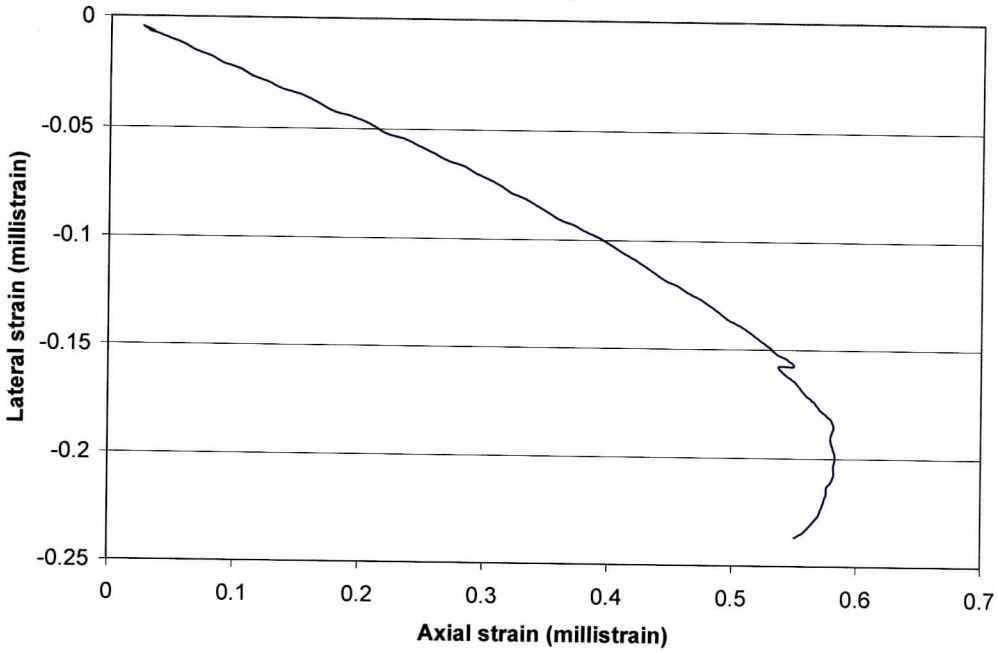

Fig. C1.4: Lateral strain (gage 8) vs. axial strain (gage 7) – first loading cycle.

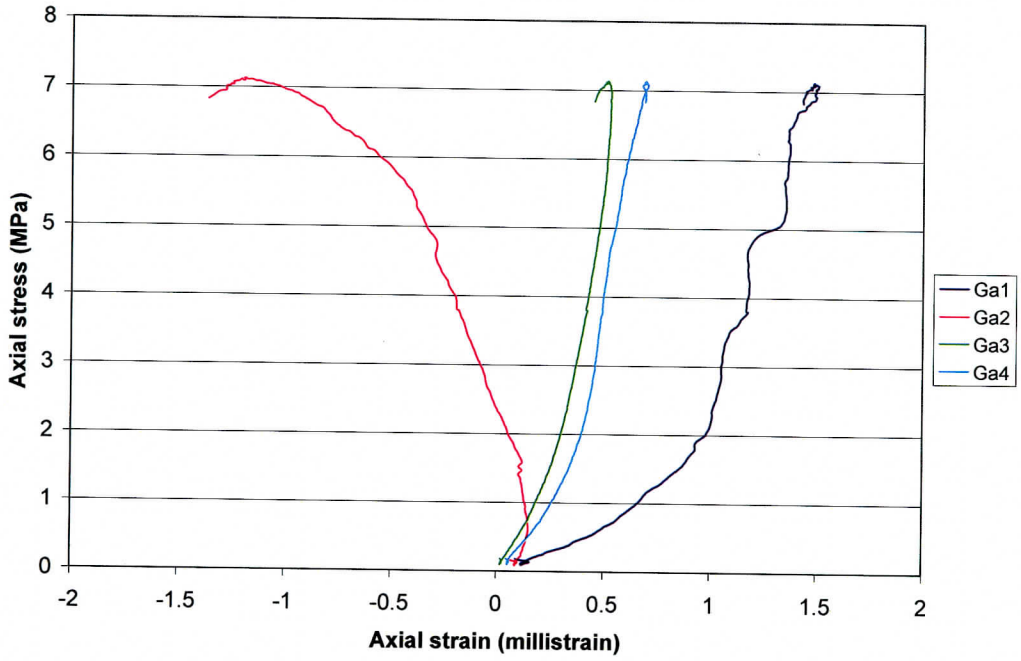

Fig. C1.5: Axial stress vs. axial strain for gages 1, 2, 3 and 4 installed across the joints (second loading cycle).

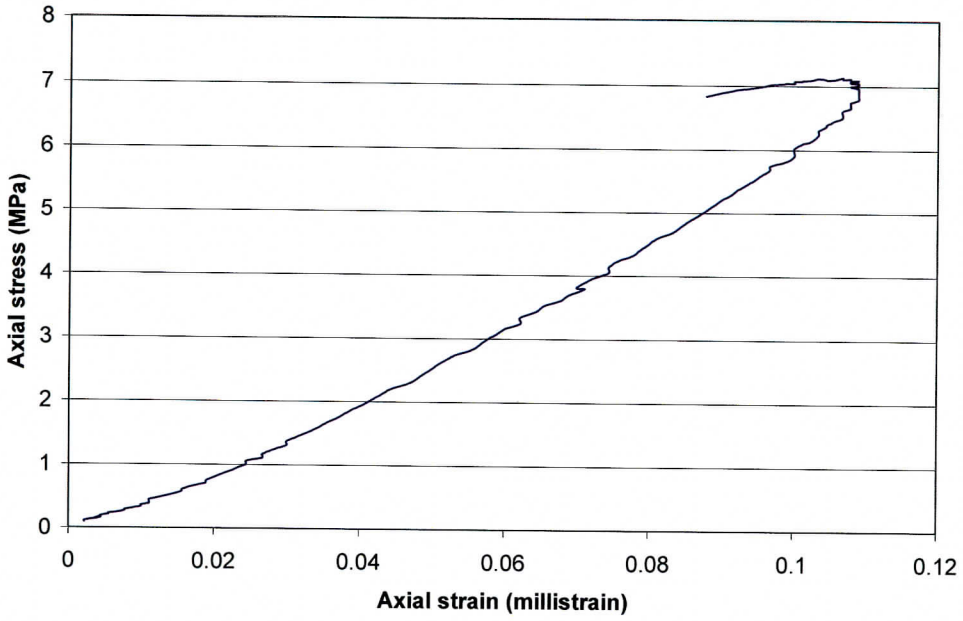

Fig C1.6 Axial stress vs. axial strain for gage 7 installed on intact rock (second loading cycle).

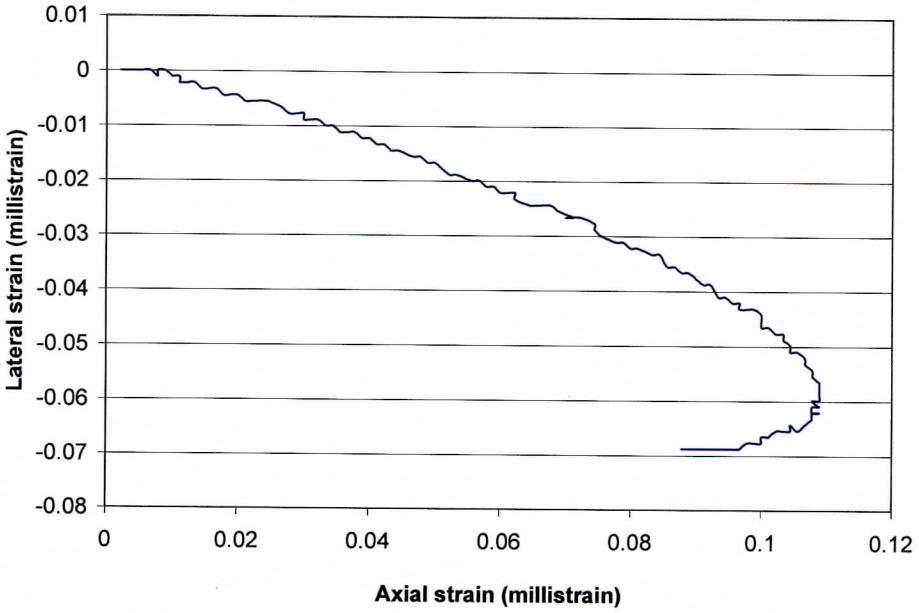

Fig C1.7 Lateral strain (gage 8) vs. axial strain (gage 7) – second loading cycle.

Results of strain gage measurements during the first cycle

Table C1.1 Young's modulus and normal stiffness

Section of rock	Strain gage	E (GPa)	Normal stiffness (GPa/mm)	Range* (% of σ_{max})
3.2 mm rock section with the joint	Gage 1**	3.38	1.06	43.4 - 77.4
	Gage 2	8.41	2.63	
	Gage 3	8.86	2.79	
3.2 mm intact rock	Gage 7	50.39	15.75	18.8 – 82.3

* Range indicates the range of the stress-strain and stress-displacement curves over which E and the normal stiffness are calculated.
** Results obtained from gage 1 were not included in the analysis because they are significantly too low according to ASTM E 178 - 94.

Table C1.2 Poisson's ratio

Strain gage	ν	Range (% σ_{max})
Lateral gage 8 vs. axial gage 7	0.29	14.3 - 77.4

Maximum stress (σ_{max}) = 28.7 MPa

Results of strain gage measurements during the second cycle

Table C1.3 Young's modulus and normal stiffness

Section of rock	Strain gage	E (GPa)	Normal stiffness (GPa/mm)	Range (% of σ_{max})
3.2 mm rock section with the joint	Gage 1	8.14	2.55	16.2 - 85.6
	Gage 2	7.32	2.29	
	Mean	**7.73**	**2.42**	
	Std. Deviation	**0.41**	**0.13**	
	Gage 3	16.28	5.09	
	Gage 4	16.87	5.27	
	Mean	**16.58**	**5.18**	
	Std. Deviation	**0.3**	**0.09**	
3.2 mm intact rock	Gage 7	65.55	20.48	16.2 - 85.6

Table C1.4 Poisson's ratio

Sensor	ν	Range (% of σ_{max})
Lateral Gage 8 vs. axial gage 7	0.5	16.2 - 85.6

σ_{max} = 7.13 MPa

NB: σ_{max} = maximum stress; ν = Poisson's ratio; E = Young's modulus

Calculation of the joint stiffness for the first loading cycle

Area (A) of 54.61 mm diameter specimen = $\frac{\pi x(54.61)^2}{4} = 2342.26\,mm^2 = 0.0023\ m^2$

Joint "a"

$$Intact\ rock\ stiffness\ \ k_r = \frac{EA}{L}$$

Where E = intact rock Young's modulus, L = length of rock specimen over which the gage was installed = gage length – joint thickness

L = 3.2 – 0.4 = 2.8 mm = 0.0028 m (joint thickness measured for joint "a"= 0.4 mm)
E = 50.39 GPa (see Table C1.1)

$$\Rightarrow k_r = \frac{EA}{L} = \frac{50.39 \times 0.0023}{0.0028} = 41.39\ MN/mm$$

Converting to GPa/mm gives 18.0 GPa/mm

$$k_n = \frac{k_{eq} \times k_r}{k_r - k_{eq}} \quad \text{.....(1)}$$

k_{eq} = equivalent normal stiffness obtained for the 3.2 mm rock section with the joint
= 2.63 GPa/mm (see Table C1.1)

k_n = joint normal stiffness

From (1) $\Rightarrow k_n = \frac{2.63 \times 18.0}{18.0 - 2.63} = 3.10\, GPa/mm$

Calculated shear stiffness (k_s) from $k_s = \frac{k_n}{2(1+\nu)}$ = 1.20 GPa/mm

Where ν = 0.29 (see Table C1.2).

Joint "b"

L = 3.2 – 0.4 = 2.8 mm = 0.0028 m (joint thickness measured for joint "b"= 0.4 mm)
E = 50.39 GPa
Intact rock stiffness is the same as obtained for joint "a" = 18.0 GPa/mm

k_{eq} = equivalent normal stiffness obtained for the 3.2 mm rock section with joint "b"
= 2.79 GPa/mm (see Table C1.1)

From (1) $\Rightarrow k_n = \frac{2.79 \times 18.0}{18.0 - 2.79} = 3.30\, GPa/mm$

Calculated shear stiffness (k_s) from $k_s = \frac{k_n}{2(1+\nu)}$ = 1.28 GPa/mm

Calculation of the joint stiffness for the second loading cycle

Joint "a"

$Intact\ rock\ stiffness\ \ k_r = \frac{EA}{L}$

L = 3.2 – 0.4 = 2.8 mm = 0.0028 m (joint thickness measured for joint "a"= 0.4 mm)

E = 65.55 GPa (see Table C1.3), A = 0.0023 m^2

$\Rightarrow k_r = \frac{EA}{L} = \frac{65.55 \times 0.0023}{0.0028} = 53.84\, MN/mm$

Converting to GPa/mm gives 23.4 GPa/mm

k_{eq} = 2.42 GPa/mm (see Table C1.3)

From (1) $\Rightarrow k_n = \dfrac{2.42 \times 23.4}{23.4 - 2.42} = 2.70 GPa/mm$

Calculated shear stiffness (k_s) from $k_s = \dfrac{k_n}{2(1+\nu)}$ = 0.9 GPa/mm

Joint "b"

Intact rock stiffness is the same as obtained for joint "a" = 23.4 GPa/mm

k_{eq} = 5.18 GPa/mm (see Table C1.3)

From (1) $\Rightarrow k_n = \dfrac{5.18 \times 23.4}{23.4 - 5.18} = 6.65 GPa/mm$

Calculated shear stiffness (k_s) = 2.22 GPa/mm

NB: Above calculations assume that the joints are perpendicular to the axial stress. A more realistic calculation would take into account the orientation (45°), and the fact that both stiffnesses (normal and shear) affect the axial strain/displacement.

Summary of stiffness results

Cycle	Joint	k_n (GPa/mm)	k_S (GPa/mm)
First loading cycle	Joint "a"	3.10	1.20
	Joint "b"	3.30	1.28
Second loading cycle	Joint "a"	2.70	0.90
	Joint "b"	6.65	2.22

Fig. C1.8 Specimen 01023540-2-JU in a four – post 220 kip MTS machine after the second loading cycle.

Appendix C2 – Specimen 01023540-5-JU

Brief description of test

A uniaxial joint compression test has been performed on a 49.78 mm diameter, 107.62 mm long specimen 01023540-5-JU of moisture content 0.68 %. The specimen had a healed undulating joint (i.e. type 1 fracture filled by vapor-phase minerals) of thickness of 0.35 mm and an angle of 50° measured with respect to the loading axis along the 90° and 270° axes of the specimen (Figure C2.1). The joint is nearly horizontal along the 0° and 180° axes. Unlike the previous tests on specimens with nearly horizontal joints whose failure appeared to be tensile fracturing (axial splitting), this specimen showed an initial failure along its joint at a maximum stress of 18.02 MPa. We unloaded as soon as the force-displacement curve showed a failure behavior. We reloaded the specimen through three additional cycles until it completely failed along its joint. Failure was due to compression, shearing and rotation.

The test was run in LME 112 on a four-post 220 kip MTS closed servo-controlled hydraulic testing machine. Instrumentation of specimen 01023540-5-JU is similar to the instrumentation shown in Appendix A (i.e. Fig A1.1). Six strain gages were installed on the specimen for the measurement of rock/joint deformation. Gages 3 and 4 were installed across the joint at 0° and 90° axes respectively. Axial gage 5, lateral gage 6, axial gage 7 and lateral gage 8 were installed on intact rock along the 90° and 180° axes respectively. One of the two gages (gage 4) installed across the joint along the 90° behaved non-linearly from the beginning of the test and failed to respond just about a minute into the test. The second gage across the joint (gage 3) worked well during the first loading cycle but became insensitive during the remaining loading cycles possibly due to stress relief. The other four gages (i.e. two axial and two horizontal gages) installed to measure the rock properties gave meaningless data. It seems shearing and rotation along the joint might have caused the stress relief and the data fluctuations observed.

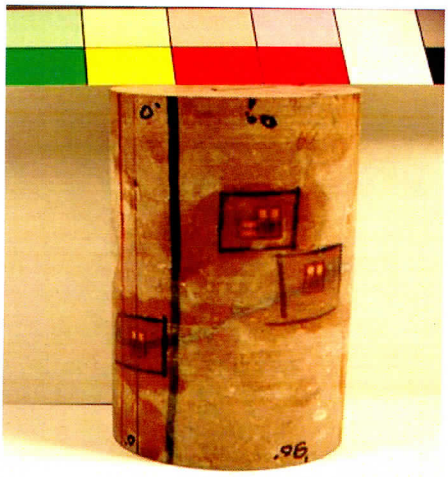

Fig C.2.1: Pre-failure photograph of specimen 01023540-5-JU with strain gages along the 0° and 90° axes. Note complex joint geometry.

Calculations Used

The test has been treated as a triaxial test in which the minor principal stress (σ_3) is zero and the major principal stress (σ_1) is the maximum stress attained during each cycle. The normal and the shear stresses along the joint have been calculated for each cycle.

In general, the normal and shear stresses, σ,τ, across a plane whose normal is inclined at θ to σ_1 are given as below (Jaeger and Cook, 1976, p. 14):

$$\sigma = \frac{1}{2}(\sigma_1 + \sigma_3) + \frac{1}{2}(\sigma_1 - \sigma_3)\cos 2\theta \quad \ldots\ldots\ldots\ldots\ldots\ldots 1$$

$$\tau = -\frac{1}{2}(\sigma_1 - \sigma_3)\sin 2\theta \ldots\ldots\ldots\ldots\ldots\ldots\ldots\ldots\ldots\ldots\ldots 2$$

Using equations 1 and 2, and $\theta = 40^0$, results in Table C2.1 were obtained.

Table C2.1: Calculated normal and shear stresses

Loading Cycle	Maximum Stress (σ_1)/MPa	Normal Stress/MPa	Shear Stress/MPa
1	18.07	10.6	8.90
2	8.51	4.99	4.19
3	4.02	2.36	1.98
4	3.08	1.81	1.52

The angle of friction (40°) and cohesion (0.5 kPa) were obtained from the linear best fit plot of shear stress versus normal stress as shown in Figure C2.2.

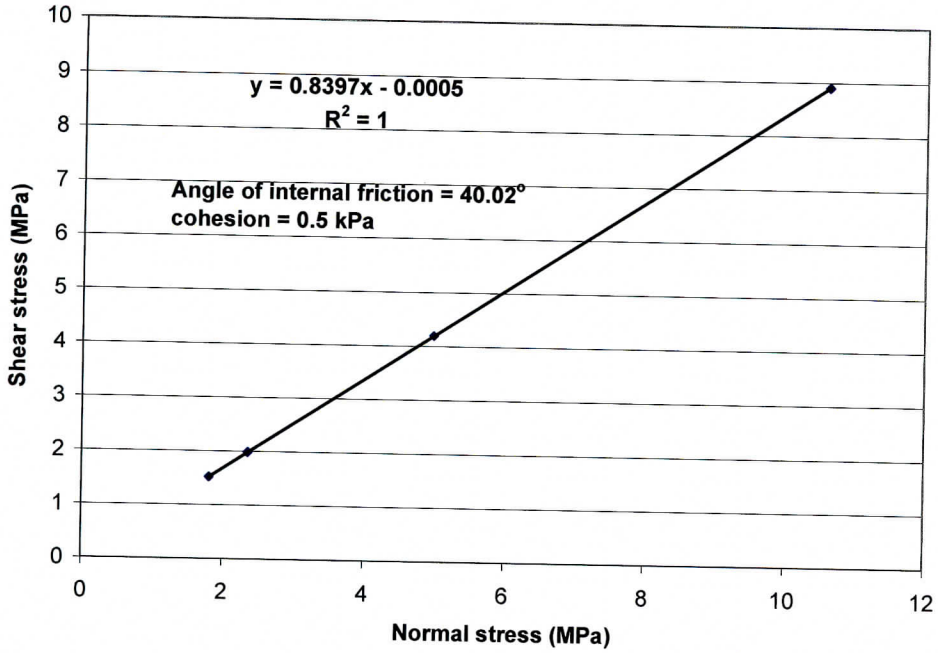

Fig. C2.2: Linear best fit plot of shear stress vs. normal stress.

When criterion for failure in a plane of weakness has been used, average angle of internal friction of 40.1^0 and an approximate zero cohesion value were obtained as shown below.

$$\text{i.e. } (\sigma_1 - \sigma_3) = \frac{2(S_w + \mu_w \sigma_3)}{(1 - \mu_w \cot\beta)\sin 2\beta} \quad \text{.....3} \qquad \text{(Jaeger \& Cook, 1976, p.106)}$$

At zero unconfining pressure, $\sigma_3 = 0$

$$\Rightarrow \sigma_1 = \frac{2S_w}{(1 - \mu_w \cot\beta)\sin 2\beta} \quad \text{.....4}$$

Where β = angle between σ_1 and the normal to the plane of weakness
μ_w = coefficient of internal friction
S_w = inherent shear strength (cohesion) in the plane of weakness

The following equations can be written from equation 4:

$$18.07 = \frac{2S_w}{(1 - \mu_w \cot 40)\sin 80} \quad \text{for the first cycle}$$

$$8.51 = \frac{2S_w}{(1-\mu_w \cot 40)\sin 80} \quad \text{for the second cycle}$$

$$4.02 = \frac{2S_w}{(1-\mu_w \cot 40)\sin 80} \quad \text{for the third cycle}$$

$$3.08 = \frac{2S_w}{(1-\mu_w \cot 40)\sin 80} \quad \text{for the fourth cycle}$$

Solving equations for first and second cycles gave zero cohesion (i.e.$S_w = 0$) and internal angle of friction (ϕ) of 40.04^0.

From second and third cycles, $S_w = 0$ and $\phi = 40.04^0$

From third and fourth cycles, $S_w \approx 0$ and $\phi = 40.21^0$

.

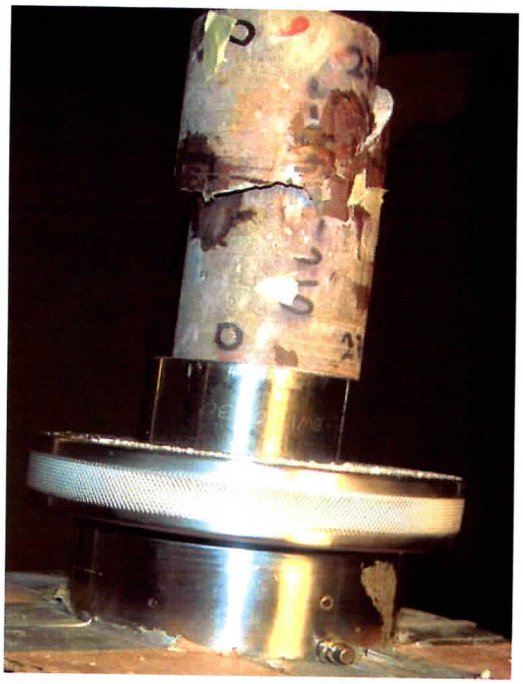

Fig C2.3 Specimen 01023540-5-JU after the third loading cycle. Planar joint at 50° from specimen axis (right) bends into a nearly horizontal joint on the left of the specimen.

Appendix D. Data collected from direct shear tests, calculated joint properties, and specimen and equipment photographs

This Appendix presents information about direct shear tests performed on specimens 01023540-1-DS, 01014781-DS, 01014782-DS, 01023540-3-DS and 01023540-6-DS. Test on specimen 01023540-1-DS was the first direct shear test performed with the direct shear machine shown in Figure D1.1 and therefore considered as a trial test. Joint roughness coefficients were estimated for the specimens before and after testing using the profile/scale shown in Figure D1 below.

Appendix D1: Specimen 01023540-1-DS
Appendix D2: Specimen 01014781-DS
Appendix D3: Specimen 01014782-DS
Appendix D4: Specimen 01023540-3-DS
Appendix D5: Specimen 01023540-6-DS

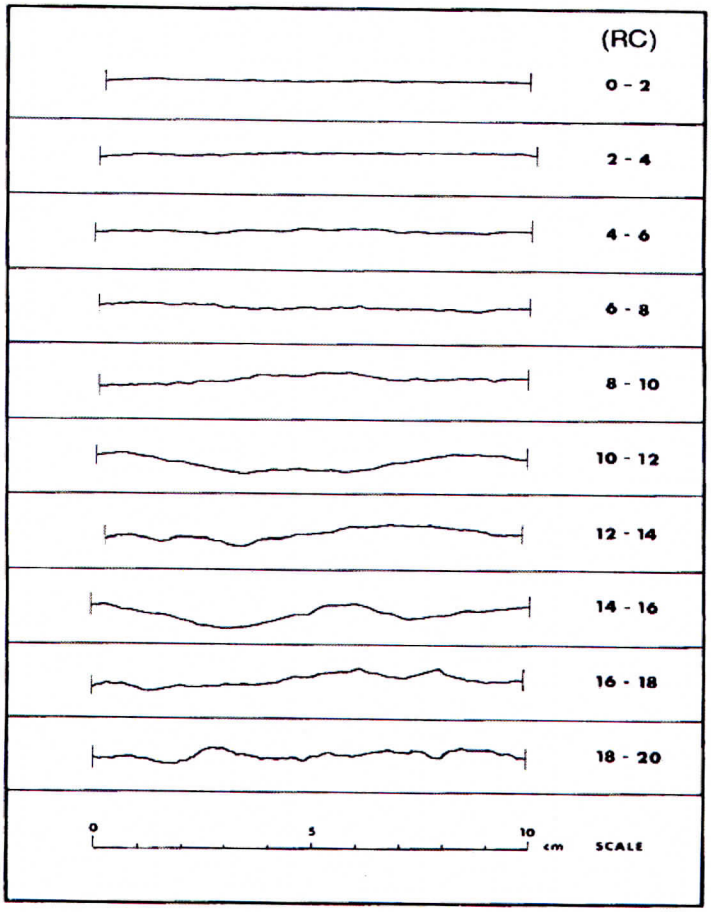

Fig D1: Profiles of fracture-surface roughness (Barton and Choubey, 1977, p.19). (Non-Q, for information only)

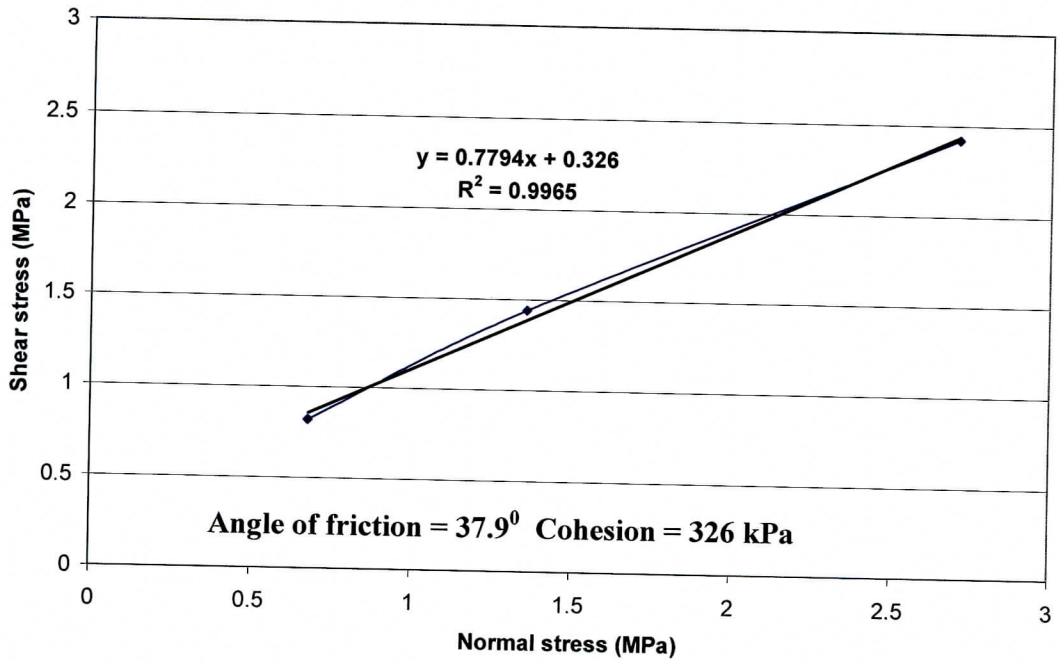

Fig. D2.1: Linear best fit plot of shear stress vs. normal stress.

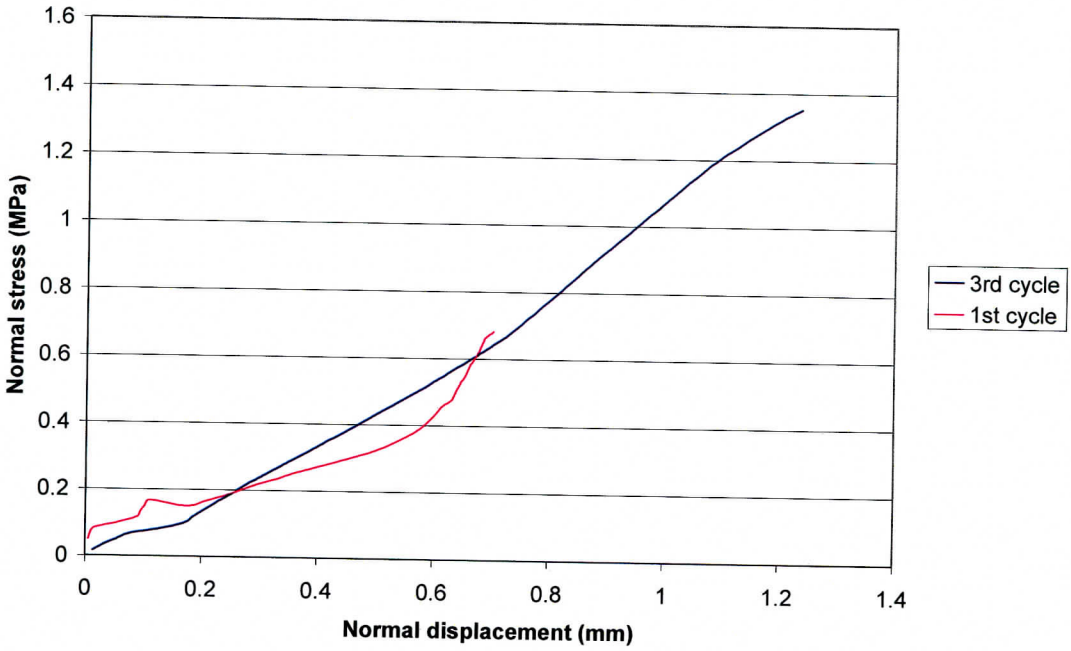

Fig. D2.2: Normal stress-normal displacement curves for the first and third loading cycles.

Appendix D1: Direct shear test on specimen 01023540-1-DS

A direct shear test was performed on specimen 01023540-1-DS (contact area approximately 13572 mm^2) using the procedures described in chapter 2, sections 2.3.1 and 2.3.2. Figure D1.1 shows the direct shear machine with four Linear Variable Differential Transformers (LVDTs) used to measure the normal and the shear displacements.

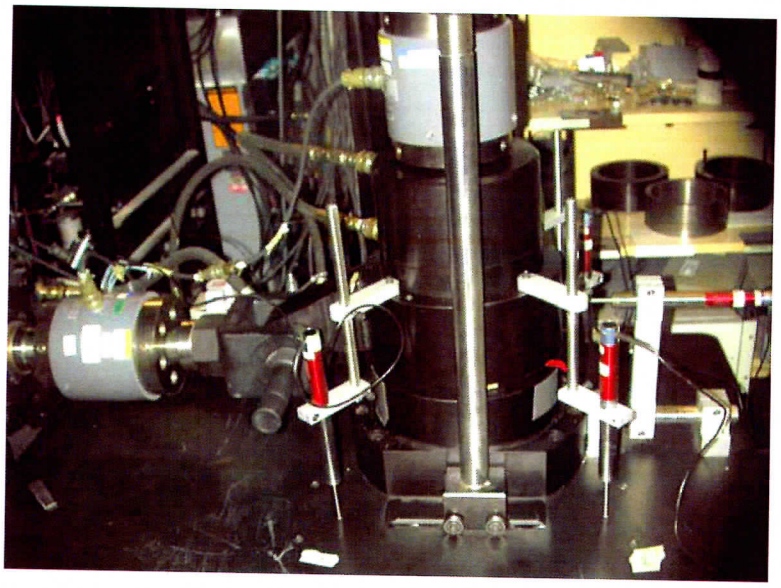

Fig. D1.1 A Direct shear machine with LVDTs installed in LME 112

There were fluctuations in the data collected due to a severe tilt/rotation of the machine during testing and steel to steel contact in some cases. Data for some of the loading cycles were difficult to analyze due to the rotation of the machine and, therefore it was not possible to determine any joint parameter for those cycles. No shear displacement data were collected during the test because the shear displacement control system on the MTS control machine was not activated prior to starting the test. Therefore it was not possible to calculate the shear stiffness. Peak shear loads (shear stresses) and normal loads (normal stresses) are shown in Table D1.1. The peak shear and normal stresses were calculated by dividing the loads by the apparent contact area. Angle of friction (34.5°) was obtained from the linear best fit plot of shear stress vs. normal stress, assuming zero cohesion for the joint surface (Figure D1.2).

The joint normal stiffness was calculated for the third and the fifth cycles as shown in Figures D1.3 and D1.4 respectively. Joint normal stiffness obtained for the third cycle (maximum stress of 0.9 MPa) is 4.88 MPa/mm (Fig.D1.3) while joint normal stiffness for the fifth cycle (maximum stress of 1.6 MPa) is 6.28 MPa/m (Fig. D1.4).

Table D1.1 Peak normal and shear loads (stresses).

Cycle	Normal load(kN)	Shear load (kN)	Normal stress(MPa)	Shear stress (MPa)
2	2.25	0.41	0.17	0.03
3	6.02	4.09	0.44	0.3
4	12.0	8.62	0.88	0.63
5	24.0	16.39	1.76	1.21

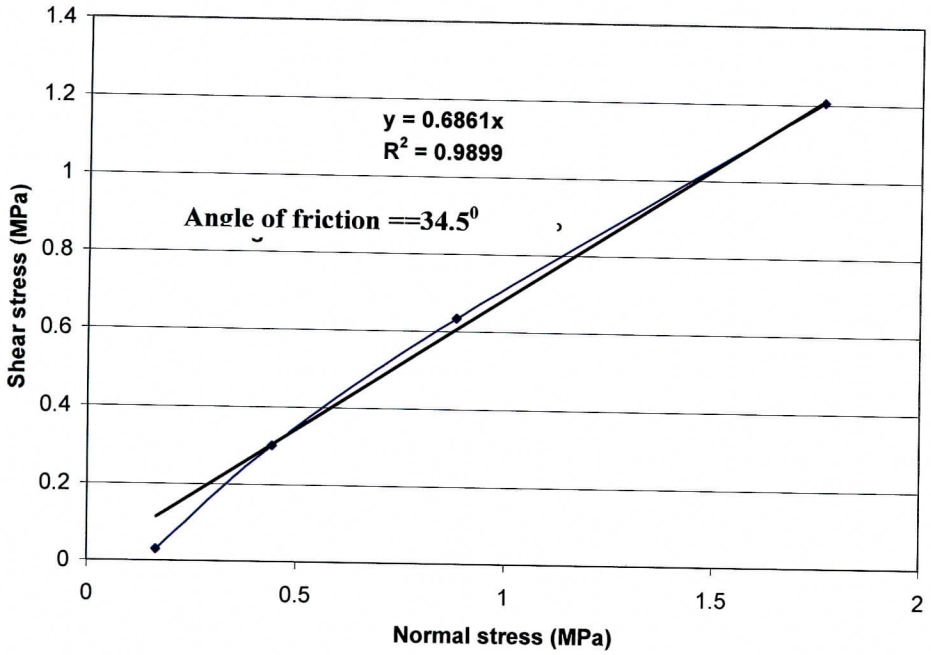

Fig. D1.2: Linear best fit plot of shear stress vs. normal stress

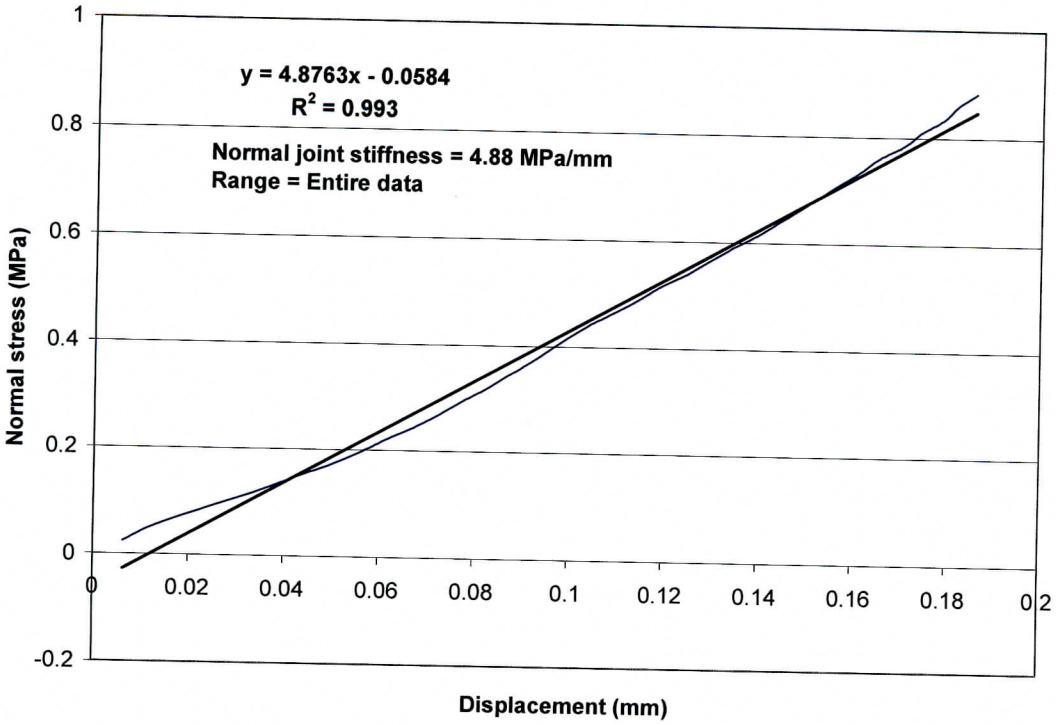

Fig. D1.3 Linear best fit plot of normal stress vs. normal displacement (third cycle)

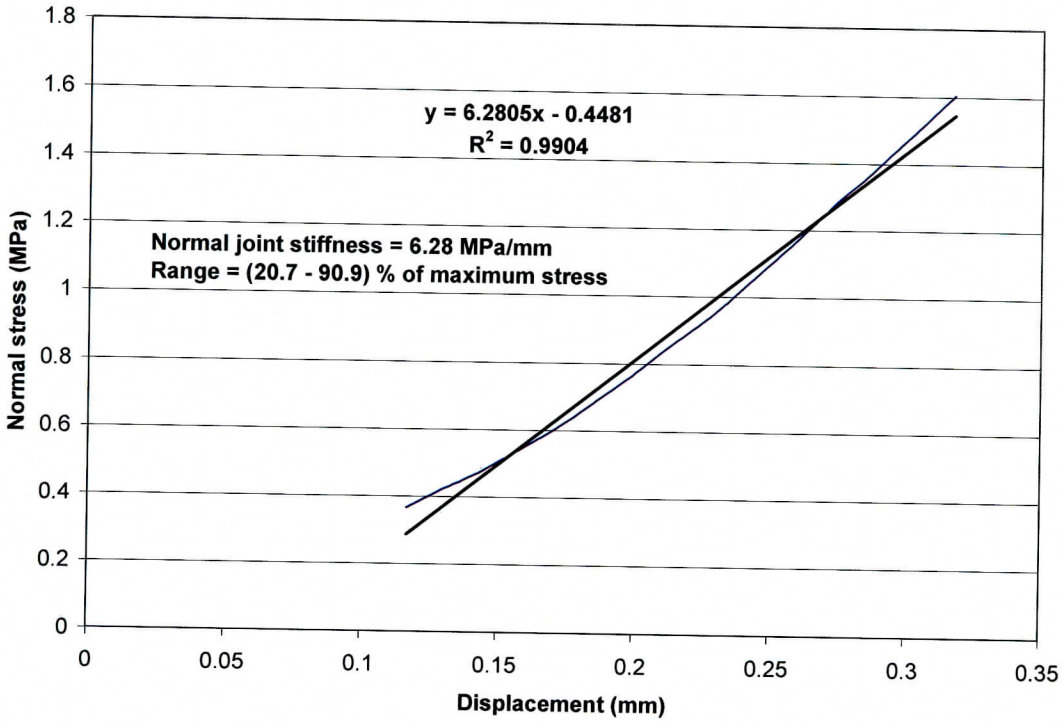

Fig. D1.4 Linear best fit plot of normal stress vs. normal displacement (fifth cycle)

Fig. D1.5: Pre-testing surfaces of specimen 01023540-1-DS (lower half-left, upper half -right).

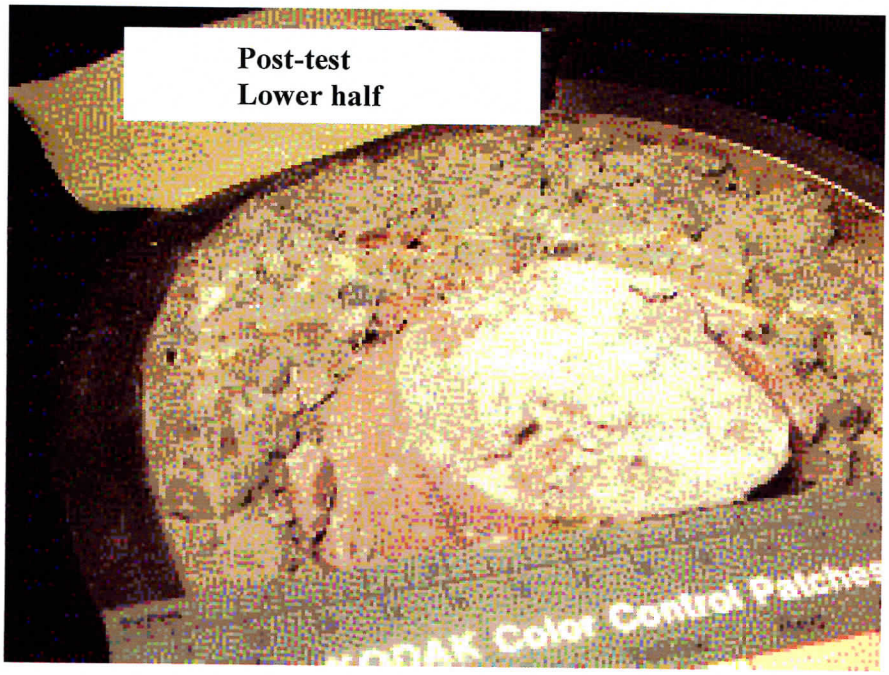

Fig. D1.6: Lower half of specimen 01023540-1-DS after testing

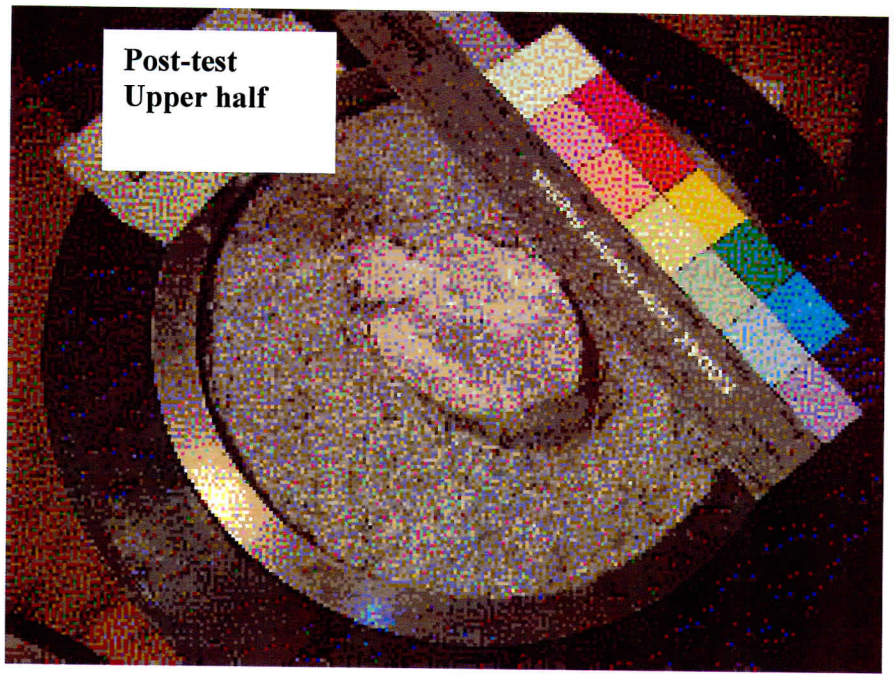

Fig. D1.7: Upper half of specimen 01023540-1-DS after testing

Appendix D2: Direct shear test on specimen 01014781-DS

A direct shear test was performed on specimen 01014781-DS (contact area approximately 5852 mm^2) using the same procedures used for specimen 01023540-1-DS. The test was run through seven shear cycles under progressively increasing normal loads. The second and the seventh runs of the test were incomplete due to tilt/rotation of the machine. In the middle of the fourth cycle, the MTS machine turned off due to overheating and no data were collected. Peak shear loads (shear stresses) and normal loads (normal stresses) during four cycles (cycles 1, 3, 5 and 6) are shown in Table D2.1. The peak shear and normal stresses were calculated by dividing the loads by the apparent contact area. Angle of friction (37.9°) and cohesion (326 kPa) were obtained from the linear best fit plot of shear stress vs. normal stress (Figure D2.1).

The joint normal and shear stiffnesses were calculated from the slopes of normal stress versus normal displacement and shear stress versus shear displacement respectively. (Refer to Figure D2.2 through Figure D2.5). Figures D2.6 through D2.9 show photographs of the specimen before and after testing. The joint roughness coefficients estimated before and after testing ranged from 8 to 10 and 4 to 6 respectively. (Figures D 2.10 and D 2.11).

Table D2.2 summarizes the stiffness results for the four loading cycles. Apart from the sixth run in which a very low normal stiffness was obtained, the joint stiffnesses (normal and shear) increase with increasing normal stress. Higher joint shear stiffnesses for the first and the third runs ($k_n < k_s$) may be due to shearing through the asperities of the joint which smoothens out during the fifth cycle ($k_n > k_s$).

Table D2.1 Peak normal and shear loads (stresses).

Cycle	Normal load(kN)	Shear load (kN)	Normal stress(MPa)	Shear stress (MPa)
1	4.01	4.84	0.68	0.82
3	8.02	8.50	1.36	1.44
5	15.99	14.28	2.71	2.42
6	31.98	16.70	5.42	2.83

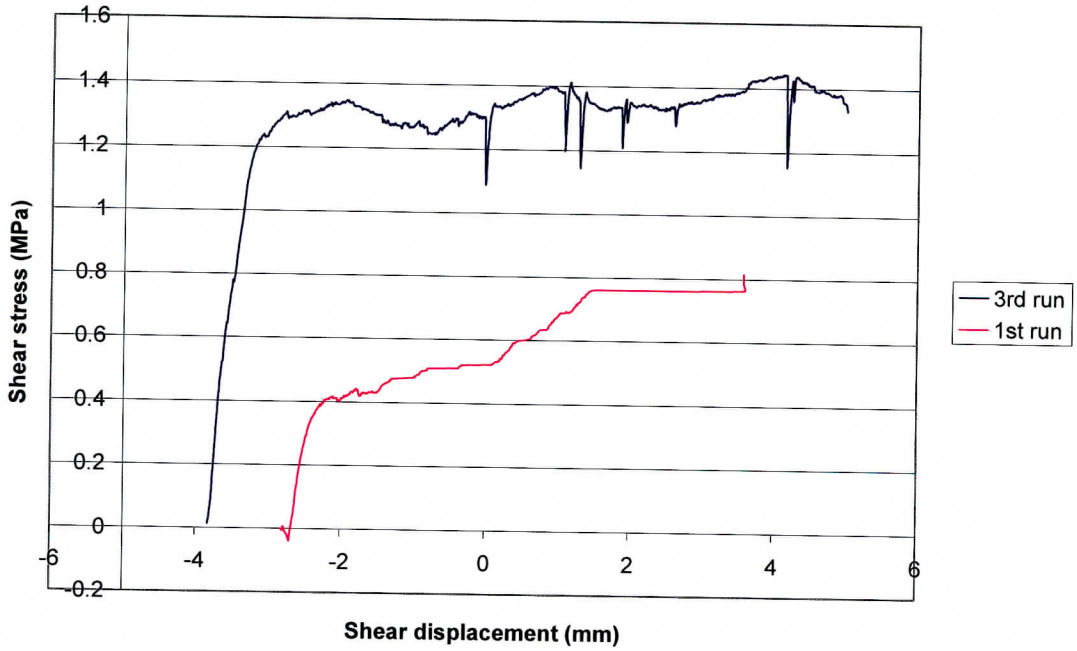

Fig. D2.3: Shear stress-shear displacement curves for the first and third loading cycles.

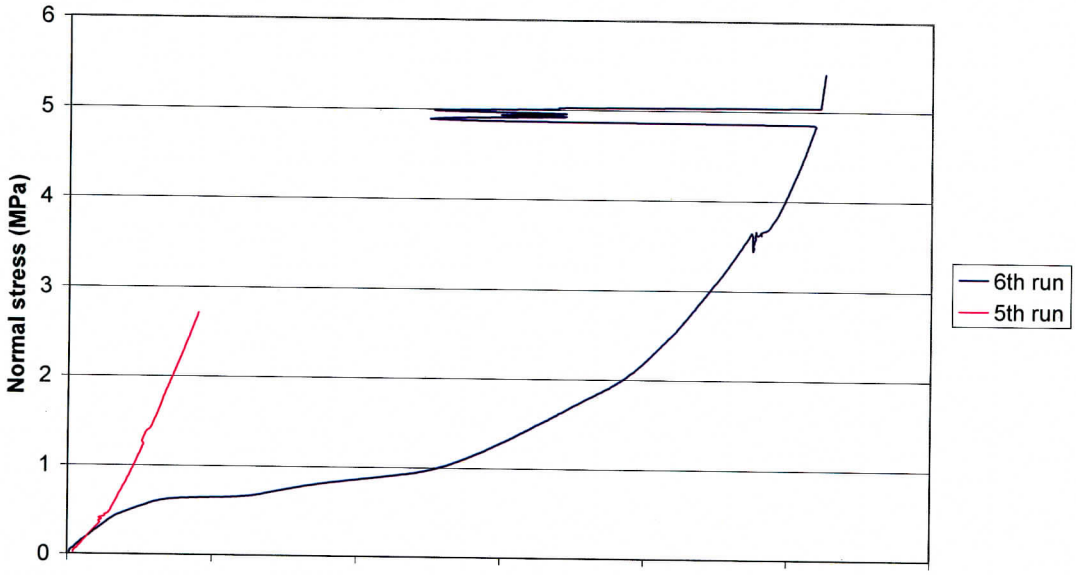

Fig. D2.4: Normal stress-normal displacement curves for the fifth and sixth loading cycles.

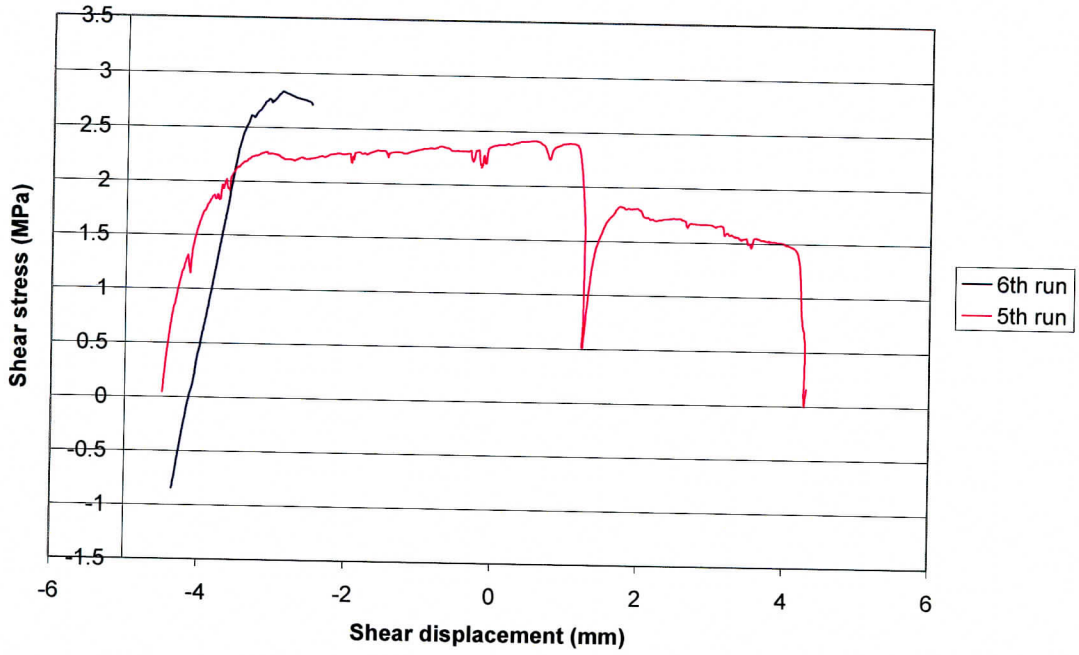

Fig. D2.5: Shear stress-shear displacement curves for the fifth and sixth loading cycles.

Table D2.2: Joint normal and shear stiffnesses.

Cycle	Maximum normal stress (MPa)	k_n MPa/mm	k_s MPa/mm
1	0.68	0.6	0.61
3	1.36	1.22	1.70
5	2.71	3.67	3.45
6	5.42	1.28	3.60

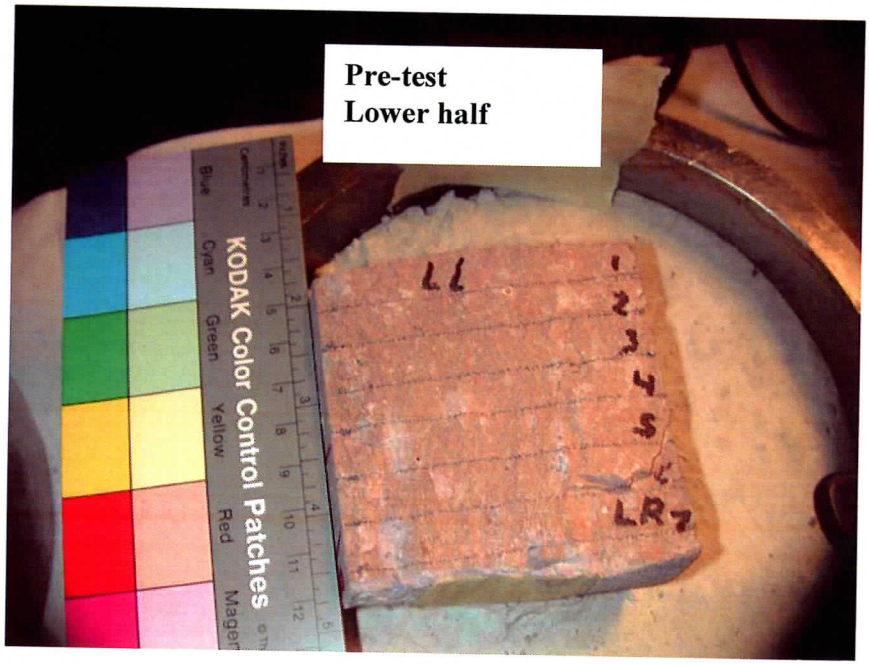

Fig D2.6: Pre-test lower half surface of specimen 01014781-DS

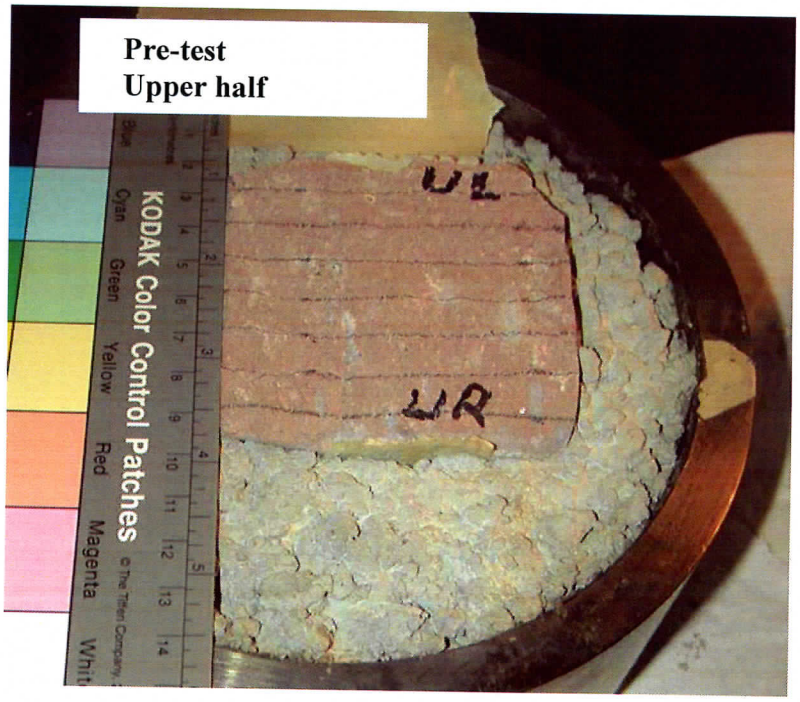

Fig D2.7: Pre-test upper half surface of specimen 01014781-DS

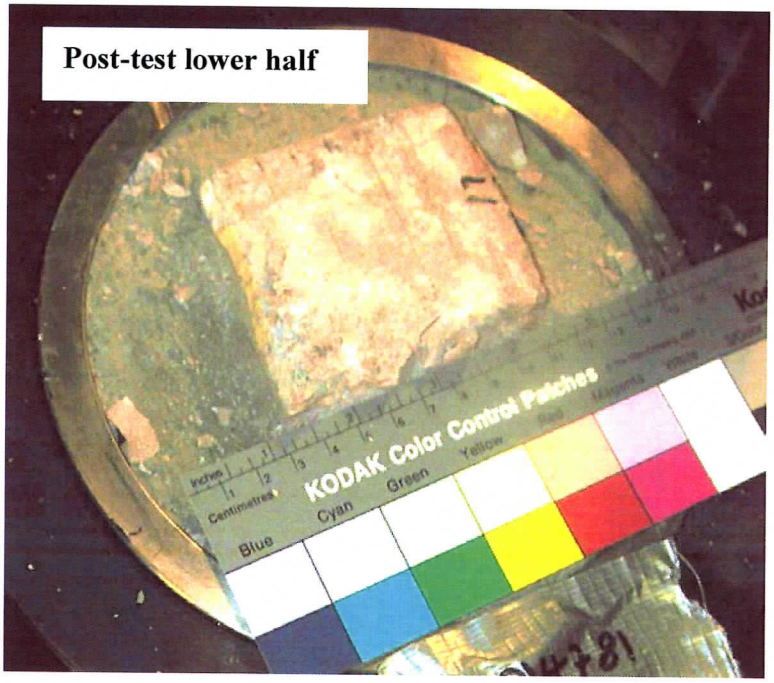

Fig. D2.8: Post-failure lower half of specimen 01014781-DS

Fig D2.9: Post-failure upper half of specimen 01014781-DS

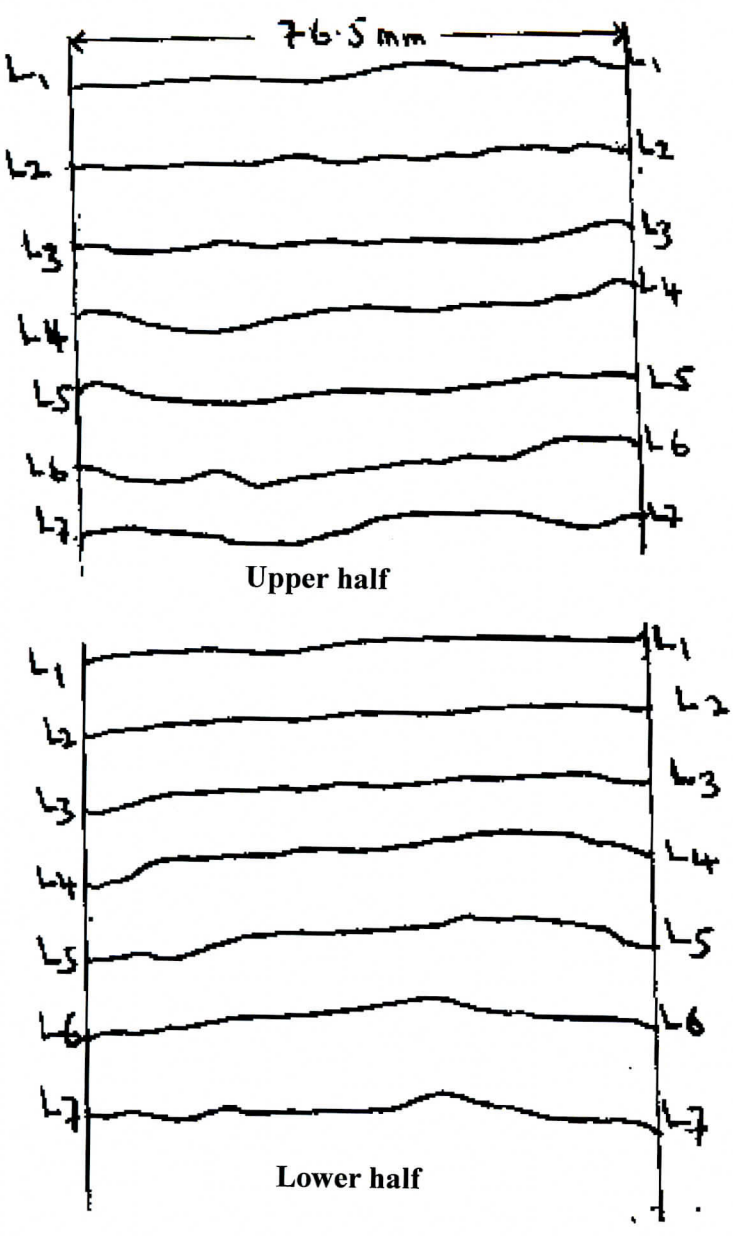

Fig. D2.10: Pre-test profiles of the fracture-surfaces of specimen 01014781-DS (Scale 1:1) (Non-Q, for information only).

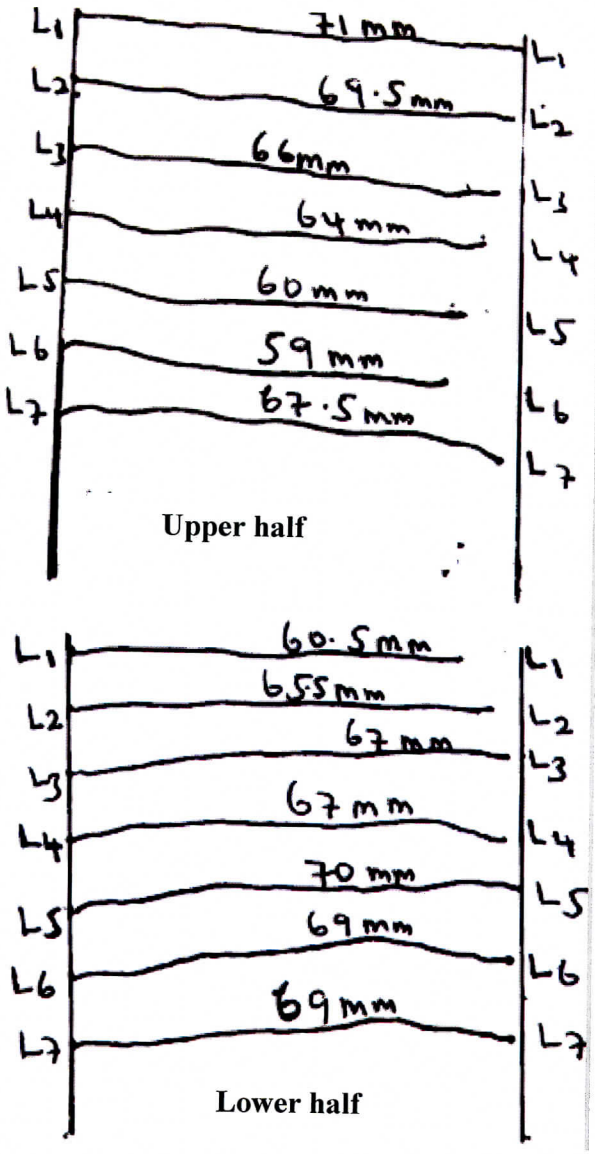

Fig D2.11: Profiles of the fracture-surfaces of specimen 01014781-DS after testing (Scale 1:1) (Non-Q, for information only).

Appendix D3: Direct shear test on specimen 01014782-DS

A direct shear test was performed on specimen 01014782-DS (contact area approximately 5624 mm^2). The test was run through six shear cycles at increasing normal load. The second run of the test was incomplete due to tilt/rotation of the machine. We, however, collected data for the normal loading. There was a severe tilt/rotation just at the end of the normal load application and the beginning of the shear load application during the sixth cycle. We manually adjusted the machine before applying the shear load. Peak shear loads (shear stresses) and normal loads (normal stresses) during the tests are shown in Table D3.1. The peak shear and normal stresses were calculated by dividing the loads by the apparent contact area. Angle of friction (32°) and cohesion (719 kPa) were obtained from the linear best-fit plot of shear stress vs. normal stress (Figure D3.1).

The joint normal and shear stiffnesses were calculated from the slopes of normal stress versus normal displacement and shear stress versus shear displacement respectively. (Refer to Figure D3.2 through Figure D3.7). Figures D3.8 through D3.11 show photographs of pre-test and post-test surfaces. The joint roughness coefficients estimated before and after testing ranged from 8 to 10 and 2 to 4 respectively (Figures D 3.12 and D 3.13).
Table D3.2 summarizes the stiffness results for the six loading cycles. Apart from the second and the sixth runs in which we had tilt/rotation of the direct shear machine, the normal joint stiffness increases with increasing normal stress.

Table D3.1 Peak normal and shear loads (stresses).

Cycle	Normal Load (kN)	Shear force (kN)	Normal stress (MPa)	Shear Stress (MPa)	Test observations
1	2.00	2.48	0.36	0.44	Specimen seemed to slide nicely along peak.
2	3.93	N/A	0.70	N/A	Displacement was too small to reach residual.Tilt/rotation observed.
3	8.01	8.50	1.43	1.52	Severe fracturing of the front left corner of the sample.
4	15.99	13.34	2.86	2.38	Broken pieces on bottom left front Pieces were blown out before the 5^{th} run.
5	31.58	24.85	5.64	4.44	Upper left rear corner broke off.
6	63.1	43.1	11.26	7.7	Type of persistent repeated fracturing.

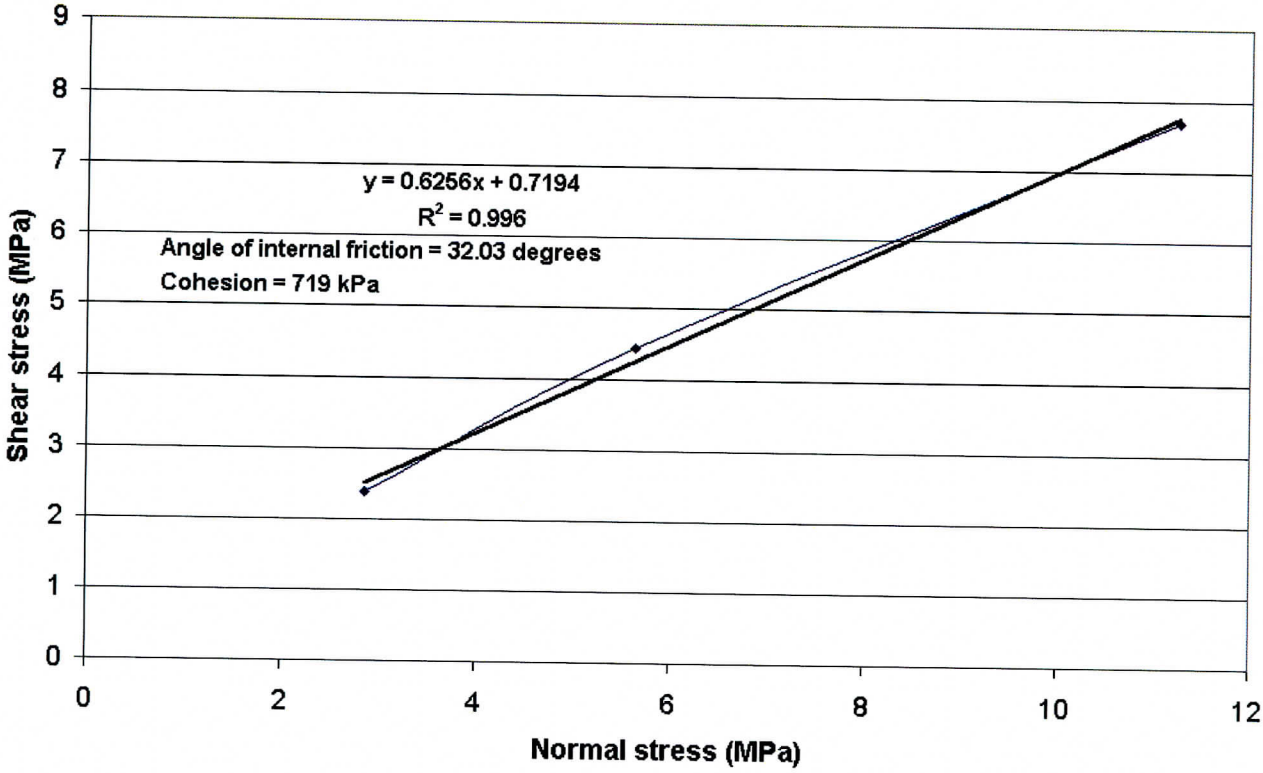

Fig. D3.1 Linear best-fit plot of shear stress vs. normal stress

Table D3.2: Joint normal and shear stiffnesses

Cycle	Maximum normal stress (MPa)	k_n MPa/mm	k_s MPa/mm
1	0.36	1.82	0.03
2	0.70	3.27	N/A
3	1.43	3.17	2.13
4	2.86	4.22	3.41
5	5.64	4.44	0.25
6	11.26	2.93	0.60

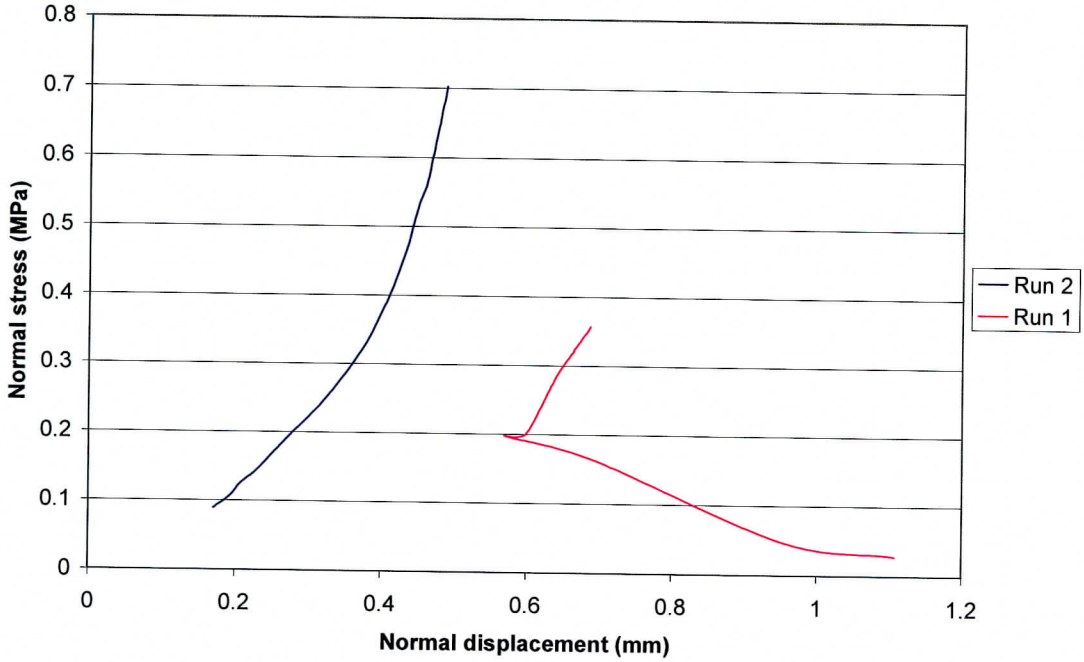

Fig D3.2. Normal stress-normal displacement curves for the first and second cycles

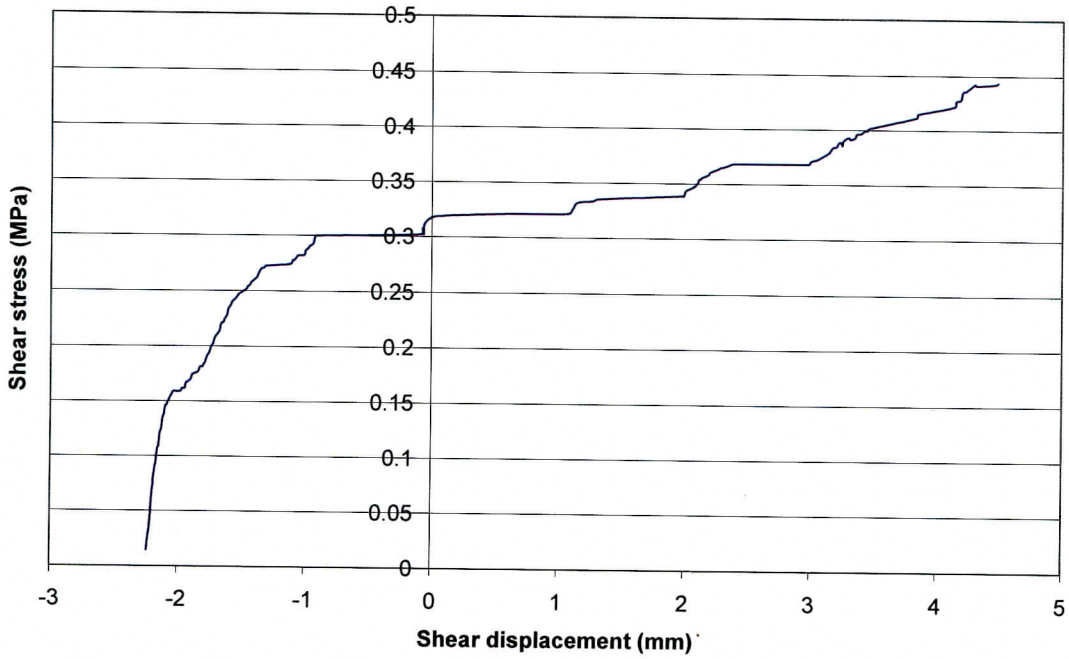

Fig D3.3 Shear stress vs. shear displacement for the first cycle

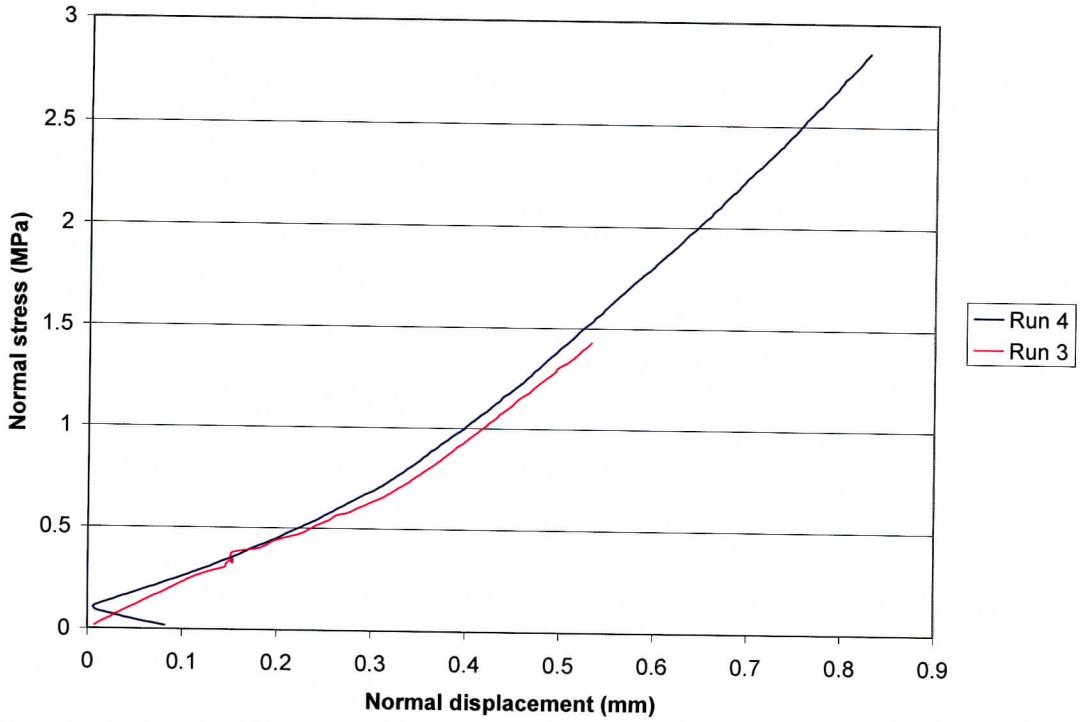

Fig D3.4 Normal stress-normal displacement curves for the third and fourth cycles

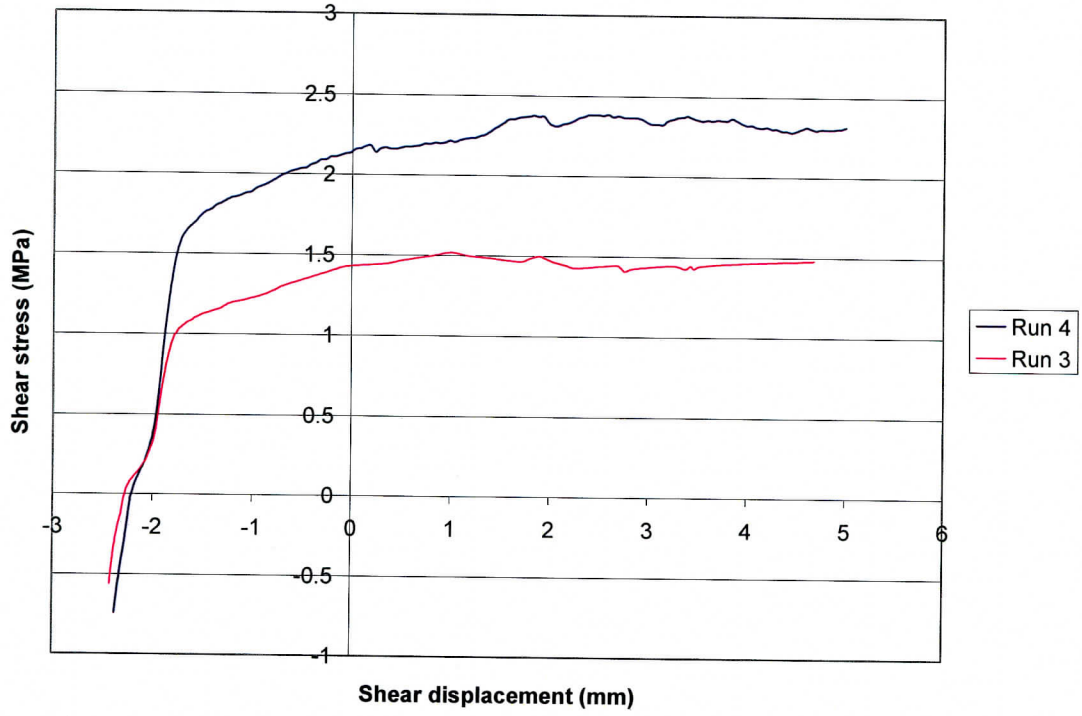

Fig D3.5 Shear stress-shear displacement curves for the third and fourth cycles

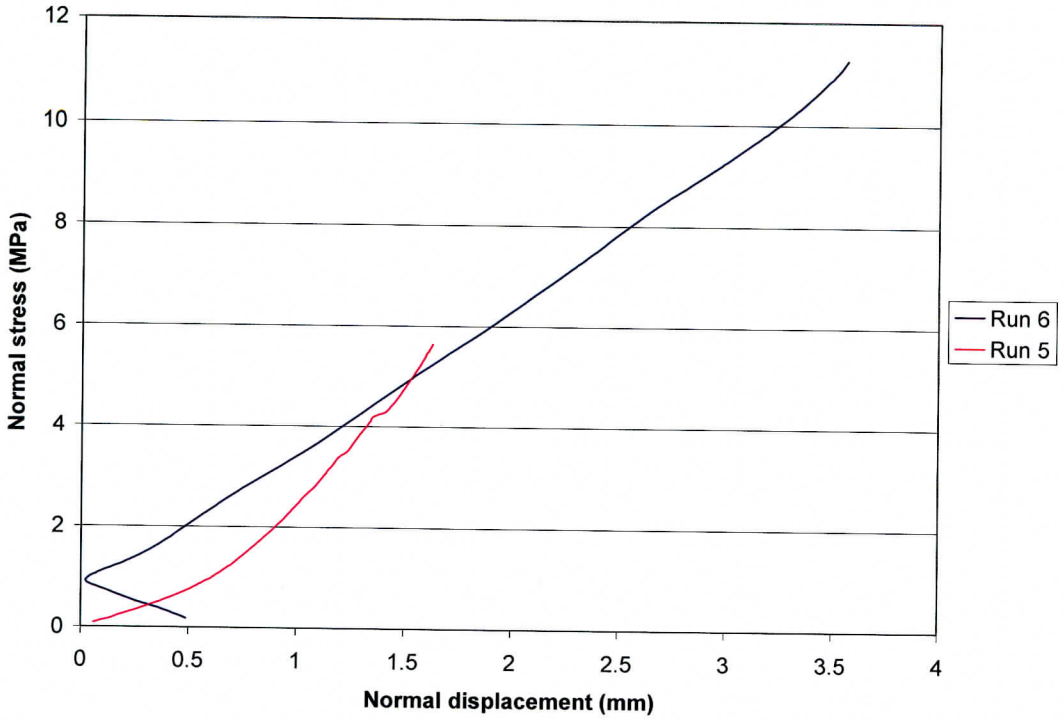

Fig D3.6 Normal stress-normal displacement curves for the fifth and sixth cycles

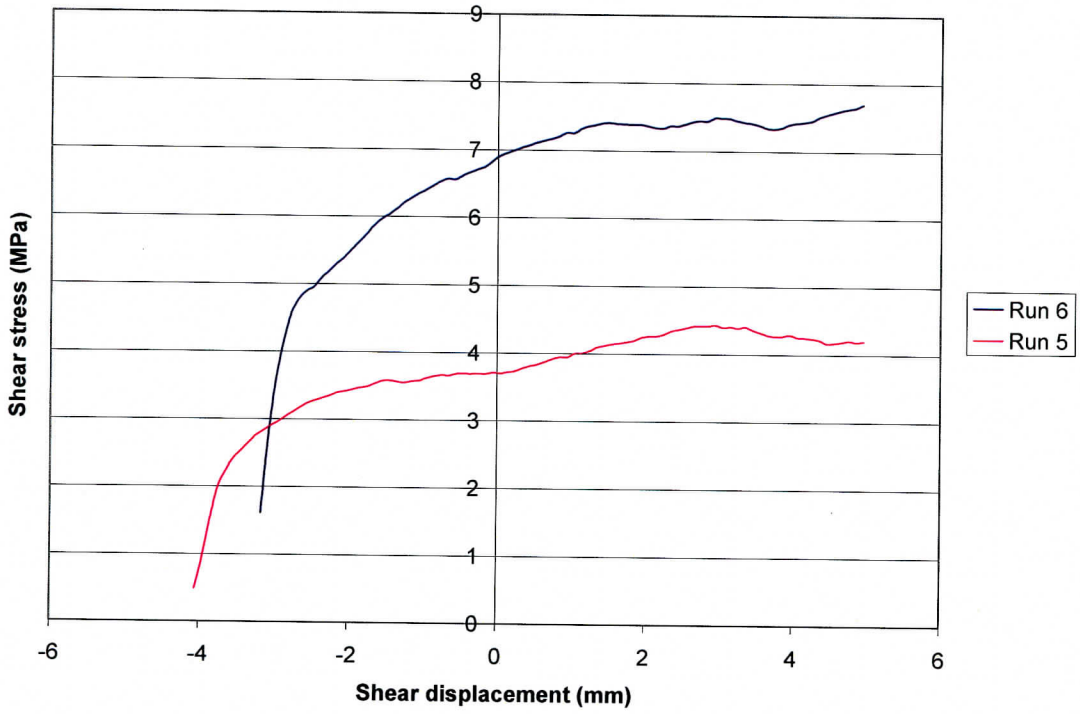

Fig D3.7 Shear stress-shear displacement curves for the fifth and sixth cycles

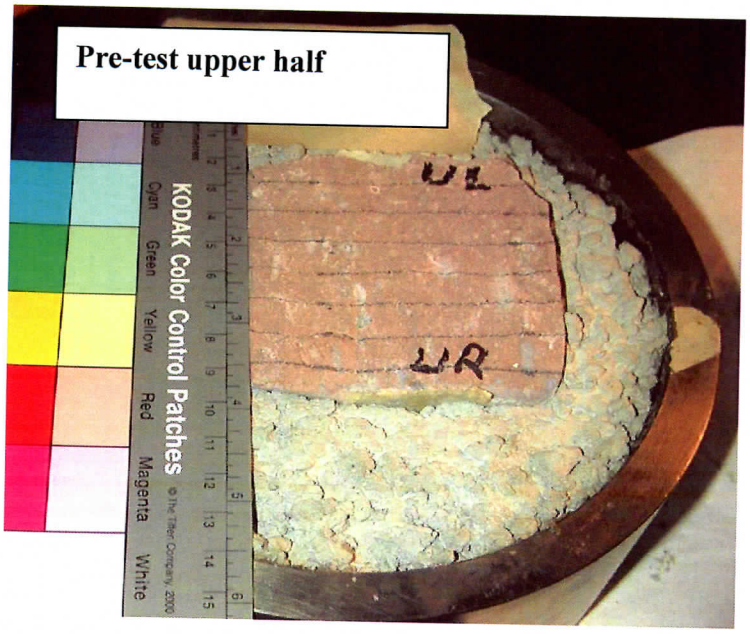

Fig. D 3.8 Pre-test upper half surface of specimen 01014782-DS

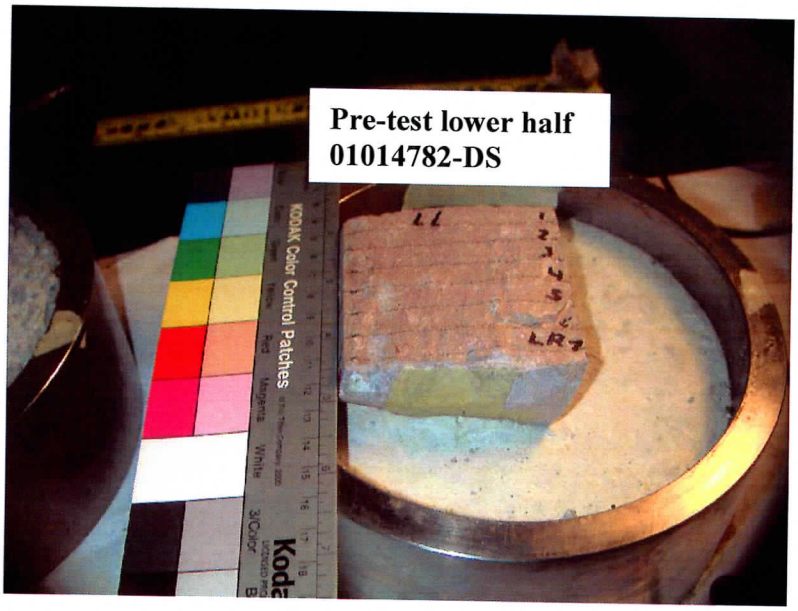

Fig. D 3.9 Pre-test lower half surface of specimen 01014782-DS

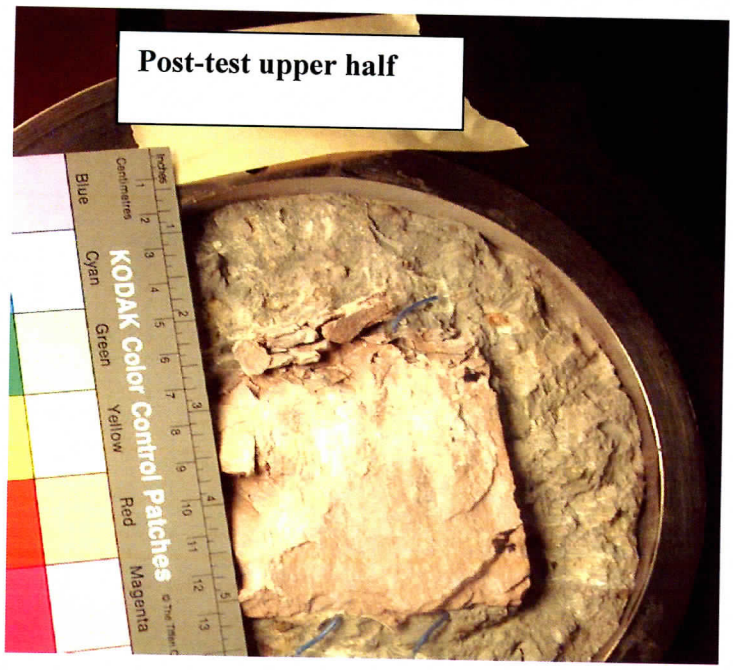

Fig. D 3.10 Post-test upper half surface of specimen 01014782-DS

Fig. D 3.11 Post-test lower half surface of specimen 01014782-DS

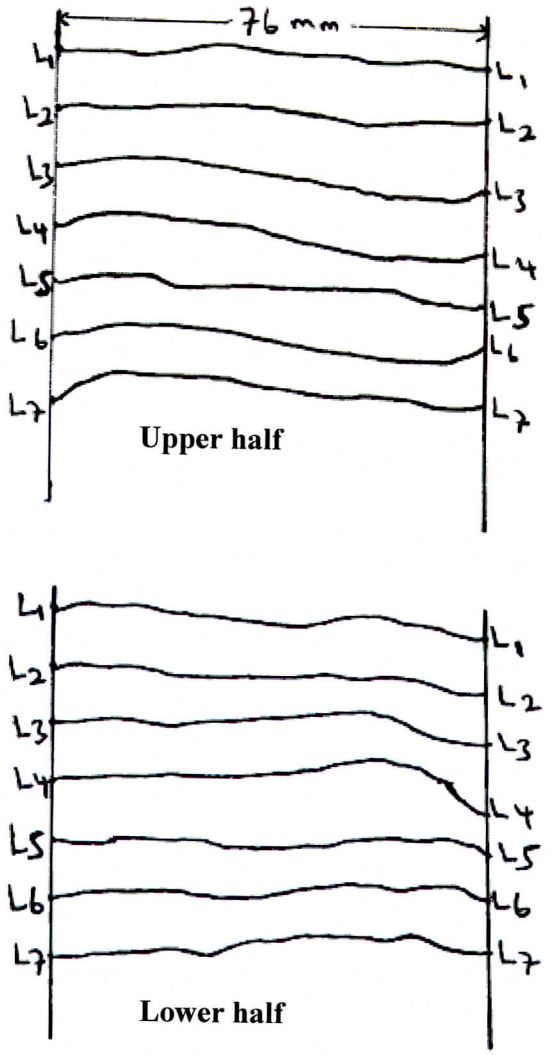

Fig. D3.12 Pre-test profiles of the fracture surfaces of specimen 01014782-DS (Scale 1:1).

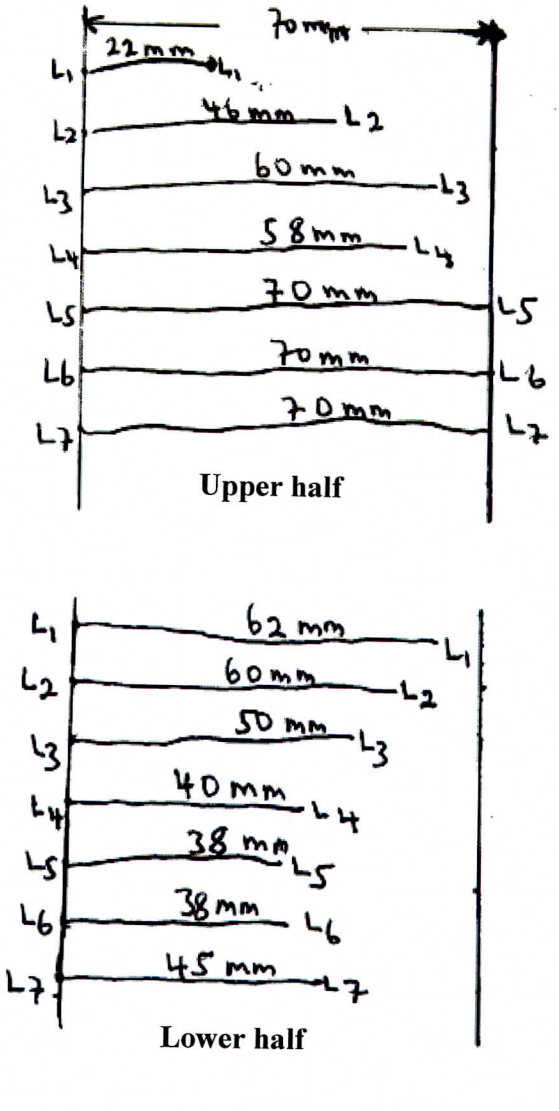

Fig. D3.13 Profiles of the fracture surfaces of specimen 01014782-DS after testing. Scale 1:1.

Appendix D4: Direct shear test on specimen 01023540-3-DS

A direct shear test was performed on an artificial saw cut of specimen 01023540-3-DS (contact area approximately 1964 mm^2). Moisture content measured before testing is 0.45%.

The test was run through six shear cycles under progressively increasing normal loads. No significant tilt/rotation was observed during the test. However, there was a progressive fracture of the upper half (seemed very weak) of the specimen from first run through the sixth run which made the shear data to fluctuate. We, however, collected data for the normal loading. Peak shear loads (shear stresses) and normal loads (normal stresses) during the tests are shown in Table D4.1. The peak shear and normal stresses were calculated by dividing the loads by the apparent contact area. Angle of friction of 31° was obtained from the linear best-fit plot of shear stress vs. normal stress, assuming zero cohesion (Figure D4.1). Roughness coefficients estimated before and after testing ranged from 2 to 4 and 0 to 2 respectively (see Figures D4.2 and D4.3). Figures D4.4 through D4.7 show photographs of pre-test and post-test surfaces.

The joint normal stiffness was calculated from the slopes of normal stress versus normal displacement for all the six cycles. Table D4.2 summarizes the stiffness results for the six loading cycles. The normal joint stiffness increases with increasing normal stress.

Table D4.1 Peak normal and shear loads (stresses).

Cycle	Normal load (kN)	Shear load (kN)	Normal stress (MPa)	Shear Stress (MPa)	Test observations
1	2	1.98	1	0.99	Fracturing of upper half surface observed.
2	3.93	3.65	1.96	1.83	Audible fracture of upper half observed at about 4.5 minutes into the cycle.
3	8	5.93	4	2.96	An extensive breaking up of tail end of upper half.
4	15.99	10.02	8	5.01	Severe fracturing on right side of upper half. No visible damage on left side
5	32.07	18.6	16.04	9.3	Significant fracturing of upper half. Lower half started fracturing as soon as shearing started.
6	64	N/A	32	N/A	Type of bottom half of specimen started breaking up as soon as shearing started. Very large load on wooden insert between steel rings.

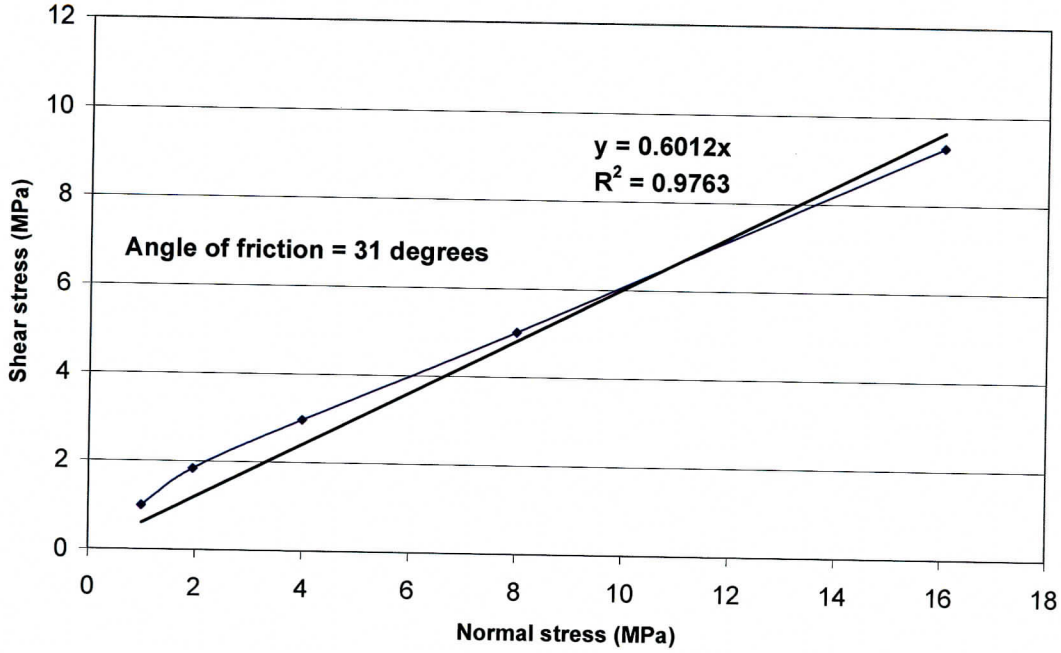

Fig. D4.1 Linear best-fit plot of shear stress vs. normal stress. Best fit straight line is forced through origin (i.e. cohesion assumed equal to zero).

Table D4.2: Joint normal stiffness for the six loading cycles.

Cycle	Maximum normal stress (MPa)	k_n MPa/mm
1	1	0.3
2	1.96	6.13
3	4.0	16.8
4	8.0	33.94
5	16.04	34.9
6	32.0	38.9

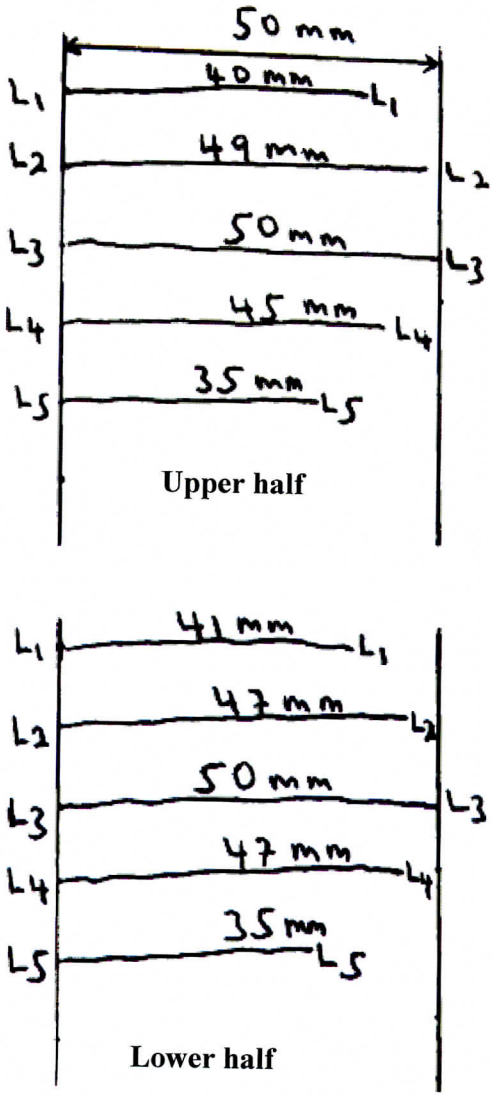

Fig D4.2 Profiles of fracture-surface roughness before testing.

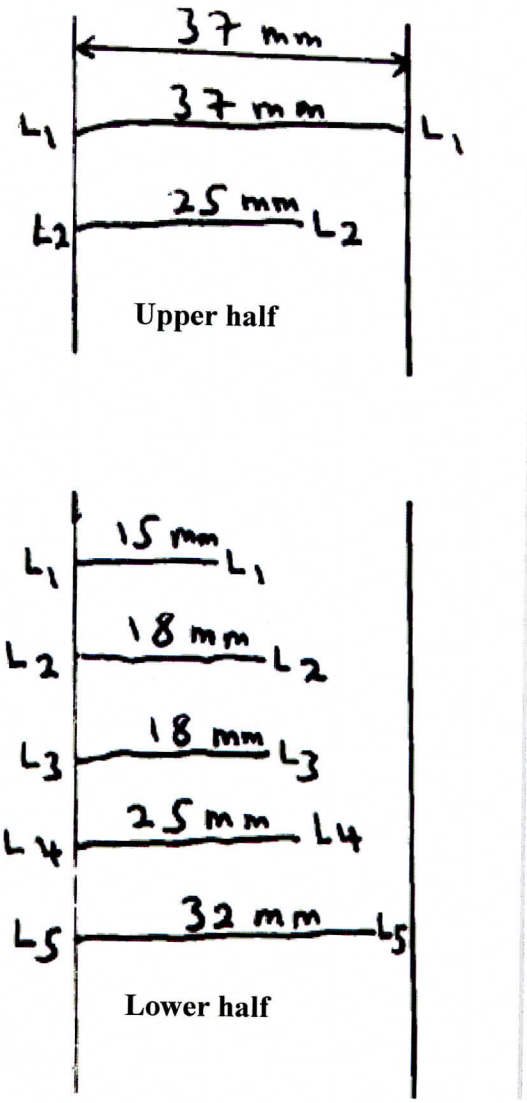

Fig D4.3 Profiles of fracture-surface roughness after testing.

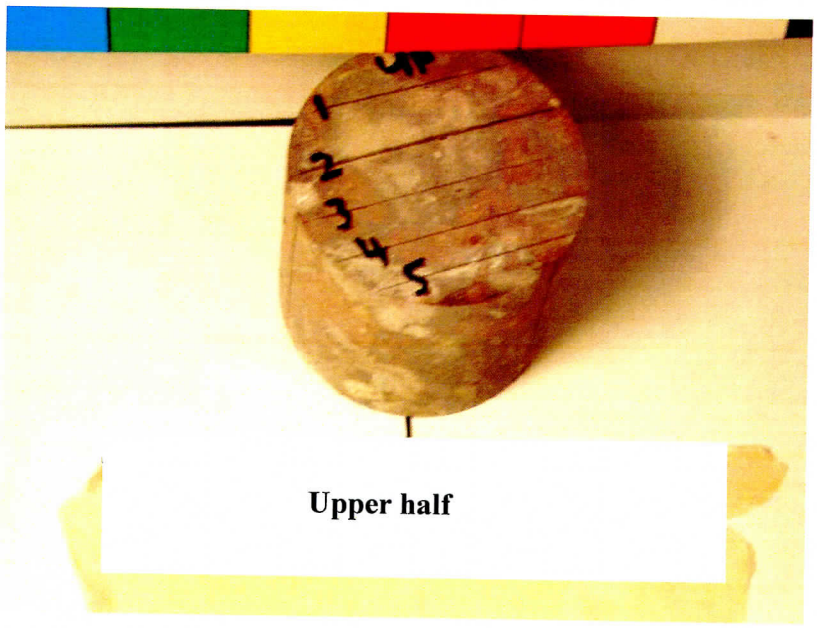

Fig D4.4 Pre-test upper half of specimen 01023540-3-DS

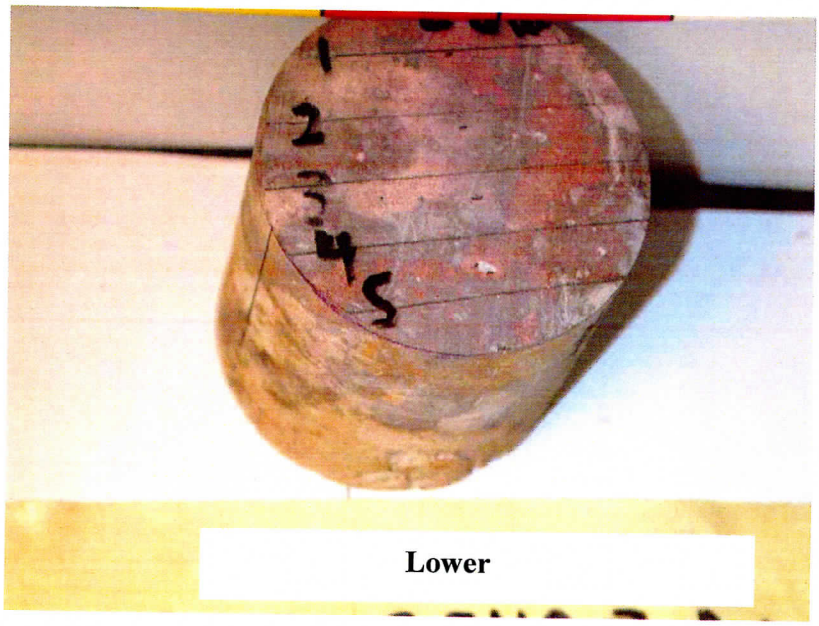

Fig D4.5 Pre-test lower half of specimen 01023540-3-DS

Fig D4.6 Post-test upper half of specimen 01023540-3-DS

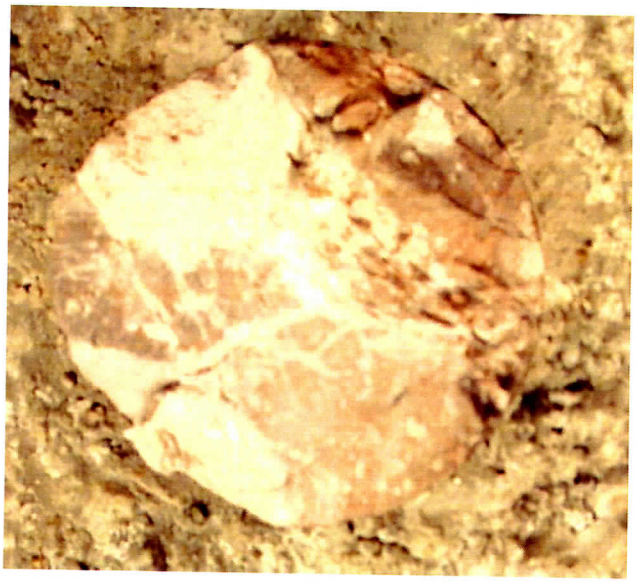

Fig D4.7 Post-test lower half of specimen 01023540-3-DS

Appendix D5: Direct shear test on specimen 01023540-6-DS

A direct shear test was performed on an artificial saw cut of specimen 01023540-6-DS (contact area approximately 2376 mm^2). Moisture content measured before testing is 0.34%.

The test was run through five cycles at incremental normal stresses. At the end of each shear cycle the specimen was repositioned to its initial position. We had an alignment problem during the first run of the test. Most of the front half of the tested area was not in contact during most, probably all of this run. Also, the lower front half of the specimen was dragged forward during the fourth run and we had steel to steel contact at about 2 minutes after shearing was started. Peak shear loads (shear stresses) and normal loads (normal stresses) during the tests are shown in Table 5.1. The peak shear and normal stresses were calculated by dividing the loads by the apparent contact area. Angle of friction (25.9°) was obtained from the linear best-fit plot of shear stress vs. normal stress assuming zero cohesion (Figure 5.1). Roughness coefficients estimated before and after testing ranged from 4 to 6 and 0 to 2 respectively (see Figures 5.2 and 5.3). Figures 5.4 through 5.7 show photographs of pre-test and post-test surfaces.

The joint normal and shear stiffnesses were calculated from the slopes of normal stress versus normal displacement and shear stress versus shear displacements respectively. Table 5.2 summarizes the stiffness results for the five loading cycles.

Table D5.1 Peak normal and shear loads (stresses).

Cycle	Normal load (kN)	Shear load (kN)	Normal stress (MPa)	Shear Stress (MPa)	Test observations
1	1.92	2.19	0.8	0.91	Upper back half, especially on right severely damaged.
2	3.93	3.57	1.64	1.49	Considerable breakage of upper back half.
3	7.94	6.77	3.31	2.82	No contact on front half of nominal contact area.
4	16.0	10.16	6.67	4.23	We had steel to steel contact because the lower front half had been dragged forward.
5	31.97	13.38	13.32	5.57	Severe forward tilting of upper half as soon as shearing was started.

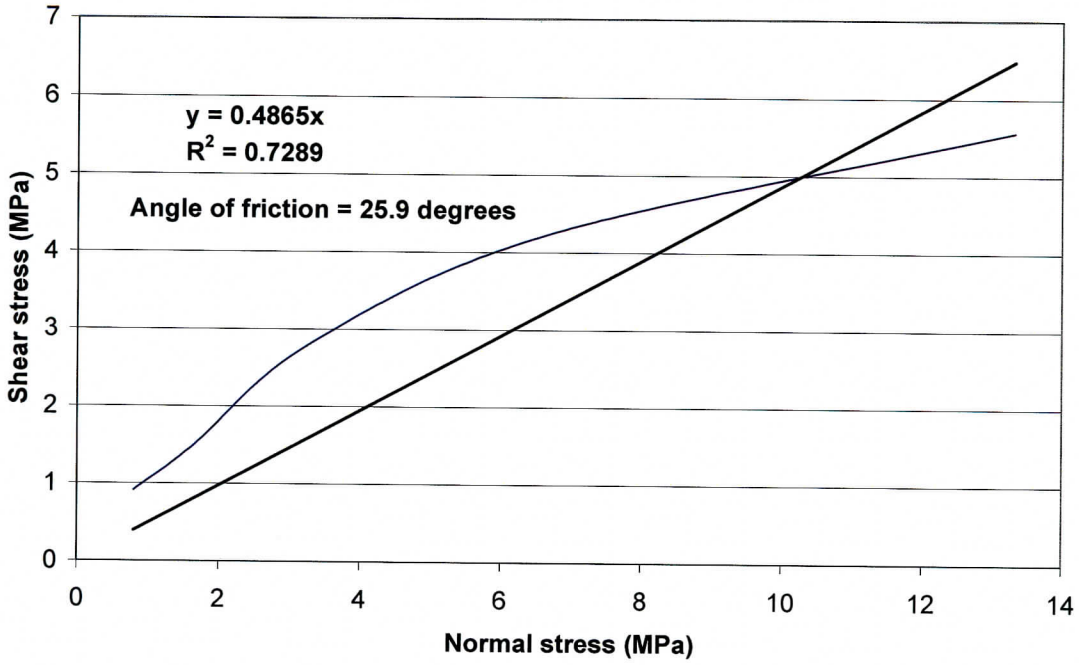

Fig. D5.1 Linear best-fit plot of shear stress vs. normal stress. Best fit straight line is forced through origin (i.e. cohesion assumed equal to zero).

Table D5.2: Joint normal and shear stiffnesses

Cycle	Maximum normal stress (MPa)	k_n MPa/mm	k_s MPa/mm
1	0.8	N/A	0.91
2	1.64	5.4	1.49
3	3.31	7.8	2.82
4	6.67	24.3	4.23
5	13.32	7.31	5.57

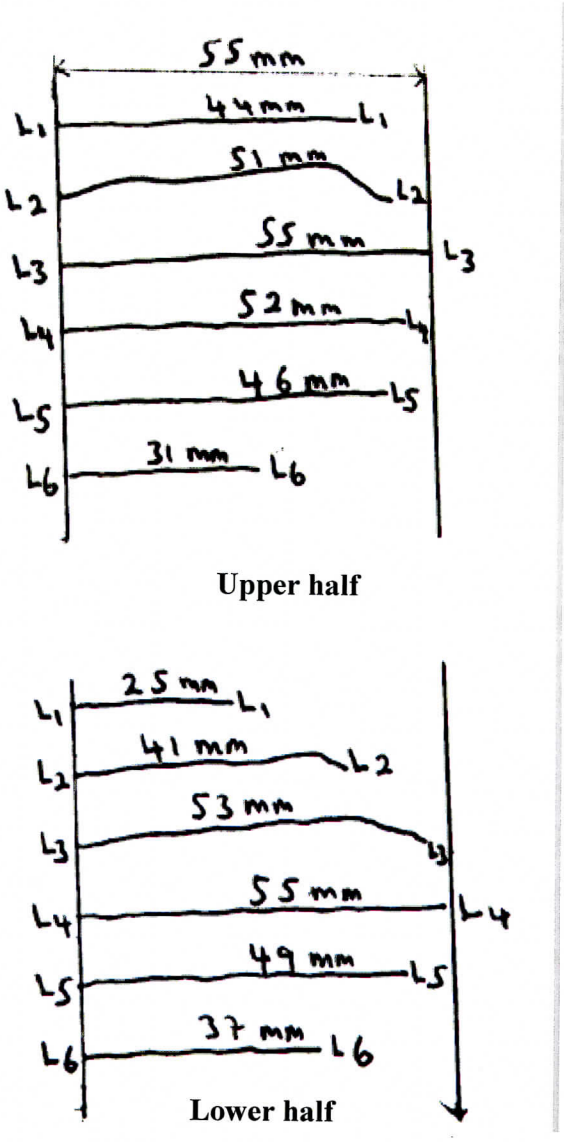

Fig. D5.2 Profiles of fracture-surfaces before testing.

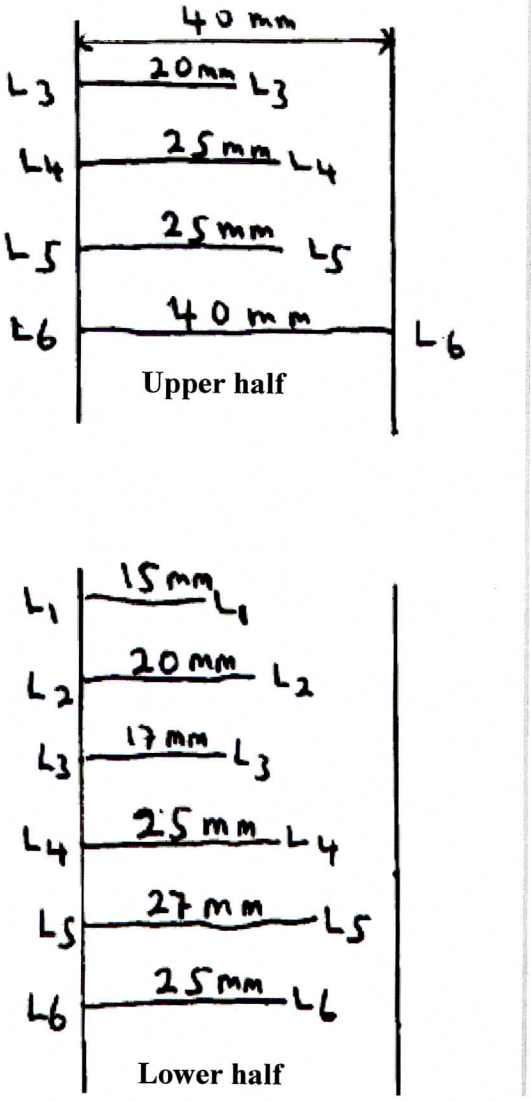

Fig. D5.3 Profiles of fracture-surfaces after testing.

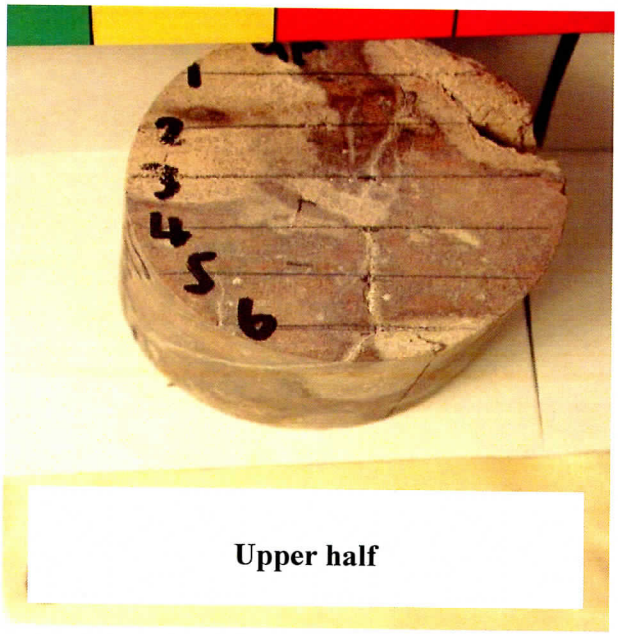

Fig. D5.4 Pre-test upper half of specimen 01023540-6-DS

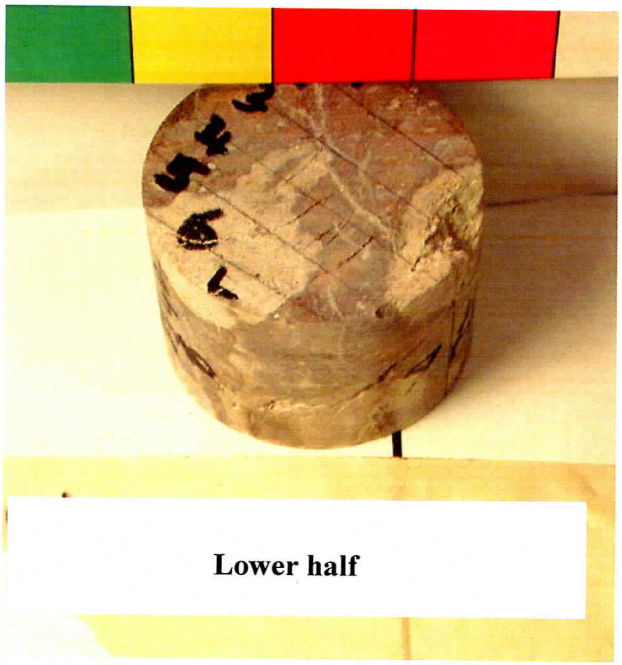

Fig. D5.5 Pre-test lower half of specimen 01023540-6-DS

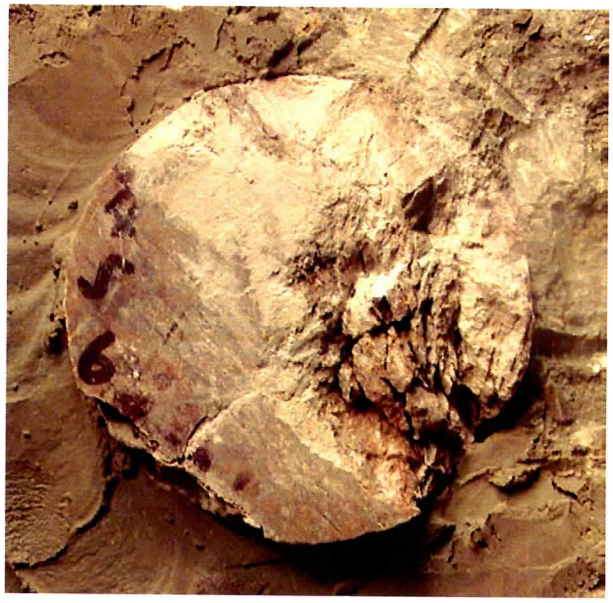

Fig D5.6 Upper half of specimen 01023540-6-DS after testing

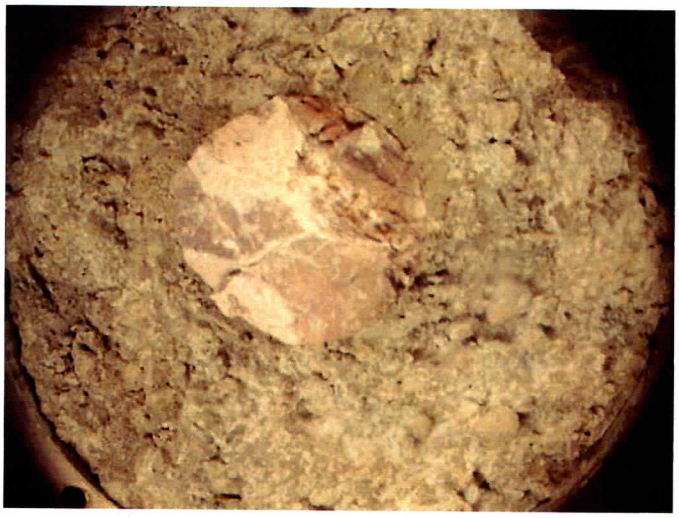

Fig D5.7 Lower half of specimen 01023540-6-DS after testing

Appendix E: Source Information Table

Fig. or Table #	DTN #	Source file within TDA	Scientific Notebook
Table 1.1	Non-Q source with table. Used for information only.	Not applicable	Not applicable
Table 1.2	Non-Q source with table. Used for information only.	Not applicable	Not applicable
Fig 2.5	018LM.004	01023573-3-JU (Photos).doc	UCCSN-UNR-024 vol. 11, attachment 7
Fig. 2.10	018LM.004	01015464-JU (Photos).doc	UCCSN-UNR-024 vol. 8. p. 56
Fig. 2.11	018LM.004	01015013-2-JU (Photos).doc	UCCSN-UNR-024 vol. 8. p. 60
Fig 2.12	018LM.004	01014781-DS (Photos lower half encapsulated).doc	UCCSN-UNR-024 vol. 11, attachment 16
Fig. 2.13	018LM.004	01014781-DS (Photos upper half encapsulated).doc	UCCSN-UNR-024 vol. 11, attachment 16
Fig. 2.14	018LM.004	010243540-1-DS (Photos post failure lower).doc	UCCSN-UNR-024 vol. 11, attachment 15
Fig. 2.15	018LM.004	010243540-1-DS (Photos post failure upper).doc	UCCSN-UNR-024 vol. 11, attachment 15
Fig. 3.1	018LM.004	01023573-3-JU (Analysis, LabView data analysis).xls	Summary of results from the graphs can be found in UCCSN-UNR-024 vol. 11 p. 3
Fig. 3.3 (A)	018LM.004	01023584-3-JU (Analysis, LabView data analysis).xls	Summary of results can be found in UCCSN-UNR-024 vol. 11 p. 26

Fig. or Table #	DTN #	Source file within TDA	Scientific Notebook
Fig 3.3 (C)	018LM.004	01023584-3-JU (Analysis, LabView data analysis).xls	Summary of results can be found in UCCSN-UNR-024 vol. 11 p. 26
Fig 3.4 (A)	018LM.004	01023573-3-JU (Analysis, LabView data analysis).xls	Summary of results from the graphs can be found in UCCSN-UNR-024 vol. 11 p. 5
Fig 3.4 (B)	018LM.004	01023573-3-JU (Analysis, LabView data analysis).xls	Summary of results from the graphs can be found in UCCSN-UNR-024 vol. 11 p. 5
Fig. 3.4 (C)	018LM.004	01023573-3-JU (Analysis, LabView data analysis).xls	Summary of results from the graphs can be found in UCCSN-UNR-024 vol. 11 p. 5
Fig 3.5 (A)	018LM.004	01023584-3-JU (Analysis, LabView data analysis).xls	Summary of results can be found in UCCSN-UNR-024 vol. 11 p. 26
Fig. 3.5 (B)	018LM.004	01023584-3-JU (Analysis, LabView data analysis).xls	Summary of results can be found in UCCSN-UNR-024 vol. 11 p. 26
Fig. 3.6 (A)	018LM.004	01023584-3-JU (Analysis, LabView data analysis).xls	Summary of results can be found in UCCSN-UNR-024 vol. 11 p. 26
Fig. 3.6 (B)	018LM.004	01023584-3-JU (Analysis, LabView data analysis).xls	Summary of results can be found in UCCSN-UNR-024 vol. 11 p. 26
Fig. 3.7	018LM.004	01023570-1-JU (Analysis, extensometer data analysis).xls	Summary of results can be found in UCCSN-UNR-024 vol. 8 p. 93

Fig. or Table #	DTN #	Source file within TDA	Scientific Notebook
Fig. 3.8	018LM.004	01023570-1-JU (Analysis, extensometer data analysis).xls	Summary of results can be found in UCCSN-UNR-024 vol. 8 p. 93
Fig. 3.9	018LM.004	01023570-1-JU (Analysis, extensometer data analysis).xls	Summary of results can be found in UCCSN-UNR-024 vol. 8 p. 93
Table 3.1	018LM.004	01023584-3-JU (Summary of results).doc 01023575-3-JU (Summary of results).doc	UCCSN-UNR-024 vol. 11 p. 5 and p. 26
Table 3.2	018LM.004	01023570-1-JU (Summary of results).doc	UCCSN-UNR-024 vol. 8 p. 93
Table 4.1	018LM.004	01015464-JU (Analysis, LabView data analysis).xls 01015013-2-JU (Analysis, LabView data analysis).xls 01015463-JU (Analysis, LabView data analysis).xls 01014953-1-JU (Analysis, LabView data analysis).xls 01014731-JU (Analysis, LabView data analysis).xls 01023570-1-JU (Analysis, LabView data analysis).xls 01023575-3-JU (Analysis, LabView data analysis).xls 01023682-1-JU (Analysis, LabView data analysis).xls 01023663-3-JU (Analysis, LabView data analysis).xls	UCCSN-UNR-024 vol. 8 pp. 2, 20-25 UCCSN-UNR-024 vol. 8 pp. 30, 37-43 UCCSN-UNR-024 vol. 8 pp. 45-53 UCCSN-UNR-024 vol. 8 pp. 63-69 UCCSN-UNR-024 vol. 8 pp. 70-77 UCCSN-UNR-024 vol. 8 pp. 91-93 UCCSN-UNR-024 vol. 11 pp. 2-7 UCCSN-UNR-024 vol. 11 pp. 9-10 UCCSN-UNR-024 vol. 11 pp. 13-15

continued

Fig. or Table #	DTN #	Source file within TDA	Scientific Notebook
Table 4.1 continued		01023752-JU (Analysis, LabView data analysis).xls 01023696-JU (Analysis, LabView data analysis).xls 01023584-3-JU (Analysis, LabView data analysis).xls	UCCSN-UNR-024 vol. 11 pp. 17-19 UCCSN-UNR-024 vol. 11 pp. 21-24 UCCSN-UNR-024 vol. 11 pp. 25-27
Table 4.2	018LM.004	01015464-JU (Summary).doc 01015013-2-JU (Summary).doc 01015463-JU (Summary).doc 01014953-1-JU (Summary).doc 01014731-JU (Summary).doc 01023570-1-JU (Summary).doc 01023575-3-JU (Summary).doc 01023682-1-JU (Summary).doc 01023663-3-JU (Summary).doc 01023752-JU (Summary).doc 01023696-JU (Summary).doc 01023584-3-JU (Summary).doc SMF Specimen Custody Receipt, Shipment ID: 01000527, Shipping date: 28-Nov.-2001.	UNR-024 vol. 8 p.2 UNR-024 vol. 8 p.30 UNR-024 vol. 8 p.45 UNR-024 vol. 8 p.63 UNR-024 vol. 8 p.70 UNR-024 vol. 8 p.91 UNR-024 vol. 11 p.2 UNR-024 vol. 11 p.8 UNR-024 vol. 11 p.13 UNR-024 vol. 11 p.17 UNR-024 vol. 11 p.21 UNR-024 vol. 11 p.25
Table 4.3	018LM.004	01015464-JU (Summary).doc 01015013-2-JU (Summary).doc 01015463-JU (Summary).doc 01014953-1-JU (Summary).doc 01014731-JU (Summary).doc 01023570-1-JU (Summary).doc 01023575-3-JU (Summary).doc 01023682-1-JU (Summary).doc 01023663-3-JU (Summary).doc	Joint normal and shear stiffness calculations were reviewed and corrected by the PI. Final results can be found on page 36 of the technical report.

continued		01023752-JU (Summary).doc 01023696-JU (Summary).doc	
Fig. or Table #	**DTN #**	**Source file within TDA**	**Scientific Notebook**
Table 4.3		01023584-3-JU (Summary).doc	
Fig A1.2	018LM.004	01015464-JU (Analysis, LabView data analysis).xls	Summary of results can be found in UCCSN-UNR-024 vol. 8 pp. 20 and 23
Fig A1.3	018LM.004	01015464-JU (Analysis, LabView data analysis).xls	Summary of results can be found in UCCSN-UNR-024 vol. 8 pp. 20 and 24
Fig. A1.4	018LM.004	01015464-JU (Analysis, LabView data analysis).xls	Summary of results can be found in UCCSN-UNR-024 vol. 8 pp. 21 and 25
Fig A1.5	018LM.004	01015464-JU (Analysis, extensometer data analysis).xls	Summary of results can be found in UCCSN-UNR-024 vol. 8 pp. 22 and 26
Table A1.1	018LM.004	01015464-JU (summary).doc	UCCSN-UNR-024 vol. 8 p. 20
Table A1.2	018LM.004	01015464-JU (summary).doc	UCCSN-UNR-024 vol. 8 p. 21
Table A1.3	018LM.004	01015464-JU (summary).doc	UCCSN-UNR-024 vol. 8 p. 22
Table A1.4	018LM.004	01015464-JU (summary).doc	UCCSN-UNR-024 vol. 8 p. 22
Fig. A1.6	018LM.004	01015464-JU (Photos).doc	UCCSN-UNR-024 vol. 8 attachment 1
Fig. A2.1	018LM.004	01015013-2-JU (Analysis, LabView data analysis).xls	UCCSN-UNR-024 vol. 8 pp. 38, 40
Fig A2.2.	018LM.004	01015013-2-JU (Analysis, LabView data analysis).xls	UCCSN-UNR-024 vol. 8 p.42
Fig A2.3.	018LM.004	01015013-2-JU (Analysis, extensometer data analysis).xls	Summary of results can be found in UCCSN-UNR-024 vol. 8 p.43

Fig. or Table #	DTN #	Source file within TDA	Scientific Notebook
Table A2.1	018LM.004	01015013-2-JU (summary).doc	UCCSN-UNR-024 vol. 8 p. 37-42. (Calculations corrected later in the technical report)
Table A2.2	018LM.004	01015013-2-JU (summary).doc	UCCSN-UNR-024 vol. 8 p. 37-42. (Calculations corrected later in technical report)
Table A2.3	018LM.004	01015013-2-JU (summary).doc	UCCSN-UNR-024 vol. 8 p. 43. (Calculations corrected later in the electronic data base "Summary of Results" section)
Table A2.4	018LM.004	01015013-2-JU (photos test arrangement).doc	UCCSN-UNR-024 vol. 8 attachment 2 (the same set up after testing)
Fig A3.1	018LM.004	01015463-JU (Analysis, LabView data analysis).xls	Summary of results can be found in UCCSN-UNR-024 vol. 8 p.47-51. (Calculations corrected later in the technical report)
Fig A3.2	018LM.004	01015463-JU (Analysis, LabView data analysis).xls	Summary of results can be found in UCCSN-UNR-024 vol. 8 p.47. (Calculations corrected later in the technical report)
Fig A3.3	018LM.004	01015463-JU (Analysis, LabView data analysis).xls	Summary of results can be found in UCCSN-UNR-024 vol. 8 p.47. (Calculations

			corrected later in the technical report)
Fig. or Table #	**DTN #**	**Source file within TDA**	**Scientific Notebook**
Table A3.1	018LM.004	01015463-JU (summary).doc	UCCSN-UNR-024 vol. 8 p.47. (Calculations corrected later in the technical report)
Table A3.2	018LM.004	01015463-JU (summary).doc	UCCSN-UNR-024 vol. 8 p.47. (Calculations corrected later in the technical report)
Table A3.3	018LM.004	01015463-JU (summary).doc	UCCSN-UNR-024 vol. 8 p.54.
Fig A3.4	018LM.004	01015013-2-JU (photos along 270).doc	UCCSN-UNR-024 vol. 8 attachment 3
Fig A3.5	018LM.004	01015013-2-JU (photos test arrangement).doc	UCCSN-UNR-024 vol. 8 attachment 3
Fig A4.1	018LM.004	01014953-1-JU (Analysis).xls	UCCSN-UNR-024 vol. 8 p.64. (Calculations corrected later in the technical report)
Fig A4.2	018LM.004	01014953-1-JU (Analysis).xls	UCCSN-UNR-024 vol. 8 p.64.
Table A4.1	018LM.004	01014953-1-JU (Summary, summary of results).doc	UCCSN-UNR-024 vol. 8 p.64. (Calculations corrected later in the technical report)
Table A4.2	018LM.004	01014953-1-JU (Summary, summary of results).doc	UCCSN-UNR-024 vol. 8 p.64.
Table A4.3	018LM.004	01014953-1-JU (Summary, summary of results).doc	UCCSN-UNR-024 vol. 8 p.69.
Fig A4.3	018LM.004	01014953-1-JU (photos along 0).doc	UCCSN-UNR-024 vol. 8 attachment 4
Fig A4.4	018LM.004	01014953-1-JU (photos post-top).doc	UCCSN-UNR-024 vol. 8 attachment 4

Fig. or Table #	DTN #	Source file within TDA	Scientific Notebook
FigA5.1	018LM.004	01014731-JU (Analysis, LabView data analysis).xls	UCCSN-UNR-024 vol. 8 p.71. (Calculations corrected later in the technical report)
FigA5.2	018LM.004	01014731-JU (Analysis, LabView data analysis).xls	UCCSN-UNR-024 vol. 8 p.71.
Table A5.1	018LM.004	01014731-JU (Summary, summary of results).doc	UCCSN-UNR-024 vol. 8 p.71. (Calculations corrected later in the technical report)
Table A5.2	018LM.004	01014731-JU (Summary, summary of results).doc	UCCSN-UNR-024 vol. 8 p.71. (Calculations corrected later in the technical report)
Table A5.3	018LM.004	01014731-JU (Summary, summary of results).doc	UCCSN-UNR-024 vol. 8 p.77.
Fig A5.3	018LM.004	01014731-JU (Photos, photo along 180).doc	UCCSN-UNR-024 vol. 8 attachment 5
Fig A5.4	018LM.004	01014731-JU (Photos, photo along 0).doc	UCCSN-UNR-024 vol. 8 attachment 5
Fig A6.1	018LM.004	01023570-1-JU (Analysis, LabView data analysis).xls	UCCSN-UNR-024 vol. 8 p.92. (Calculations corrected later in the technical report)
Fig A6.2	018LM.004	01023570-1-JU (Analysis, LabView data analysis).xls	UCCSN-UNR-024 vol. 8 p.92. (Calculations corrected later in the technical report)
Fig A6.3	018LM.004	01023570-1-JU (Analysis, LabView data analysis).xls	UCCSN-UNR-024 vol. 8 p.92. (Calculations corrected later in the technical report)

Fig. or Table #	DTN #	Source file within TDA	Scientific Notebook
Fig A6.4	018LM.004	01023570-1-JU (Analysis, LabView data analysis).xls	This graph was used for information purposes to calculate the strain rate.
Fig A6.5	018LM.004	01023570-1-JU (Analysis, extensometer data analysis).xls	UCCSN-UNR-024 vol. 8 p.93.
Table A6.1	018LM.004	01023570-1-JU (Summary, summary of results).doc	UCCSN-UNR-024 vol. 8 p.92. (Calculations corrected later in the technical report)
Table A6.2	018LM.004	01023570-1-JU (Summary, summary of results).doc	UCCSN-UNR-024 vol. 8 p.93.
Table A6.3	018LM.004	01023570-1-JU (Summary, summary of results).doc	UCCSN-UNR-024 vol. 8 p.96.
Table A6.4	018LM.004	01023570-1-JU (Summary, summary of results).doc	UCCSN-UNR-024 vol. 8 p.93.
Fig A6.6	018LM.004	01023570-1-JU (Photos instrument).doc	UCCSN-UNR-024 vol. 8 attachment 6
Fig A6.7	018LM.004	01023570-1-JU (Photos post failure).doc	UCCSN-UNR-024 vol. 8 attachment 6
Fig A7.1	018LM.004	01023575-3-JU (Analysis, LabView data analysis).xls	Summary of results can be found in UCCSN-UNR-024 vol. 11 p.3.
Fig A7.2	018LM.004	01023575-3-JU (Analysis, LabView data analysis).xls	Summary of results can be found in UCCSN-UNR-024 vol. 11 p.3.
Fig A7.3	018LM.004	01023575-3-JU (Analysis, LabView data analysis).xls	Summary of results can be found in UCCSN-UNR-024

			vol. 11 p.4.
Fig. or Table #	**DTN #**	**Source file within TDA**	**Scientific Notebook**
Fig A7.4	018LM.004	01023575-3-JU (Analysis, LabView data analysis).xls	Summary of results can be found in UCCSN-UNR-024 vol. 11 p.4.
Fig A7.5	018LM.004	01023575-3-JU (Analysis, LabView data analysis).xls	Summary of results can be found in UCCSN-UNR-024 vol. 11 p.4.
Fig A7.6	018LM.004	01023575-3-JU (Analysis, LabView data analysis).xls	Summary of results can be found in UCCSN-UNR-024 vol. 11 p.5.
Fig A7.7	018LM.004	01023575-3-JU (Analysis, LabView data analysis).xls	Summary of results can be found in UCCSN-UNR-024 vol. 11 p.5.
Fig A7.8	018LM.004	01023575-3-JU (Analysis, LabView data analysis).xls	Summary of results can be found in UCCSN-UNR-024 vol. 11 p.5.
Fig A7.9	018LM.004	01023575-3-JU (Analysis, LabView data analysis).xls	Summary of results can be found in UCCSN-UNR-024 vol. 11 p.5.
Fig A7.10	018LM.004	01023575-3-JU (Analysis, LabView data analysis).xls	Summary of results can be found in UCCSN-UNR-024 vol. 11 p.5.
Fig A7.11	018LM.004	01023575-3-JU (Analysis, extensometer analysis).xls	Summary of results can be found in UCCSN-UNR-024 vol. 11 p.6.
Fig A7.12	018LM.004	01023575-3-JU (Analysis, extensometer	Summary of results can be

		analysis).xls	found in UCCSN-UNR-024 vol. 11 p.6.
Fig. or Table #	**DTN #**	**Source file within TDA**	**Scientific Notebook**
Table A7.1	018LM.004	01023575-3-JU (Summary, summary of results).doc	UCCSN-UNR-024 vol. 11 p.3.
Table A7.2	018LM.004	01023575-3-JU (Summary, summary of results).doc	UCCSN-UNR-024 vol. 11 p.3.
Table A7.3	018LM.004	01023575-3-JU (Summary, summary of results).doc	UCCSN-UNR-024 vol. 11 p.4.
Table A7.4	018LM.004	01023575-3-JU (Summary, summary of results).doc	UCCSN-UNR-024 vol. 11 p.4.
Table A7.5	018LM.004	01023575-3-JU (Summary, summary of results).doc	UCCSN-UNR-024 vol. 11 p.5.
Table A7.6	018LM.004	01023575-3-JU (Summary, summary of results).doc	UCCSN-UNR-024 vol. 11 p.5.
Table A7.7	018LM.004	01023575-3-JU (Summary, summary of results).doc	UCCSN-UNR-024 vol. 11 p.5.
Table A7.8	018LM.004	01023575-3-JU (Summary, summary of results).doc	UCCSN-UNR-024 vol. 11 p.5.
Table A7.9	018LM.004	01023575-3-JU (Summary, summary of results).doc	UCCSN-UNR-024 vol. 11 p.6.
Table A7.10	018LM.004	01023575-3-JU (Summary, summary of results).doc	UCCSN-UNR-024 vol. 11 p.6.
Table A7.11	018LM.004	01023575-3-JU (Summary, summary of results).doc	UCCSN-UNR-024 vol. 11 p.6.
Table A7.12	018LM.004	01023575-3-JU (Summary, summary of results).doc	UCCSN-UNR-024 vol. 11 p.7.
Fig A7.13	018LM.004	01023573-3-JU (photos, instrument).doc	UCCSN-UNR-024 vol. 11 attachment 7

Fig A7.14	018LM.004	01023575-3-JU (photos, along 270).doc	UCCSN-UNR-024 vol. 11 attachment 7
Fig. or Table #	**DTN #**	**Source file within TDA**	**Scientific Notebook**
Fig A8.1	018LM.004	01023682-1-JU (Analysis, LabView data analysis).xls	Summary of results can be found in UCCSN-UNR-024 vol. 11 p.9.
Fig A8.2	018LM.004	01023682-1-JU (Analysis, LabView data analysis).xls	Summary of results can be found in UCCSN-UNR-024 vol. 11 p.9.
Fig A8.3	018LM.004	01023682-1-JU (Analysis, LabView data analysis).xls	Summary of results can be found in UCCSN-UNR-024 vol. 11 p.10.
Fig A8.4	018LM.004	01023682-1-JU (Analysis, LabView data analysis).xls	Summary of results can be found in UCCSN-UNR-024 vol. 11 p.10.
Fig A8.5	018LM.004	01023682-1-JU (Analysis, LabView data analysis).xls	Summary of results can be found in UCCSN-UNR-024 vol. 11 p.9.
Fig A8.6	018LM.004	01023682-1-JU (Analysis, extensometer data analysis).xls	Summary of results can be found in UCCSN-UNR-024 vol. 11 p.12.
Table A8.1	018LM.004	01023682-1-JU (Summary, summary of results).doc	UCCSN-UNR-024 vol. 11 p.9.
Table A8.2	018LM.004	01023682-1-JU (Summary, summary of results).doc	UCCSN-UNR-024 vol. 11 p.10.
Table A8.3	018LM.004	01023682-1-JU (Summary, summary of results).doc	UCCSN-UNR-024 vol. 11 p.10.
Table A8.4	018LM.004	01023682-1-JU (Summary, summary of results).doc	UCCSN-UNR-024 vol. 11 p.12.

Fig A8.7	018LM.004	01023682-1-JU (Photos, inst).doc	UCCSN-UNR-024 vol. 11 attachment 8
Fig. or Table #	**DTN #**	**Source file within TDA**	**Scientific Notebook**
Fig A8.8	018LM.004	01023682-1-JU (Photos, post failure bottom).doc	UCCSN-UNR-024 vol. 11 attachment 8
Fig A9.1	018LM.004	01023663-3-JU (Analysis, LabView data analysis).xls	Summary of results can be found in UCCSN-UNR-024 vol. 11 p.14.
Fig A9.2	018LM.004	01023663-3-JU (Analysis, LabView data analysis).xls	Summary of results can be found in UCCSN-UNR-024 vol. 11 p.14.
Fig A9.3	018LM.004	01023663-3-JU (Analysis, LabView data analysis).xls	Summary of results can be found in UCCSN-UNR-024 vol. 11 p.14.
Fig A9.4	018LM.004	01023663-3-JU (Analysis, LabView data analysis).xls	Summary of results can be found in UCCSN-UNR-024 vol. 11 p.14.
Table A9.1	018LM.004	01023663-3-JU (Summary, summary of results).doc	UCCSN-UNR-024 vol. 11 p.14.
Table A9.2	018LM.004	01023663-3-JU (Summary, summary of results).doc	UCCSN-UNR-024 vol. 11 p.14.
Table A9.3	018LM.004	01023663-3-JU (Summary, summary of results).doc	UCCSN-UNR-024 vol. 11 p.14.
Fig A9.5	018LM.004	01023663-3-JU (Photos, pre-failure top).doc	This Photograph has been used for explanation purposes only.
Fig A9.6	018LM.004	01023663-3-JU (Photos, post-failure 180).doc	UCCSN-UNR-024 vol. 11 attachment 9
Fig A10.1	018LM.004	01023752-JU (Photos, pre-failure along 90).doc	Photograph of this specimen after testing can be found in

			UCCSN-UNR-024 vol. 11 attachment 10
Fig. or Table #	**DTN #**	**Source file within TDA**	**Scientific Notebook**
Fig A10.2	018LM.004	01023752-JU (Photos, pre-failure along 270).doc	UCCSN-UNR-024 vol. 11 attachment 10
Fig A10.3	018LM.004	01023752-JU (Analysis, LabView data analysis).xls	Summary of results can be found in UCCSN-UNR-024 vol. 11 p.18.
Fig A10.4	018LM.004	01023752-JU (Analysis, LabView data analysis).xls	Summary of results can be found in UCCSN-UNR-024 vol. 11 p.18.
Fig A10.5	018LM.004	01023752-JU (Analysis, LabView data analysis).xls	Summary of results can be found in UCCSN-UNR-024 vol. 11 p.18.
Fig A10.6	018LM.004	01023752-JU (Analysis, LabView data analysis).xls	Summary of results can be found in UCCSN-UNR-024 vol. 11 p.18.
Fig A10.7	018LM.004	01023752-JU (Analysis, LabView data analysis).xls	Summary of results can be found in UCCSN-UNR-024 vol. 11 p.19.
Fig A10.8	018LM.004	01023752-JU (Analysis, extensometer data analysis).xls	Summary of results can be found in UCCSN-UNR-024 vol. 11 p.20.
Table A10.1	018LM.004	01023752-JU (Summary, summary of results).doc	UCCSN-UNR-024 vol. 11 p.18.
Table A10.2	018LM.004	01023752-JU (Summary, summary of results).doc	UCCSN-UNR-024 vol. 11 p.18.
Table A10.3	018LM.004	01023752-JU (Summary, summary of results).doc	UCCSN-UNR-024 vol. 11 p.19.

Table A10.4	018LM.004	01023752-JU (Summary, summary of results).doc	UCCSN-UNR-024 vol. 11 p.20.
Fig. or Table #	**DTN #**	**Source file within TDA**	**Scientific Notebook**
Fig A10.9	018LM.004	01023752-JU (Photos, post-failure deeper litho).doc	UCCSN-UNR-024 vol. 11 attachment 10
Fig A10.10	018LM.004	01023752-JU (Photos, post-failure).doc	UCCSN-UNR-024 vol. 11 attachment 10
Fig A10.11	018LM.004	01023752-JU (Photos, pre-failure bottom).doc	This Photograph has been used for explanation purposes only.
Fig A10.12	018LM.004	01023752-JU (Photos, post-failure bottom).doc	This Photograph has been used for explanation purposes only.
Fig A11.1	018LM.004	01023696-JU (Analysis, LabView data analysis).xls	Summary of results can be found in UCCSN-UNR-024 vol. 11 p.22.
Fig A11.2	018LM.004	01023696-JU (Analysis, LabView data analysis).xls	Summary of results can be found in UCCSN-UNR-024 vol. 11 p.22.
Fig A11.3	018LM.004	01023696-JU (Analysis, LabView data analysis).xls	Summary of results can be found in UCCSN-UNR-024 vol. 11 p.22.
Fig A11.4	018LM.004	01023696-JU (Analysis, LabView data analysis).xls	Summary of results can be found in UCCSN-UNR-024 vol. 11 p.22.
Table A11.1	018LM.004	01023696-JU (Summary, summary of results).doc	UCCSN-UNR-024 vol. 11 p.22.
Table A11.2	018LM.004	01023696-JU (Summary, summary of results).doc	UCCSN-UNR-024 vol. 11 p.22.
Table A11.3	018LM.004	01023696-JU (Summary, summary of results).doc	UCCSN-UNR-024 vol. 11 p.22.

Fig. or Table #	DTN #	Source file within TDA	Scientific Notebook
Fig A11.5	018LM.004	01023696-JU (Photos, pre-failure along 90).doc	UCCSN-UNR-024 vol. 11 attachment 11 (Photographs are shown in the 0^0 and 270^0 directions)
Fig A11.6	018LM.004	01023696-JU (Photos, post-failure pieces).doc	UCCSN-UNR-024 vol. 11 attachment 11
Fig A12.1	018LM.004	01023584-3-JU (Analysis, LabView data analysis).xls	Summary of results can be found in UCCSN-UNR-024 vol. 11 p.26.
Fig A12.2	018LM.004	01023584-3-JU (Analysis, LabView data analysis).xls	Summary of results can be found in UCCSN-UNR-024 vol. 11 p.26.
Fig A12.3	018LM.004	01023584-3-JU (Analysis, LabView data analysis).xls	Summary of results can be found in UCCSN-UNR-024 vol. 11 p.26.
Fig A12.4	018LM.004	01023584-3-JU (Analysis, LabView data analysis).xls	Summary of results can be found in UCCSN-UNR-024 vol. 11 p.26.
Table A12.1	018LM.004	01023584-3-JU (Summary, summary of results).doc	UCCSN-UNR-024 vol. 11 p.26.
Table A12.2	018LM.004	01023584-3-JU (Summary, summary of results).doc	UCCSN-UNR-024 vol. 11 p.26.
Table A12.3	018LM.004	01023584-3-JU (Summary, summary of results).doc	UCCSN-UNR-024 vol. 11 p.26.
Fig A12.5	018LM.004	01023584-3-JU (Photos, pre-failure along 0).doc	UCCSN-UNR-024 vol. 11 attachment 12.

Fig. or Table #	DTN #	Source file within TDA	Scientific Notebook
Fig A12.6	This Photograph has been used for explanation purposes only.	Not applicable	Not applicable
Fig A12.7	This Photograph has been used for explanation purposes only.	Not applicable	Not applicable
Figures B1 through B7	018LM.004	01015464-JU (Analysis, LabView data analysis).xls 01015013-2-JU (Analysis, LabView data analysis).xls 01015463-JU (Analysis, LabView data analysis).xls 01014953-1-JU (Analysis, LabView data analysis).xls 01014731-JU (Analysis, LabView data analysis).xls 01023570-1-JU (Analysis, LabView data analysis).xls 01023575-3-JU (Analysis, LabView data analysis).xls 01023682-1-JU (Analysis, LabView data analysis).xls 01023663-3-JU (Analysis, LabView data analysis).xls	UCCSN-UNR-024 vol. 8, pp. 2-28, 55, 58, 60, 78-81, 87, 90. UCCSN-UNR-024 vol. 8, pp. 29-44, 55, 58, 60, 78, 84-85, 87, 88, 90. Vol. 11, pp. 29-37. UCCSN-UNR-024 vol. 8, pp. 45-57, 59, 61-62, 78-80, 82, 86, 87-89, 90. UCCSN-UNR-024 vol. 8 pp. 63-69, 78, 86, 90. UCCSN-UNR-024 vol. 8 pp. 70-78, 87, 89, 90. UCCSN-UNR-024 vol. 8 pp. 91-95. UCCSN-UNR-024 vol. 11 pp. 2-7 UCCSN-UNR-024 vol. 11 pp. 8-12. UCCSN-UNR-024 vol. 11 pp. 13-16.

continued		01023752-JU (Analysis, LabView data analysis).xls	UCCSN-UNR-024 vol. 11 pp. 17-20.
Fig. or Table #	**DTN #**	**Source file within TDA**	**Scientific Notebook**
Figures B1 through B7 continued		01023696-JU (Analysis, LabView data analysis).xls 01023584-3-JU (Analysis, LabView data analysis).xls Plus 01014731-JU (Summary), 01015464-JU (Summary), 01015013-2-JU (Summary, Summary of Results), 01015463-JU (Summary, Summary of Results), 01014953-1-JU (Summary), 01023570-1-JU\(Summary), 01023575-3JU\MTS data, 01023682-1-JU\MTS data, 01023663-3JU\MTS data, 01023752-JU\MTS data, 01023696-JU\MTS data, 01023584-3JU\Summary of Results. Additional Data in Report\Appendix B.xls.	UCCSN-UNR-024 vol. 11 pp. 21-24. UCCSN-UNR-024 vol. 11 pp. 25-28.
Figures B8 through B9	018LM.004	01015464-JU (Analysis, LabView data analysis).xls 01015013-2-JU (Analysis, LabView data analysis).xls 01015463-JU (Analysis, LabView data analysis).xls 01014953-1-JU (Analysis, LabView data analysis).xls 01014731-JU (Analysis, LabView data analysis).xls 01023570-1-JU (Analysis, LabView data analysis).xls	UCCSN-UNR-024 vol. 8 pp. 2, 20-25 UCCSN-UNR-024 vol. 8 pp. 30, 37-43 UCCSN-UNR-024 vol. 8 pp. 45-53 UCCSN-UNR-024 vol. 8 pp. 63-69 UCCSN-UNR-024 vol. 8 pp. 70-77 UCCSN-UNR-024 vol. 8 pp. 91-93

continued		01023575-3-JU (Analysis, LabView data analysis).xls	UCCSN-UNR-024 vol. 11 pp. 2-7
Fig. or Table #	**DTN #**	**Source file within TDA**	**Scientific Notebook**
Figures B8 through B9 continued		01023682-1-JU (Analysis, LabView data analysis).xls 01023663-3-JU (Analysis, LabView data analysis).xls 01023752-JU (Analysis, LabView data analysis).xls 01023696-JU (Analysis, LabView data analysis).xls 01023584-3-JU (Analysis, LabView data analysis).xls Additional Data in Report\Appendix B.xls.	UCCSN-UNR-024 vol. 11 pp. 9-10 UCCSN-UNR-024 vol. 11 pp. 13-15 UCCSN-UNR-024 vol. 11 pp. 17-19 UCCSN-UNR-024 vol. 11 pp. 21-24 UCCSN-UNR-024 vol. 11 pp. 25-27
Fig C1.1	018LM.004	01023540-2-JU (Photos, photos).doc	UCCSN-UNR-024 vol. 11 attachment 14.
Fig C1.2	018LM.004	01023540-2-JU (Analysis, LabView data analysis).xls	Summary of results can be found in UCCSN-UNR-024 vol. 11 p.30.
Fig C1.3	018LM.004	01023540-2-JU (Analysis, LabView data analysis).xls	Summary of results can be found in UCCSN-UNR-024 vol. 11 p.30.
Fig C1.4	018LM.004	01023540-2-JU (Analysis, LabView data analysis).xls	Summary of results can be found in UCCSN-UNR-024 vol. 11 p.30.
Fig C1.5	018LM.004	01023540-2-JU (Analysis, LabView data analysis).xls	Summary of results can be found in UCCSN-UNR-024 vol. 11 p.31.
Fig C1.6	018LM.004	01023540-2-JU (Analysis, LabView data	Summary of results can be

		analysis).xls	found in UCCSN-UNR-024 vol. 11 p.31.
Fig. or Table #	**DTN #**	**Source file within TDA**	**Scientific Notebook**
Fig C1.7	018LM.004	01023540-2-JU (Analysis, LabView data analysis).xls	Summary of results can be found in UCCSN-UNR-024 vol. 11 p.31.
Table C1.1	018LM.004	01023540-2-JU (Summary, summary of results).doc	UCCSN-UNR-024 vol. 11 p.30.
Table C1.2	018LM.004	01023540-2-JU (Summary, summary of results).doc	UCCSN-UNR-024 vol. 11 p.30.
Table C1.3	018LM.004	01023540-2-JU (Summary, summary of results).doc	UCCSN-UNR-024 vol. 11 p.31.
Table C1.4	018LM.004	01023540-2-JU (Summary, summary of results).doc	UCCSN-UNR-024 vol. 11 p.31.
Fig C1.8	018LM.004	01023540-2-JU (Photos, photos).doc	UCCSN-UNR-024 vol. 11 attachment 14.
Fig C2.1	018LM.004	01023540-5-JU (Photos, pre-failure).doc	UCCSN-UNR-024 vol. 11 attachment 13.
Table C2.1	018LM.004	01023540-5-JU (Summary, summary of results).doc	UCCSN-UNR-024 vol. 11 p.41.
Fig C2.2	018LM.004	01023540-5-JU (Analysis, analysis).xls	UCCSN-UNR-024 vol. 11 p.42
Fig C2.3	018LM.004	01023540-5-JU (Photos, pre-failure in machine).doc (Photograph taken from another view).	UCCSN-UNR-024 vol. 11 attachment 13. (Photograph taken from another view).
Table D1.1	018LM.004	01023540-1-DS (Analysis, analysis).xls	UCCSN-UNR-024 vol. 11 p.46
Fig D.1.2	018LM.004	01023540-1-DS (Analysis, analysis).xls	UCCSN-UNR-024 vol. 11 p.46

Fig D.1.3	018LM.004	01023540-1-DS (Analysis, analysis).xls	UCCSN-UNR-024 vol. 11 p.47
Fig. or Table #	**DTN #**	**Source file within TDA**	**Scientific Notebook**
Fig D.1.4	018LM.004	01023540-1-DS (Analysis, analysis).xls	UCCSN-UNR-024 vol. 11 p.47
Fig D1.5	018LM.004	01023540-1-DS (Photos, pre-failure surface).doc	UCCSN-UNR-024 vol. 11 attachment 15. (Photograph taken after testing).
Fig D1.6	018LM.004	01023540-1-DS (Photos, post-failure lower).doc	UCCSN-UNR-024 vol. 11 attachment 15.
Fig D1.7	018LM.004	01023540-1-DS (Photos, post-failure upper).doc	UCCSN-UNR-024 vol. 11 attachment 15.
Table D2.1	018LM.004	01014781-DS (Analysis, analysis).xls	UCCSN-UNR-024 vol. 11 p.48
Fig D2.1	018LM.004	01014781-DS (Analysis, analysis).xls	UCCSN-UNR-024 vol. 11 p.49
Fig D2.2	018LM.004	01014781-DS (Analysis, analysis).xls	UCCSN-UNR-024 vol. 11 p.49
Fig D2.3	018LM.004	01014781-DS (Analysis, analysis).xls	UCCSN-UNR-024 vol. 11 p.50
Fig D2.4	018LM.004	01014781-DS (Analysis, analysis).xls	UCCSN-UNR-024 vol. 11 p.50
Fig D2.5	018LM.004	01014781-DS (Analysis, analysis).xls	UCCSN-UNR-024 vol. 11 p.51
Table D2.2	018LM.004	01014781-DS (Summary, summary of results).doc	UCCSN-UNR-024 vol. 11 p.51

Fig D2.6	018LM.004	01024781-DS (Photos, lower half encapsulated).doc	UCCSN-UNR-024 vol. 11 attachment 16.
Fig. or Table #	**DTN #**	**Source file within TDA**	**Scientific Notebook**
Fig D2.7	018LM.004	01024781-DS (Photos, upper half encapsulated).doc	UCCSN-UNR-024 vol. 11 attachment 16.
Fig D2.8	018LM.004	01024781-DS (Photos, post-failure lower half).doc	UCCSN-UNR-024 vol. 11 attachment 16.
Fig D2.9	018LM.004	01024781-DS (Photos, post-failure upper half).doc	UCCSN-UNR-024 vol. 11 attachment 16.
Fig D2.10	018LM.004	01014781-DS.doc (Fig. 2.6).	UCCSN-UNR-024 vol. 11 attachment 16.
Fig D2.11	018LM.004	01014781-DS.doc (Fig. 2.7).	UCCSN-UNR-024 vol. 11 attachment 16.
Table D3.1	018LM.004	01014782-DS (Summary, summary of results).doc	UCCSN-UNR-024 vol. 11 p.52
Fig D3.1	018LM.004	01014782-DS (Analysis, analysis 1).xls	UCCSN-UNR-024 vol. 11 p.53
Table D3.2	018LM.004	01014782-DS (Summary, summary of results).doc	UCCSN-UNR-024 vol. 11 p.53
Fig D3.2	018LM.004	01014782-DS (Analysis, analysis 1).xls	Summary of results can be found in UCCSN-UNR-024 vol. 11 p.53
Fig D3.3	018LM.004	01014782-DS (Analysis, analysis 1).xls	Summary of results can be

			found in UCCSN-UNR-024 vol. 11 p.53
Fig. or Table #	**DTN #**	**Source file within TDA**	**Scientific Notebook**
Fig D3.4	018LM.004	01014782-DS (Analysis, analysis 2).xls	Summary of results can be found in UCCSN-UNR-024 vol. 11 p.53
Fig D3.5	018LM.004	01014782-DS (Analysis, analysis 2).xls	Summary of results can be found in UCCSN-UNR-024 vol. 11 p.53
Fig D3.6	018LM.004	01014782-DS (Analysis, analysis 3).xls	Summary of results can be found in UCCSN-UNR-024 vol. 11 p.53
Fig D3.7	018LM.004	01014782-DS (Analysis, analysis 3).xls	Summary of results can be found in UCCSN-UNR-024 vol. 11 p.53
Fig D3.8	018LM.004	01024782-DS (Photos, pre-test upper).doc	UCCSN-UNR-024 vol. 11 attachment 17.
Fig D3.9	018LM.004	01024782-DS (Photos, pre-test lower).doc	UCCSN-UNR-024 vol. 11 attachment 17.
Fig D3.10	018LM.004	01024782-DS (Photos, post-test upper).doc	UCCSN-UNR-024 vol. 11 attachment 17.
Fig D3.11	018LM.004	01024782-DS (Photos, post-test lower).doc	UCCSN-UNR-024 vol. 11 attachment 17.
Fig D3.12	018LM.004	01024782-DS (Summary of Results), Fig. 3.2.	UCCSN-UNR-024 vol. 11. p. 54.
Fig D3.13	018LM.004	01024782-DS (Summary of Results), Fig. 3.3.	UCCSN-UNR-024 vol. 11 p. 55.
Table D4.1	018LM.004	01023540-3-DS (Summary, summary of results).doc	UCCSN-UNR-024 vol. 11 p.57

Fig. or Table #	DTN #	Source file within TDA	Scientific Notebook
Fig. D4.1	018LM.004	01023540-3-DS (Analysis, analysis).xls	UCCSN-UNR-024 vol. 11 p.57
Table D4.2	018LM.004	01023540-3-DS (Summary, summary of results).doc	UCCSN-UNR-024 vol. 11 p.58
Fig D4.2	018LM.004	01023540-3-DS (Summary), Fig. 4.2.	UCCSN-UNR-024 vol. 11 p.58
Fig D4.3	018LM.004	01023540-3-DS (Summary), Fig. 4.3.	UCCSN-UNR-024 vol. 11 p.59
Fig D4.4	018LM.004	01023540-3-DS (Photos, pre-test upper).doc	UCCSN-UNR-024 vol. 11 attachment 18.
Fig D4.5	018LM.004	01023540-3-DS (Photos, pre-test lower).doc	UCCSN-UNR-024 vol. 11 attachment 18.
Fig D4.6	018LM.004	01023540-3-DS (Photos, post-test upper).doc	UCCSN-UNR-024 vol. 11 attachment 18.
Fig D4.7	018LM.004	01023540-3-DS (Photos, post-test lower).doc	UCCSN-UNR-024 vol. 11 attachment 18.
Table D5.1	018LM.004	01023540-6-DS (Summary, summary of results).doc	UCCSN-UNR-024 vol. 11 p.61
Fig. D5.1	018LM.004	01023540-6-DS (Analysis, analysis).xls	UCCSN-UNR-024 vol. 11 p.61
Table D5.2	018LM.004	01023540-6-DS (Summary, summary of results).doc	UCCSN-UNR-024 vol. 11 p.62
Fig D5.2	018LM.004	01023540-6DS (Summary), Fig. 5.2.	UCCSN-UNR-024 vol. 11 p.62
Fig D5.3	018LM.004	01023540-6-DS (Summary), Fig. 5.3.	UCCSN-UNR-024 vol. 11 p.62

Fig D5.4	018LM.004	01023540-6-DS (Photos, pre-test upper).doc	UCCSN-UNR-024 vol. 11 attachment 19.
Fig. or Table #	**DTN #**	**Source file within TDA**	**Scientific Notebook**
Fig D5.5	018LM.004	01023540-6-DS (Photos, pre-test lower).doc	UCCSN-UNR-024 vol. 11 attachment 19.
Fig D5.6	018LM.004	01023540-6-DS (Photos, post-test upper).doc	UCCSN-UNR-024 vol. 11 attachment 19.
Fig D5.7	018LM.004	01023540-6-DS (Photos, post-test lower).doc	UCCSN-UNR-024 vol. 11 attachment 19.